

**N-Confused Porphyrin Derivatives:
Syntheses, Tautomeric Existence, Exchange,
Aggregation Properties and Photodynamic Therapy**

BY

**AJESH P. THOMAS
CHEM07201004001**

**National Institute of Science Education and Research
Bhubaneswar, Odisha-751005**

*A thesis submitted to the
Board of Studies in Chemical Sciences
In partial fulfillment of requirements
For the degree of*

DOCTOR OF PHILOSOPHY

of

HOMI BHABHA NATIONAL INSTITUTE



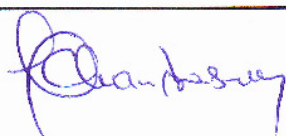
January, 2014

Homi Bhabha National Institute

Recommendations of the Viva Voce Committee

As members of the Viva Voce Committee, we certify that we have read the dissertation prepared by **Ajesh P. Thomas** entitled “**N-Confused Porphyrin Derivatives: Syntheses, Tautomeric Existence, Exchange, Aggregation Properties and Photodynamic Therapy**” and recommend that it may be accepted as fulfilling the thesis requirement for the award of Degree of Doctor of Philosophy.

Chairman - Prof. V. Chandrasekhar



Date:

8/5/14

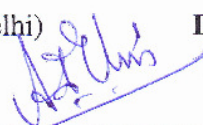
Guide/Convener - Prof. A. Srinivasan



Date:

08-05-'14

External Examiner – Prof. Anil J. Elias (IIT-Delhi)



Date:

8/5/14

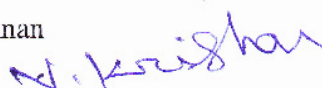
Member 1- Dr. U. Lourderaj



Date:

8/5/14

Member 2- Dr. V. Krishnan



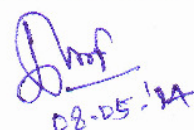
Date:

8/5/14

Final approval and acceptance of this thesis is contingent upon the candidate's submission of the final copies of the thesis to HBNI.

I/We hereby certify that I/we have read this thesis prepared under my/our direction and recommend that it may be accepted as fulfilling the thesis requirement.

Signature of Guide: (Prof. A. Srinivasan)



Date:

08-05-'14

Place: NISER-Bhubaneswar

STATEMENT BY AUTHOR

This dissertation has been submitted in partial fulfillment of requirements for an advanced degree at Homi Bhabha National Institute (HBNI) and is deposited in the Library to be made available to borrowers under rules of the HBNI.

Brief quotations from this dissertation are allowable without special permission, provided that accurate acknowledgement of source is made. Requests for permission for extended quotation from or reproduction of this manuscript in whole or in part may be granted by the Competent Authority of HBNI when in his or her judgment the proposed use of the material is in the interests of scholarship. In all other instances, however, permission must be obtained from the author.



Ajesh P. Thomas

DECLARATION

I, hereby declare that the investigation presented in the thesis has been carried out by me.
The work is original and has not been submitted earlier as a whole or in part for a degree
/ diploma at this or any other Institution / University.



Ajesh P. Thomas

List of Publications

a) Published

1. 9,10,19,20-Tetraarylporphycenes: K. S. Anju, S. Ramakrishnan, **Ajesh P. Thomas**, E. Suresh, and A. Srinivasan, *Org. Lett.* **2008**, *10*, 5545-5548.
2. Calix[n]metallocenyl[m]phyrins (n = 1, 2 and m = 2, 4): aryl vs. alkyl: S. Ramakrishnan, K. S. Anju, **Ajesh P. Thomas**, E. Suresh, and A. Srinivasan, *Chem. Commun.* **2010**, *46*, 4746-4748.
3. Calix[2]-m-benzo-[4]phyrin with Aggregation-Induced Enhanced Emission Characteristics: Application as Hg²⁺ Chemosensor: P. S. Salini, **Ajesh P. Thomas**, R. Sabarinathan, S. Ramakrishnan, K. C. Gowri Sreedevi, M. L. P. Reddy, and A. Srinivasan, *Chem. Eur. J.* **2011**, *17*, 6598-6601.
4. 5,5-Diaryldipyrromethanes: syntheses and anion binding properties: K. C. Gowri Sreedevi, **Ajesh P. Thomas**, P. S. Salini, S. Ramakrishnan, K. S. Anju, M. G. Derry Holaday, M. L. P. Reddy, C. H. Suresh, and A. Srinivasan. *Tetrahedron Lett.* **2011**, *52*, 5995-5999.
5. 4,4,9,9-Tetraphenyl pyrroloindolizine: A Structural Analogue of Calix[2]pyrrole: K. C. Gowri Sreedevi, **Ajesh P. Thomas**, S. Ramakrishnan, P. S. Salini, M. G. Derry Holaday, M. L. P. Reddy, and A. Srinivasan. *Org. Biomol. Chem.* **2012**, *10*, 3600-3605.
6. *meso-Tetrakis(p-sulfonatophenyl) N-Confused Porphyrin Tetrasodium Salt: A Potential Sensitizer for Photodynamic Therapy: **Ajesh P. Thomas**, P. S. Saneesh Babu, S. Asha Nair, S. Ramakrishnan, Danaboyina Ramaiah, T. K. Chandrashekar, A. Srinivasan and M. Radhakrishna Pillai. *J. Med. Chem.* **2012**, *55*, 5110-5120.
7. ansa-Ferrocene-Incorporated Calixpyrroles and Calixphyrins: Syntheses and Spectral/Structural Characterization. S. Ramakrishnan, K. S. Anju, **Ajesh P. Thomas**,

K. C. Gowri Sreedevi, P. S. Salini, M. G. Derry Holaday, Eringathodi Suresh, and A. Srinivasan. *Organometallics* **2012**, *31*, 4166-4173.

8. **meso*-Tetrakis(3,5-dihydroxyphenyl)N-Confused Porphyrin: Influence of polar protic and aprotic solvents in tautomeric existence, exchange and morphology. **Ajesh P. Thomas**, K. C. Gowri Sreedevi, B. Adinarayana, S. Ramakrishnan, and A. Srinivasan. *RSC Adv.* **2013**, *3*, 16967-16972.

*Pertaining to thesis

b) Communicated

1. Photoenolization of Diformyl Diaryldipyrromethane *via* ESDPT to Result in “Turn On” Fluorescence. K. C. Gowri Sreedevi, **Ajesh P. Thomas**, K. H. Aparna, Renuka Pradhan, M. L. P. Reddy, U. Lourderaj, and A. Srinivasan. *Chem. Sci.*

c) Manuscript under preparation

1. *Anion Induced Aggregation of *meso*-tetrakis(3,5-dihydroxyphenyl)N-Confused Porphyrin.
2. *Photodynamic Therapeutic application of *meso*-tetrakis(3,5-dihydroxyphenyl)N-Confused Porphyrin.
3. *Morphological changes of free base and Ag(III) complex of long chain substituted derivatives of N-confused porphyrin.

Conferences attended

1. Symposium on Advanced Biological Inorganic Chemistry (SABIC–2009), November 04-07, 2009, organised by Tata Institute of Fundamental Research, Mumbai. India.
2. National Seminar on frontiers in chemistry, November 11-14, 2010, conducted at School of Chemical Sciences, National Institute of Science Education and Research (NISER), Bhubaneswar, India.
3. Symposium in chemistry, Chemical Research Society of India (CRSI-2011), Feb 4-6, 2011, conducted at Kalinga Institute of Industrial Technology (KIIT), Bhubaneswar, India. Presented a poster entitled “N-Confused Porphyrins: Sensitizers for PDT Applications”.
4. Indo-European symposium on frontiers of chemistry, November 10-12, 2011, conducted at School of Chemical Sciences, National Institute of Science Education and Research (NISER), Bhubaneswar, India.



Ajesh P. Thomas

Dedicated to

My ammachi and appachan

ACKNOWLEDGEMENTS

I would like to express my gratitude to Prof. A. Srinivasan, my guide, for continuous support, encouragement, patience exhibited and freedom provided for free thinking.

I am thankful to Prof. T. K. Chandrashekar, Director-NISER for the laboratory facilities, CSIR-New Delhi and DST for financial support.

I thank my TMC members, Dr. U. Lourderaj and Dr. J. N. Behra, chairperson-SCS, Dr. M. Sarkar, all other faculties in SCS and scientific officer Dr. Arun Kumar for their support. Also, I appreciate the help provided by Mr. Sanjay during NMR analyses.

I remember our collaborators in RGCB-Trivandrum, Dr. Asha Nair and Mr. Saneesh Babu with immense pleasure for their valuable contributions.

I thank all my friends and seniors in NIIST, especially Dr. Ramakrishnan, Salini, Derry, Dr. Anju, Biju, Rony, Anoop, Vimal, Sajith, karu, Adarsh, Suneesh, Veda, Dr. Sreejith, Dr. Gokul, Dr. Rajesh Kompan, Dr. Abhilash, Dr. Biju A. T., Dr. Suneesh C. V. and Dr. Ratheesh K. V. for their sincere company and suggestions. And obviously, Daisy chechy, for the food she served and the sincere affection and care offered.

I thank Adi, my junior in NISER for his support and also other group members, Gourav, Garima and Kavya for their help. I remember, Suchitra, Sabari, Divya, Apramita, Amol, Narashimha, Prerna and Kushal, who have worked with me in different time period.

I remember all my friends in NISER with great gratitude, especially, Sudir, Anoop, Subbu, Janni (Manoj), Giri, Sadu (Mriganka), prabhat, Abhash, Asim, Om and Baalu.

I am greatly thankful to my wife Dr. Gowri Sreedevi for her support, suggestions, care and being with me during this period.

Finally, above all I thank my teachers, brother (Sajesh), father (Thomas) and mother (Rosy) for their unconditional love, care, affection and support.

Ajesh

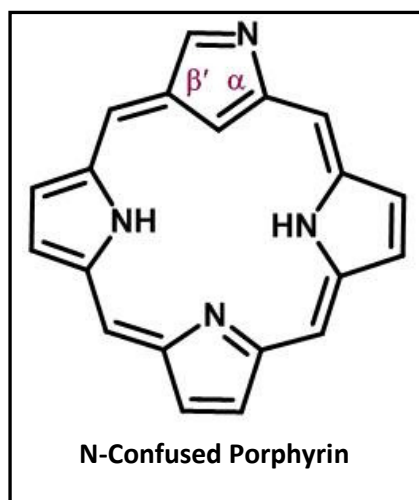
CONTENTS

	Page No.
Thesis title	1
Recommendations of Viva Voce Board	2
Statement by the Author	3
Declaration	4
Publication List	5
Dedications	8
Acknowledgements	9
Contents	10
Synopsis	11
List of Schemes	21
List of Figures	22
List of Tables	29
List of Abbreviations	30
Chapter 1	32
Chapter 2	71
Chapter 3	109
Chapter 4	139
Summary	185
References	186

SYNOPSIS

Porphyrins represent one of the most widely studied of all known macrocyclic ring systems [1]. Interest in these tetrapyrrolic macrocycles is broadly based on the multiple biological functions which includes electron transfer, oxygen transport and catalytic substrate oxidation. Porphyrins and their reduced derivatives such as chlorins, bacteriochlorins, isobacteriochlorins and corrins are backbones of many important natural pigments of life, including heme, vitamin B₁₂, chlorophyll, bacteriochlorophyll etc [1]. Porphyrin derivatives are also known for their ability to form wide variety of metal complexes. Apart from these, porphyrins in their freebase as well as metallated state found applications in many scientific fields ranging from biology, electronics, material science, catalysis and medicine. This chemical richness has inspired the study of a whole range of porphyrin analogues in past few decades [2, 3].

The term ‘porphyrin analogue’ is used in broad sense in porphyrin chemistry. In the most general sense, porphyrin analogues may be defined as cyclic systems consisting of pyrrolic units which are not naturally occurring [4]. These analogues were further classified in order to distinguish systems with no conjugation, partial conjugation and with complete electronic conjugation. The first and second type are represented as calixpyrrole and calixphyrin respectively, while the last set represents systems with contracted, expanded and isomeric structures with respect to porphyrin. A rearrangement of pyrrole and methine bridges resulted in porphyrin isomers, which have the same molecular formula, C₂₀H₁₄N₄ and 18 π electrons in their cyclic conjugated pathway. These porphyrin isomers have been classified into two groups, ‘nitrogen in’ isomers and ‘nitrogen out’ isomers. The “nitrogen in” porphyrin isomers include porphycene (2.0.2.0), corrrhycene (2.1.0.1), hemiporphycene (2.1.1.0) and isoporphycene (3.0.1.0) [5-7].



On the other hand the ‘nitrogen out’ isomer includes a porphyrin isomer known as N-confused porphyrin (**NCP**), where one or more nitrogen atoms are outside the ring. **NCP** differs largely from the parent porphyrin in physical, chemical, structural, and coordination properties. The $\alpha\alpha'$ -linkage in normal porphyrin is replaced with $\alpha\beta'$ -linkage in **NCP** and

are considered as the true isomer of porphyrin, where the *meso*-carbons are arranged in the same fashion (1.1.1.1) as in the case of normal porphyrin. The fascinating isomer of porphyrin was introduced in 1994 by two independent groups, Furuta and co-workers from Japan and Latos-Grażyński and co-workers from Poland [8, 9].

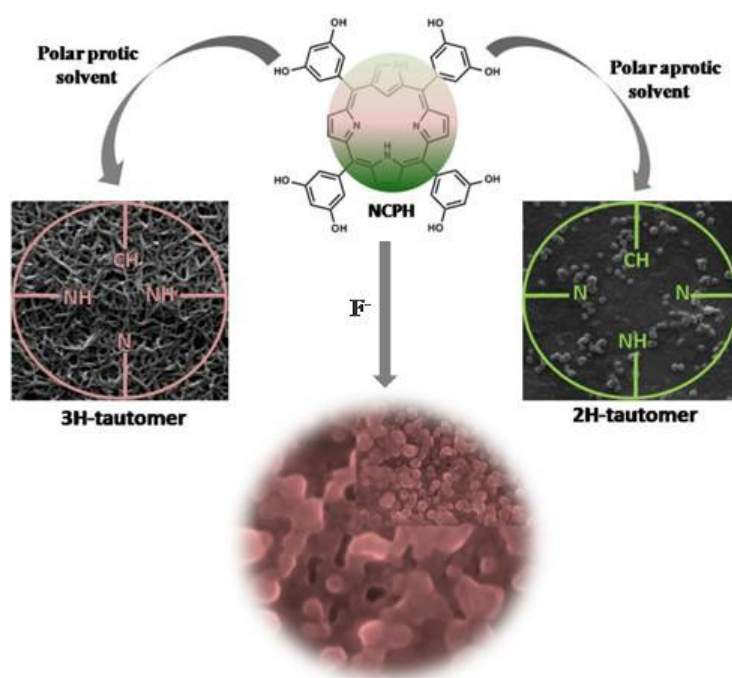
Since after the discovery of the isomer, research based on this molecule was preferentially targeting the structural modification as well as the versatile coordination ability of the molecule to stabilize various metal ions of usual and unusual oxidation states [10]. However, there are very few reports that explore properties like anion binding ability and applications in the area of biological and material science [11, 12]. Hence, the main objective of this thesis is to investigate the possible applications of various **NCP** derivatives in such areas. The thesis is organized into the following four chapters.

Chapter 1: Introduction (N-Confused Porphyrin: Past and Present)

A general introduction about **NCP**, which includes various synthetic methodologies, structural modifications and coordination chemistry is described in this chapter. Different synthetic methodologies were adopted for the synthesis of various **NCP** derivatives, starting from the first report of Furuta *et. al* and Latos-Grażyński *et. al* the modified procedure of Lindsey *et. al* [13] and multistep synthetic methodologies for doubly N-confused porphyrin, core-modified and expanded **NCP**. Apart from the structural and

synthetic modifications, **NCP** derivatives are known for their versatile coordination chemistry, which was elaborately studied and a significant number of metal complexes were reported [10]. The chapter reviews the metal complexes of **NCP**, where it stabilizes different unusual oxidation states of metals, which ranges from main group elements to late and early transition metal complexes. Also, applications of **NCP** derivatives are explained briefly, including anion binding studies and catalytic applications. Finally, the chapter ends with discussing the aim of the present thesis.

Chapter 2: *meso*-Tetrakis(3,5-dihydroxyphenyl)*N*-Confused Porphyrin: Tautomeric Existence, Exchange and Influence of Tautomerism and Anions on Morphological Features



Even though porphyrin based nanoarchitectures are well established, supramolecular assemblies of **NCP** and its derivatives are not explored much. This chapter describes the synthesis, spectral and structural characterization, solvent dependent tautomeric existence, exchange and aggregation behaviour of a novel octa-hydroxy *N*-confused porphyrin derivative; *meso*-tetrakis(3,5-dihydroxyphenyl)*N*-Confused porphyrin

(NCPH) [14]. The first part of the chapter investigates the tautomeric existence and exchange of NCPH in polar protic and aprotic solvents. The chapter demonstrates that the existence and switch over between the 3H and 2H tautomeric forms of NCP derivatives can be controlled exclusively by polar protic and aprotic solvents, rather than the established polar and non-polar nature of the solvent.

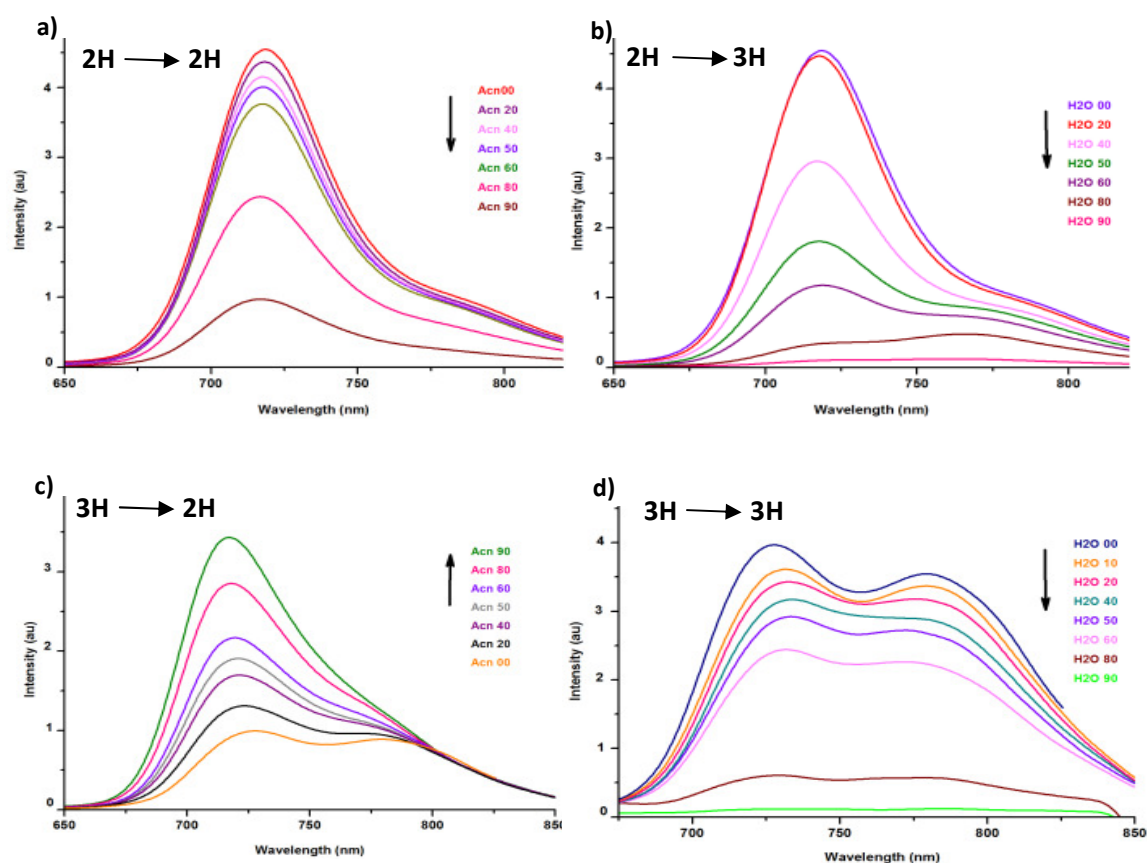
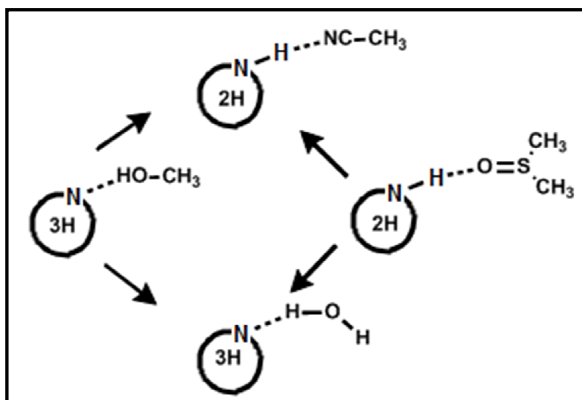


Figure A. Change in the emission characteristics of NCPH in (a) DMSO/ACN, (b) DMSO/H₂O, (c) MeOH/ACN and (d) MeOH/H₂O with increasing amount of ACN and H₂O.



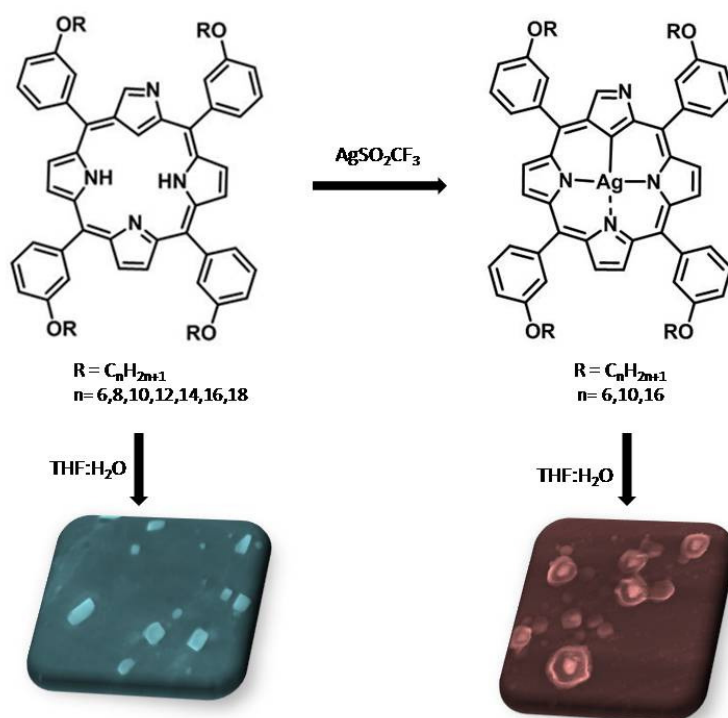
The tautomeric existence and exchange were investigated in solvent combinations such as (a) DMSO/ACN, (b) DMSO/H₂O (c) MeOH/ACN and (d) MeOH/H₂O by various spectroscopic techniques. Figure A shows change in the emission spectra

of **NCPH** during aggregation, which proves tautomeric existence and exchange of **NCPH** in the mixture of solvents, depending upon their protic and aprotic nature facilitated by the hydrogen bonding formation in the particular solvent as shown here. The solvent driven aggregation were also monitored through scanning electron microscopy (SEM) and atom force microscopy (AFM) analysis. The different morphological features observed in the different solvent combinations were explained on the basis of change in the planarity of the tautomeric forms and there by difference in the intermolecular hydrogen bonding formation possible in the two tautomers in the particular medium.

The second part of the chapter demonstrates the anion induced aggregation of **NCPH**, where the peripheral hydroxyl and NH protons participate in hydrogen bonding with anions to facilitate the formation of aggregated structures. In addition to routine spectral analyses, the anion induced aggregation was monitored by ITC, SEM and DLS analysis. Upon addition of initial 4 equiv of fluoride (F⁻) ions resulted in gradual decrease in the absorbance of Soret (450 nm) and Q-bands of **NCPH**. Further addition (up to 20 equivalents) of F⁻ ions accompanied with the appearance of red-shifted Soret band at 472 nm, corresponds to the J-aggregates which were formed by the complexation. Interestingly, the emission maximum of **NCPH** experienced a prominent blue-shift of about 30 nm by the addition of F⁻ ions with significance increase in the fluorescence quantum yield. This can be attributed to the enhanced rigidity, which can be expected

during aggregation by intermolecular hydrogen bonding. Further, the involvement of peripheral hydroxyl and NH protons in the hydrogen bonding formation with anions is confirmed by ^1H NMR, IR and ITC analysis. Formation of nanospheres during aggregation was observed by SEM analysis and the size of nanostructure by DLS analysis.

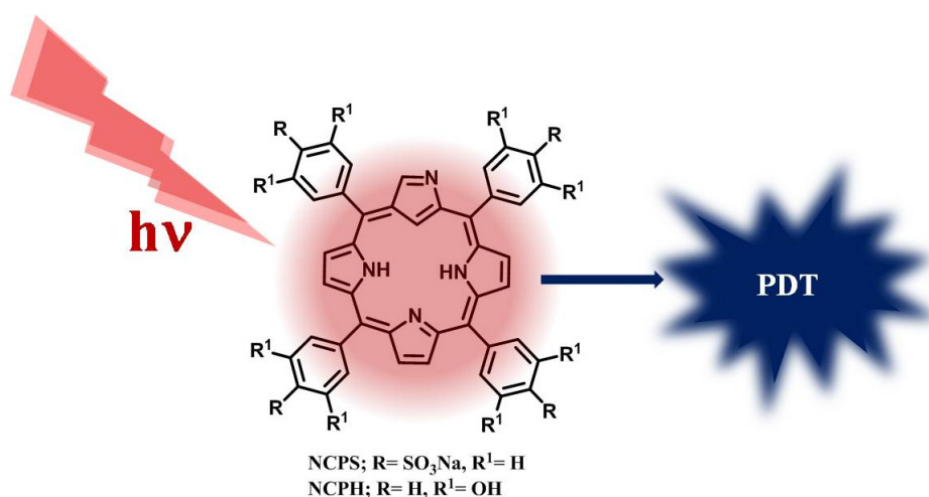
Chapter 3: *meso*-Tetrakis(3-alkoxyphenyl)N-Confused Porphyrins and Their Ag(III) Complexes; Synthesis, Characterization and Aggregation Behaviour



Porphyrins substituted with alkyl chains are found suitable in different areas such as liquid crystalline material and self assembled nanostructures [15]. The synthesis of porphyrins with alkyl chains at β -positions is difficult due to the high steric hindrance induced by the alkyl substituents, where insertions of alkyl chains on the *meso*-aryl rings are comparatively easy. Usually, alkyl substitution to the porphyrin fragment increases the solubility of the porphyrin in organic solvents. This chapter describes the synthesis, structural, spectral characterization and aggregation behaviour of long chain substituted

NCP derivatives, *meso*-tetrakis(3-alkoxyphenyl)*N*-confused porphyrins and their Ag(III) complexes. The number of carbon atoms in the alkyl side chain varies from 6 to 18 in the free base **NCP**. Ag(III) complexes of **NCP** derivatives were synthesized for the 6, 8 and 10 derivatives and the formation of desired compounds were confirmed by different spectral analyses. This chapter further describes the influence of metallation on the morphological features during aggregation, where aggregation in each case was achieved by increasing the amount of H₂O in a THF solution of compounds. Both in the case of free base and metallated forms, as the H₂O concentration increases from 50% to 90%, due to extended hydrophobic interaction the morphology of aggregated structures deforms continuously to attain cubic and flower like structures at 10:90 (THF/H₂O) ratio of solvents respectively. The different morphological features exhibited by the free base and metallated **NCP** is explained on the basis of structural changes occurred to the free base structure on metallation.

Chapter 4: N-Confused Porphyrin Derivatives as PDT Sensitizers



In recent years, photodynamic therapy (PDT) has emerged as a promising and noninvasive treatment for various types of cancer. The technique involves controlled generation of short-lived cytotoxic agents within a cell on irradiation of a prodrug or

photosensitizer, which in turn destroys the affected cells. This chapter describes the PDT application of two **NCP** derivatives, *meso*-hydroxy (**NCPH**) and *p*-sulfonato-phenyl substituted (**NCPS**) derivatives [16], which have better molar extinction coefficient in the red region of visible light compared with normal porphyrin derivatives. The chapter documents photophysical studies of these molecules, which give promising values for parameters required for PDT such as triplet and singlet oxygen quantum yield. The results encouraged us to investigate *in vitro* anticancer studies with both **NCP** derivatives. The photodynamic activity of **NCPS** was evaluated against eight different cell lines, namely, human colon cancer cells (HCT-116), human breast cancer cells (MCF7-ER, PR positive, and MDA-MB-231-ER, PR negative), human pancreatic cancer cells (MIA-PaCa-2), human cervical cancer cells (HeLa and SiHa), and human oral cancer cells (SCC-172 and SCC-131), where **NCPS** exhibited more photocytotoxicity to adenocarcinomas than the other epithelial cell lines, and maximum activity has been attributed toward breast adenocarcinoma MDA-MB-231 cells, with an IC₅₀ value as low as 6 μM, where corresponding value for **NCPH** was 12 μM. Upon illumination, generation of reactive oxygen species and apoptosis induced pathway of cell death was also described in the chapter. Apoptosis mediated cell death was established by a set of experiments, which proves cell membrane asymmetry, chromatin condensation, mitochondrial potential change and PARP [poly(ADP-ribose)polymerase] cleavage.

Over all, the thesis exhibits different **NCP** derivatives and reveal their properties and applications, which were not explored till date.

References

1. Kadish, K. M.; Smith, K. M.; Guillard, R. *The Porphyrin Handbook*, Academic Press: San Diego, CA, **2000**.
2. Jasat, A.; Dolphin, D. *Chem. Rev.* **1997**, *97*, 2267-2340.
3. Sessler, J. L.; Weghorn, S. J. *Tetrahedron Organic Chemistry series*, Expanded, Contracted and Isomeric Porphyrins, Pergamon, New York, **1997**.
4. Sessler, J. L. *J. Porphyrins Phthalocyanines* **2000**, *4*, 331-336.
5. Vogel, E.; Kocher, M.; Schmickler, H.; Lex, J. *Angew. Chem. Int. Ed.* **1986**, *25*, 257-259.
6. Sessler, J. L.; Brucker, E. A.; Weghorn, S. J.; Kisters, M.; Schafer, M.; Lex, J.; Vogel, E. *Angew. Chem. Int. Ed.* **1994**, *33*, 2308-2312.
7. Callot, H. J.; Rohrer, A.; Tschamber, T. *New J. Chem.* **1995**, *19*, 155-159.
8. Furuta, H.; Asano, T.; Ogawa, T. *J. Am. Chem. Soc.* **1994**, *116*, 767-768.
9. Chmielewski, P. J.; Latos-Grażyński, L.; Rachlewicz, K.; Głowiak, T. *Angew. Chem. Int. Ed.* **1994**, *33*, 779-781.
10. Toganoh, M.; Furuta, H. *Chem. Commun.* **2012**, *48*, 937-954.
11. Xie, Y.; Morimoto, T.; Furuta, H. *Angew. Chem. Int. Ed.* **2006**, *45*, 6907-6910.
12. Niino, T.; Toganoh, M.; Andrioletti, B.; Furuta, H. *Chem. Commun.* **2006**, 4335-4337.
13. Geier, G. R. III; Haynes, D. M.; Lindsey, J. S. *Org. Lett.* **1999**, *1*, 1455-1458.
14. Thomas, A. P.; Gowri Sreedevi, K. C.; Adinarayana, B.; Ramakrishnan, S.; Srinivasan, A. *RSC Adv.* **2013**, *3*, 16967-16972.
15. Shearman, G. C.; Yahioğlu, G.; Kirstein, J.; Milgromb, L. R.; Seddon, J. M. *J. Mater. Chem.* **2009**, *19*, 598-604.

16. Thomas, A. P.; Saneesh Babu, P. S.; Asha Nair, S.; Ramakrishnan, S.; Ramaiah, D.; Chandrashekar, T. K.; Srinivasan, A.; Radhakrishna Pillai, M. *J. Med. Chem.* **2012**, *55*, 5110-5120.

List of Schemes

1.	Scheme 1.1	Rothemund synthesis of tetraphenylporphyrin	36
2.	Scheme 1.2	Synthesis of C₆F₅-NCP	48
3.	Scheme 1.3	Synthesis of <i>meso</i> -free NCP by (a) [2 + 2] and (b) [3 + 1] MacDonald Condensation	48
4.	Scheme 1.4	Synthesis of <i>cis</i> - N₂CP	49
5.	Scheme 1.5	Synthesis of <i>trans</i> - N₂CP	49
6.	Scheme 1.6	Synthesis of thiophene and furan incorporated NCP	50
7.	Scheme 1.7	Synthesis of selenophene incorporated NCP	50
8.	Scheme 1.8	Synthesis of dithia NCP	51
9.	Scheme 1.9	Modified synthesis of thiophene, furan and selenophene incorporated NCP	51
10.	Scheme 1.10	Synthesis of N₂CP-Hex derivatives	52
11.	Scheme 1.11	Synthesis of N₃CP-Hex	53
12.	Scheme 1.12	Synthesis of NCP-Hex derivatives	53
13.	Scheme 1.13	Synthesis of NCP₂	54
14.	Scheme 2.1	Synthetic scheme for NCP	86
15.	Scheme 3.1	Synthetic scheme for NCP-n and NCP-n-Ag	118
16.	Scheme 4.1	Synthetic route for NCPS	160

List of Figures

1.	Figure 1.1	Porphyrin and reduced porphyrin derivatives	33
2.	Figure 1.2	Biologically relevant porphyrin derivatives	34
3.	Figure 1.3	(a) β -substituted and (b) <i>meso</i> -substituted porphyrin	35
4.	Figure 1.4	Porphyrin analogues	37
5.	Figure 1.5	X-ray crystal structure of (a) Calix[4]pyrrole and (b) chloride complex of calix[4]pyrrole	39
6.	Figure 1.6	X-ray crystal structure of (a) MeOH and (b) DMF adduct of Me₈-CPy	39
7.	Figure 1.7	UV-Vis absorption spectral changes of Pyr-Cphy with F ⁻ addition	41
8.	Figure 1.8	Contracted porphyrinoids	41
9.	Figure 1.9	Tetrapyrrolic expanded porphyrins	43
10.	Figure 1.10	Pentapyrrolic expanded porphyrins	43
11.	Figure 1.11	Hexapyrrolic expanded porphyrins	44
12.	Figure 1.12	Porphyrin isomers	45
13.	Figure 1.13	N-confused porphyrin	46
14.	Figure 1.14	Reported metal complexes of NCP	55
15.	Figure 1.15	Ni and Ag metal complexes of NCP	55
16.	Figure 1.16	Structure of Cu and Sb complex of NCP	56
17.	Figure 1.17	Structures of Pd-NCTTP complexes	57
18.	Figure 1.18	Structure of [NCP-Fe(II)-1]	58
19.	Figure 1.19	Structure of Rh complexes of NCP	59
20.	Figure 1.20	X-ray structure of Mn, Zn and Fe complexes of NCP	61
21.	Figure 1.21	Structure of Pt complexes of NCP	62

22.	Figure 1.22	Structure of Co complexes of NCP	63
23.	Figure 1.23	Structure of Mo complex of NCP	65
24.	Figure 1.24	Structure of (a) Ir and (b) Sn complexes of NCP	65
25.	Figure 1.25	Structure of Li complexes of NCP	67
26.	Figure 1.26	Synthesis of Ln(III) double-decker complex, [M^{III}Pc-NTBPP]	67
27.	Figure 1.27	X-ray crystal structure of (a) [NCP-Au(III)-Hex] and (b) [NCP-Au(III)-Pt(II)-Hex]	68
28.	Figure 2.1	Possible tautomeric structures of NCP	75
29.	Figure 2.2	Relative stabilization energy of different tautomers of NCP	77
30.	Figure 2.3	(a) Absorption spectra and the colour of two confused porphyrin tautomers and (b) emission spectrum of the tautomers	77
31.	Figure 2.4	X-ray single crystal structure of NCTTP obtained from (a) DMF-MeOH (2H) and (b) DCM-MeOH (3H)	79
32.	Figure 2.5	(a) Structure of the charged porphyrin units (b) TEM images of porphyrin nanotubes formed through ionic interactions between the porphyrin units	82
33.	Figure 2.6	TEM images of cobalt-porphyrin nanorods at different temperatures: (a) 273 K, (b) 298 K, (c) 308 K, (d) 318 K, and (e) 328 K	82
34.	Figure 2.7	I) Structure of PG, and II) absorption spectra of PG in (a) MeOH, (b) H ₂ O, (c) 10 mM acetate and (d) 0.5 mM anthraquinone-1,5-disulfonate	84
35.	Figure 2.8	(a) Structure of [H₄T(4-STh)P²⁻], (b) AFM images of the	84

deposited J-aggregate prepared from the aqueous solution of $[\text{H}_4\text{T}(\text{4-STh})\text{P}^{2-}]$ with 2 M HCl and (c) scheme for the H- and J- aggregate formation

- | | | | |
|-----|-------------|--|----|
| 36. | Figure 2.9 | ^1H -NMR spectrum of NCPH in $\text{DMSO-}d_6$ (a) structure of NCPH and (b) upfield region of ^1H NMR spectrum | 87 |
| 37. | Figure 2.10 | Absorption spectra of NCPH in different solvent systems | 88 |
| 38. | Figure 2.11 | Emission spectra of NCPH in different solvent systems | 90 |
| 39. | Figure 2.12 | FT-IR spectra of NCPH in (a) MeOH solution, (b) 1:1 mixture of MeOH/ACN (c) 1:9 mixture of MeOH/ACN, (d) DMSO solution, (e) 1:1 mixture of DMSO/ACN and (f) 1:9 mixture of DMSO/ACN | 92 |
| 40. | Figure 2.13 | Change in the absorption profile of NCPH on aggregation in mixture of solvents (a) MeOH/ACN, (b) MeOH/ H_2O , (c) DMSO/ACN and (d) DMSO/ H_2O | 93 |
| 41. | Figure 2.14 | Change in the absorption spectra of NCPH during acid titration in (a) MeOH and (b) DMSO | 94 |
| 42. | Figure 2.15 | Change in the emission characteristics of NCPH in (a) DMSO/ACN, (b) DMSO/ H_2O , (c) MeOH/ACN and (d) MeOH/ H_2O with increasing amount of ACN and H_2O | 95 |
| 43. | Figure 2.16 | Schematic representation of possible tautomeric structures in polar protic and aprotic solvents | 96 |
| 44. | Figure 2.17 | (a) SEM image of NCPH in MeOH/ H_2O (b) AFM image of NCPH in MeOH/ H_2O drop cast on mica sheet (c) SEM image of NCPH in MeOH/ACN (d) and (e) higher magnified images in MeOH/ACN mixture | 97 |

45.	Figure 2.18	SEM images of NCPH in a mixture of (a) DMSO/ACN and (b) DMSO/H ₂ O	98
46.	Figure 2.19	Changes observed in the absorption spectra of NCPH (8μM) in DMSO by the addition of (a) F ⁻ ions, (b) CN ⁻ ions, (c) CH ₃ CO ₂ ⁻ ions and (d) H ₂ PO ₄ ⁻ ions	99
47.	Figure 2.20	(a) The emission spectral changes of NCPH (8μM) in DMSO by the addition of F ⁻ ions, (b) The decay profile of NCPH and NCPH-F⁻ ions aggregate in DMSO	100
48.	Figure 2.21	IR spectral change of NCPH with gradual addition of F ⁻ ion	101
49.	Figure 2.22	¹ H NMR spectral change of NCPH with increased F ⁻ ion concentration	102
50.	Figure 2.23	ITC analysis for the complexation of NCPH and F ⁻ ions in DMSO	103
51.	Figure 2.24	SEM images of NCPH in DMSO after the addition of F ⁻ ion	104
52.	Figure 2.25	DLS analysis of NCPH in DMSO with F ⁻ ion	105
53.	Figure 3.1	Schematic representation of the ZnP3 rod	113
54.	Figure 3.2	Optical textures for the Zn porphyrins with differing chain lengths after cooling slowly from the isotropic phase. (a) dendritic texture of the C ₈ , (b) flower-like texture of the C ₁₀ , and (c) spherulitic texture of the C ₁₂	113
55.	Figure 3.3	SEM image of (a) a single (C ₇ H ₁₅) ₃ -NO ₂ P microrod and (b) sheet of (C ₇ H ₁₅) ₄ -P	114
56.	Figure 3.4	SEM images of Pt-AceZnPor prepared in DCM–hexane	115

(a-c) and DCM–MeOH (d-f), respectively

57.	Figure 3.5	SEM images of (a) Free base porphyrin and (b) Zn metallated form in hexane	116
58.	Figure 3.6	¹ H NMR spectrum of (a) NCP-6 and (b) NCP-6-Ag in CDCl ₃	119
59.	Figure 3.7	ESI-TOF-MS of NCP-6	120
60.	Figure 3.8	ESI-TOF-MS of NCP-6-Ag	121
61.	Figure 3.9	UV-Vis absorption spectrum of NCP-6 and NCP-6-Ag in THF	122
62.	Figure 3.10	UV-Vis absorption changes of NCP-6 during aggregation	123
63.	Figure 3.11	UV-Vis absorption changes of NCP-10 during aggregation	124
64.	Figure 3.12	UV-Vis absorption changes of NCP-16 during aggregation	125
65.	Figure 3.13	SEM images of NCP-10 in different volume of H ₂ O in a THF/H ₂ O mixture (v/v) (a) 50:50, (b) 40:60, (c) 30:70 and (d) 10:90	125
66.	Figure 3.14	Absorption changes of NCP-10-Ag with increased volume of H ₂ O	127
67.	Figure 3.15	SEM images of NCP-10-Ag in different volume of H ₂ O in a THF/H ₂ O (v/v) mixture; (a) 40:60, (b) 30:70, (c) 20:80, (d) 10:90 and (e) EDX analysis of NCP-10-Ag	128
68.	Figure 4.1	Modified Jablonski diagram for the formation of singlet oxygen	141
69.	Figure 4.2	Clinically used porphyrin photosensitizers	147
70.	Figure 4.3	Timeline of selected milestones in the historical	148

		development of PDT	
71.	Figure 4.4	Different shape diffusers for PDT	151
72.	Figure 4.5	Electronic transitions involved in the generation of singlet oxygen in solution	151
73.	Figure 4.6	Triplet absorption of NCPH in methanol. Inset shows the transient decay at 500 nm	155
74.	Figure 4.7	(a) Change in the absorption spectra of DPBF upon Irradiation with (i) NCPH (ii) TPPS in MeOH and (b) Plot of change in absorbance of DPBF at 411 nm vs irradiation time ($\lambda_{irr} > 600$ nm) in the presence of NCPH against TPPS as the standard in MeOH	158
75.	Figure 4.8	(a) Change in the absorption spectra of DPBF upon Irradiation with (i) NCPH (ii) TPPS in MeOH/ACN and (b) Plot of change in absorbance of DPBF at 411 nm vs irradiation time ($\lambda_{irr} > 600$ nm) in the presence of NCPH against TPPS as the standard in MeOH/ACN	159
76.	Figure 4.9	(a) ^1H NMR spectrum of NCPS in $\text{DMSO-}d_6$, (b) Expanded ^1H NMR spectrum of NCPS in the aromatic region.	161
77.	Figure 4.10	(a) Absorption spectra of NCPS in water and MeOH, (b) Emission spectra of NCPS with respect to TPP	162
78.	Figure 4.11	Triplet absorption of NCPS in deionized water recorded at 7.2 μs . Inset shows the transient decay at 490 nm	163
79.	Figure 4.12	Change in the absorption spectra of DPBF upon irradiation (a) NCPS , (b) TPPS in water (c) with NCPS (d) TPPS in MeOH. Plot of change in absorbance of DPBF at 411 nm	165

- vs irradiation time ($\lambda_{\text{irr}} > 600 \text{ nm}$) in the presence of **NCPS** against **TPPS** as the standard in (e) water and (f) MeOH
80. Figure 4.13 MTT assay was done on a panel of cancer cells and shows 167 cytotoxicity of **NCPS** in the presence and absence of light. **NCPS** shows significant cytotoxicity in the presence of light in all cells but shows negligible cytotoxicity in the absence of light.
81. Figure 4.14 (a) Flow Cytometry analysis, (b) Fluorescence images of 169 MDA-MB-231 cells shows enhanced fluorescence after PDT with 6 μM and 12 μM of **NCPS**
82. Figure 4.15 Flow cytometric analysis of the cell death mechanism 171 induced by **NCPS** upon PDT treatment
83. Figure 4.16 Characterization of cytotoxic actions of **NCPS** in PDT 172 using Hoechst stain after PDT with **NCPS** (6 μM and 12 μM). In Hoechst staining, chromatin condensation was visualized using fluorescence microscope
84. Figure 4.17 Characterization of cytotoxicity of **NCPS** during PDT 173 using JC1 Fluorescence cytochemistry. In JC1 staining, cells with red colour indicate healthy cells with high mitochondrial membrane potential and green coloured apoptotic cells with low mitochondrial membrane potential
85. Figure 4.18 PARP cleavage observed after PDT with **NCPS**. Here 174 there is no PARP cleavage observed in both light and dark controls but there is significant cleavage at a concentration of 6 and 12 μM of **NCPS**

86.	Figure 4.19	MTT assay of NCPH in the presence and absence of light.	175
		NCPH shows significant cytotoxicity in the presence of light but shows negligible cytotoxicity in the absence of light	
87.	Figure 4.20	Flow cytometric analysis of the cell death mechanism induced by NCPH upon PDT treatment	176
88.	Figure 4.21	Characterization of cytotoxic actions of NCPH in PDT using Hoechst stain after PDT with NCPH (10 μ M and 20 μ M). In Hoechst staining, chromatin condensation was visualized using fluorescence microscope	177

List of Table

1.	Table 4.1	Comparison of IC ₅₀ Values of NCPS in a panel of cancer cells.	168
----	-----------	--	-----

List of Abbreviations

CH ₃ CN	Acetonitrile
CH ₃ CO ₂ ⁻	Acetate
BF ₃ .OEt ₂	Borontrifluoride diethyletherate
BBr ₃	Borontribromide
C ₆ H ₅ CO ₂ ⁻	Benzoate
CCD	Cambridge crystallographic data
CHCl ₃	Chloroform
CN ⁻	Cyanide ion
CD ₂ Cl ₂	Deuteriated dichloromethane
CDCl ₃	Deuteriated chloroform
CD ₃ CN	Deuteriated acetonitrile
DCM	Dichloromethane
DDQ	2,3-dichloro-5,6-dicyano-1,4-benzoquinone
DMAc	Dimethylacetamide
DMF	Dimethylformamide
MTT	3-(4,5-Dimethylthiazol-2-yl)-2,5-diphenyltetrazolium bromide
DPBF	1,3-Diphenylisobenzofuran
H ₂ PO ₄ ⁻	Dihydrogen phosphate
DMSO	Dimethylsulphoxide
DMEM	Dulbecco's Modified Eagle Medium
EtOAc	Ethyl acetate
equiv.	Equivalents
FAB	Fast atomic bombardment

FT-IR	Fourier transformation infra red
F ⁻	Fluoride ion
h	Hours
min	Minutes
NCP	N-confused porphyrin
NMR	Nuclear magnetic resonance
H ₂ SO ₄	Sulfuric acid
TFA	Trifluoroacetic acid
THF	Tetrahydrofuran
TBAF	Tetrabutylammonium fluoride
TLC	Thin layer chromatography
TMS	Tetramethylsilane
<i>p</i> -TSA	<i>para</i> -toluene sulphonic acid
UV	Ultraviolet

CHAPTER 1

N-Confused Porphyrin; Past and Present

1.1	Porphyrin	33
1.2	Porphyrin analogues	37
1.2.1	Calixpyrrole	38
1.2.2	Calixphyrin	40
1.2.3	Contracted Porphyrin	41
1.2.4	Expanded Porphyrin	42
1.2.5	Porphyrin Isomers	46
1.2.5.1	N-confused Porphyrin	46
1.2.5.1.1	Synthesis and spectral properties of NCP derivatives	47
1.2.5.1.2	Metal complexes of NCP	54
1.2.5.1.3	Applications of NCP metal complexes	69
1.3	Objective of the present thesis	70

1.1 Porphyrin

Porphyrins represent one of the most widely studied of all known macrocyclic ring systems [1]. Interest in these tetrapyrrolic macrocycles is broadly based on the multiple biological functions which includes electron transfer, oxygen transport and catalytic substrate oxidation [1]. Porphyrins and their reduced derivatives such as chlorins, bacteriochlorins, isobacteriochlorins and corrins (Figure 1.1) are backbones of many important natural pigments of life, including heme, vitamin B₁₂, chlorophyll, bacteriochlorophyll etc (Figure 1.2). Porphyrin derivatives are also known for their ability to form wide variety of metal complexes [1]. Apart from these, porphyrins in its freebase as well as metallated state found applications in many scientific fields ranging from biology, electronics, material science, catalysis and medicine [1]. This chemical richness has inspired the study of a whole range of porphyrin analogues in past few decades [2, 3].

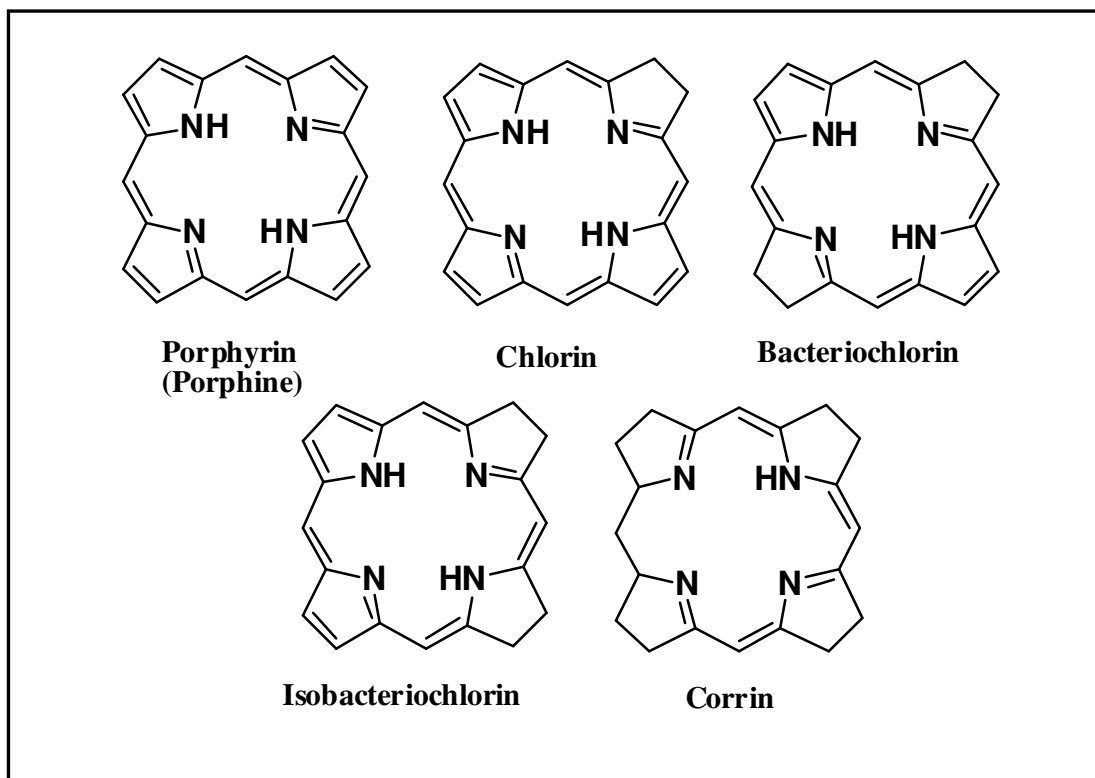


Figure 1.1. Porphyrin and reduced porphyrin derivatives.

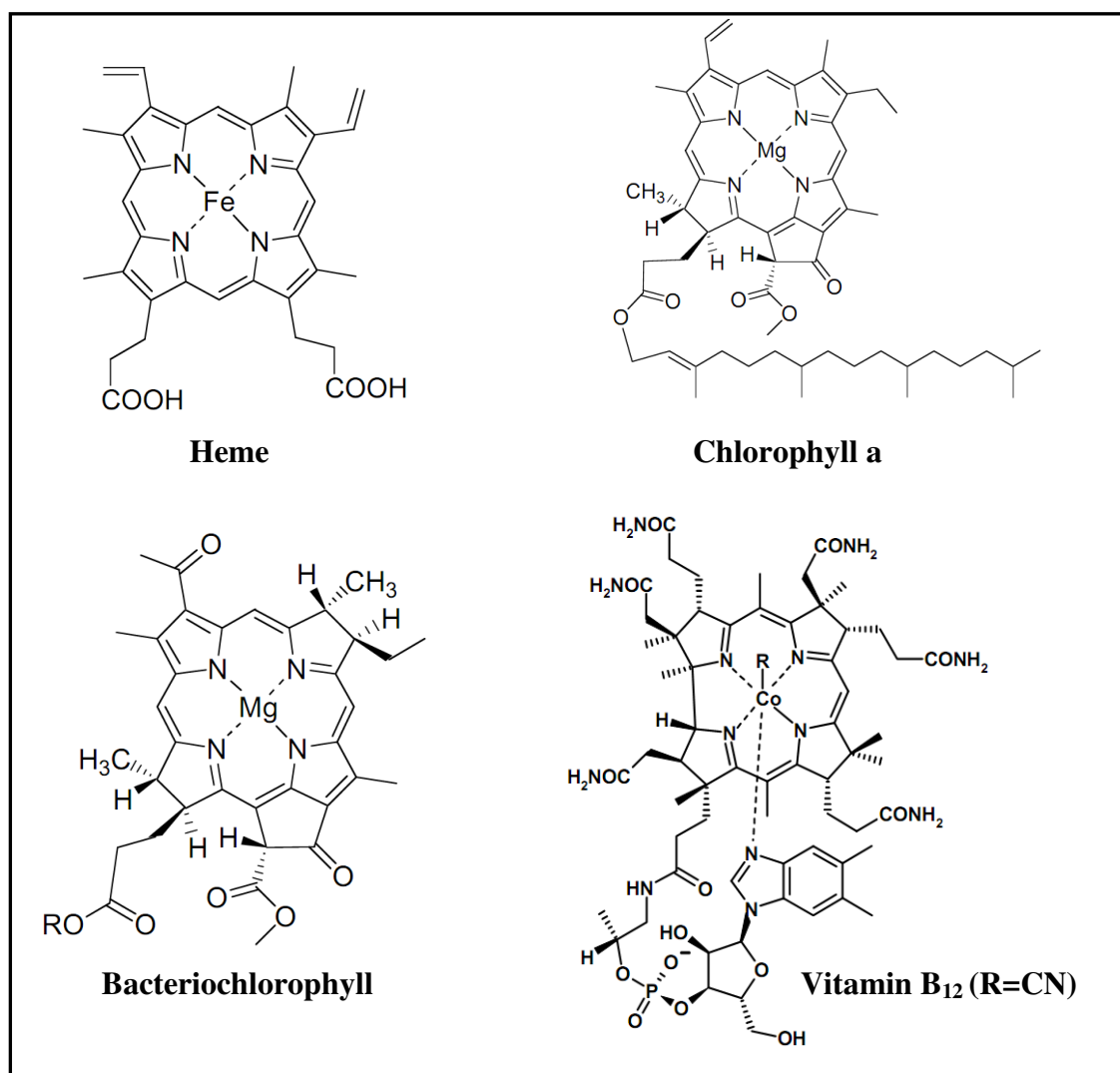


Figure 1.2. Biologically relevant porphyrin derivatives.

The term ‘porphyrin’ comes from the Greek word, ‘porphyrus’, meaning reddish-purple. The parent form of these tetrapyrrolic macrocycles is known as porphine (Figure 1.1). Four pyrrolic subunits linked together by four methine bridges (sp^2 -hybridized carbon) to form the macrocycle and has molecular formula of $C_{20}H_{14}N_4$. In fact, the derivatives of porphine are called porphyrins which have a porphine core with various substituents attached around the ring. Porphyrin is a 22π electron system whose main conjugation pathway contains 18π electrons and thus obeys the Hückel’s rule for aromaticity $(4n + 2)\pi$ electrons that provides an electron ring current at the core of the macrocycle. The diamagnetic anisotropy of the porphyrin ring is evident from the 1H

NMR spectral analysis, where the *meso* and pyrrolic protons resonate at the downfield region, while the inner NH protons appear in the negative region of the ^1H NMR spectrum [1].

The history of the porphyrins begins with the work of Lecanu, Berzelius, Scherer and Miilder [4, 6]. It was first thought that the reddish colour of blood was from iron. But, Scherer added $\text{con.H}_2\text{SO}_4$ to dried and powdered blood and washed the precipitate free of iron and found that the red colouration of blood was not due to iron, instead some other component present in blood. Since then, the chemistry of porphyrin synthesis has come across many stages and new methods were introduced that provide foundation for studies of porphyrins across a broad spectrum of scientific disciplines. The synthetic modifications mainly include diverse substituents in specific patterns about the periphery of the macrocycle and thus control the photophysical properties of the molecule for various applications. Two distinct pattern of substituent found highly useful, β -substituted porphyrin (Figure 1.3.a) and *meso*-substituted porphyrins (Figure 1.3.b). The β -substituted porphyrins exhibit close resemblance with many naturally occurring porphyrin derivatives, while *meso*-substituted porphyrins are not have directly linked to any biological counterpart, however found application as biomimetic models and as useful components in material chemistry [1].

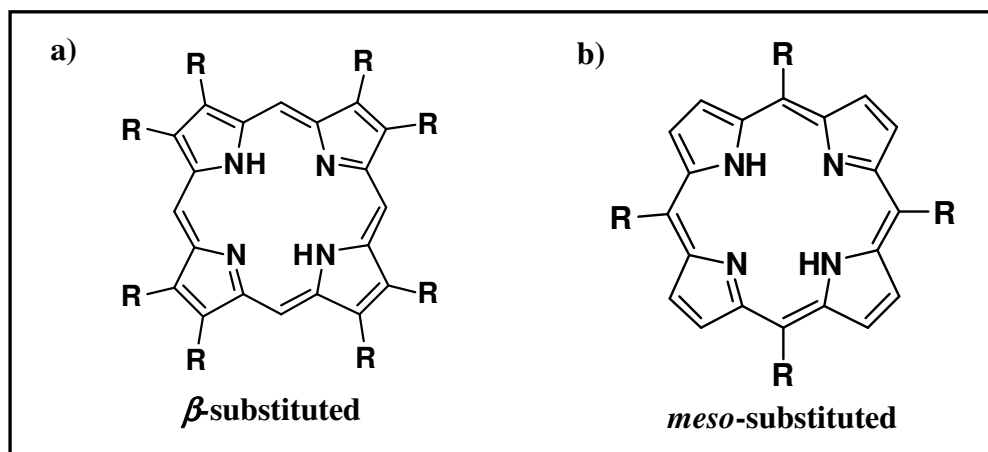
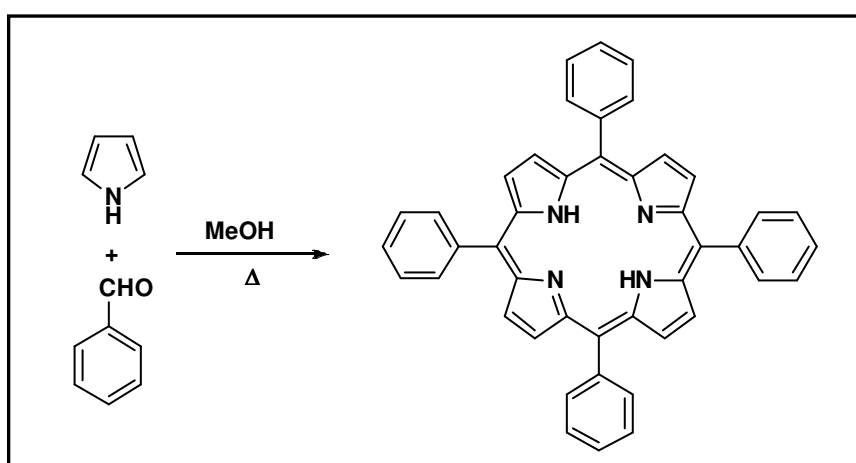


Figure 1.3. (a) β -substituted and (b) *meso*-substituted porphyrin.

In 1935, Rothmund introduced the first synthetic approach to *meso*-substituted porphyrins, by condensation reaction between pyrrole and a series of aryl aldehydes in MeOH at various temperatures (Scheme 1.1) [7]. The distinguishing feature of Rothmund synthesis was reaction at high temperature in sealed tube in the absence of added oxidizing agents. The improved synthesis was achieved by Adler and Longo upon refluxing the mixture of pyrrole and benzaldehyde in propionic acid under open air conditions [8].



Scheme 1.1. Rothmund synthesis of tetraphenyl porphyrin (TPP).

The most effective route for synthesis of symmetrical *meso*-aryl porphyrins was reported by Lindsey and co-workers [9]. The acid-catalyzed condensation of pyrrole and benzaldehyde using protic or Lewis acid followed by oxidation with chloranil or DDQ results in the syntheses of porphyrins under mild reaction conditions in good yields. The syntheses of less symmetrical *trans*-substituted porphyrins were achieved by the MacDonald [2 + 2] condensation of a dipyrromethane and a dipyrromethane dialdehyde [10]. However, syntheses of *cis*-substituted porphyrins were difficult [11].

1.2 Porphyrin analogues

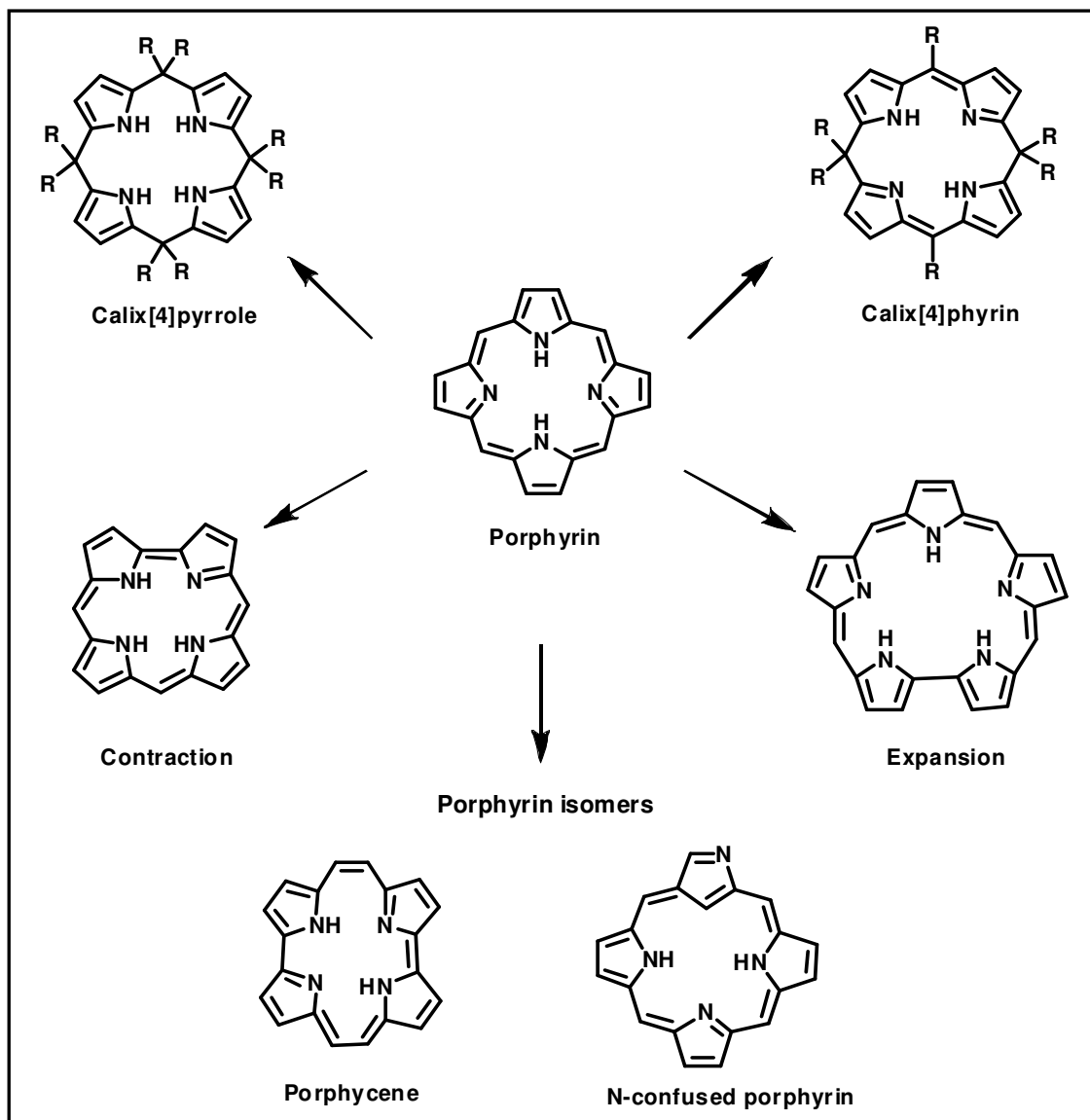


Figure 1.4. Porphyrin analogues.

The term 'porphyrin analogue' is used in broad sense in porphyrin chemistry. In the most general sense, porphyrin analogues may be defined as cyclic systems consisting of all pyrrole and are not naturally occurring [12]. These porphyrin analogues were further classified in order to distinguish systems with no conjugation, partial conjugation and with complete electronic conjugation. First and second of these group has been represented by porphyrin analogues that are well established under the title of calixpyrrole and calixphyrin respectively, where the last set represents systems with

contracted, expanded and isomeric structures with respect to porphyrin (Figure 1.4). These porphyrin analogues have versatile electronic and structural characteristics and found applications in diverse scientific areas.

1.2.1 Calixpyrrole

Over the last several decades, considerable effort has been devoted for developing efficient artificial receptors capable of forming complexes with selectively targeted guests, particularly anions and cations. One of the more attractive neutral anion receptors among this category is calix[4]pyrrole and derivatives. Calix[4]pyrrole, first synthesized by Bayer in 1886, has been found to bind F^- , Cl^- , and $H_2PO_4^-$ anions in organic solvents [13-16]. But, surprisingly the chemistry of calixpyrroles was not explored in the literature for nearly a century, even new synthetic methodologies were introduced in between [15]. The chemistry of this macrocycle attained momentum in 1990s, when Floriani and co-workers introduced series of metal complexes by using deprotonated calixpyrroles [16, 17]. However, these derivatives attained much attraction only after the contributions of Gale and Sessler that mainly focused on studying the anion binding properties of the calix[4]pyrroles [15, 18-20]. The N-H groups of the pyrrole moieties act as receptors through H-bond interactions whereas the tetrahedral *meso*-carbon bridges linking the pyrrole units assure an adequate conformational flexibility shifting from 1,3-alternate conformation in the absence of an anion (Figure 1.5.a) to a cone like conformation upon binding with anionic guests, which was proved by NMR analysis and single crystal X-ray structural studies (Figure 1.5.b) [14, 15].

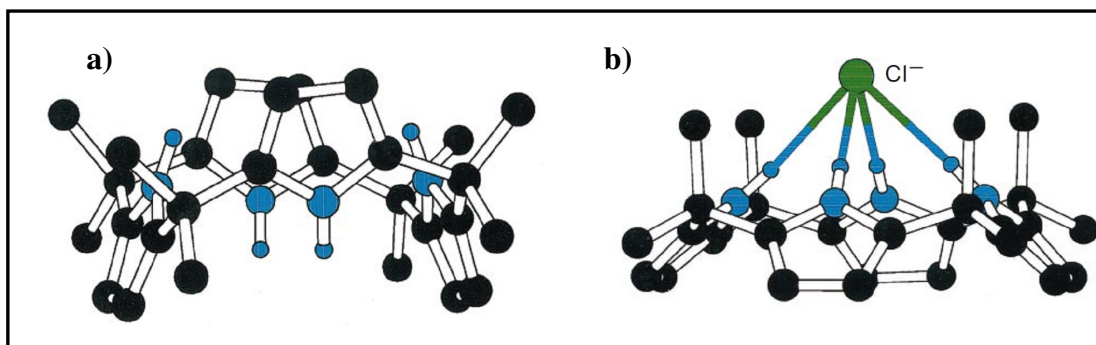


Figure 1.5. X-ray crystal structure of (a) Calix[4]pyrrole and (b) chloride complex of calix[4]pyrrole [15].

Also, investigations revealed that calix[4]pyrrole can form complexes with neutral species, even though the binding constants were modest. Sessler and co-workers describes the binding of a calixpyrrole system with MeOH and DMF by using X-ray crystal structure, where an octamethyl calixpyrrole (**Me₈-CPy**) unit binds with two MeOH molecule and adopts a 1,3-alternate conformation in the solid state. Two molecules of MeOH lie above and below the macrocycle with each one form hydrogen bonds to two pyrrolic NH groups (Figure 1.6.a). As observed in the MeOH adduct, for DMF also two molecules of guest bound above and below the host by an intermolecular hydrogen bonding and adopts a 1,2-alternate conformation of the calixpyrrole (Figure 1.6.b) [21].

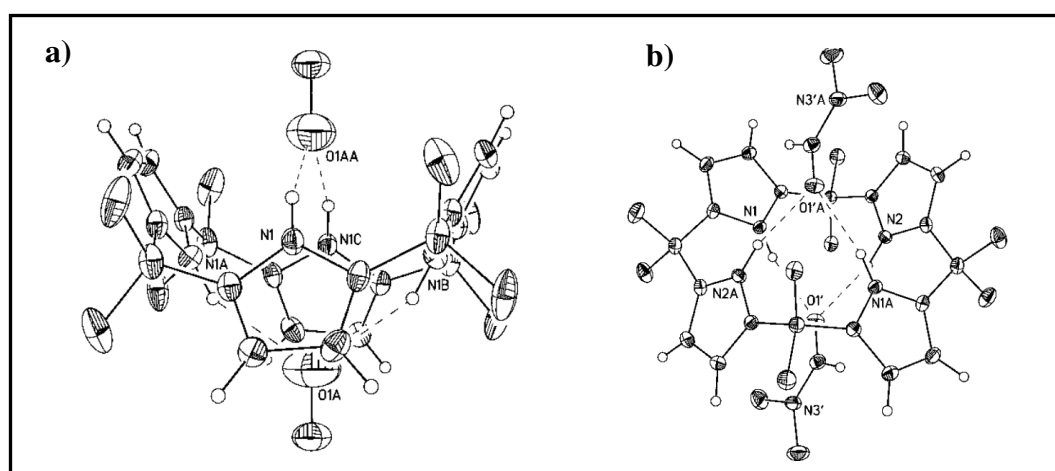


Figure 1.6. X-ray crystal structure of (a) MeOH and (b) DMF adduct of **Me₈-CPy** [21].

1.2.2 Calixphyrin

Calixphyrins, another porphyrin analogue have both sp^2 and sp^3 hybridized bridging *meso*-carbon atoms, possess reasonably flexible frameworks as well as π -conjugated networks, and are distinguishable from porphyrins and calixpyrroles [22]. Several research groups have established convenient methods for the synthesis of various calixphyrins and demonstrated their host-guest chemistry which shows affinity towards both anion and cations [23-28].

Calix[4]phyrins have proved more difficult to isolate and study than porphyrins due to their relative conformational and electronic instability, something that drives to oxidize to the corresponding porphyrin. Initial proof for the formation of these species thus came from spectroscopic analyses carried out during studies of porphyrin formation or reduction. Many initial species were isolated as metal complexes. The factors influencing stability were studied in terms of electronic and steric effects, allowing the evolution of stable non metallated species [24, 25]. In the *meso*-substituted aryl calixphyrins the sp^3 carbon atoms perturb their π -electron system and significantly modify the molecular shape and the flexibility thus can be used for fine tuning of the mechanical and chemical properties of these compounds [24].

Seong-Jin Hong and co-workers reported the synthesis and anion binding studies of a *meso*-pyrrylcalixphyrin derivative (**Pyr-Cphy**, Figure 1.7) [29]. The anion binding ability of the *meso*-pyrrylcalixphyrin was investigated using UV-Vis spectroscopy with F^- anion. A colour change from deep green to yellow was observed during the binding process with F^- ion. This colour change exclusively occurs with F^- and no detectable change in colour was observed with other halides. Benzicalixphyrins, introduced by Latos-Grażyński, found applicable in cation sensing by Hung *et al.* The non-fluorescent

solution of the free-base benzicalixpyrin changes to a red emitting solution with Zn^{2+} [27].

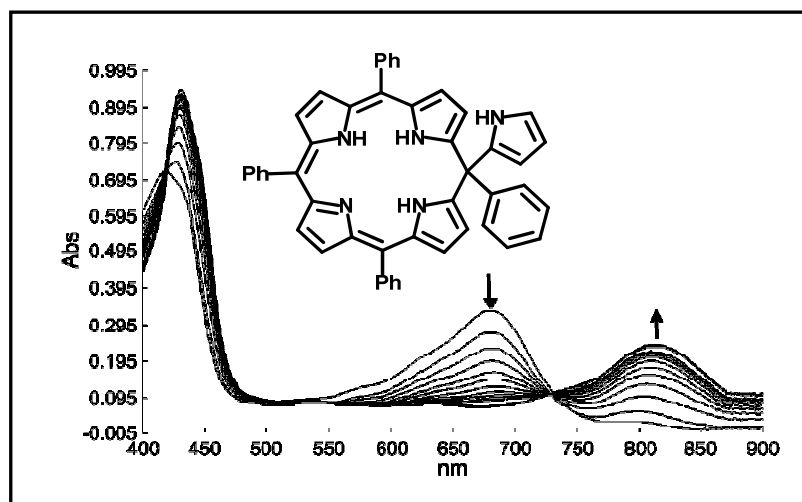


Figure 1.7. UV-Vis absorption spectral changes of **Pyr-Cphy** with F^- addition. Inset shows structure of **Pyr-cphy** [26].

1.2.3. Contracted porphyrin

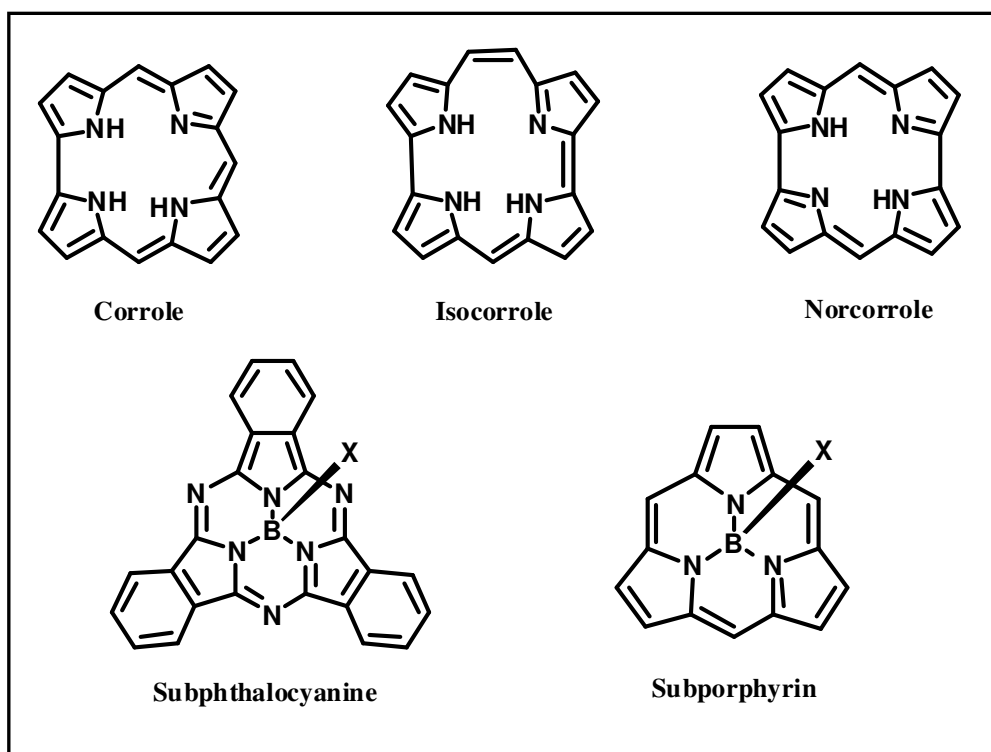


Figure 1.8. Contracted porphyrinoids.

The chemistry of contracted porphyrin was initiated by the structural elucidation of a naturally occurring molecule, vitamin B₁₂ in 1955. The contracted porphyrinoids have smaller macrocyclic π -conjugation as compared to the 18 π -electron conjugated system of normal porphyrins. After this, various contracted porphyrins such as corroles, isocorroles, norcorroles, subphthalocyanines and subporphyrins (Figure 1.8) were introduced in the last two three decades and coordination properties of these derivatives were explored further [30-36].

1.2.4 Expanded porphyrin

Woodward and co-workers were the first to report the probable existence of an expanded porphyrin, sapphyrin, a pentapyrrolic system [37]. Their pioneering efforts directed towards the synthesis of vitamin B₁₂ led to the serendipitous discovery of sapphyrin. Sapphyrin contains five pyrrole rings linked to each other with four *meso*-carbons and one direct pyrrole-pyrrole bond. Systematic syntheses of sapphyrin were not published until, when two independent reports, one by Woodward and co-workers and another by Broadhurst *et al.* were published [38, 39]. However, J. L. Sessler *et al.* introduced an improved method for the synthesis of the macrocycle [40].

Expanded porphyrins have larger internal cavity as compared to those present in natural tetrapyrroles. Expansion in the macrocycle can be achieved by three methods, (i) by increasing the number of bridging atoms separating the heterocyclic, (ii) by increasing the number of heterocyclic ring and (iii) by increasing both. The simplest expanded porphyrin known is homoporphyrin, contains an extra carbon atom between a *meso* and an α -pyrrolic carbon (Figure 1.9) [41].

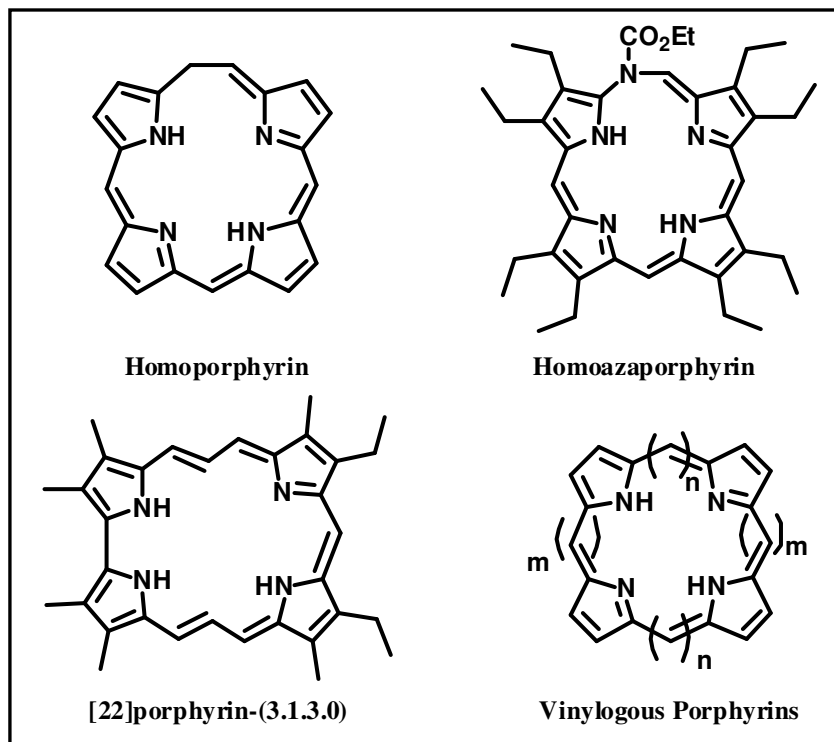


Figure 1.9. Tetrapyrrolic expanded porphyrins.

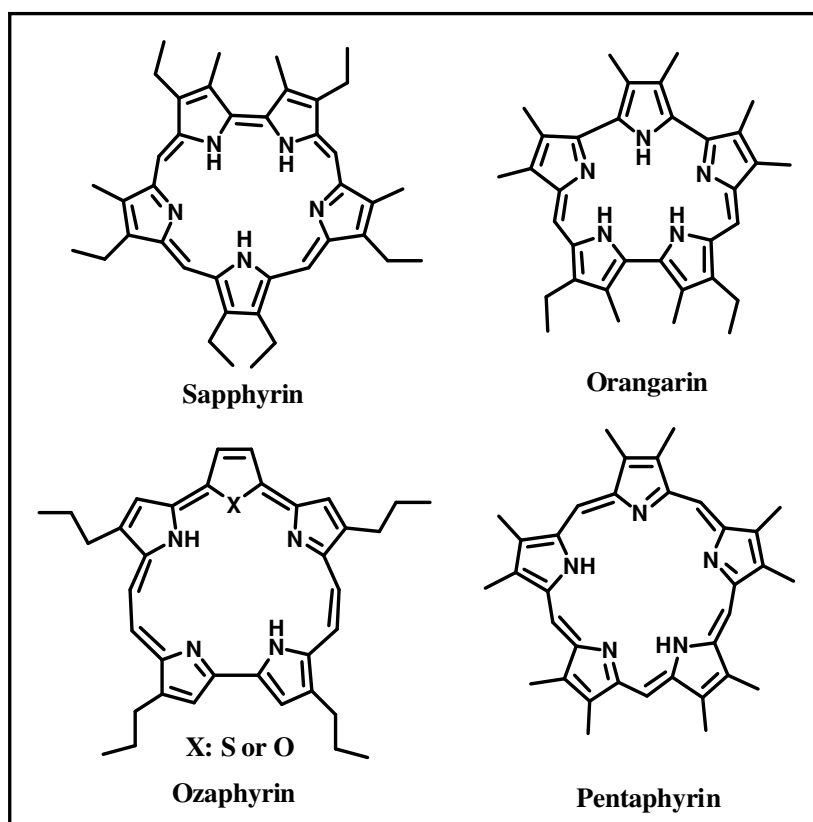


Figure 1.10. Pentapyrrolic expanded porphyrins.

In pentapyrrolic systems, other than sapphyrin, few more derivatives are known, which differ by number of *meso*-carbons connecting the pyrrolic rings. Pyrrole units are connected by (a) two methine bridges in a (1.0.1.0.0) fashion in orangarin, (b) four methine bridges connected in (2.0.2.0.0) fashion in ozaphyrin and five pyrrole rings are connected with five methine bridges in (1.1.1.1.1) fashion in pentaphyrin (Figure 1.10). Also, heteroatom incorporated pentaphyrins are also known in the literature [42-45].

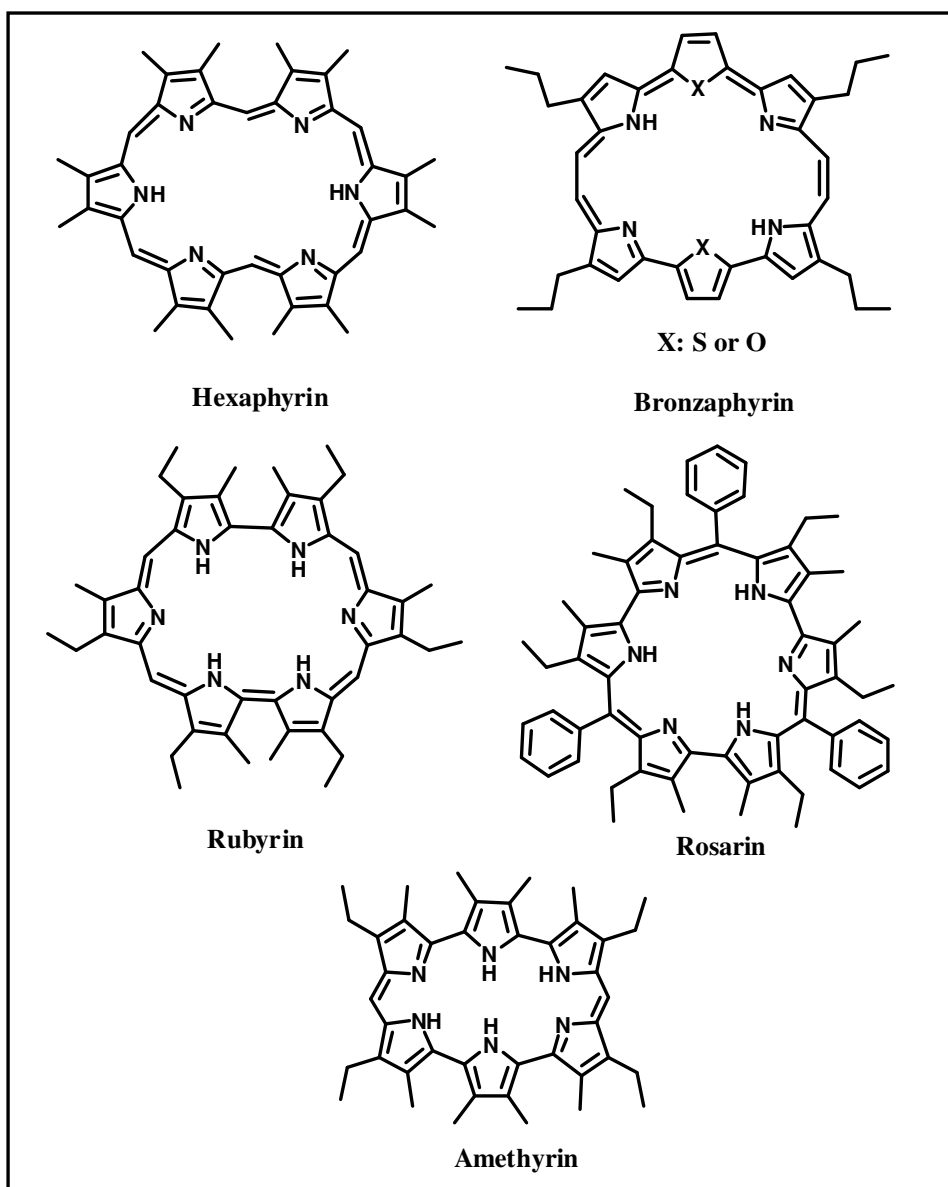


Figure 1.11. Hexapyrrolic expanded porphyrins.

A group of hexapyrrolic systems are also known in the literature and have different names depending on the number of *meso*-carbons present, which includes hexaphyrin (1.1.1.1.1.1), rubyrin (1.1.0.1.1.0), bronzaphyrin (2.0.0.2.0.0), rosarin (1.0.1.0.1.0) and amethyrin (1.0.0.1.0.0) as shown in Figure 1.11 [46-50].

Sessler's group reported the first planar 28π heptaphyrin with two *meso*-carbons and later 30π aromatic heptaphyrin [51-52]. Octaphyrins, macrocycle with eight pyrrole rings in conjugation reported by Vogel's group turned out to have figure eight conformation, leading to loss of aromaticity in the macrocycles [53]. In order to avoid the figure eight twist in the macrocycle, Sessler *et al.* adopted a strategy that reduce the number of *meso*-carbons linking the eight pyrrole rings and thus retain the aromaticity [54]. The next higher analogue, nonaphyrin was introduced by Osuka *et al.* where the nine pyrrole units are linked by equal number of *meso*-carbons [55]. Turcasarin, a decapyrrolic system was introduced by Sessler *et al.* in 1994 [56].

1.2.5. Porphyrin isomers

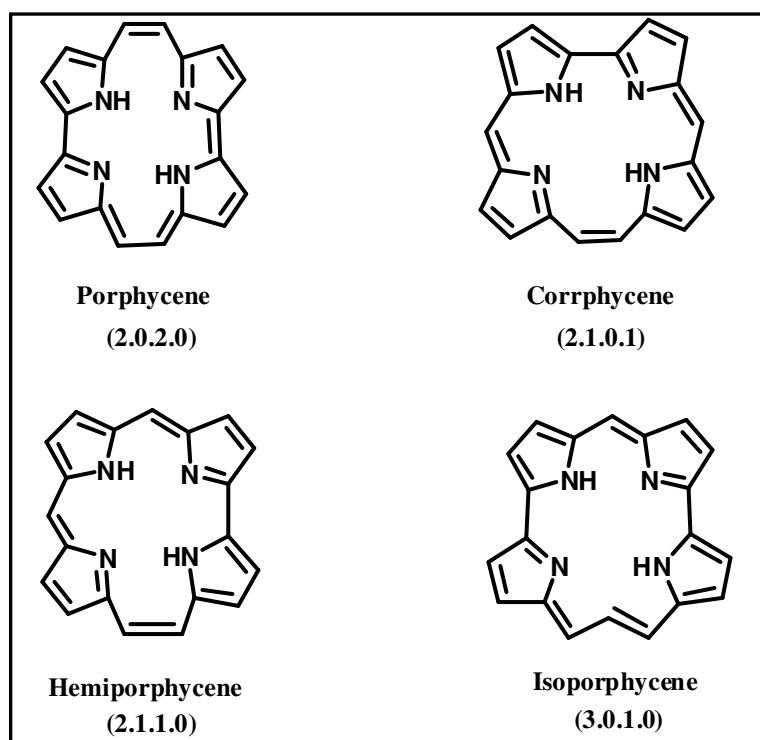


Figure 1.12. Porphyrin isomers.

A rearrangement of pyrrole and methine bridges resulted in porphyrin isomers, which have the same molecular formula, $C_{20}H_{14}N_4$ and 18π electrons in their cyclic conjugated pathway. These porphyrin isomers have been classified into two groups, ‘nitrogen in’ isomers and ‘nitrogen out’ isomers. The “nitrogen in” porphyrin isomers include porphycene (2.0.2.0), corphycene (2.1.0.1), hemiporphycene (2.1.1.0) and isoporphycene (3.0.1.0) as shown in Figure 1.12 [57-60]. On the other hand the ‘nitrogen out’ isomer includes a porphyrin isomer known as N-confused porphyrin (**NCP**), where one or more nitrogen atoms are outside the ring. These porphyrin isomers have emerged as attractive synthetic targets owing to their potential chemical interest and versatile coordination chemistry.

1.2.5.1 N-confused porphyrin

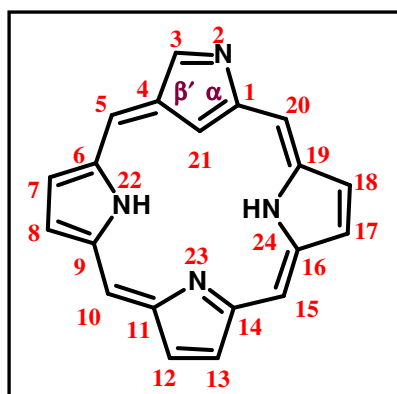


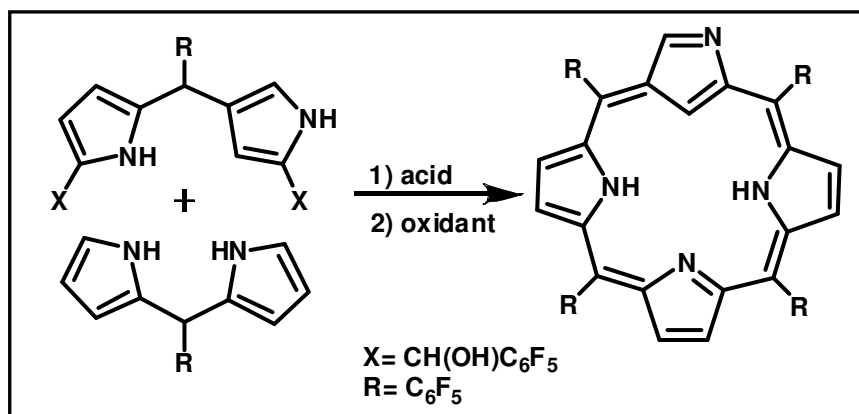
Figure 1.13. N-confused porphyrin (**NCP**).

N-confused porphyrin (**NCP**, Figure 1.13) is a porphyrin isomer which differ largely from the parent porphyrin, particularly in the physical, chemical, structural, and coordination properties. The $\alpha\alpha'$ -linkage in the normal porphyrin is replaced with $\alpha\beta'$ -linkage in N-confused porphyrin derivative (Figure 1.13) and are considered as the true isomer of porphyrin, where the *meso*-carbons are arranged in the same fashion (1.1.1.1) as of normal porphyrin. Introduction of a confused pyrrole into the normal and expanded

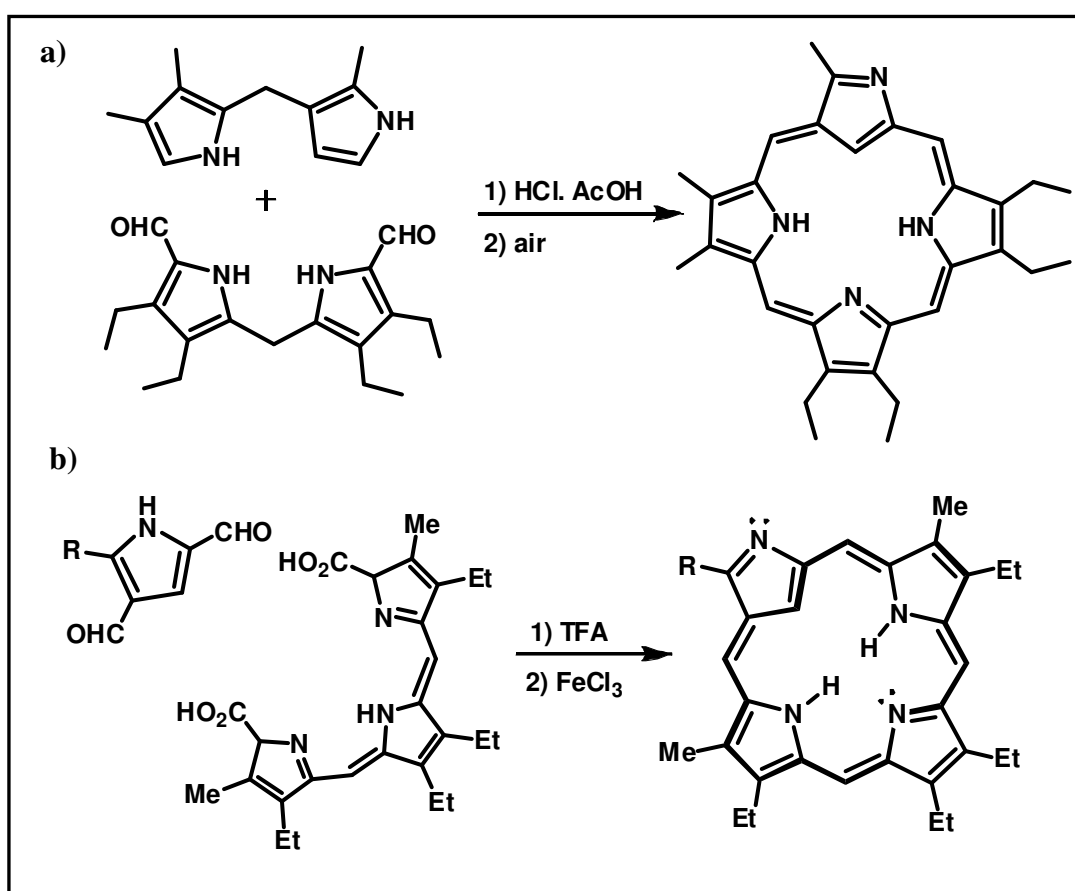
porphyrins leads to the generation of confused porphyrinoids having rich structural diversity [61].

1.2.5.1.1. Synthesis and spectral properties of NCP derivatives

The fascinating isomer of porphyrin was introduced in 1994 by two independent groups, Furuta and co-workers from Japan and Latos-Grażyński and co-workers from Poland [62, 63]. Latos-Grażyński reported the reaction of *p*-tolylaldehyde with excess pyrrole in DCM, catalyzed by $\text{BF}_3 \cdot \text{OEt}_2$, yields a novel porphyrin derivative, 2-aza-21-carba-5,10,15,20-tetra-*p*-tolylporphyrin in 4% yield along with normal porphyrin. At the same time Furuta *et al.* modified the well-known procedure for synthesis of **TPP** that involves the acid-catalyzed condensation between aldehyde and pyrrole. In place of propionic acid, *t*-BuOH/DCM (1:1) and con. HBr (1 equiv.) were used and the mixture was stirred for 2 days at room temperature in dark. Oxidation with 2 equiv. of chloranil yielded the porphyrin isomer in 5-7% yield. ^1H NMR signals resonating at -4.99 and -2.41 ppm assigned for inner CH and NH signals reflect the ring current effect of 18π system and the presence of confused pyrrolic ring. UV-Vis absorption spectrum shows Soret band at 438 nm and Q-bands ranging from 550-725 nm in DCM and is largely red-shifted from the normal porphyrin. However, the improved synthetic methodology for **NCP** was performed by Lindsey *et al.* where methane sulfonic acid (MSA) catalyzed condensation reaction of pyrrole and benzaldehyde afforded tetraphenyl N-confused porphyrin (**NCTPP**) in 39% yield [64, 65]. However, for the synthesis of pentafluorophenyl substituted N-confused porphyrin ($\text{C}_6\text{F}_5\text{-NCP}$), Lindsey's modified procedure was not efficient, where the acid-catalyzed [2 + 2] condensation was helpful (Scheme 1.2) [66]. Also, *meso*-free derivatives of **NCP** were prepared by step wise synthesis by using MacDonald type [2 + 2] and [3 + 1] condensation (Scheme 1.3) [67, 68].



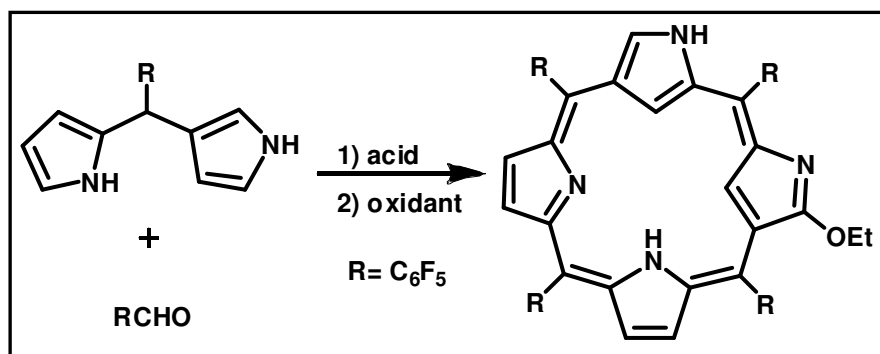
Scheme 1.2. Synthesis of C₆F₅-NCP.



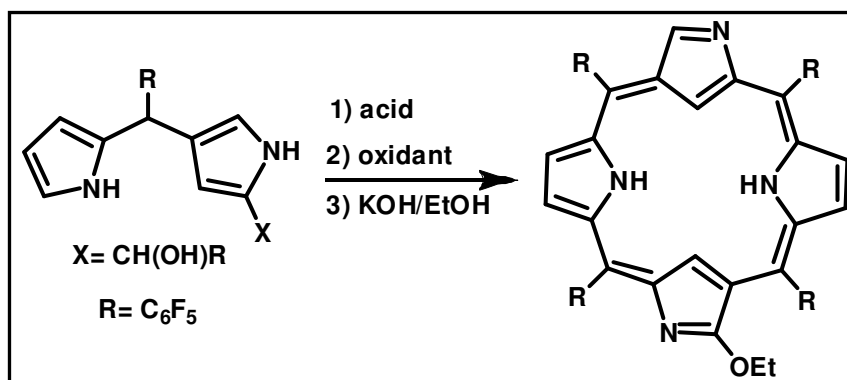
Scheme 1.3. Synthesis of *meso*-free NCP by (a) [2 + 2] and (b) [3 + 1] MacDonal condensation.

Further, series of NCP derivatives were introduced, where the new derivatives with more than one confusion, confused derivative with heterocyclic ring other than pyrrole, expanded derivatives, confused calixpyrrole, confused ring with fusion etc. Doubly N-

confused porphyrin (N_2CP) holds two confused pyrrole rings in the cyclic structure which includes *cis*- N_2CP and *trans*- N_2CP . *Cis*- N_2CP was synthesized by acid-catalyzed condensation of pentafluorobenzaldehyde with N-confused dipyrromethane in $CHCl_3$ containing a trace of EtOH. After oxidation with DDQ, the expected product was obtained in green colour in 2% yield (Scheme 1.4). The inner β -CH protons of two confused pyrrole rings were observed at 3.50 and 3.20 ppm in the 1H NMR spectrum, while the outer NH proton resonated at 8.95 and inner at 6.4 ppm, suggesting the weak aromatic nature of the compound [69]. *Trans*- N_2CP was obtained in 53% yield from the [2 + 2] acid-catalyzed condensation of C_6F_5 -substituted N-confused dipyrromethane monocarbinol, followed by oxidation and base treatment (Scheme 1.5). The two inner NH and CH protons were observed at -2.73, -3.21 ppm and -4.34, -4.36 ppm, respectively, indicating better aromatic character than *cis* derivative, which is further supported by the sharp Soret-like band at 449 nm [70].

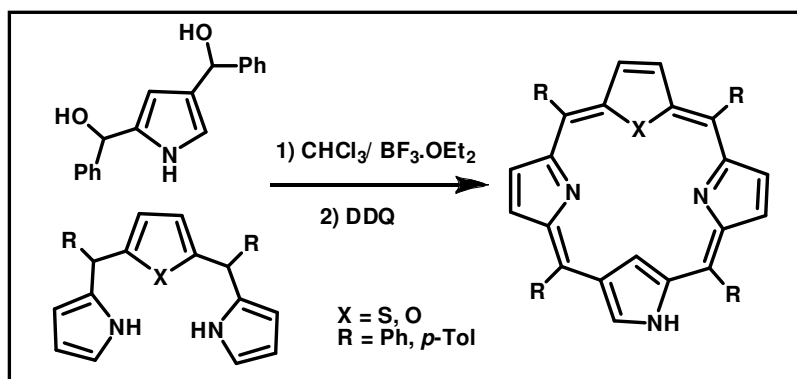


Scheme 1.4. Synthesis of *cis*- N_2CP .

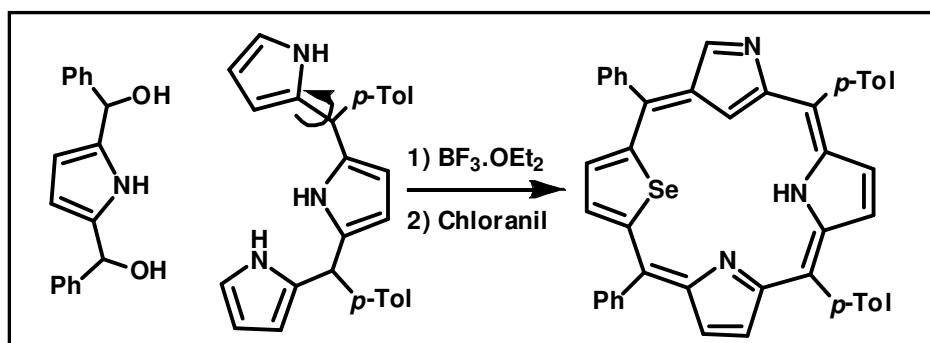


Scheme 1.5. Synthesis of *trans*- N_2CP .

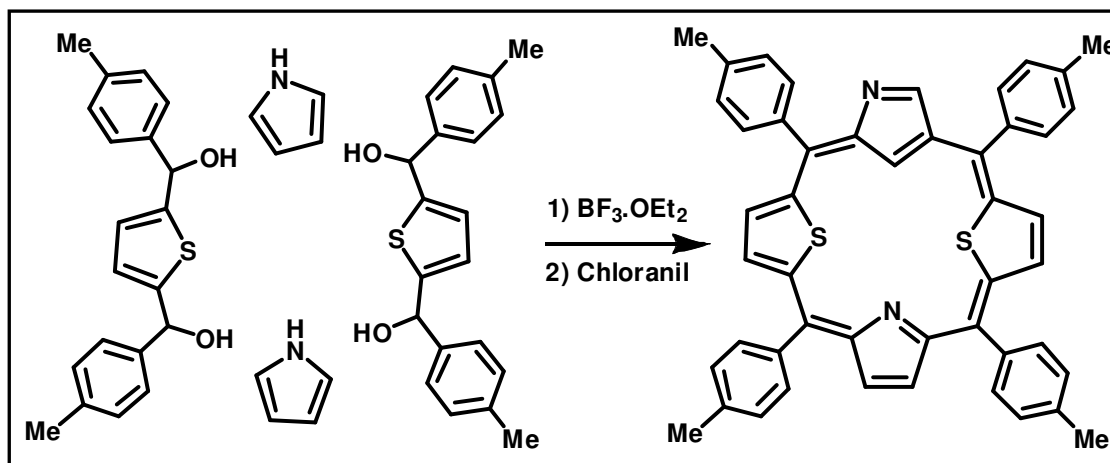
NCP analogues containing hetero atoms such as O, S, and Se have also been synthesized by the groups of Chang-Hee Lee, Latos-Grażyński, and Chandrashekar [71-75]. Acid-catalysed [3 + 1] condensation method was adopted by most of them to synthesize the corresponding **NCP** derivative. Chang-Hee-Lee and co-workers has synthesised thiophene and furan incorporated **NCP** by using modified tripyrrane (with furan or thiophene) and a confused pyrrole diol (Scheme 1.6) [71]. Latos-Grażyński and co-workers have isolated a selenophene containing **NCP** derivative by condensation of 2,5-bis(phenylhydroxymethyl)selenophene and 5,10-bis(*p*-tolyl)tripyrane in DCM (Scheme 1.7) [73]. Later, in 2001 the same group introduced dithiaporphyrin and dithiasapphyrin with N-confused pyrrole ring present in the macrocycle (Scheme 1.8) [74]. The synthetic methodology was modified by Chandrashekar and co-workers, where they used a confused tripyrrane and diol to synthesize series of core-modified **NCP** derivatives (Scheme 1.9) [75].



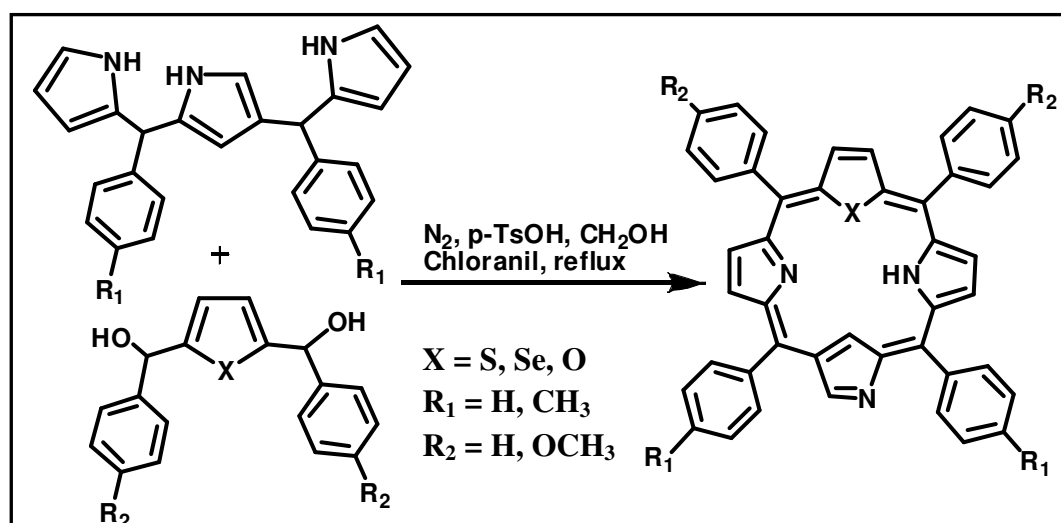
Scheme 1.6. Synthesis of thiophene and furan incorporated **NCP**.



Scheme 1.7. Synthesis of selenophene incorporated **NCP**.



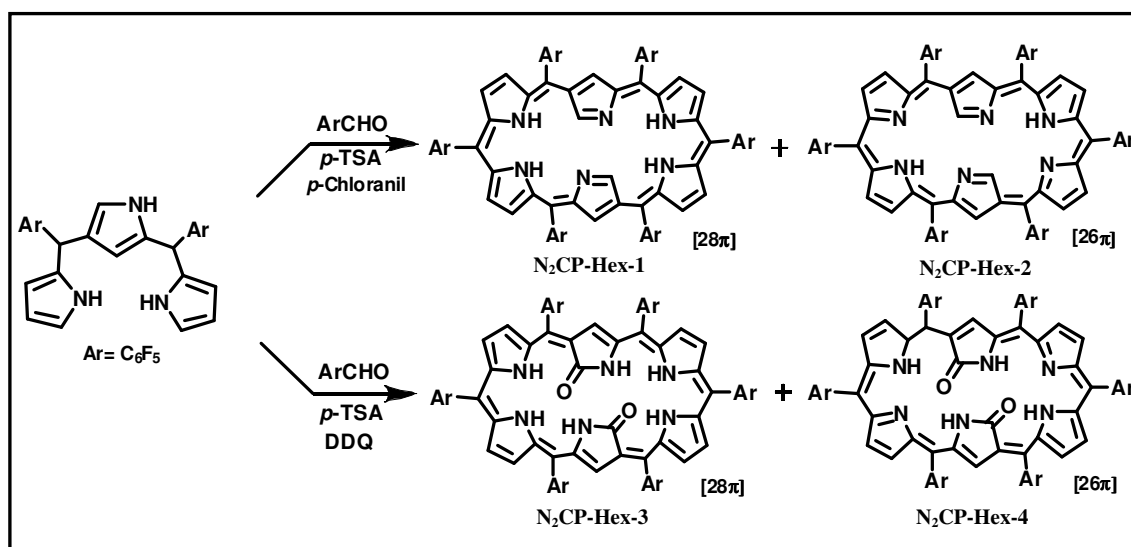
Scheme 1.8. Synthesis of dithia NCP.



Scheme 1.9. Modified synthesis of thiophene, furan and selenophene incorporated NCP.

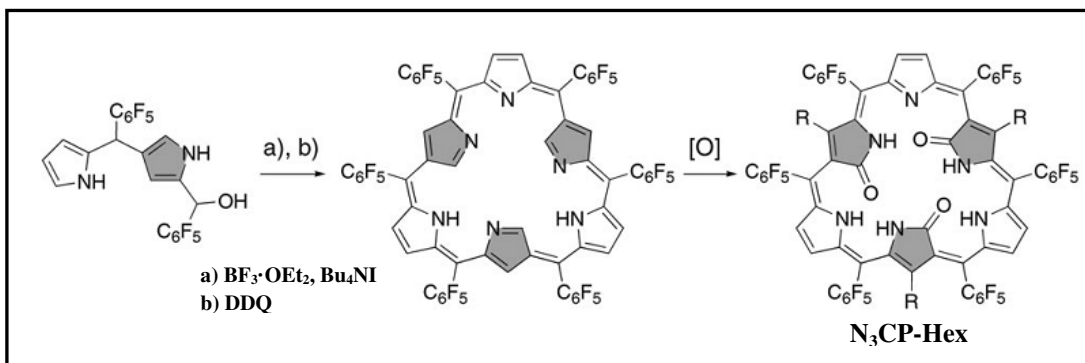
The chemistry of expanded derivatives of NCP was initiated by Chandrashekar and co-workers group by the introduction of N-confused modified sapphyrin. The synthetic methodology involves an acid-catalyzed [3 + 2] MacDonald type condensation of N-confused tripyrrane and bithiophene or biselenophene diol [76]. Later, in 2003, Furuta and co-workers introduced a doubly N-confused hexaphyrin, where they adopted an acid-catalyzed condensation reaction with pentafluorobenzaldehyde and a confused tripyrrane [77]. Interestingly, they could isolate four different products by varying the oxidizing agent such as *p*-chloranil and DDQ (Scheme 1.10). *p*-Chloranil oxidation yielded in two

doubly N-confused hexaphyrins where one was nonaromatic (28π , **N₂CP-Hex-1**) and the other was aromatic with 26π electrons in the ring (**N₂CP-Hex-2**). However, DDQ oxidation provided two oxo substituted N-confused hexaphyrins with similar aromatic character as in *p*-chloranil (28π , **N₂CP-Hex-3** and 26π , **N₂CP-Hex-4**).



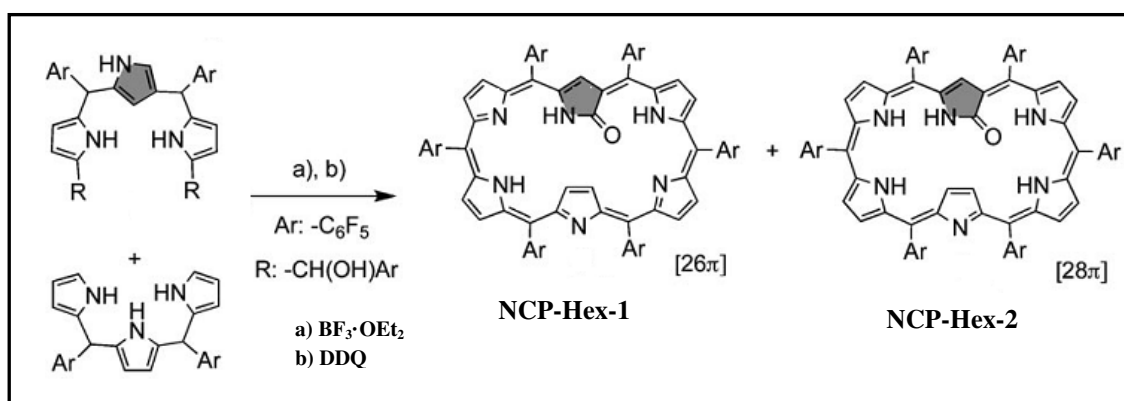
Scheme 1.10. Synthesis of **N₂CP-hex** derivatives.

In 2009, Furuta and co-workers reported a triangular shape tri-oxo derivative of triply N-confused hexaphyrin [78]. The triply N-confused *meso*-pentafluorophenylhexaphyrin (**N₃CP-Hex**) was synthesized by an acid-catalyzed [2 + 2 + 2] self-condensation of N-confused dipyrromethane carbinol in DCM (Scheme 1.11). Oxidation with DDQ followed by chromatography on silica gel led the isolation of tri-oxo substituted hexaphyrin in 13% yield.



Scheme 1.11. Synthesis of **N₃CP-Hex** [78].

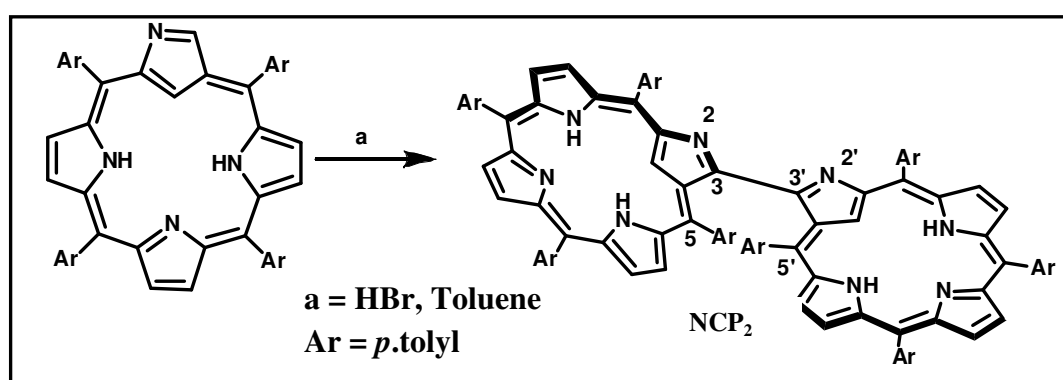
Recently, the same group reported singly N-confused hexaphyrins which can stabilize variable oxidation state metal ions [79]. An acid-catalysed [3 + 3] condensation of N-confused tripyrrane dicarbinol and tripyrrane yielded an aromatic (26π) singly N-confused hexaphyrin (**NCP-hex-1**) and a nonaromatic derivative (**NCP-Hex-2**, 28π) as shown in scheme 1.12.



Scheme 1.12. Synthesis of **NCP-Hex** derivatives [79].

A comparative analysis of the photophysical properties of normal hexaphyrin, doubly N-confused hexaphyrin and triply N-confused hexaphyrin showed that the confusion of pyrrole rings in macrocycles and the modification of molecular symmetry perturb their electronic structures. Accordingly, the absorption and fluorescence spectra were found to be gradually red-shifted in going from normal to triply N-confused derivative. Steady state spectroscopic measurements and theoretical calculations done by

Dongho Kim and co-workers proved that the reduced HOMO–LUMO gaps from normal to triply N-confused derivative is the reason for the red-shifted absorption spectra and shorter singlet excited-state lifetimes. On the basis of two-photon absorption (TPA) cross-section values and quantum mechanical calculations, it was suggested that the contribution of the π -orbital on confused pyrrole rings results in effective elongation of π -conjugation pathways along with the modification of the TPA selection rule by higher symmetric structures [80].



Scheme 1.13. Synthesis of \mathbf{NCP}_2 .

P. J. Chmielewski reported the synthesis of directly linked \mathbf{NCP} dimer (\mathbf{NCP}_2). The dimer was obtained by the acid-catalyzed reaction from a tetraphenyl \mathbf{NCP} [81]. The coupling process was carried out in the presence of air, act as strong oxidant for the dehydrogenation step for the formation of bond between the two porphyrin subunits (Scheme 1.13). The interaction between the two aromatic rings was reflected by a strong bathochromic shift of the Soret and Q bands in the electronic absorption spectra with respect to the monomeric species.

1.2.5.1.2. Metal complexes of \mathbf{NCP}

Coordination chemistry of \mathbf{NCP} was elaborately studied and a significant number of metal complexes were reported. There are a series of late-transition metal complexes of \mathbf{NCP} and its derivatives are reported in the literature but only a few examples for early

transition metals and main group metals. Figure 1.14 summarizes the **NCP** metal complexes known in the literature till now.

H																		
Li	Be												B	C	N			
Na	Mg												Al	Si	P			
K	Ca	Sc	Ti	V	Cr	Mn	Fe	Co	Ni	Cu	Zn	Ga	Ge	As				
Rb	Sr	Y	Zr	Nb	Mo	Tc	Ru	Rh	Pd	Ag	Cd	In	Sn	Sb				
Cs	Ba	Ln	Hf	Ta	W	Re	Os	Ir	Pt	Au	Hg	Tl	Pb	Bi				
Fr	Ra																	

Figure 1.14. Reported metal complexes of **NCP** (highlighted in red).

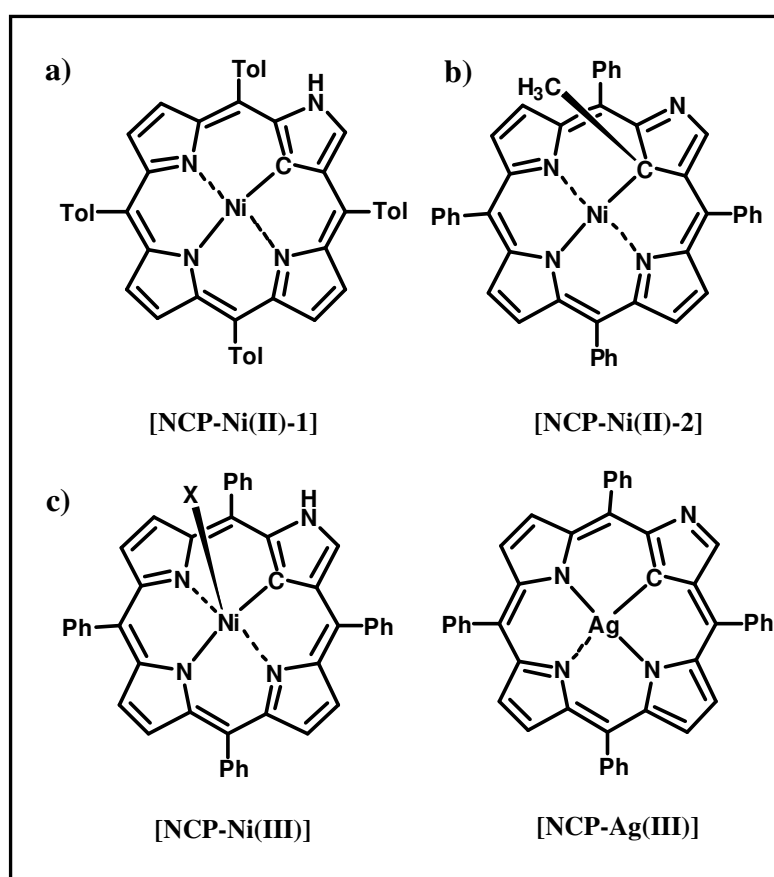


Figure 1.15. Ni and Ag metal complexes of **NCP**.

The first **NCP** metal complex was reported by Latos-Grażyński and co-workers in 1994 [63]. The Ni(II) complex was confirmed by NMR and single crystal X-ray analysis and found that the Ni(II) complex $[NCP-Ni(II)-1]$, Figure 1.15.a] has a Ni-C bond as well as three Ni-N bonds. In 1996, the same group also introduced the paramagnetic

Ni(II) complex **[NCP-Ni(II)-2]** of **NCP**, methylated at the inner carbon (21C) atom (Figure 1.15.b) [82]. They have also shown that these nickel compounds can be oxidized either chemically or electrochemically to yield an one electron oxidized unusual product, organometalic Ni(III) complexes **[NCP-Ni(III).X, X=Br ,NO₃ ,CN ,OH , etc.]** as shown in Figure 1.15.c [83]. Utilization of the unusual labile nature of the inner CH promotes the introduction of more metal complexes with the stabilization of rare and unstable metal oxidation state. In 1999 Furuta and co-workers reported a Ag(III) complex of **NCTPP**, **[NCP-Ag(III)]** as shown in Figure 1.15.d [84].

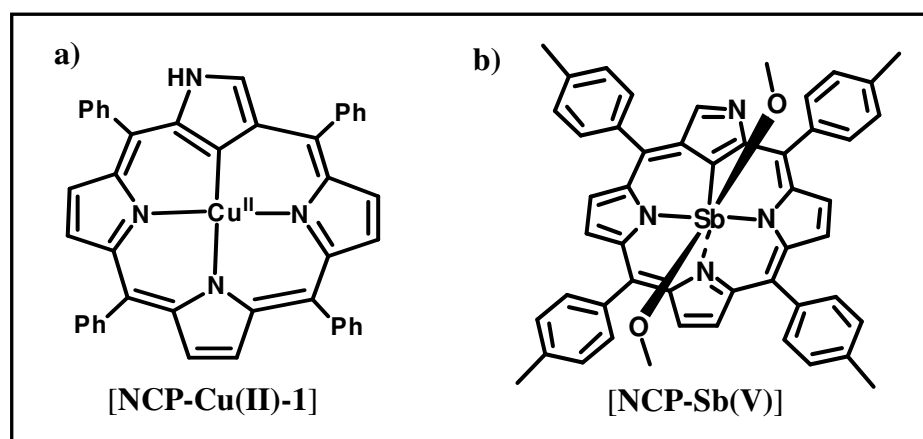


Figure 1.16. Structure of Cu and Sb complex of **NCP**.

Soon after the introduction of silver complex, a unusual organocopper(II) species **[NCP-Cu(II)-1]** was reported by Latos-Grażyński in 2000 (Figure 1.16.a) [85], where the copper derivative was isolated by mixing copper acetate with **NCTPP** in THF under anaerobic conditions. Absorption spectrum of the product in DCM showed a change in the absorption characteristics relative to free base. In the same year, the main group element antimony was incorporated into the core of the macrocycle by stirring **NCTPP** in dry pyridine in the presence of a large excess of SbBr₃ under nitrogen to yield **[NCP-Sb(V)]** [86]. The structure of the porphyrin ring is planar with a six coordinate antimony lying directly in the center of the core and axially coordinated methoxy groups are orienting above and below of the mean macrocyclic plane (Figure 1.16.b). ¹H NMR data

showed no interior carbon or exterior nitrogen protons, indicate that the **NCP** was acting as a trianion. Single crystal X-ray analysis confirms antimony in the +5 oxidation state [86, 87].

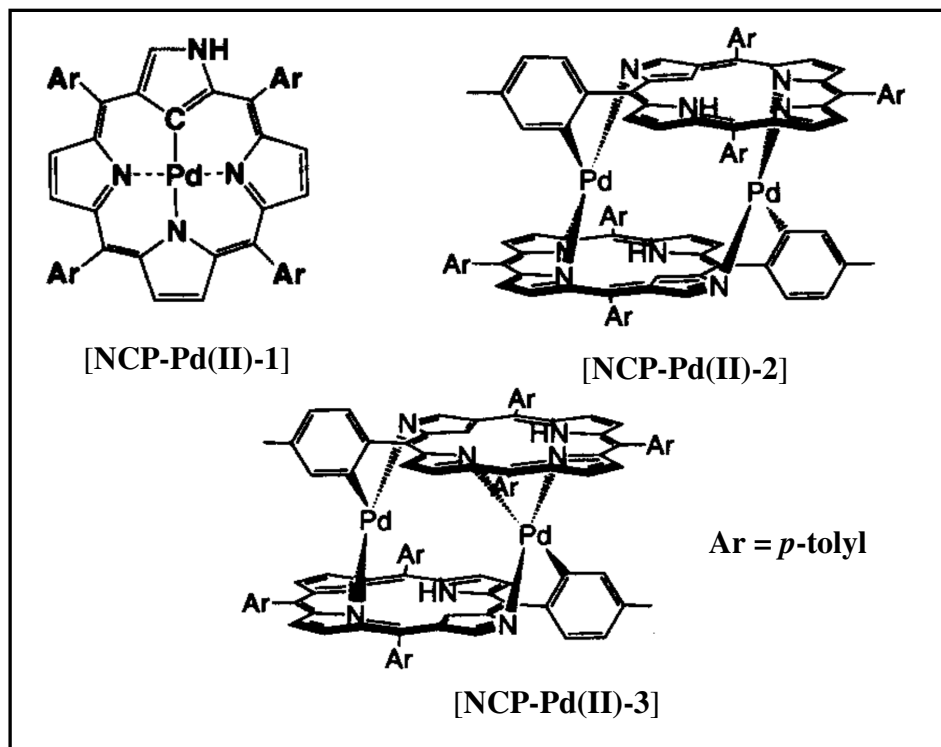


Figure 1.17. Structures of **Pd-NCTTP** complexes [88].

In the same year, Furuta *et al.* experimented the solvent effect on metal coordination of palladium to tetratolyl N-confused porphyrin (**NCTTP**) [88]. The reaction of $\text{Pd}(\text{OAc})_2$ with **NCTTP** in CHCl_3 yields internally metallated form **[NCP-Pd(II)-1]** and X-ray crystallographic analysis showed that Pd is in the plane of the macrocycle and internal carbon is coordinated to the metal. However, upon changing the solvent from CHCl_3 to toluene, apart from **[NCP-Pd(II)-1]** two dimeric species were formed, **[NCP-Pd(II)-2]** and **[NCP-Pd(II)-3]** which have symmetric and asymmetric structures respectively, along with the internally metallated monomer (Figure 1.17). The external nitrogen and an ortho carbon from the tolyl group of one macrocycle and two internal nitrogens from the second macrocycle coordinate to each palladium. The two Pd metal

sites in this compound are quite different, where one is nearly square planar while the second one is in tetrahedral geometry, which were confirmed by ^1H NMR and X-ray crystal analysis [88].

In 2001, C.-H. Hung *et al.* isolated the first iron complex of NCP [**NCP-Fe(II)-1**] (Figure 1.18) by reacting **NCTPP** with 5 equiv. of iron(II) bromide in a solution of ACN/THF with a few drops of lutidine [89]. UV-Vis absorption spectrum of the product in DCM showed a large Soret band at 461 nm and a broad Q band at 744 nm. Magnetic susceptibility measurements showed the formation of high spin Fe^{2+} complex and single crystal data confirmed the structure, where the internal CH proton generate an agostic interaction with the metal ion.

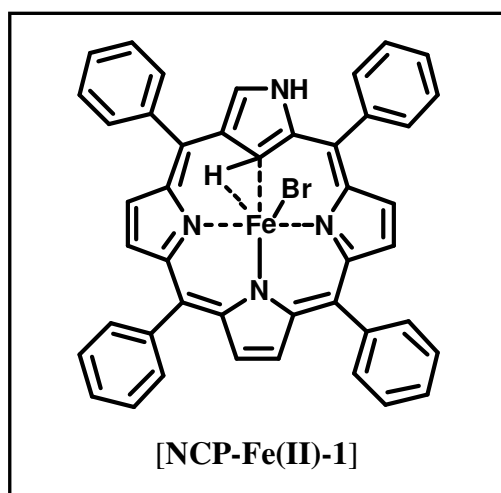


Figure 1.18. Structure of [**NCP-Fe(II)-1**].

In the same year, Furuta and co-workers demonstrated another example of external nitrogen participation in metal binding by the bis-rhodium complex of NCP, [**NCP-Rh(I)-1**] [90]. The complex exhibited both interior and exterior coordination to two rhodium ions (Figure 1.19). X-ray crystal structure showed that one rhodium center is coordinated to the external nitrogen, while the second rhodium is coordinated to one imine and amino nitrogens on the interior of the macrocycle. Both rhodium ions are located above the plane of the macrocycle and exhibit square planar geometries. The UV-

Vis absorption spectrum of this complex displays a 50 nm red shifted Soret band compared to **NCTPP** at 488 nm with four less intense red-shifted Q bands ranging from 545 to 780 nm.

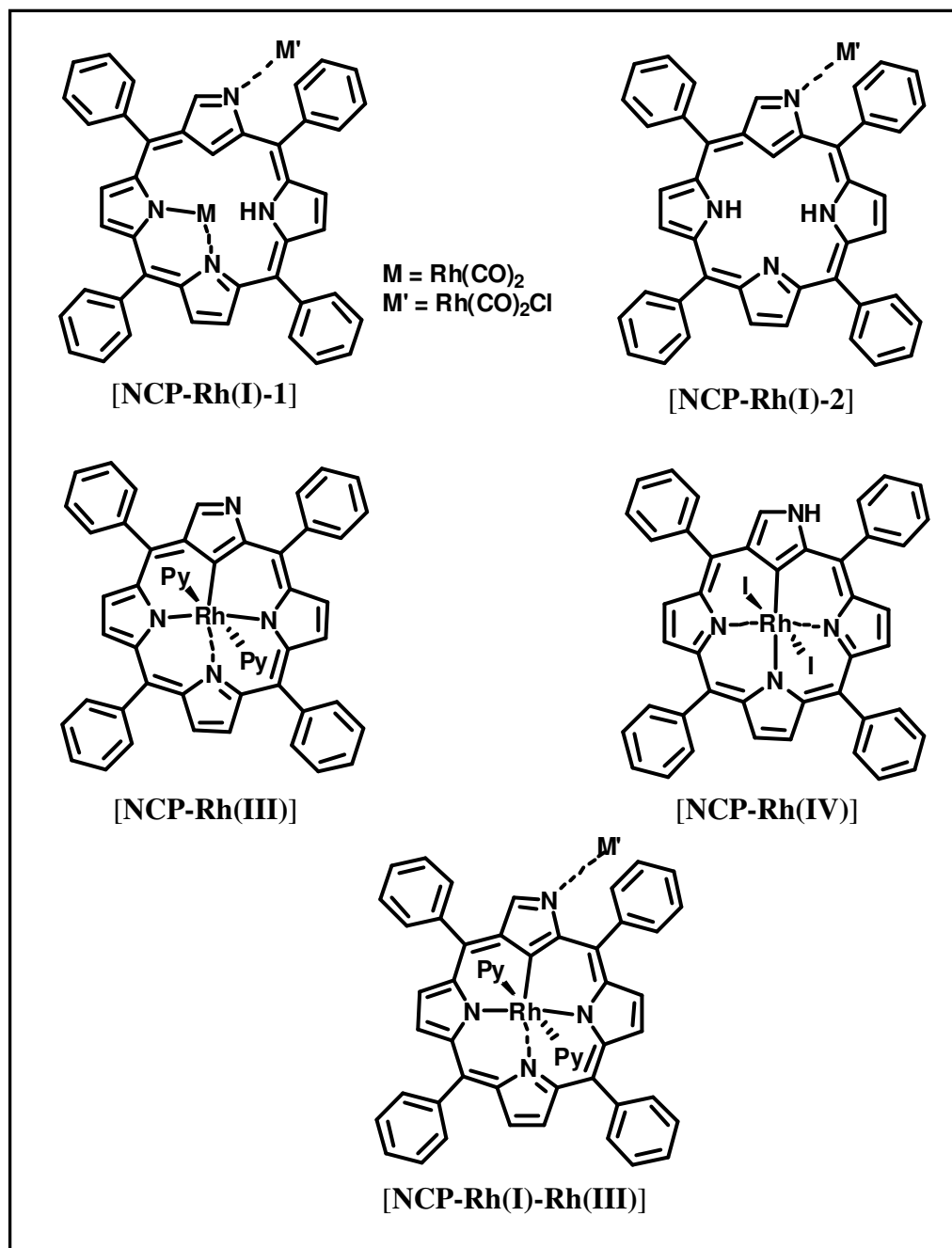


Figure 1.19. Structure of Rh complexes of NCP.

Further, few years later Furuta and co-workers extended their work on rhodium complexes by synthesizing rhodium complexes of different oxidation state [91]. Upon treatment of **NCTPP** with 0.5 equiv. of $[\text{RhCl}(\text{CO})_2]_2$ in DCM at ambient temperature for 10 min yielded the mono-rhodium complex, **[NCP-Rh(I)-2]** in good yield. However, 1.0 equiv. of $[\text{RhCl}(\text{CO})_2]_2$ in the presence of 10 equiv. of NaOAc resulted in the formation of bis-rhodium complex **[NCP-Rh(I)-1]** as reported earlier. Interestingly, treatment of **[NCP-Rh(I)-1]** with pyridine and iodine generated another two mono-rhodium complexes with higher oxidation states, **[NCP-Rh(III)]** and **[NCP-Rh(IV)]** with pyridyl and iodide axial substitution respectively (Figure 1.19) [91]. Also, **[NCP-Rh(III)]** further treatment with 0.5 equiv. of $[\text{RhCl}(\text{CO})_2]_2$ resulted in a bimetallic complex where rhodium exist both in +1 and +3 oxidation state **[NCP-Rh(I)-Rh(III)]**.

In 2002, Bohle *et al.* incorporated manganese into the core of **NCP** using manganese(II) bromide following the same metallation procedure for iron, yielding **[NCP-Mn(II)-1]** in 82% yield (Figure 1.20.a) [89, 92]. The formation of high spin Mn(II) complex was confirmed by superconducting quantum interference device (SQUID) magnetic susceptibility and electron spin resonance (ESR) analyses. The absorption spectrum exhibits a Soret band at 462 nm and two Q bands at 715 and 782 nm and single crystal X-ray analysis confirms the structure of the complex. Interestingly, air oxidation of **[NCP-Mn(II)-1]** immediately yielded **[NCP-Mn(III)-1]**, Figure 1.20.b]. Almost same time, Ziegler and co-workers presented an alternate synthesis of **Mn-NCP** complex [93]. Reaction of **NCTPP** with $\text{Mn}_2(\text{CO})_{10}$ in toluene under anaerobic conditions yielded **[NCP-Mn(II)-2]** in quantitative yield (Figure 1.20.c). The crystals obtained from pyridine/heptane showed the presence of axial pyridine coordination in the X-ray analysis, where the internal pyrrolic carbon–hydrogen bond is still present in the complex. However, crystallization from hot toluene yielded a dimeric structure

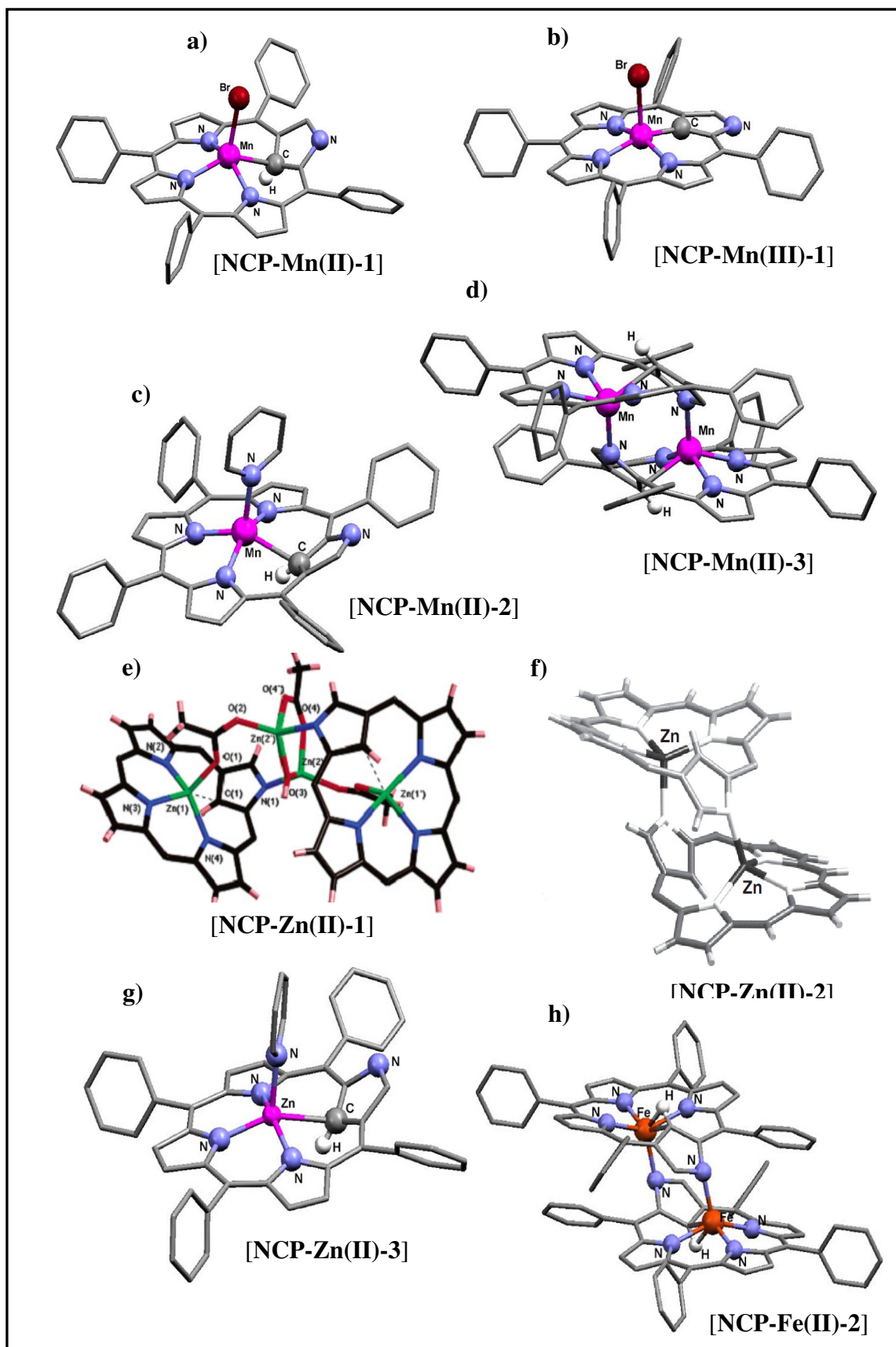


Figure 1.20. X-ray structure of Mn, Zn and Fe complexes of NCP [87, 98].

[NCP-Mn(II)-3] as shown in Figure 1.20.d [93]. Later in the same year, Furuta *et al.* synthesized two types of NCP dimers incorporating zinc ions [94]. NCTPP was reacted with 2 equiv. of zinc acetate dihydrate in DCM at room temperature. Removal of the solvent and crystallization from toluene/hexane afforded a dimeric complex containing four zinc atoms [NCP-Zn(II)-1] as shown in Figure 1.20.e. The external nitrogen was coordinated to a bridging dizinc acetate unit with the acetate oxygens occupying the axial positions of the [NCP-Zn(II)-1]. The geometries about bridging zinc atoms are tetrahedral while the zinc atoms in the NCTPP core are pentacoordinate. The complex after treated with 1% tetraethylammonium hydroxide removed the acetate ligand to give another dimeric complex [NCP-Zn(II)-2, Figure 1.20.f], and was further transformed into monomeric pyridine complex [NCP-Zn(II)-3] by adding pyridine (Figure 1.20.g) [94]. An iron complex [NCP-Fe(II)-2] with similar dimeric structure was also isolated in the same time by Hung *et. al* (Figure 1.20.h) [95].

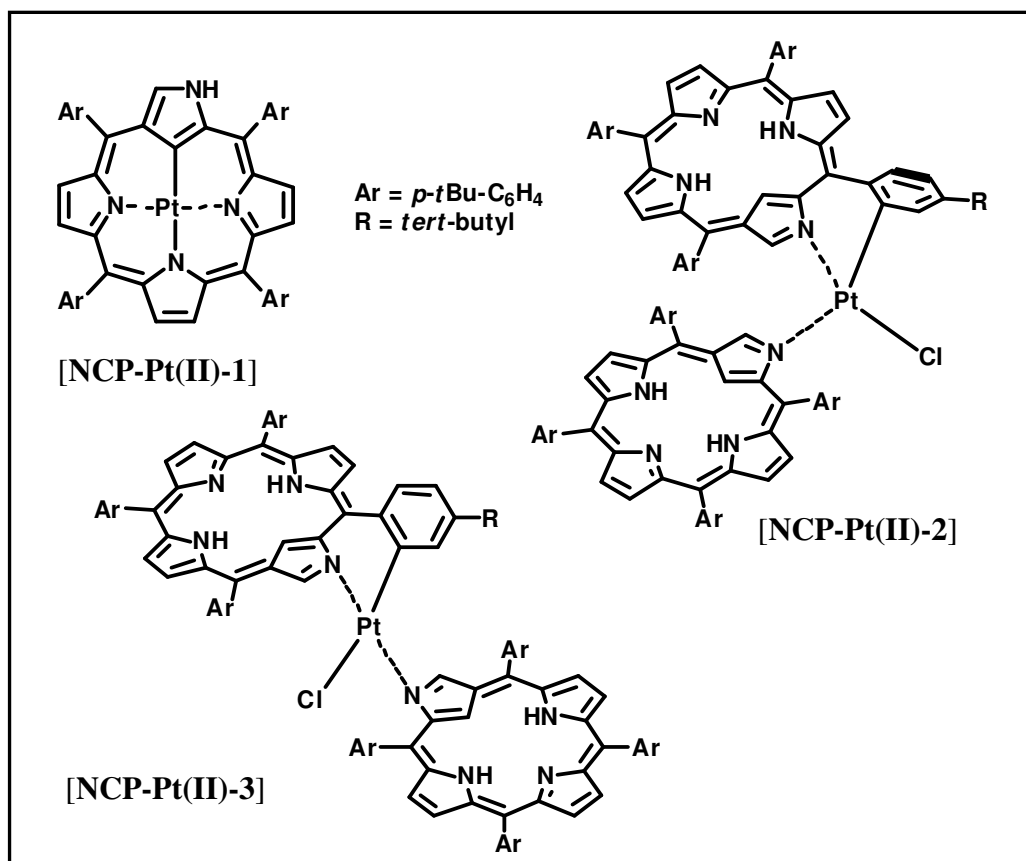


Figure 1.21. Structure of Pt complexes of NCP.

In 2003, Furuta and co-workers synthesized a Pt(II) monomeric [NCP-Pt(II)-1] and two dimeric complexes, [NCP-Pt(II)-2] and [NCP-Pt(II)-3], of N-confused 5,10,15,20-tetrakis(4-tert-butylphenyl)-porphyrin (NCT_{tBu}PP) in refluxing toluene by changing the PtCl₂ equiv. from 0.5 to 1 (Figure 1.21) [96]. As in the Pd complex [88], ortho carbon activation of one of the aryl rings is also seen in the Pt-dimeric complexes. Both dimer complexes were bound to the external nitrogens on both porphyrin units, an ortho carbon from one aryl ring, and a chloride. Platinum is in a square planar geometry in both complexes, and the only difference in structure between the two isomers was, whether the NCP units are bound *cis* or *trans* to the metal.

In the same year, Furuta and co-workers showed the conversion of a Cu(II) complex of C₆F₅-NCP to Cu(III) upon oxidation with DDQ [97]. Also, introduced a Cu(III) complex of alkoxy substituted trans-doubly N-confused porphyrin [70]. The Cu(III) complex forms intermolecular hydrogen-bonding to form rode-like linear chains.

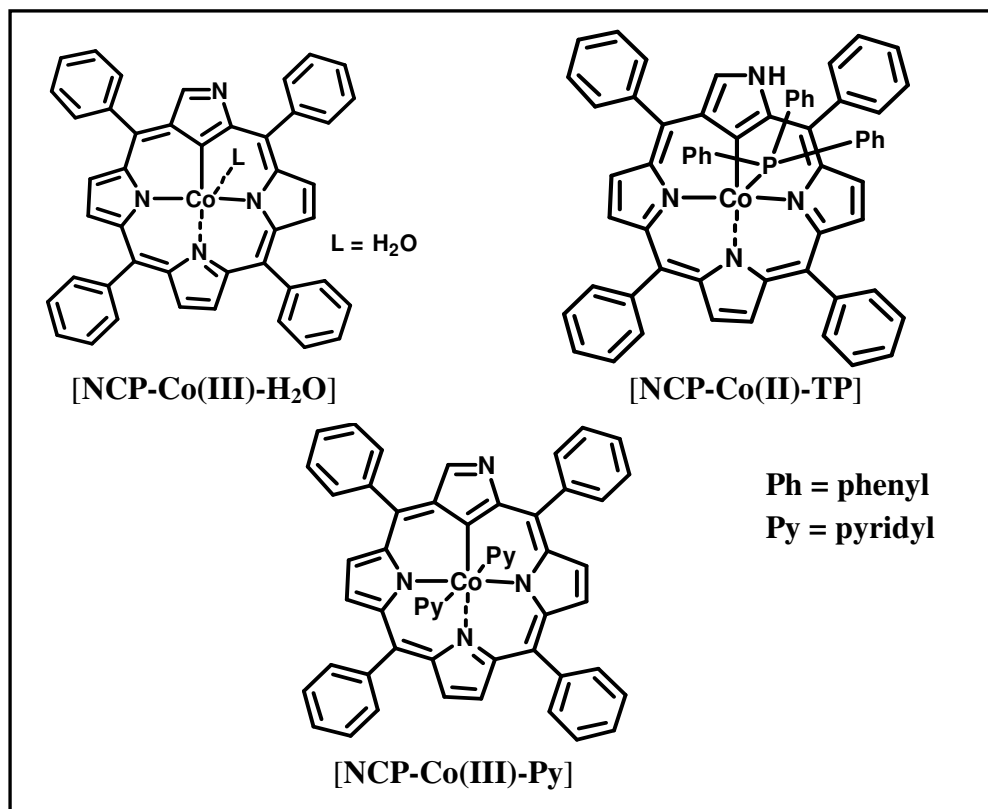


Figure 1.22. Structure of Co complexes of NCP.

In 2004, Furuta *et al.* have reported the **NCP** dimeric metallic complexes with group X metals such as Zn(II), Cd(II), and Hg(II). The structure of Zn(II) and Cd(II) complexes were explained with single crystal X-ray analyses [98]. In the same year Ziegler reported a series of cobalt complexes of **NCP** by changing the solvent conditions [99]. [**NCP-Co(III)-H₂O**] (Figure 1.22.a) was generated by heating **NCTPP** solution in THF under anaerobic conditions with an excess of Co(NO₃)₂·6H₂O. Absorption spectra of the complex showed broad absorbance near 460 nm and Q-bands ranging from 550 to 700 nm. Single crystal X-ray analysis showed a disordered axially coordinating water molecule. Interestingly, when the reaction was carried out in the presence of a toluene solution of triphenylphosphine resulted in a triphenylphosphine coordinated complex, [**NCP-Co(II)-TP**] (Figure 1.22.b). Both the Soret and Q-bands found to be shifted to 428, 478 and 551 nm respectively compared to [**NCP-Co(III)-H₂O**]. Further, a solution of [**NCP-Co(III)-H₂O**] in pyridine showed a sharp Soret at 462 nm and Q bands at 555, 736 and 808 nm, corresponds to a six coordinated complex [**NCP-Co(III)-Py**] (Figure 1.22.c). The axial coordination of pyridine was confirmed by single crystal X-ray analysis.

In 2005, Furuta and co-workers reported a Re complex of N-methylated **NCP** [100]. Reaction of **NCTPP** with Re₂(CO)₁₀ resulted in rhenium complex of N-Fused porphyrin [101]. The first lanthanide complex of **NCP** was also reported in the same year by Wong and co-workers, Where **NCTPP** refluxed in toluene for 12 h with excess Ln[(N(SiMe₃)₂)₃·LiCl(THF)₃]_x (Ln = Yb or Er) under nitrogen, followed by addition of excess NaLOMe (LOMe = (η⁵-C₅H₅)Co[P(=O)(OMe)₂]) at room temperature, resulted in crystals of [**Ln(NCTPP)(LOMe)**] [102].

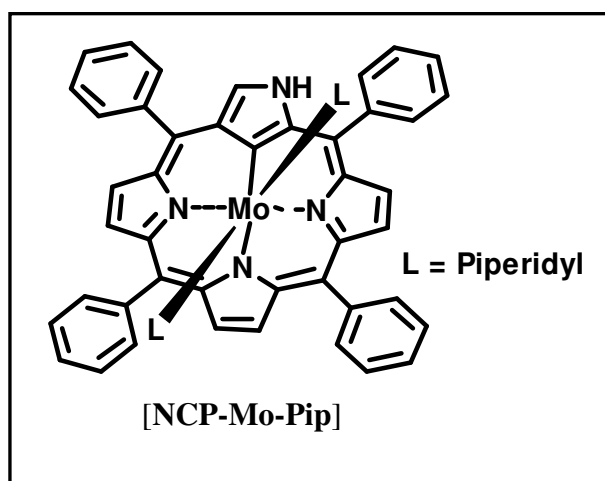


Figure 1.23. Structure of Mo complex of NCP.

Zeigler and co-workers reported a Mo complex of **NCTPP**, where an equimolar ratio of a piperidine carbonyl complex of molybdenum [*cis*-Mo(NHC₅H₁₀)₂(CO)₄] with **NCTPP** in refluxing toluene under anaerobic conditions for 3 h resulted in the species [**NCP-Mo-Pip**] as shown in Figure 1.23 [103]. Absorption spectrum of the complex showed a blue-shifted Soret band at 420 nm with a shoulder at 481 nm and a Q band at 686 nm with a shoulder at 633 nm. The single crystal structure confirmed the Mo atom lies in the core of the ring with two axial piperidines.

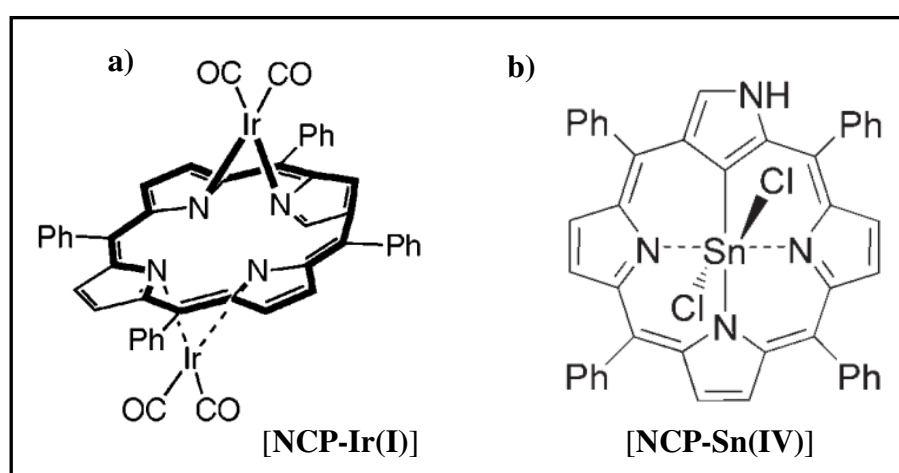


Figure 1.24. Structure of (a) Ir and (b) Sn complexes of NCP.

Furuta and co-workers reported a bis-Ir(I) and Sn(IV) complexes of **NCP** in 2006. **NCTPP** was treated with 2.0 equiv. of IrCl(CO)₂(*p*-toluidine) and 10 equiv. of NaOAc

in toluene/THF (20/1, v/v) at 100 °C for 3.5 h yielded bis-Ir(I) complex [**NCP-Ir(I)**, Figure 1.24.a] [104]. The Sn(IV) complex [**NCP-Sn(IV)**, Figure 1.24.b] was prepared by the reaction of **NCTPP** with excess SnCl₂ in pyridine under aerobic conditions, where the axial position was occupied by Cl⁻ anions [105].

In 2007, Latos-Grażyński showed that **NCP** provides an appropriate environment for coordination of the main group ion, B(III) [106]. The mismatch between the core size of an **NCP** and the boron radius leads to a structure in which the boron is bound by two nitrogen atoms having the *o*-phenyl ligand in the third position, resembling BF₂-coordinated dipyrromethene complexes. One year later Furuta and co-workers reported a luminescent Au(III) complex **NCP**, where the complex was synthesized by a two step synthetic strategy, where in the first step **NCTPP** was brominated on treatment with 3.3 equiv. of AuCl.SMe₂ in toluene under reflux for 11 h resulted in the complex [107].

In 2010, Ziegler and co-workers isolated Li(I) complexes of **NCP** [108]. **NCTPP** was refluxed with excess lithium bis(trimethylsilyl)amide in toluene under dry anaerobic conditions for 4 h to isolate [**NCP-Li(I)-1**], and the structure was confirmed by X-ray analysis (Figure 1.25.a). The complex adopts a pseudo-square-planar geometry, where the three internal nitrogen atoms of the **NCP** are bound to the Li atom. The internal carbon position remains protonated, forming an agostic interaction with the metal center. It was observed that the metal complex, [**NCP-Li(I)-1**] on recrystallization with THF under anhydrous condition yielded in axially coordinated THF complex [**NCP-Li(I)-2**], where the geometry around the metal center is pseudo-square-pyramidal (Figure 1.25.b).

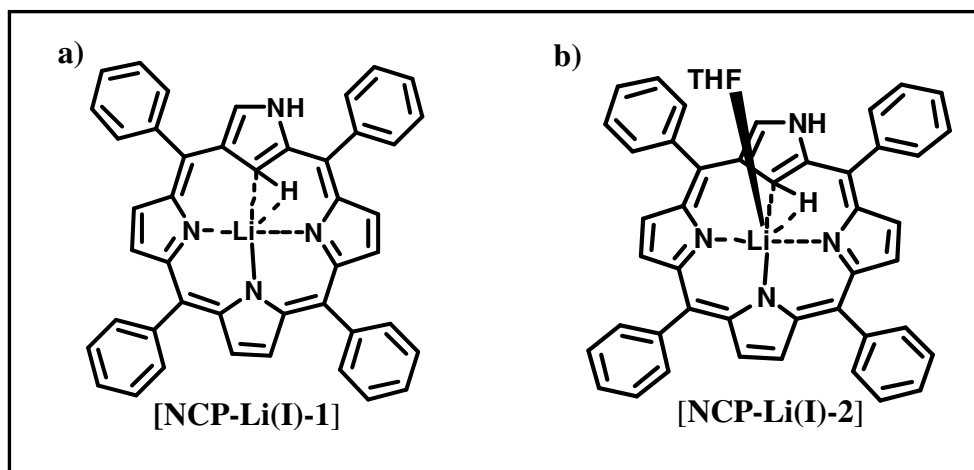


Figure 1.25. Structure of Li complexes of NCP.

In 2012, Jiang and co-workers synthesized rare earth double-decker complexes with phthalocyaninato and regular/methylated N-confused porphyrinato ligands [109]. Treatment of the half-sandwich complexes of rare earth metal such as La(III), Eu(III), Y(III), and Lu(III) with phthalocyanine [$M^{III}(\text{Pc})(\text{acac})$] and metal-free NCP, N-confused 5,10,15,20-tetrakis[(4-tert-butyl)phenyl]porphyrinate} [$\text{H}(\text{R})\text{NTBPP}$] at refluxing condition in 1,2,4-trichlorobenzene (TCB) for 4 h, led to the formation of mixed (phthalocyaninato)(N-confused porphyrinato) lanthanum(III) double-decker complexes [$M^{III}\text{Pc-NTBPP}$] as shown in Figure 1.26.

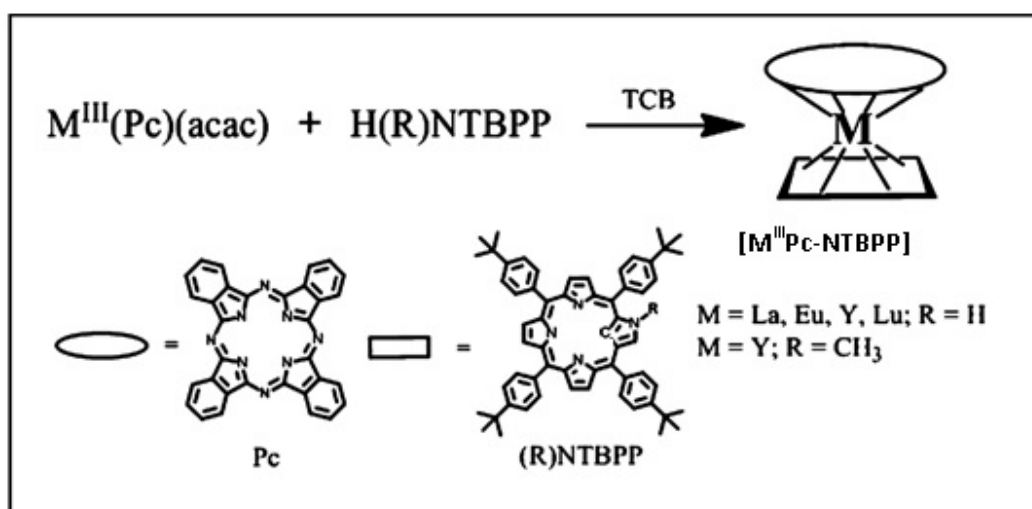


Figure 1.26. Synthesis of Ln(III) double-decker complex, [$M^{III}\text{Pc-NTBPP}$].

In 2011, Furuta and co-workers succeeded in incorporating two different metal ions of different oxidation states in the core of a singly N-confused hexaphyrin (**SNCP-Hex**) [110]. The authors treated [26]hexaphyrin and $\text{AuCl}\cdot\text{S}(\text{CH}_3)_2$ in a mixture of DCM and MeOH (5:1) for 1 h at room temperature afforded mono-Au(III) complex of the **NCP** [**NCP-Au(III)-Hex**]. The X-ray structure showed a planar framework for [**NCP-Au(III)-Hex**], where Au atom is located within the NNNC cavity in a square-planar fashion (Figure 1.27.a). Further, [**NCP-Au(III)-Hex**] heated at reflux condition with $[\text{PtCl}_2(\text{PhCN})_2]$ in the presence of NaOAc under anaerobic conditions provided bis-Au(III)-Pt(II) complex, [**NCP-Au(III)-Pt(II)-Hex**]. The X-ray analysis showed that Pt(II) ion is coordinated to the NNCO cavity in a square-planar geometry (Figure 1.27.b).

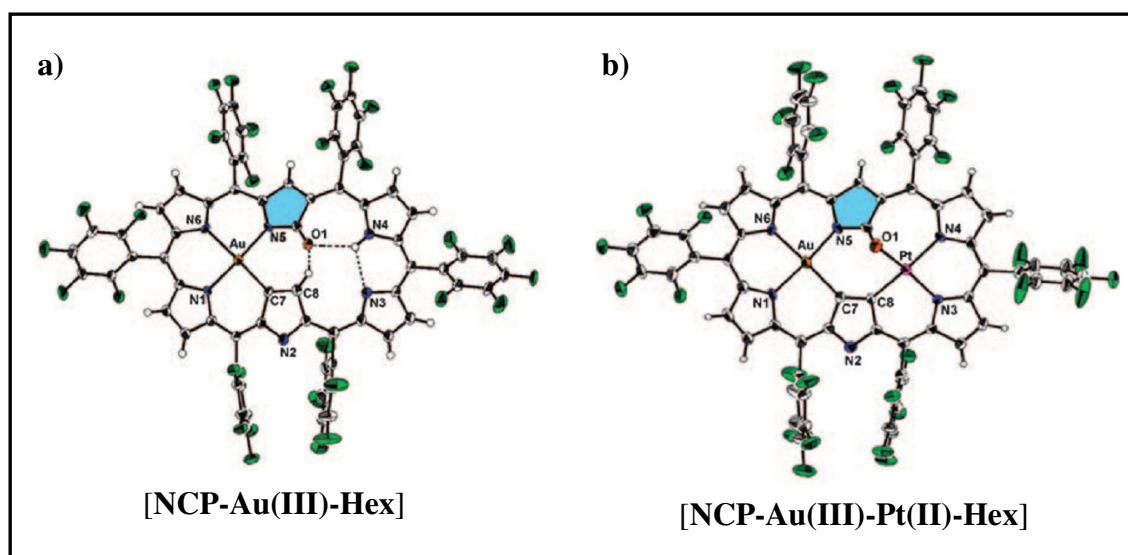


Figure 1.27. X-ray crystal structure of (a) [**NCP-Au(III)-Hex**] and (b) [**NCP-Au(III)-Pt(II)-Hex**] [110].

As in the case of singly confused porphyrin, multiply confused porphyrin also rich in their coordination chemistry. In 2000, Furuta and co-workers introduced a *cis*-doubly N-confused porphyrin (**N2CP**) with high oxidation state metal complexes of Ag(III) and Cu(III). Both complexes are diamagnetic and have a square-planar coordination with two sets of metal-carbon bonds. The trianionic nature of the **NCP** ligand was confirmed by

single crystal analysis [69]. Three years later, the same group introduced Cu(III) complex of alkoxy substituted trans-doubly N-confused porphyrin [70]. The Cu(III) complex was able to make intermolecular hydrogen-bonding to form rod like linear chains in solid state.

1.2.5.1.3. Applications of NCP metal complexes

In addition to the series of coordination metal complexes, Furuta and co-workers explored the catalytic activity of rhodium complexes of **NCP** in cyclopropanation of styrene. The catalytic activity was further compared with the activity of normal porphyrins and corroles, the experiments revealed that, in many cases, **NCPs** can outperform porphyrins and corroles [111]. Also, anion binding properties of metallated **NCP** derivatives were investigated, using a [**Sn(IV)-NCP**] derivative and Sn(IV)-oxoporphyrin complex. The binding event was followed by turn on fluorescence and exhibited high binding constant with halide anions (F^- , Cl^- , Br^- , I^-) in the order $F^- > Cl^- > Br^- > I^-$ [105]. Further, a comparative study of affinity towards anion on different singly and doubly N-confused metal complexes (Cu, Ni, Pd, Ag) revealed that *trans*-doubly N-confused Cu complex have better affinity towards Cl^- and Br^- anions [112]. Hung and co-workers, demonstrated reduction of nitrite anion by using [**Fe(II)-NCP**] complex, the results suggested that the process mimic the reactions in heme-containing nitrite reductases bacteria [113]. Recently, Ziegler and co-workers described a cyclopropanation reaction of styrene catalyzed by a cobalt N-confused porphyrin [114].

1.3 Objective of the present thesis

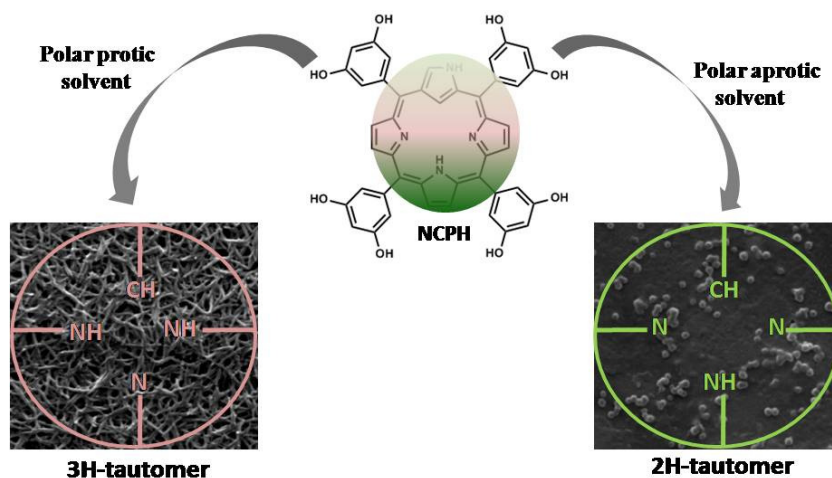
As discussed, the synthesis and rich coordination chemistry of **NCP** attracted the interest of many researchers towards this macrocycle. The porphyrin isomer, with a simple change in the position of pyrrolic linkage, differs largely from the parent porphyrin, particularly in the physical, chemical, structural, and coordination properties. Since after the discovery of the isomer in 1994, research on the molecule was preferentially targeting the structural modification as well as utilizing the versatile coordination ability of the molecule to stabilize various metal ions of usual and unusual oxidation states. Areas, where other utilities of the N-confused derivative explored were rare. However, a very few reports explore properties like anion binding ability and biological activity of the porphyrin isomer. Herein, the thesis compiles the work done on the investigation of morphological features, changes of different **NCP** derivatives during aggregation with respect to different stimuli and the utility in a biologically relevant application, photodynamic therapy, domains where the chemistry of **NCP** is not that explored.

CHAPTER 2

***meso*-Tetrakis(3,5-dihydroxyphenyl)N-Confused Porphyrin: Tautomeric Existence, Exchange and Influence of Tautomerism and Anions on Morphological Features**

2.1	Abstract	72
2.2	Introduction	73
2.2.1	Tautomerism, historical background	73
2.2.2	Tautomerism in N-confused Porphyrin	74
2.2.3	Porphyrin aggregates	80
2.3	Objective of Our Work	86
2.4	Results and Discussions	86
2.4.1	Synthesis and spectral characterization of NCPH	86
2.4.2	NH Tautomerism in NCPH	88
2.4.3	Tautomeric exchange and aggregation properties	91
2.4.4	The role of tautomeric structures in the morphology of NCPH aggregates	97
2.4.5	Anion assisted aggregation of NCPH	99
2.5	Conclusions	105
2.6	Experimental Section	106
2.6.1	Materials and methods	106
2.6.2	Synthesis of NCPH	107

2.1 Abstract



This chapter describes the synthesis, spectral and structural characterization, solvent dependent tautomeric existence and exchange of a novel octa-hydroxy N-confused porphyrin derivative; meso-Tetrakis(3,5-dihydroxyphenyl)N-Confused Porphyrin (NCPH). The tautomeric existence and exchange of NCPH was investigated through various spectroscopic techniques such as UV-Vis, fluorescence and FT-IR spectroscopy in different polar protic and aprotic solvent combinations. A combination of DMSO/ACN, DMSO/H₂O, MeOH/ACN and MeOH/H₂O were used for the investigations. Solvent driven aggregation in these combinations was also monitored through scanning electron microscopy (SEM) and atom force electron microscopy (AFM) analysis. The morphological features observed in the different solvent combinations was explained on the basis of difference in the hydrogen bonding formation possible due to the existence of different tautomeric forms in the particular medium. Further, the role of anions in determining the morphology during aggregation was studied.

2.2 Introduction

It was exactly five decades before Furuta and Latos-Grażyński isolated NCP independently [62, 63], Melvin Calvin and Linus Pauling formulated the structure of N-confused porphyrin [115]. In their 1943 paper entitled “*The porphyrin-like products of the reaction of pyrrole with benzaldehyde*” Calvin and his graduate student Sam Aronoff described about a Rothmund-type condensation reaction between pyrrole and benzaldehyde and identified six condensed products, but unable to analyze the products [116]. Notably, they formulated several porphyrin isomers with one or two inverted pyrrole rings, which they named “carboporphyrins”, similar to the current nomenclature.

On the other hand, Linus Pauling, one amongst the most influential scientific personality in the modern era, contributed in various areas of science including structure and bonding of molecules, genetics, evolution, haematology, immunology, brain research, biomedicine and nutritional therapy [115]. Particularly to the porphyrin chemistry, porphyrin isomers and the prediction of stability of various isomers including “extroverted” pyrrole rings based on his analysis of the electronic structure was remarkable. In fact, he was trying to determine the number of possible resonance structures with eleven double bonds that can be drawn for each type of system to assess their stability, where he could predict the possible existence of porphyrin derivatives with one, two and three extroverted pyrrole rings [115].

2.2.1 Tautomerism, historical background

The phenomenon tautomerism was recognized in the 19th century, where Gerhardt describes this phenomenon in his book on organic chemistry [117]. The name “tautomerism” was introduced by Laar [118], to describe the properties of organic compounds that can react as if they have two or more structures. The term “tautomerism” (in Greek, *tauto*-same and *meros*-part) refers to a compound existing in equilibrium

between two or more labile isomeric forms called the tautomers and usually the tautomers differ in the point of attachment of a hydrogen atom [119]. A common type of tautomer was found in ketones, where one proton transfer generates enolic form and is readily interconvertible constitutional isomers that exist in equilibrium with each other, usually referred as keto-enol tautomerism. The investigations on ‘keto-enol’ tautomerism initiated at the end of 19th century, when in 1863 Geuther proposed the enol structure for acetoacetate ester [118], but a few years later Frankland [120] and then Wislicenus [121] assigned the keto structure, revealed that acetoacetate can exist in these two forms. Further, the existence of keto-enol tautomerism was illustrated by Claisen in 1896 with acetyldibenzoylmethane and tribenzoylmethane [122], Wislicenus for methyl and ethyl formylphenylacetate [123] and by Knorr for ethyl dibenzoylsuccinate and ethyl diacetylsuccinate [124]. The existence of the different tautomeric forms depends on the stability of that particular tautomer due to the π -electron delocalization and in fact, this extra stability helps to explain why a particular compound prefers a different tautomeric form than the other.

2.2.2 Tautomerism in N-confused porphyrin

The inversion of one pyrrolic ring in N-confused porphyrins (**NCP**) exhibit significant differences in their physical and chemical properties with respect to normal porphyrins. Interestingly, not so longer after the introduction of N-confused derivative, the possible tautomeric existence of **NCP** was initially demonstrated by Abhik Ghosh in 1995 [125]. While investigating the unexpected labile nature of the inside C-H bond in the confused porphyrin, he compared the inverted pyrrolic ring with an imidazolium carbene and calculated the energy difference between the tautomers. Later, Latos-Grażyński and co-workers exemplified the tautomeric existence of the molecule with nickel complexes of various oxidation state [126, 127], where, the paramagnetic nickel complexes of carba-

methylated and nitrogen-methylated **NCP** adopted different geometries to stabilize the metal complexes [126].

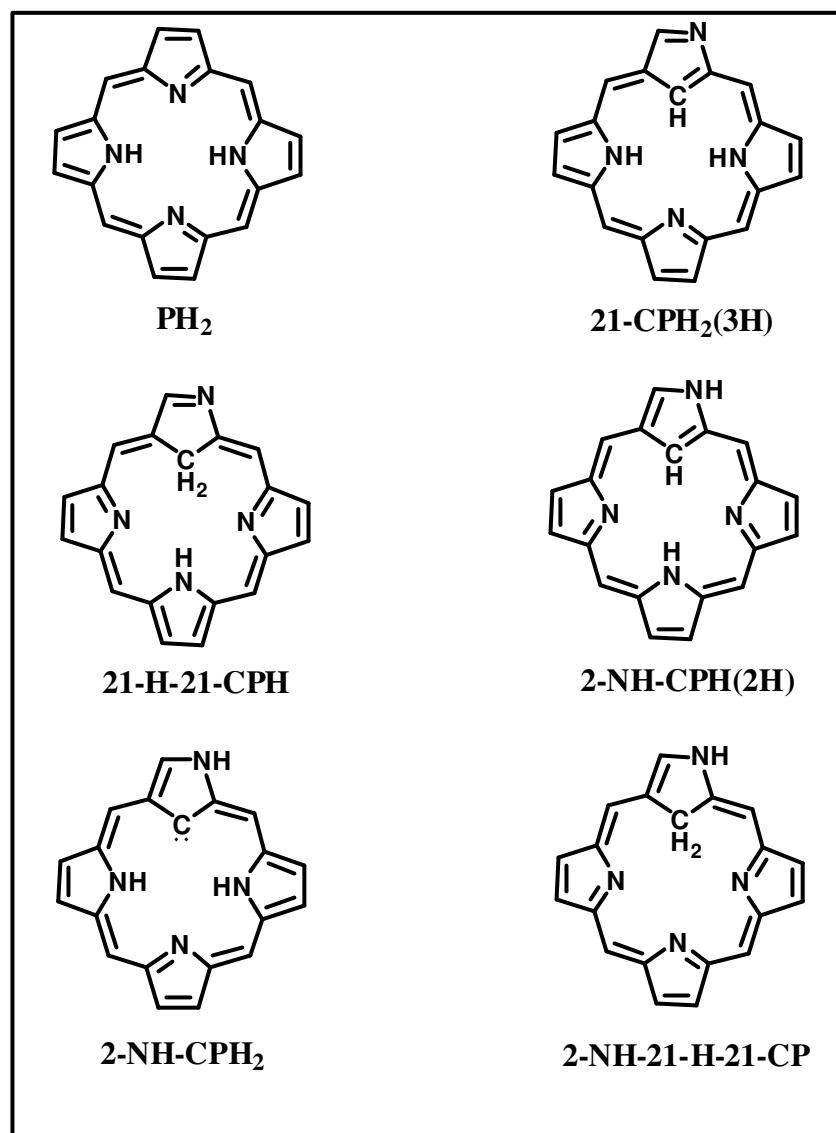


Figure 2.1. Possible tautomeric structures of **NCP**.

In 1997, the same group predicted the existence of the ‘hypothetical’ tautomers of the carbaporphyrins [128] (used the term 2-aza-21-carbaporphyrin for **NCP**) and their structures. The electronic energies have been investigated by applying density functional theory (DFT) for idealized 21-carbaporphyrin derivatives such as, **21-CPH₂** (N-confused derivative with three hydrogens inside the core, one with inside carbon and two with nitrogen atoms), **21-H-21-CPH** (three hydrogens inside the core, two with carbon and

one with nitrogen), **2-NH-CPH** (two hydrogens inside, one with carbon and another with nitrogen), **2-NH-CPH₂** (carbenic form with two hydrogens with nitrogen atom), **2-NH-21-H-21-CP** (two hydrogen atoms with the inside carbon) with respect to normal porphine derivative, **PH₂** as shown in Figure 2.1. The calculated total electronic energies, using the B3LYP/6-31-G**//B3LYP/6-31G approach, demonstrate that relative stability of the postulated tautomers decreases in the order **21-CPH₂ > 21-H-21-CPH > 2-NH-CPH >> 2-NH-CPH₂ > 2-NH-21-H-CP** [128].

Later, Ghosh *et al.* have carried out a broad survey of the molecular structures of porphyrin derivatives including **NCP** and its core modified derivatives [129]. The relative energies of different tautomeric forms have been calculated and correlated with structural features of the respective macrocycles. The DFT calculations suggested that the internally protonated three hydrogen tautomer (**3H**) is more stable compared to the externally protonated analogue (**2H**) by ~5.7 kcal/mol, which was confirmed later by Modarelli and co-workers [129, 130]. Even though there is a macrocyclic conjugation break in the **2H** tautomer with respect to **3H** form, which is resonance and hydrogen bond stabilized, the less energy difference between the two forms was attributed to the steric crowding in the **3H** form. The carbenic tautomer (**2-NH-CPH₂**) was found to be destabilized by ~33 kcal/mol compared to **3H** tautomer, which in turn destabilized by a factor of 17.7 kcal/mol with respect to normal porphyrin as shown in Figure 2.2 [129].

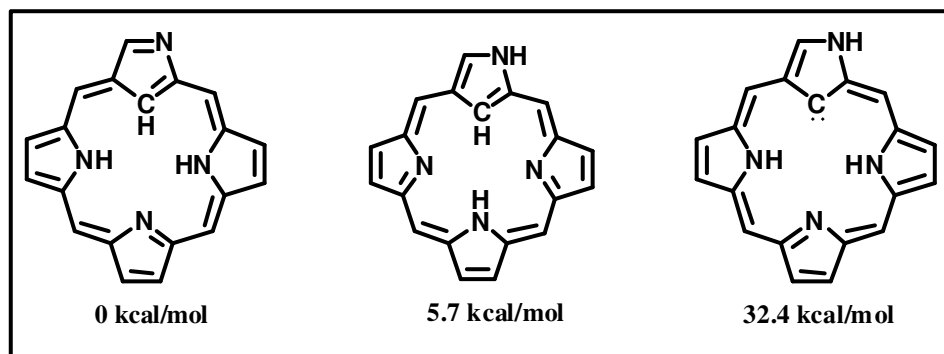


Figure 2.2. Relative stabilization energy of different tautomers of NCP.

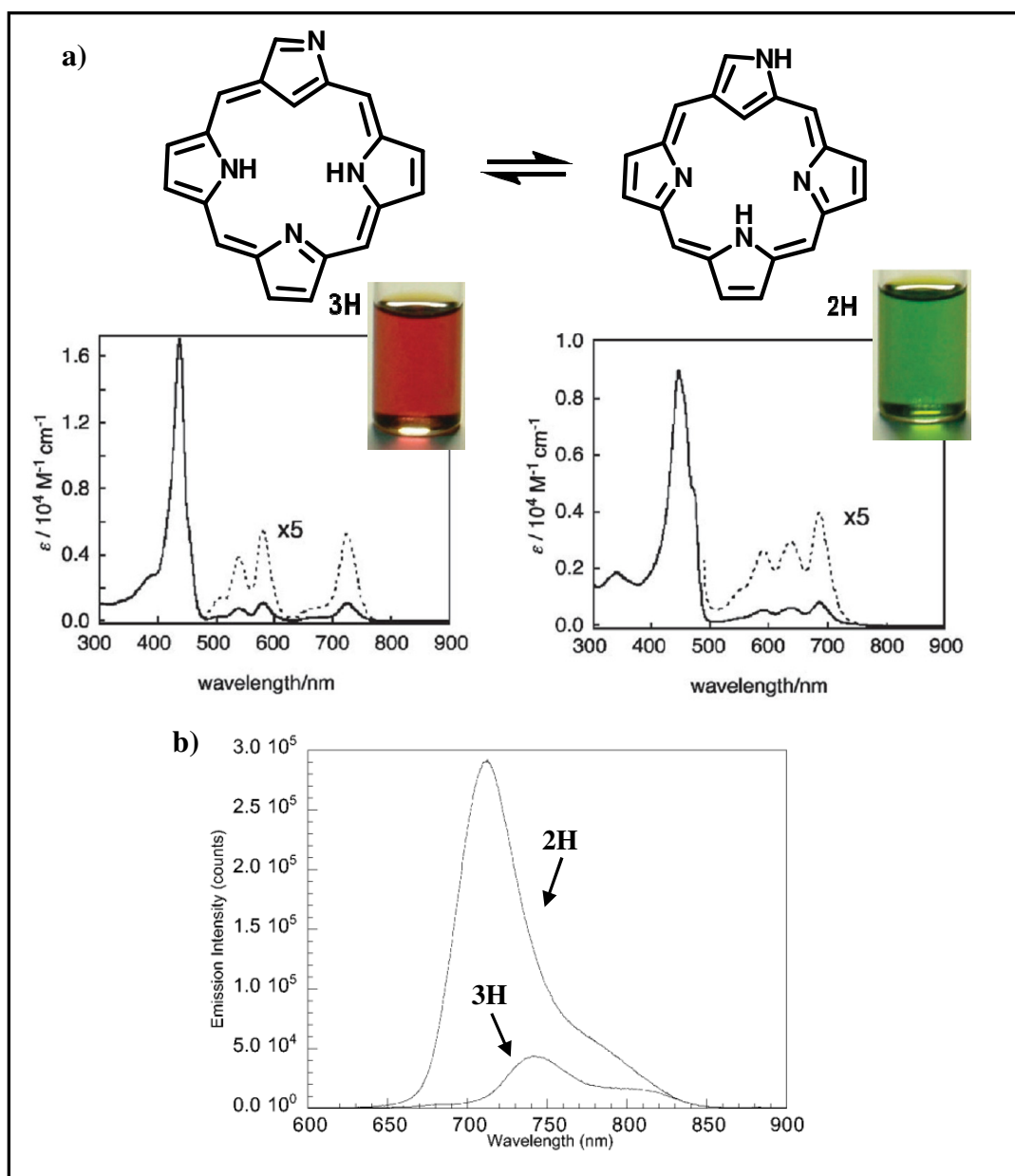


Figure 2.3. (a) Absorption spectra and the colour of two confused porphyrin tautomers [131] and (b) emission spectra of the tautomers [130].

In 2001, Furuta and co-workers demonstrated the tautomeric existence of **NCP** (**3H** and **2H**) both in solution as well as in solids [131]. A DMF solution of the compound showed green colour in solution, where the CHCl_3 solution exhibited red colour and also differ in their absorption spectra as shown in Figure 2.3. The two N-confused tetraphenylporphyrin (**NCTPP**) tautomers observed in different solutions were stabilized by hydrogen bond formation. One tautomer has an external N-H group (**2H**) and is favoured in highly polar solvents such as DMF. The second tautomer has two internal N-H groups (**3H**) and is the preferred tautomer in aromatic and halogenated solvents.

Furuta and co-workers investigated the tautomeric existence of **NCTPP** in $\text{DMF-}d_7$ and CDCl_3 using ^1H and ^{15}N NMR spectroscopy. The ^1H NMR spectra recorded in CDCl_3 showed two peaks at -4.99 and -2.41 ppm, which was assigned to the inner CH and two NH protons respectively corresponding to the **3H** tautomer. Where, ^1H NMR spectrum in DMF showed singlet peaks at 0.76, 2.27 and 13.54 ppm, assigned to the inner CH, inner and outer NH protons respectively corresponding to the **2H** tautomer. The ^{15}N NMR spectrum of **3H** tautomer showed four signals at 135.64, 137.16, 238.09 and 303.58 ppm in CDCl_3 at ambient temperature. The first two sharp peaks (135.64 and 137.16 ppm) were assigned to the inner protonated nitrogens while the third peak (238.09 ppm) was for non-protonated inner pyrrolic nitrogen. The fourth broad peak (303.58 ppm) was corresponded to the exterior pyrrolic nitrogen that is magnetically coupled to the adjacent α -CH. The ^{15}N signals for **2H** tautomer was resonated at 129.82, 175.72, 267.54, and 271.38 ppm were observed in $\text{DMF-}d_7$. The signal at 129.82 ppm was assigned to the inner NH, while the second peak (175.72 ppm) was corresponded to the outer NH. The third and fourth signals (267.54 and 271.38 ppm) was for the interior imine nitrogens, and mentioned that the weaker aromaticity of the **2H** tautomer was supported by the smaller chemical shift difference between the interior and exterior

nitrogens [131]. The structure of the tautomers in solid state were confirmed by single crystal X-ray structure, where the **2H** form crystallized in DMF showed intermolecular hydrogen bonding with solvent and attained comparatively planar structure with respect to the **3H** tautomer formed in DCM solution, which is significantly distorted from the planar structure as shown in Figure 2.4 [131].

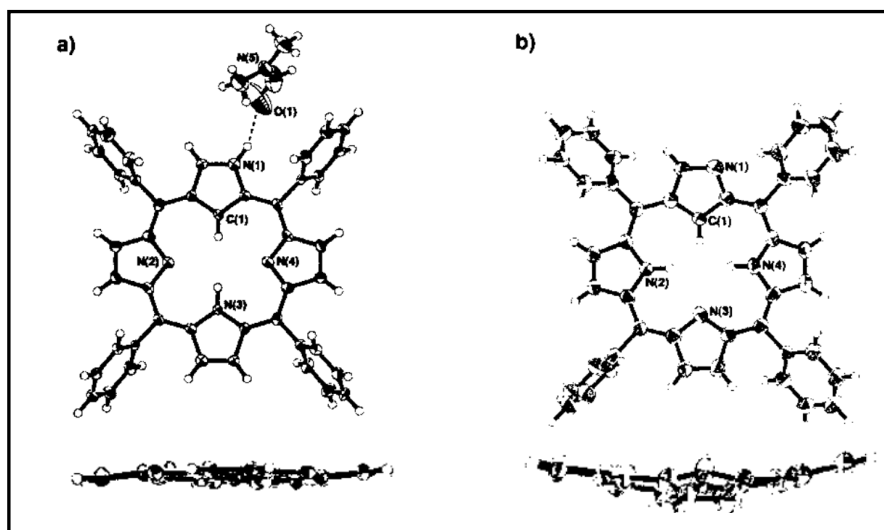


Figure 2.4. X-ray single crystal structure of NCTTP obtained from (a) DMF-MeOH (**2H**) and (b) DCM-MeOH (**3H**). For clarity *meso*-phenyl groups are omitted in the side views [131].

As explained before, the geometry of the two tautomeric structures have distinct difference, which in turn influence the shape and energy of their occupied and unoccupied orbitals. However, both for **3H** and **2H** the HOMO and HOMO-1 orbitals are reversed in energy relative to tetraphenylporphyrin (**TPP**) and have a_{2u} symmetry (HOMO) and a_{1u} symmetry (HOMO-1). The energy difference between these orbital is 0.7156 for **2H**, where for **3H** it is comparable with **TPP**. This energy difference is substantially larger than that found in either **TPP** (0.2220 eV) or tetraphenylchlorin (**TPChl**) (0.1412 eV) and according to Modarelli these energy difference arises from destabilization of the a_{2u} HOMO which is 0.4528 and 0.3034 eV higher in energy than

the HOMO of **TPP** and **TPChl**, respectively. The HOMO-LUMO gap is 2.4580 eV (compared to 2.7609 eV for **TPP**) for the **3H** form. On the other hand, the HOMO-LUMO gap in **2H** tautomer was 2.122 eV [130].

Absorption spectra of both tautomers showed distinct difference in the Soret and Q-band pattern and were red-shifted significantly with larger extinction coefficients than those of **TPP** as shown in Figure 2.3. In polar solvents such as DMAc and DMF the externally protonated form (**2H**) is more stable, which is explained either by hydrogen-bonding or dipole-dipole interactions of the exocyclic N-H bond with solvent. Whereas, less polar solvent such as CHCl_3 favors the internally protonated **3H** form. The Soret band of **2H** tautomeric form was observed at 441 nm, where as that of **3H** was at 438 nm. The Q-band pattern were also showed distinct difference for the two tautomeric structures [130, 132]. Both tautomers exhibit their characteristic emission bands (Figure 2.3.b) in different solvent systems and also differ significantly on their fluorescence quantum yield and singlet lifetime. The **3H** tautomeric form give two bands in the emission spectrum with almost similar intensities at 744 and 815 nm, where as the **2H** form shows a major band at 713 nm and a shoulder at 783 nm.

2.2.3 Porphyrin aggregates

Compared to solution phase, surface-confined molecular assemblies display much greater coherence in their orientation, structure, and ultimately, function. Intermolecular and molecule substrate interactions govern these self-assembly processes and fine-tuning of the chemical and/or physical properties that influence these interactions can allow control over the structure and molecular distribution during self-assembly. On the other hand, there are systems that consist of molecules sensitive to aggregate with certain stimulus such as pH, temperature, light, solvents, guest molecule etc and the morphology can be modulated or controlled by these stimuli.

Solvent and other external input driven self-assembled nanostructures of organic molecules driven by various interactions are of great interest in the area of storage and conversion of solar energy, sensors, catalysis and biological applications [133-135]. For example, porphyrin assemblies play major role in biologically relevant systems such as chlorophyll and bacteriochlorophyll [136, 137]. In fact, molecules of bacteriochlorophylls, a porphyrin derivatives assemble to form the nanorods in the chlorosomes of green bacteria, and these chlorosomal rods are the largest and most efficient harvesters of light known [138, 139].

Usually, self-assembly of porphyrin nanostructures can be induced by various means such as reprecipitation, coordination polymerization, surfactant induced self-assembly and ionic self-assembly [136, 137, 140]. Here, in the reprecipitation method the compound is dissolved in a suitable solvent and reprecipitates with cooling, where in coordination and ionic and self-assembly methods the respective inter molecular interactions forms the assemblies. The solvent assisted and surfactant induced assemblies make use of the rapid exchange of solvents or mixing of solvents containing the chromophoric molecules with miscible solvents in which the compound is not soluble [137].

Shelnutt and co-workers showed robust porphyrin nanotubes, which was prepared by ionic self-assembly of two oppositely charged porphyrins in aqueous solution. The nanotubes are composed entirely of two ionic porphyrins as shown in the Figure 2.5. The electrostatic forces between these porphyrin units, in addition to the van der Waals, hydrogen bonding, axial coordination, and other weak intermolecular interactions that typically contribute to the formation of porphyrin aggregates, enhance the structural stability of these nanostructures [140].

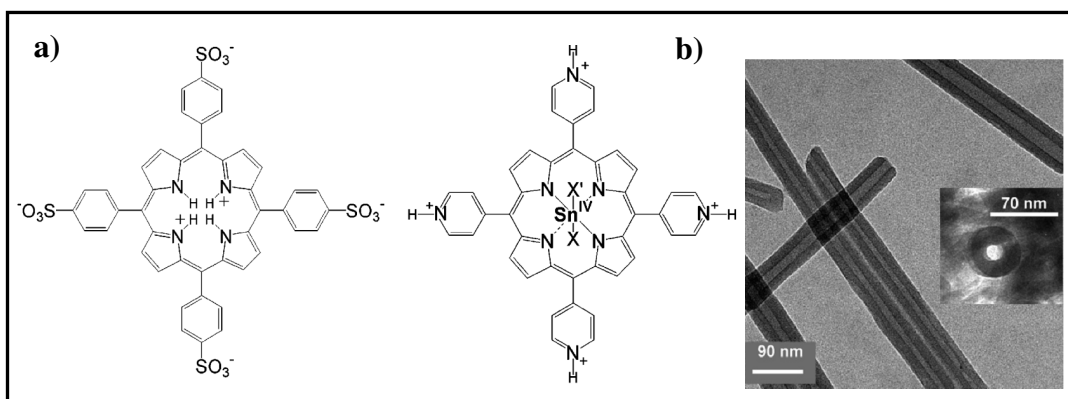


Figure 2.5. (a) Structure of the charged porphyrin units (b) TEM images of porphyrin nanotubes formed through ionic interactions between the porphyrin units [140].

Later, the same group demonstrated photoinduced self-metallization process of porphyrin nanofibers and nanosheets. The photoactivity of porphyrin nanofibers were illustrated by their self-metallization reactions with various metals such as silver, gold and platinum [141, 142].

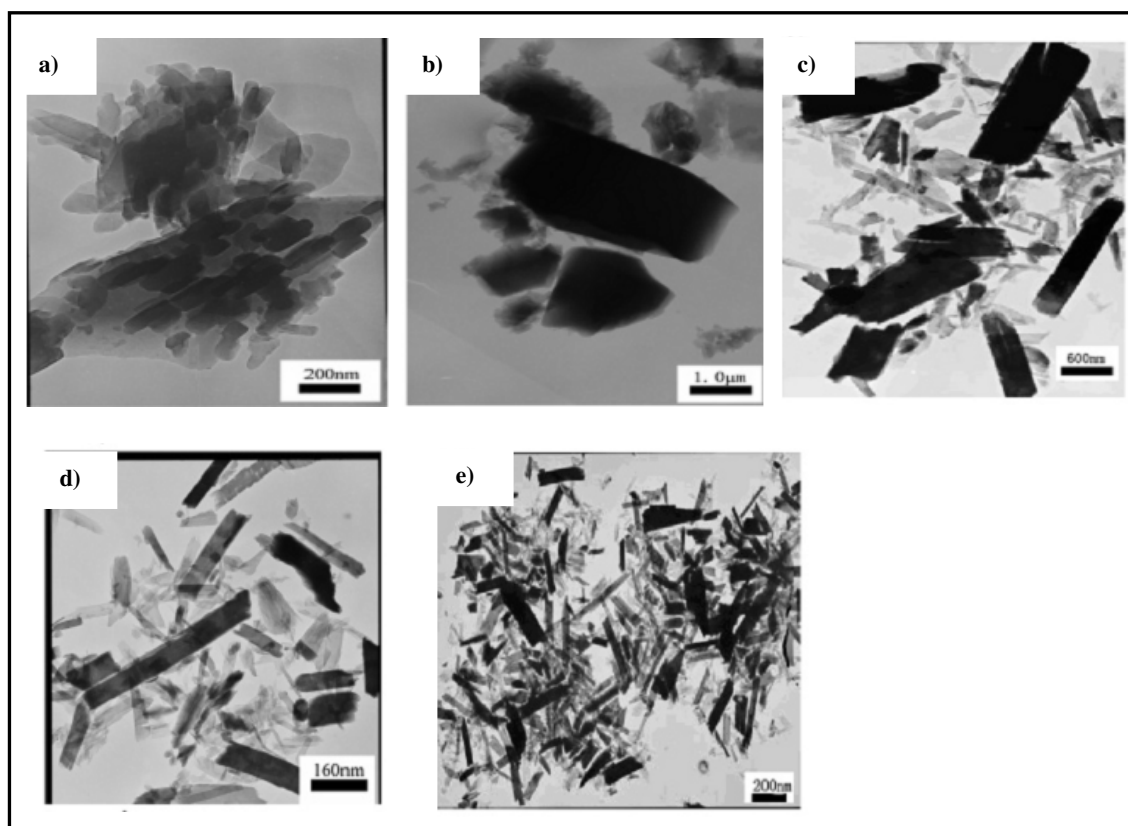


Figure 2.6. TEM images of cobalt-porphyrin nanorods at different temperatures: (a) 273 K, (b) 298 K, (c) 308 K, (d) 318 K, and (e) 328 K [143].

Guo and co-workers prepared the nanorods of a chiral cobalt porphyrin dimer by directly bridging with L-glutamic acid dimer using liquid-solid-solution technologies and found that the aggregate morphologies of the porphyrin dimer changes upon varying the temperatures (Figure 2.6). The porphyrin dimer transformed from H-aggregate to J-aggregate with an increase of the temperature under the same experimental conditions. The reason is that the J-aggregate is thermodynamically stable and hence promotes the formation of the J-aggregates with the increase in temperature [143].

In contrast to the above described physical stimuli, chemical stimuli, such as the incorporation of a specific species like anions and cations, could afford versatile supramolecular structures quite different from the previous conditions depending on the interactions between the additives and the molecules. There are several examples where the morphology transitions are controlled by cations [144, 145], but the design of anion receptors with high selectivity is challenging. To form anion-responsive dimensionally controlled organized structures, the molecules must act as anion receptors by possessing one or more of van der Waals interaction units (aliphatic chains), stacking π -planes, hydrogen-bonding sites, and metal-coordination units [146]. These interactions can be made possible by using complimentary binding sites with hydrogen-bonding groups, quaternary ammonium centres, Lewis acids and cationic metal ions. In particular, hydrogen bonding driven interaction, because of its directional nature [147]. Hence, neutral anion receptors having amide, urea, pyrrole units employed in a variety of both cyclic and acyclic receptors are an important subset of the anion binding agents [148-151].

In 2002, Král and co-workers reported the first self-assembly of porphyrin-bicyclic guanidine conjugate (**PG**) upon addition of small anions and forms chiral structures which was controlled by the type of anion used. Addition of anions such as CH_3CO_2^-

(Figure 2.7.c), H_2PO_4 , terephthalate, or anthraquinone-1,5-disulfonate (Figure 2.7.d) to **PG** in water (Figure 2.7.b) causes an additional decrease and a split of the Soret band of the monomer accompanied by the appearance of two broad maxima at about 405 and 428 nm [152].

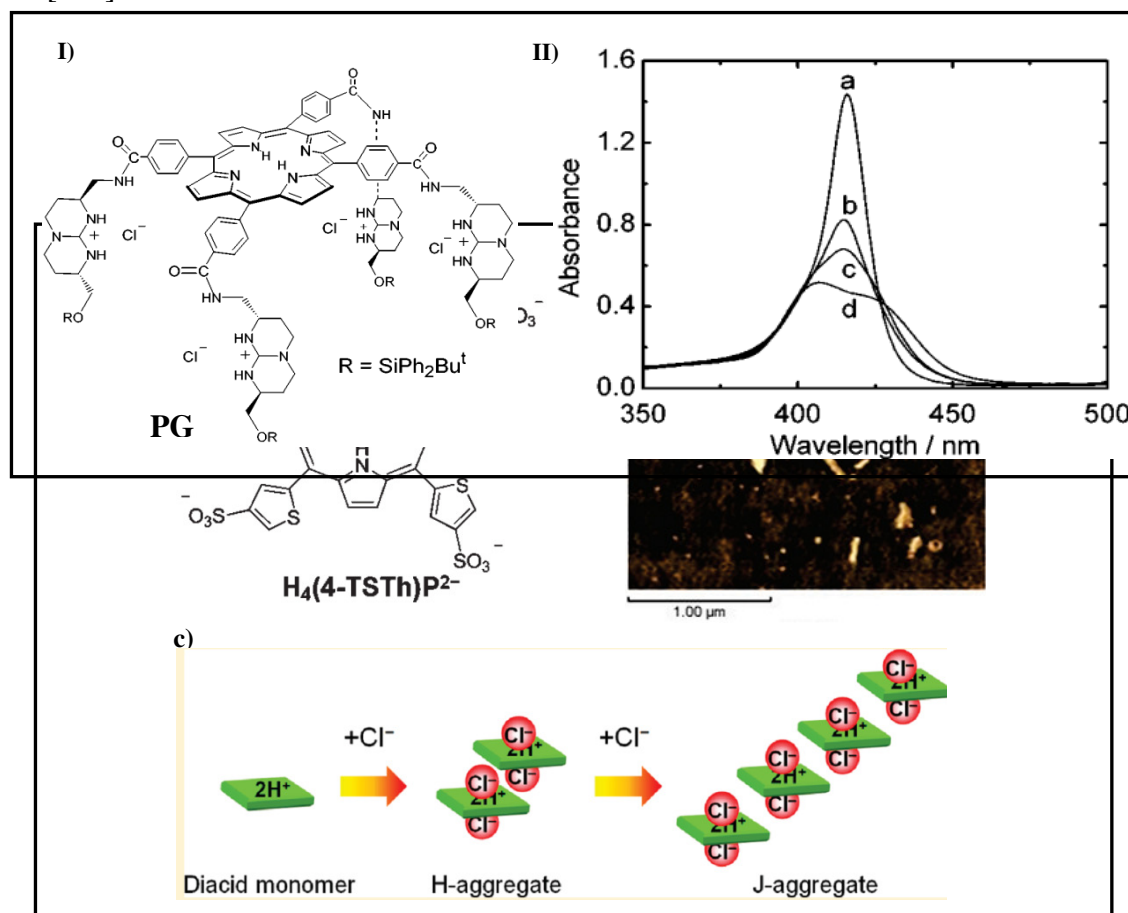


Figure 2.7. I) Structure of **PG**, and II) absorption spectra of **PG** in (a) MeOH, (b) H_2O , (c) 10 mM acetate and (d) 0.5 mM anthraquinone-1,5-disulfonate [152].

Figure 2.8. (a) Structure of $[\text{H}_4\text{T}(4\text{-STh})\text{P}^{2-}]$, (b) AFM images of the deposited J-aggregate prepared from the aqueous solution of $[\text{H}_4\text{T}(4\text{-STh})\text{P}^{2-}]$ with 2 M HCl and (c) scheme for the H- and J- aggregate formation [153].

Recently, Segawa and co-worker demonstrated the formation of both H- and J-type aggregate with porphyrin diacid, *meso*-tetrakis(4-sulfonatothienyl)porphyrin $[\text{H}_4\text{T}(4\text{-STh})\text{P}^{2-}]$, Figure 2.8.a] complexed with Cl^- ion in aqueous solution. The H-aggregate is

formed preferably at dilute conditions, but further addition of Cl^- caused the transformation of H- into J-aggregate. AFM image showed that the J-aggregate as rod-shaped nanostructures composed of highly oriented molecules (Figure 2.8.b). The stacking structures of the H- and J-aggregates are proposed to be a slipped face-to-face dimer and an edge-to-edge polymer, respectively, where the porphyrins are mediated by two Cl^- anions (Figure 2.8.c) [153].

However, aggregation properties and corresponding morphological changes of **NCP** derivatives were reported scarcely. Furuta and co-workers reported anion induced dimerization of a *meso*-unsubstituted **NCP (3-oxo-NCP)** which formed self-assembled dimer in DCM that is stabilized by complementary hydrogen-bonding interactions arising from the peripheral amide-like moieties [154, 155]. The protonated form of **3-oxo-NCP** was found to bind halide anions such as F^- and Cl^- ions through the outer NH and the inner pyrrolic NH groups, thus affording an anion bridged dimer.

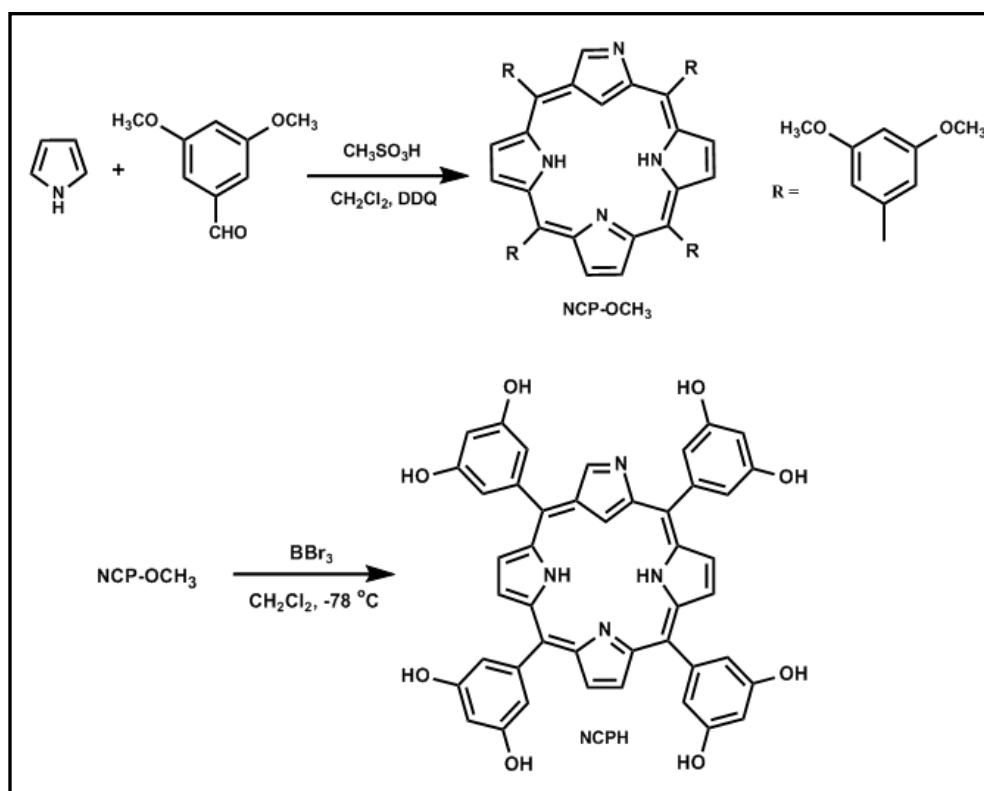
In 2008, Furuta and co-workers reported the aggregation behaviour of tetra glucamine appended N-confused derivative, **TG-NCP**. It exists as monocation in aqueous solution along with 6 mM sodium dodecyl sulfate (SDS) but forms aggregates in pure water. These properties were distinct from those of corresponding regular porphyrin, which exists as freebase in the micellar solution and practically insoluble in water. They elucidated the acid/base properties of **TG-NCP** under the monomeric and aggregated conditions, quantitatively by pH titrations in the presence/absence of 6 mM SDS and found that the dominant species of **TG-NCP** (in 6 mM SDS) solution at pH 11, 7.8-4.2, and 0.83 can be assigned as freebase, monocation and dication respectively. Whereas in acidic pH without SDS **TG-NCP** would represent a disassembly process of aggregated freebases to monomeric dications [156].

2.3 Objective of the Work

As per the above mentioned discussions, porphyrin based nanoarchitectures are well established. However, the supramolecular assemblies of N-confused porphyrin and its derivatives are not explored much in the literature. Hence, this chapter discusses the synthesis, spectral and structural characterization of an octahydroxy N-confused porphyrin derivative (**NCPH**), and demonstrates the tautomeric existence and exchange of **NCPH** in polar protic and aprotic solvents. Further, shows interesting morphological features during aggregation with respect to different stimuli such as tautomeric existence and presence of anions.

2.4 Results and discussion

2.4.1 Synthesis and structural characterization of NCPH



Scheme 2.1. Synthetic scheme for **NCPH** [157].

NCPH was prepared through a two step synthetic strategy as shown in Scheme 2.1, where in the first step corresponding methoxy derivative was prepared by using Lindsey's method, followed by demethylation using borontribromide to form **NCPH** in 80% yield [64]. The compound was found to be highly soluble in polar solvents like MeOH, DMF and DMSO however, insoluble in H₂O and ACN. The structure of **NCPH** was confirmed through various spectroscopic techniques such as ¹H, ¹³C NMR, FT-IR, FAB-MS analysis. Purity of the compound was determined as > 95% using HPLC and elemental analysis.

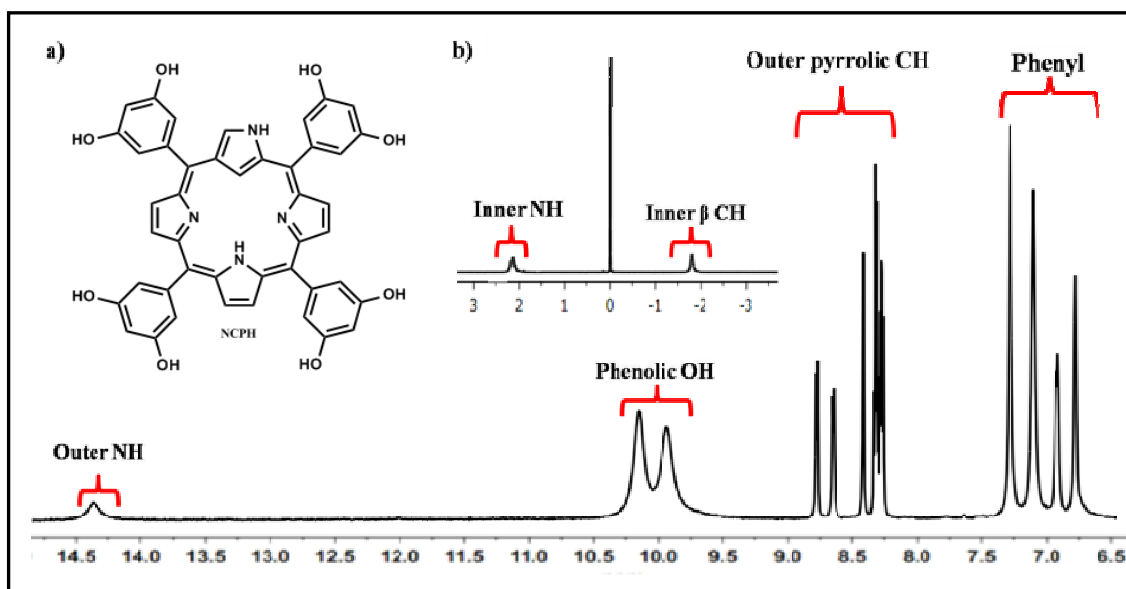


Figure 2.9. ¹H-NMR spectrum of **NCPH** in DMSO-*d*₆ (a) structure of **NCPH** and (b) upfield region of ¹H NMR spectrum.

The ¹H NMR spectrum of **NCPH** in DMSO-*d*₆ is shown in Figure 2.9 [157]. The two broad peaks centered at 10.00 ppm corresponding to the phenolic OH protons. The confused pyrrolic NH proton is resonated as a broad singlet at $\delta = 14.3$ ppm as expected for the 2H tautomer of the confused derivatives in polar solvents. The outer α and β -CH protons were resonated between 8.23-8.75 ppm and phenylic CH's between 6.77-7.27 ppm. The inner pyrrolic NH and β -CH were observed at $\delta = 2.14$ and $\delta = -1.82$ ppm respectively, which were downfield shifted compared to the other N-confused

derivatives. The presence of acidic protons such as pyrrolic NH and phenolic OH were further confirmed by deuterium exchange experiments with D₂O. The FAB-MS analysis showed the M + 1 peak at 743.83 and the phenolic OH stretching frequency observed at 3422 cm⁻¹ from the FT-IR spectral analysis confirms the structure of the molecule.

2.4.2 NH Tautomerism in NCPH

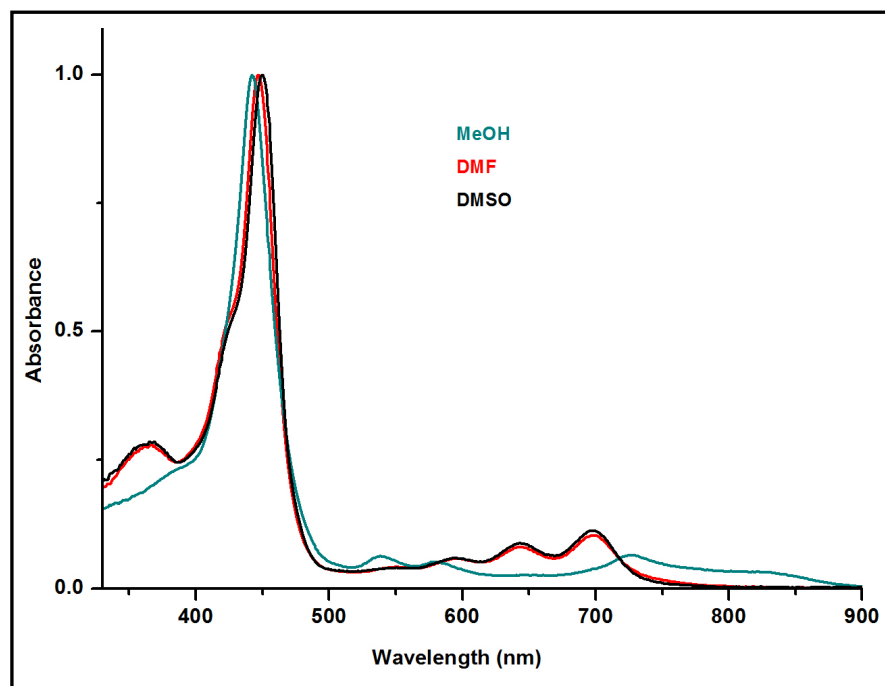


Figure 2.10. Absorption spectra of **NCPH** in different solvent systems.

Absorption spectra of **NCPH** was recorded in three different solvents such as MeOH, DMF and DMSO (Figure 2.10) to investigate the effect of solvent polarity as well as to get an insight into the stable tautomer possible for the molecule in these solvents [157]. The spectra showed the Soret band at 443, 447 and 450 nm in MeOH, DMF and DMSO respectively with progressive red-shift as expected from the increase in solvent polarity. The molar extinction coefficient of **NCPH** was found to be 9.27×10^4 , 9.35×10^4 and 9.53×10^4 M⁻¹cm⁻¹ for the Soret bands respectively. The Q-bands in MeOH solution exhibit peaks at 539 and 581 nm due to a Q_y(1,0) and Q_y(0,0) transition whereas Q_x(1,0) and Q_x(0,0) transitions were responsible for 653 and 727 nm bands

which extend up to 900 nm. On the other hand, the Q-bands in DMSO solution show bands at 547, 595, 644 and 697 nm with Q-band oscillator strengths increases with decrease in energy in a regular fashion, where $Q_x(0,0)$ showing the maximum intensity and $Q_y(1,0)$ with the lowest. Interestingly, the Q-band pattern in MeOH and DMSO shows distinct discrimination and enlightens the possible existence of different tautomeric form in these solvents irrespective of their high polar nature. The nature of **NCPH** Q-bands in MeOH was comparable with Q-band pattern of **NCTPP** in CHCl_3 to give indication about the existence of internally protonated 3H tautomer in MeOH, where, the Q-band pattern in DMSO was similar to that of **NCTPP** in DMF, which predicts the presence of **NCPH** in the externally protonated 2H tautomeric form in DMSO [157].

The emission characteristics of **NCPH** were recorded in protic and aprotic polar solvents on excitation at the respective absorption maximum as shown in Figure 2.11. In DMSO and DMF, the compound was showing emission maxima at 720 and 717 nm respectively corresponding to a $Q_x(0,0)$ emission with a shoulder at around 780 nm for $Q_x(0,1)$ emission [157]. The spectral pattern were comparable with the emission characteristic of **NCTPP** in polar solvents like DMF and DMAc, where the 2H tautomer predominates over the 3H tautomer and confirms the existence of **NCPH** in the externally protonated form in DMSO and DMF. In contrast, MeOH solution of **NCPH** shows two bands of equal intensity at 725 and 785 nm similar to **NCTPP** in CHCl_3 substantiates the occurrence of **NCPH** in the internally protonated 3H tautomeric form. Further, the fluorescence quantum yield was measured with respect to **TPP** as reference and the yield obtained was 0.0013 in MeOH. Whereas, aprotic solvents showed a tenfold increase in the emission quantum yield as 0.013 and 0.019 in DMF and DMSO respectively. The fluorescence life time of **NCPH** in the different tautomeric form has been recorded using a picosecond time-correlated single-photon counting (TCSPC)

technique (Figure 2.11 inset). The life time of the internally protonated form showed a biexponential decay profile with life time of 0.7 and 1.27 ns having 31 and 69% contribution each respectively and an average life time of 1.1 ns. On the other hand, the life time values obtained in DMF and DMSO were 1.87 ns and 2.07 ns respectively.

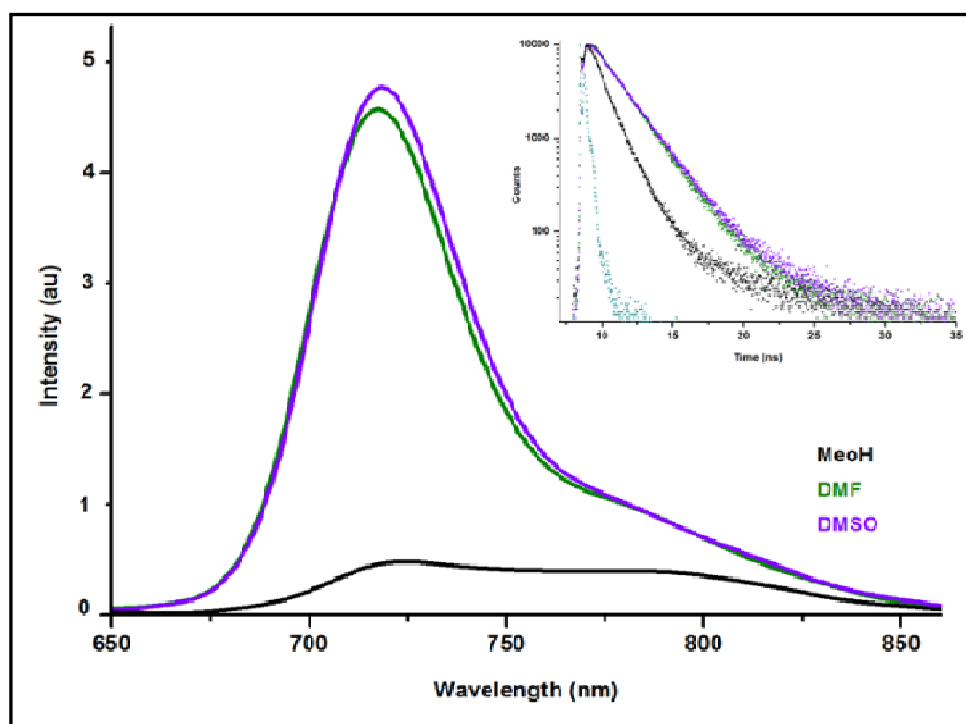


Figure 2.11. Emission spectra of NCPH in different solvent systems. Inset shows the decay profile in different solvents.

The remarkable difference in quantum yield between MeOH and DMSO solution can be attributed mainly on two factors, planarity of the molecule as well as the difference in life time in the excited state, thereby difference in the extend of possible non radiative decay pathways which decrease the emission intensity. Even though the energy difference calculated between the two tautomers was less (~ 3.4 - 5.7 kcal mol⁻¹), presence of three hydrogens inside the core contribute an extra destabilizing effect for the 3H tautomer and also disturb the planarity of the ring. Whereas, 2H tautomer is more planar due to the less steric crowding inside the core of the macrocycle, which contribute

towards the bathochromic shift in the absorption spectra as well as better emissive character. Also, a very short lived excited emissive state in the MeOH solution compared to the DMSO solution points at the various possible non-radiative decay channels as well as the accelerated rate of such decays in MeOH solution [157].

2.4.3 Tautomeric exchange and aggregation properties

The existence of a particular tautomeric form of **NCPH** in polar protic and aprotic solvents was confirmed by tautomeric exchange studies. As **NCPH** is insoluble in ACN (polar aprotic) as well as H₂O (polar protic) and the presence of eight hydroxyl group encouraged us to investigate the solvent assisted aggregation behavior. The investigation was conducted in solvent combinations such as DMSO/ACN, DMSO/H₂O, MeOH/ACN and MeOH/H₂O. The photophysical changes during aggregation were monitored through various spectroscopic techniques such as solution state FT-IR, UV-Vis absorption and emission spectroscopy.

The FT-IR spectral analysis of **NCPH** in MeOH/ACN showed OH stretching band at 3366 cm⁻¹, shifted to 3431 and then to 3541 cm⁻¹ as the ACN concentration increases from 0%, 50% and 90% as shown in Figure 2.12. a, b and c respectively [157]. The shift towards the higher energy side indicates existence of the strong solute-solvent hydrogen bonding interaction in the MeOH solution which weakens during aggregation. Analyses of IR spectra with higher ratio of ACN indicate the possibility of weak intermolecular hydrogen bonding that lead to self-assembled structures of **NCPH**. Higher ratio of ACN causes an exchange of tautomer from 3H form to 2H form. The 3H form of **NCPH** can easily make strong hydrogen bonding with MeOH through nitrogen lone pair and after the exchange, the 2H tautomer with an external NH proton prefers intermolecular interaction over the solvent-solute interaction. However, the DMSO/ACN mixture

showed a gradual drift in the OH stretching frequency as the aggregation progress.

Where, the stretching frequency observed at 3449 cm^{-1} in DMSO decreased to 3444 and

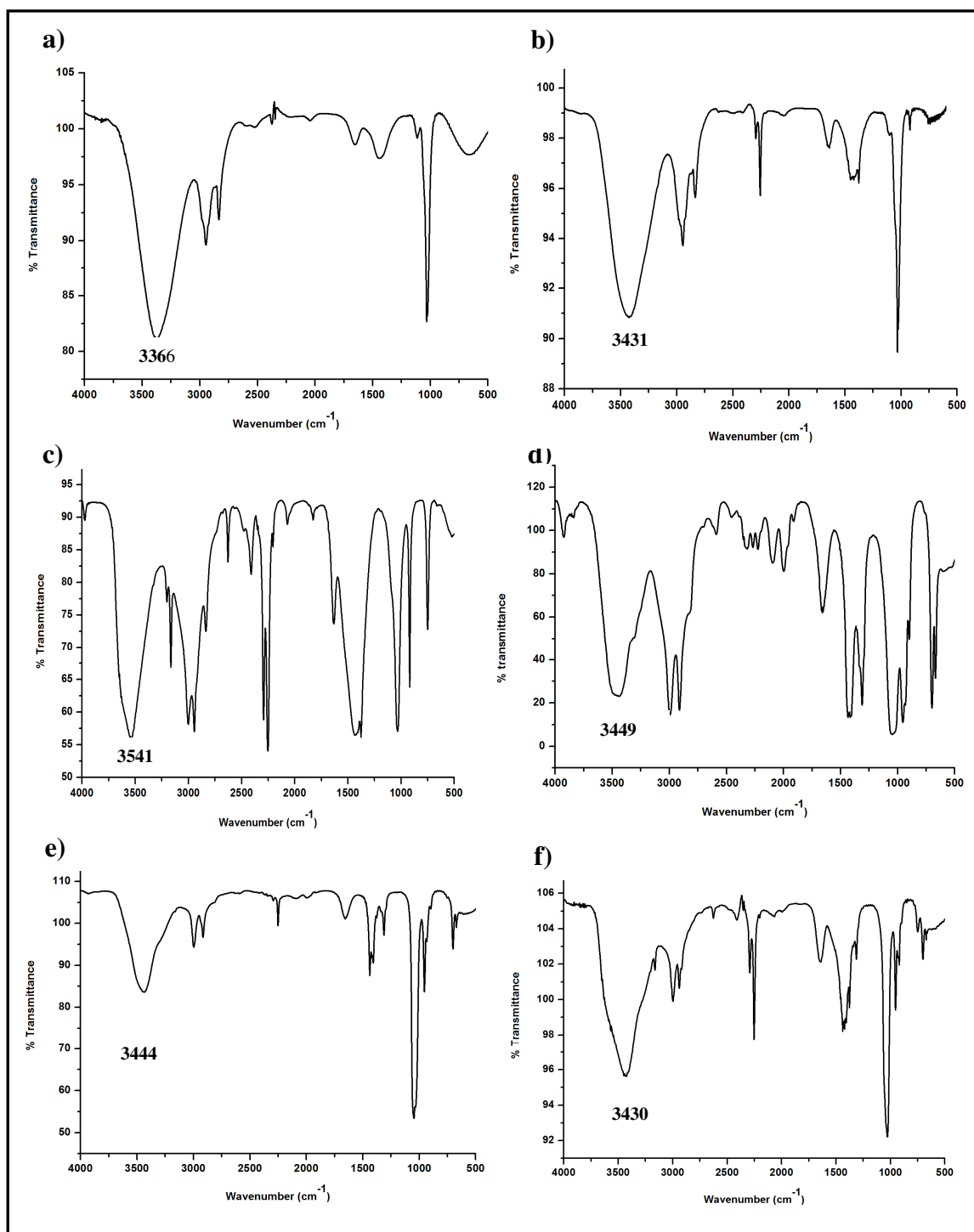


Figure 2.12. FT-IR spectra of NCPH in (a) MeOH solution, (b) 1:1 mixture of MeOH/ACN (c) 1:9 mixture of MeOH/ACN, (d) DMSO solution, (e) 1:1 mixture of DMSO/ACN and (f) 1:9 mixture of DMSO/ACN.

3430 cm^{-1} at 50% and 90% addition of ACN suggests that the intermolecular hydrogen bonding became stronger than the solute-solvent interaction as shown in Figure 2.12. d, e, and f respectively.

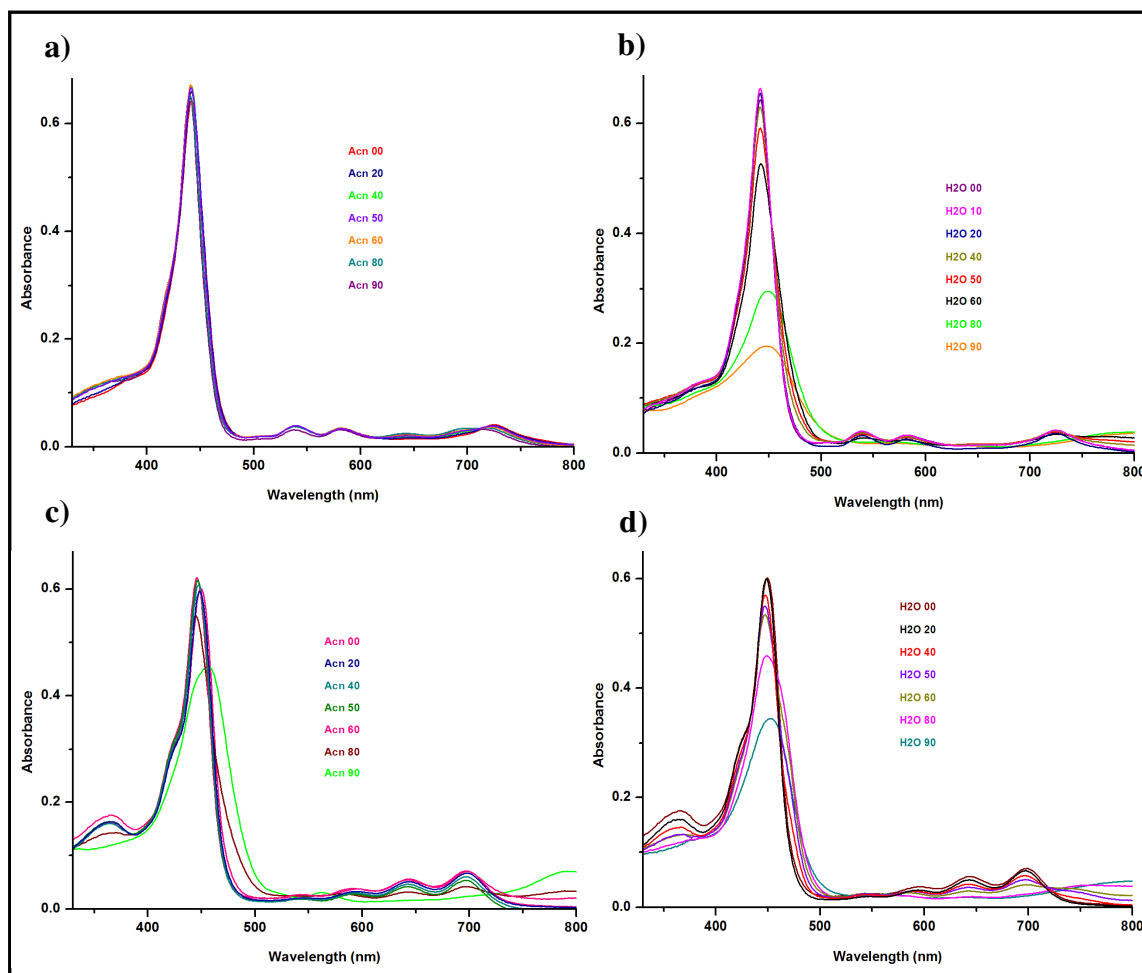


Figure 2.13. Change in the absorption profile of **NCPH** on aggregation in mixture of solvents (a) MeOH/ACN, (b) MeOH/H₂O, (c) DMSO/ACN and (d) DMSO/H₂O.

The UV-Vis absorption spectral changes in the mixture of solvents were recorded in 8 μM solution of **NCPH** (Figure 2.13). The absorption spectra displayed a hypsochromic shift in all situations with higher ratio of ACN and H₂O gives indication about formation of H-aggregates. The MeOH/ACN combination (Figure 2.13.a) was not showing considerable change for the Soret band owing to the combined effect of aggregation and tautomeric exchange. In other cases absorption spectra displayed slight hypsochromic

shift in initial stage, indicating the formation of H-aggregates. However, at higher ratio of both ACN and H₂O, spectral broadening occurs with red-shifted band.

The effect of protonation on **NCPH** was analyzed with trifluoroacetic acid (TFA), both in MeOH and DMSO solution (Figure 2.14). The absorption spectra obtained in MeOH solution was different from that obtained from MeOH/H₂O mixture, indicating the reason behind the absorption changes in MeOH/H₂O mixture is aggregation of the molecule by hydrophobic interaction, rather than protonation. The absorption profile obtained for the acid titration in DMSO solution was similar to that obtained for DMSO/H₂O mixture, which can be attributed to the possible tautomeric change by the addition of acid.

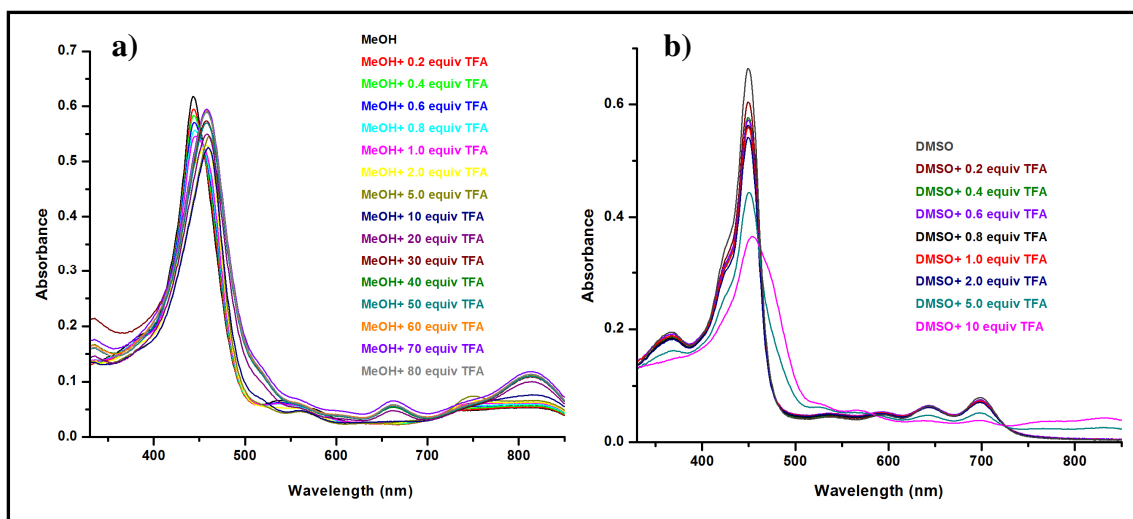


Figure 2.14. Change in the absorption spectra of **NCPH** during acid titration in (a) MeOH and (b) DMSO.

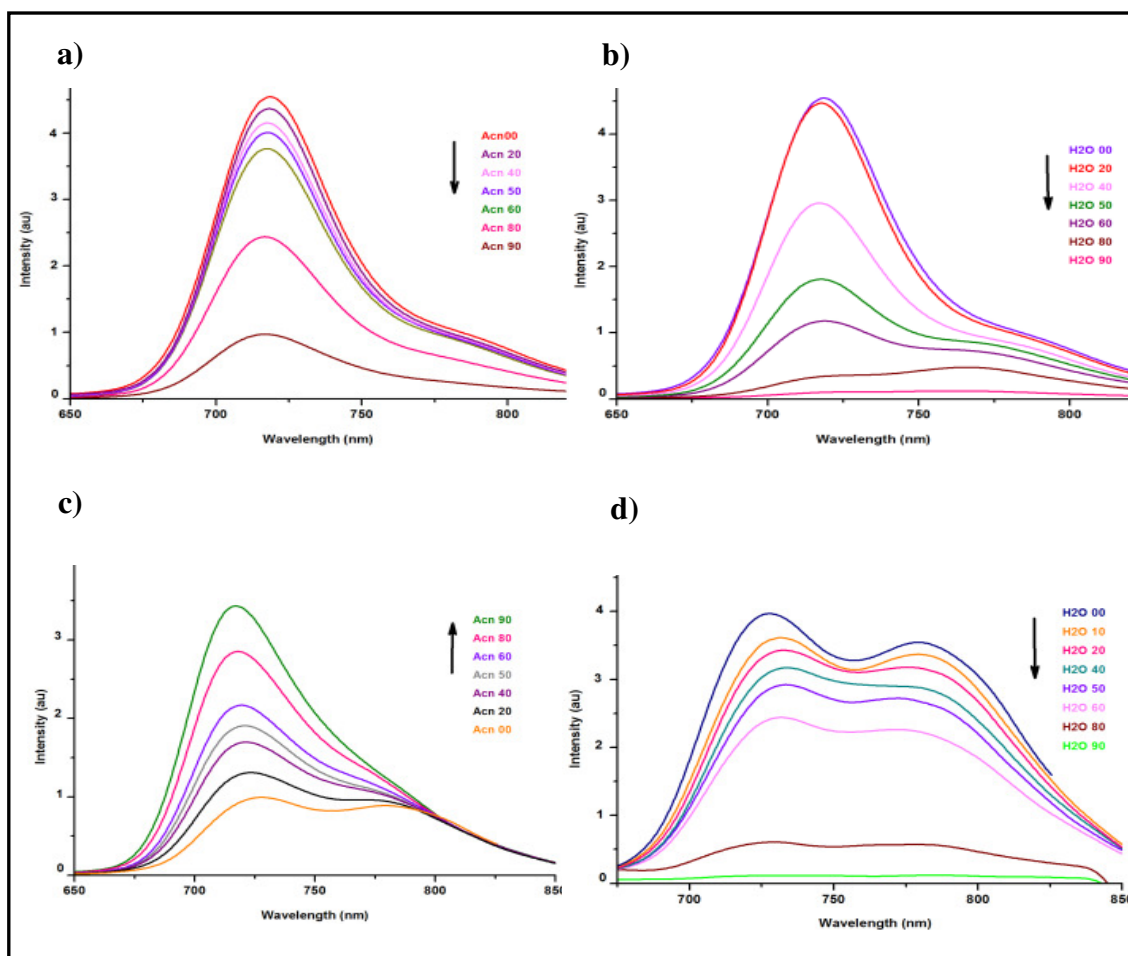


Figure 2.15. Change in the emission characteristics of **NCPH** in (a) DMSO/ACN, (b) DMSO/H₂O, (c) MeOH/ACN and (d) MeOH/H₂O with increasing amount of ACN and H₂O.

The emission profile of **NCPH** (8 μ M) upon addition of ACN and H₂O in DMSO and MeOH solution is shown in Figure 2.15. In DMSO/ACN mixture (Figure 2.15.a), when the ACN concentration increases from 20 to 90%, the emission intensity drops continuously due to solubility reasons. However, the emission profile ensures 2H tautomer of **NCPH** in the medium even in the aggregated state as both solvents are aprotic in nature. But, in DMSO/H₂O mixture (Figure 2.15.b) there was a clear display of exchange of 2H tautomer to 3H tautomer, which resulted in two equally intense emission peaks as observed in the MeOH solution. As the H₂O concentration increases from 20 to

90%, the emission intensity drops down due to aggregation. Interestingly, the gradual increase in the amount of ACN in MeOH/ACN mixture (Figure 2.15.c) shifted the emission maxima to the blue region with the maximum band at 720 nm as observed in DMSO solution of **NCPH**, indicate a tautomeric shift from 3H to 2H form. It was expected that, the insoluble nature of **NCPH** in ACN will cause aggregation and thus decreases the emission intensity as the ratio of ACN increases, but the transformation of the compound from 2H to 3H form, as explained earlier, increases the quantum yield four fold in the 1:9 mixture of MeOH/ACN as compared to MeOH solution. Further, the temperature dependent emission studies in the 1:9 MeOH/ACN mixture reveal the negligible influence of temperature on the emission intensity and concludes the tautomeric exchange as the reason for emission enhancement. In the MeOH/H₂O mixture (Figure 2.15.d), the emission pattern remains same even at the 1:9 ratio with decrease in the emission intensity, attest the existence of 3H tautomer in the medium. The possible mechanism for the tautomeric existence of **NCPH** in different protic and aprotic solvents was shown in Figure 2.16, where the hydrogen bonding formation drives the respective forms in different solvents.

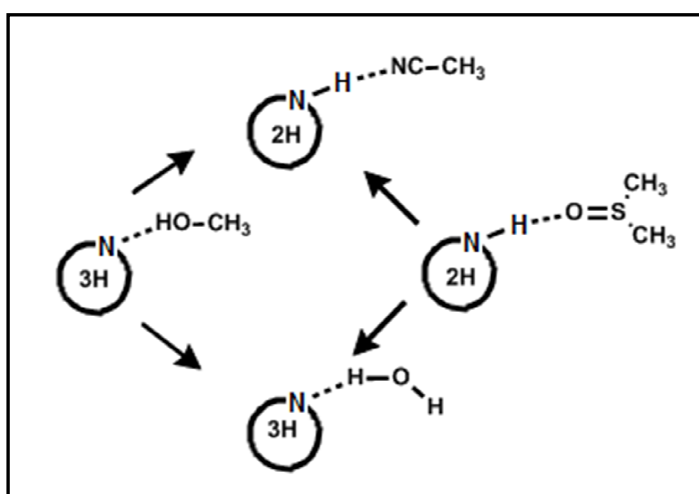


Figure 2.16. Schematic representation of possible tautomeric structures in polar protic and aprotic solvents.

2.4.4 The role of tautomeric structures in the morphology of NCPH aggregates

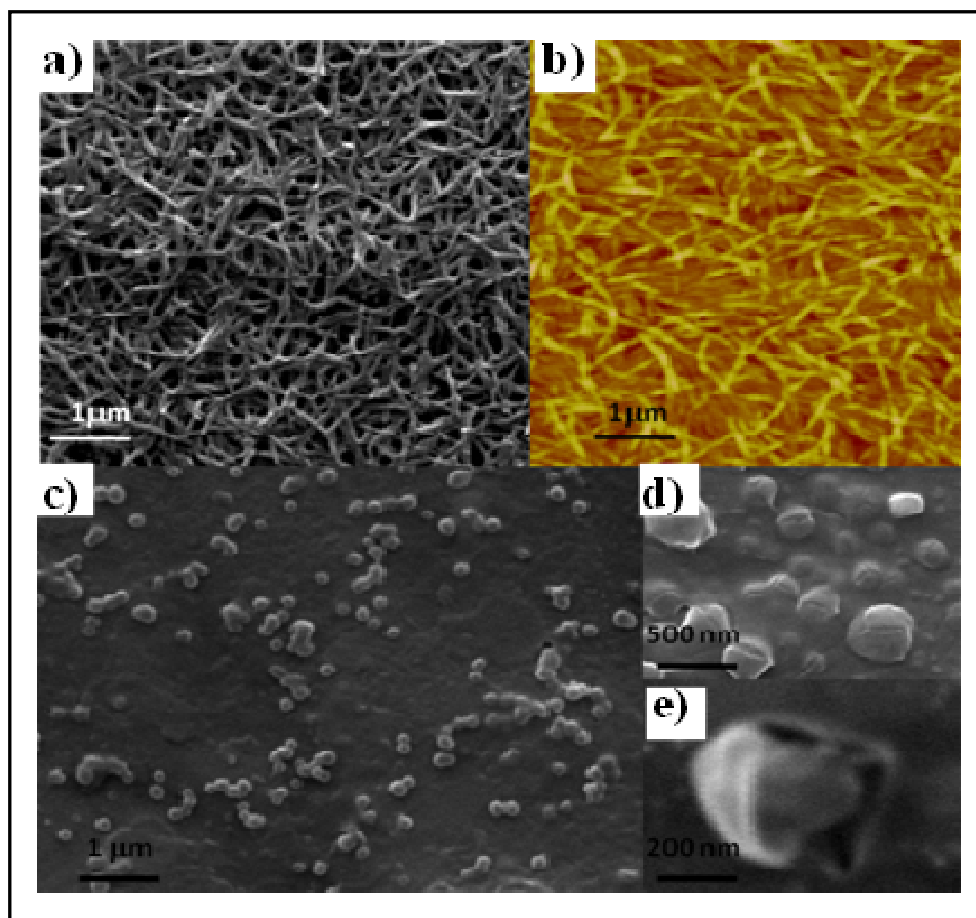


Figure 2.17. (a) SEM image of **NCPH** in MeOH/H₂O (b) AFM image of **NCPH** in MeOH/H₂O drop cast on mica sheet (c) SEM image of **NCPH** in MeOH/ACN (d) and (e) higher magnified images in MeOH/ACN mixture.

As discussed, reports associated with morphological changes in **NCP** derivatives during aggregation, with respect to any stimuli are not in the literature. Here, the tautomeric exchange of **NCPH** was studied with different solvent combinations, which was accompanied with aggregation of the molecules. Morphological features during aggregation process were investigated through SEM and AFM analysis as shown in Figure 2.17. An 80 μM solution of **NCPH** in the required solvent mixture were taken for the analysis. Interestingly, in a 1:9 MeOH/H₂O (v/v) mixture of **NCPH** forms a cluster of

fibres with size less than one micrometer (Figure 2.17.a) as obtained from SEM imaging and the morphology was confirmed by AFM studies (Figure 2.17.b). Analysis of morphological features indicate that these extended fibre structures could be formed by the nonplanar 3H tautomer through inter molecular hydrogen bonding between OH groups as well as hydrophobic interaction. Whereas the same concentration of **NCPH** in a MeOH/ACN mixture, where **NCPH** in 2H form was self-assembled in shell morphology and the average size of the shell was found to be 200 nm ranges (Figure 2.17.c, d and e). This remarkable difference in the morphological features of the self-assembly of **NCPH** in MeOH/ACN mixture can be attributed to the planar nature of 2H tautomer, and thus favourable for π - π interaction between the units in addition to the other interactions possible as described. SEM analysis of **NCPH** in DMSO/ACN and DMSO/H₂O combinations was also exhibited similar trend as in the case of MeOH combinations (Figure 2.18). Overall, the investigations concluded that existence of the particular tautomeric form has major role in determining the morphology of **NCPH** in the aggregated state.

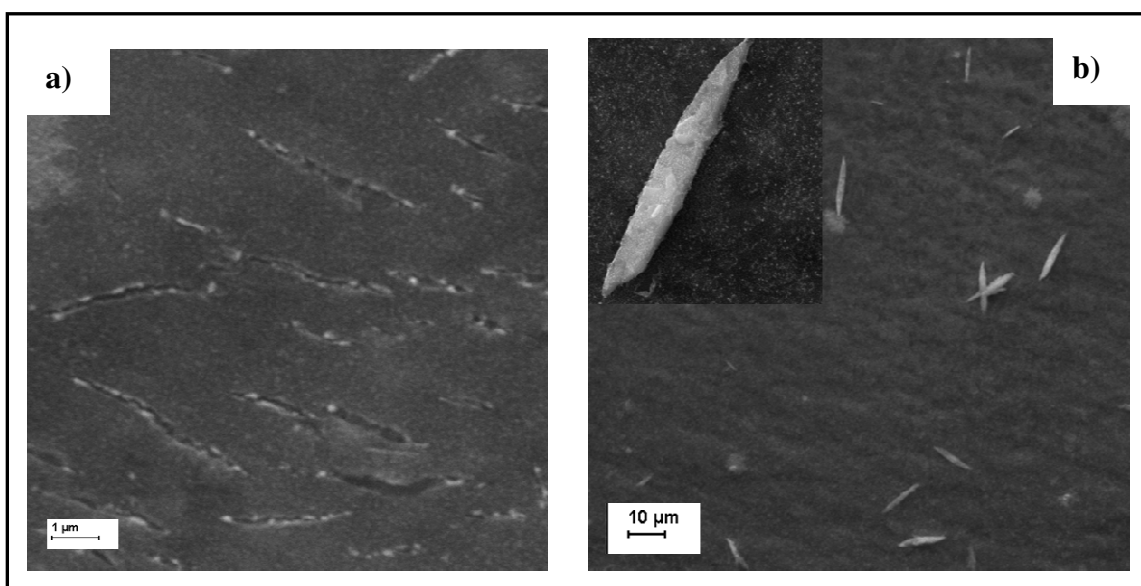


Figure 2.18. SEM images of **NCPH** in a mixture of (a) DMSO/ACN and (b) DMSO/H₂O.

2.4.5 Anion assisted aggregation of NCPH

It was an interesting observation that the tautomeric existence of the N-confused derivative has a key role in determining the morphology. On the other hand, reports with anion assisted self-assembled structure are attained much interest in recent years. The presence of eight hydroxyl group and outer NH offers suitable sites for hydrogen bonding interaction. Hence, this part of the chapter discuss about the role of anions on the aggregation behaviour of **NCPH**.

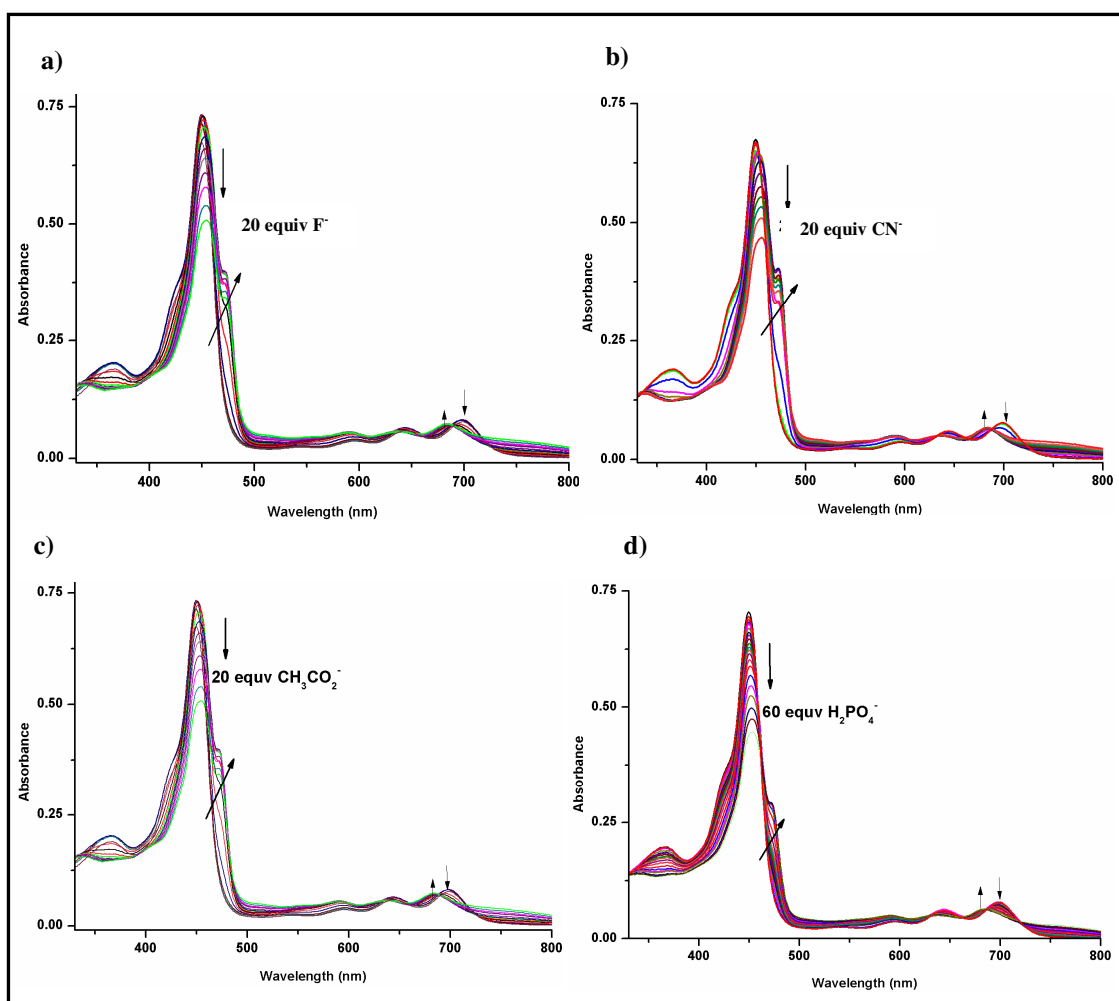


Figure 2.19. Changes observed in the absorption spectra of **NCPH** ($8\mu\text{M}$) in DMSO by the addition of (a) F^- ions, (b) CN^- ions, (c) $CH_3CO_2^-$ ions, and (d) $H_2PO_4^-$ ions.

The effect of various anions on the absorption spectrum of **NCPH** in DMSO was investigated. Anions such as F^- , CN^- , CH_3COO^- and $H_2PO_4^-$ have shown clear shift in the

absorption spectra of **NCPH** (Figure 2.19). However, other anions such as Cl^- , Br^- , SCN^- , NO_3^- , NO_2^- and BH_2^- didn't show much change. Up to 4 equiv. of F^- ions resulted in the gradual decrease in intensity of the Soret band of **NCPH** at 450 nm along with Q-bands at 644 and 697 nm. Further addition (up to 20 equiv.) of F^- ions accompanied with the appearance of red-shifted band at 472 nm. Interestingly, the Q-bands were blue-shifted to 638 and 683 nm. The red-shifted Soret band corresponds to the J-aggregates which were formed by the complexation of **NCPH** and anions using hydrogen bonds between anion and NH/OH groups of **NCPH**. Similar spectral changes were observed for other anions such as CN^- , CH_3CO_2^- , and H_2PO_4^- ions. However, further investigations on aggregation were restricted to F^- ions because of its strong acidic nature.

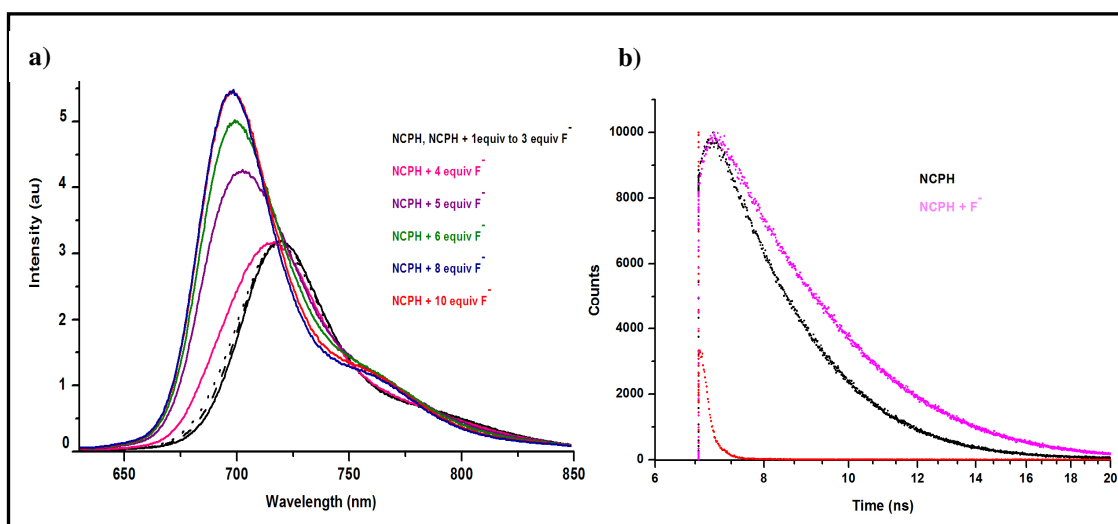


Figure 2.20. (a) The emission spectral changes of **NCPH** ($8\mu\text{M}$) in DMSO by the addition of F^- ions. (b) The decay profile of **NCPH** and **NCPH-F⁻** ions aggregate in DMSO.

Interestingly, the emission maximum of **NCPH** at 720 nm experienced a prominent blue-shift of about 30 nm by the addition of F^- ions to result in a new peak at 690 nm with significant increase in the fluorescence quantum yield (0.032) as shown in Figure 2.20. Increase in the quantum yield can be attributed to the enhanced rigidity, which can

be expected during aggregation by intermolecular hydrogen bonding. The blue-shifted emission spectrum provides the information about the possible stabilization of the higher excited state or ground state in the **NCPH-F⁻** aggregates compared to the monomeric **NCPH**. The results were further confirmed by lifetime measurements. The fluorescence lifetime of **NCPH** in DMSO was found to be 2.07 ns, where upon addition of 10 equiv. of F⁻ increased the life time to 2.95 ns. The decay profile of **NCPH** and its aggregated form in DMSO solution were found to be single exponential.

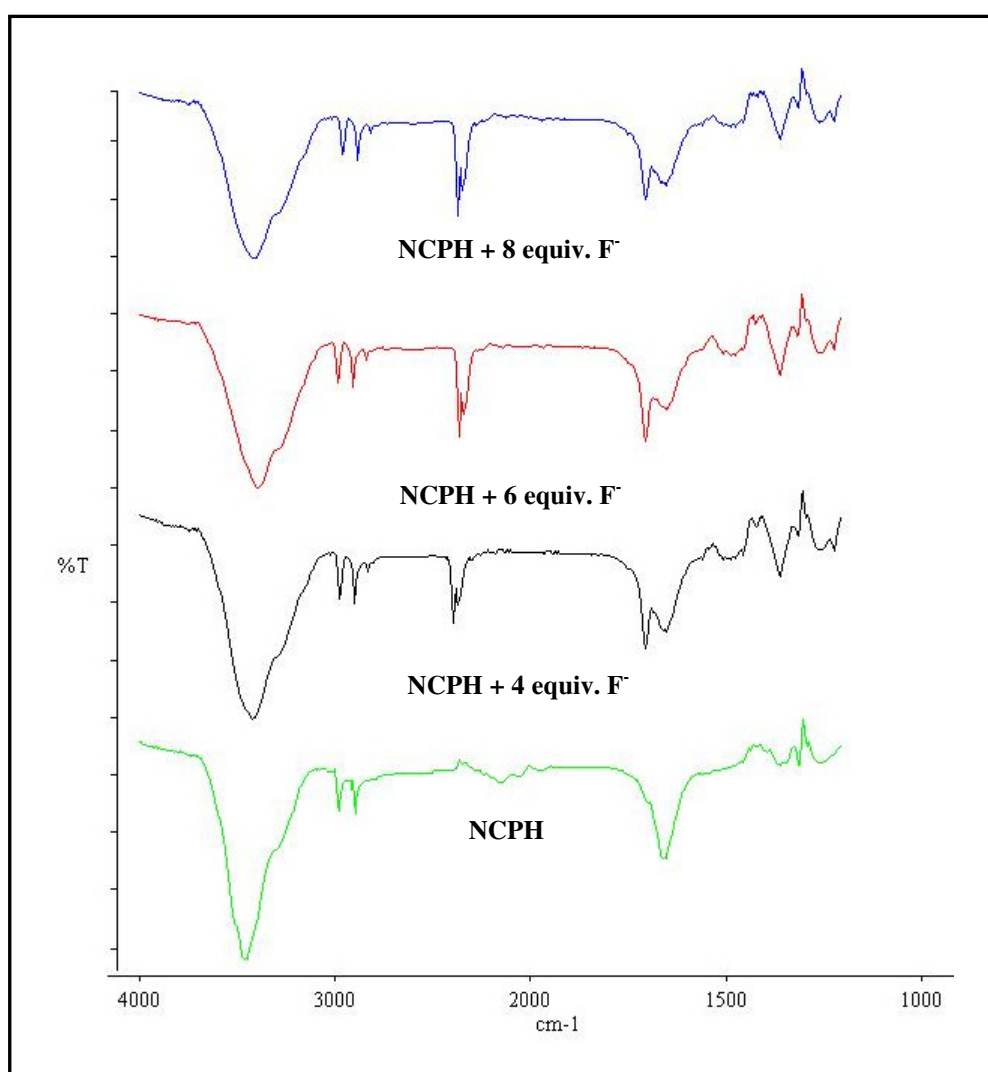


Figure 2.21. IR spectral change of **NCPH** with gradual addition of F⁻ ion.

The interaction of F^- ion with **NCPH** was monitored by using FT-IR spectroscopy (Figure 2.21) in solution state. The OH stretching frequency observed at 3449 cm^{-1} in DMSO was shifted to 3413 cm^{-1} by the addition of 4 equiv. of F^- , indicating the decrease in the OH bond strength, which can be attributed to the formation hydrogen bonding with the anion. Further addition of F^- ion leads to increase in the OH stretching frequency to 3406 and 3387 cm^{-1} as the hydrogen bonding interaction between the OH group and F^- anion get stronger.

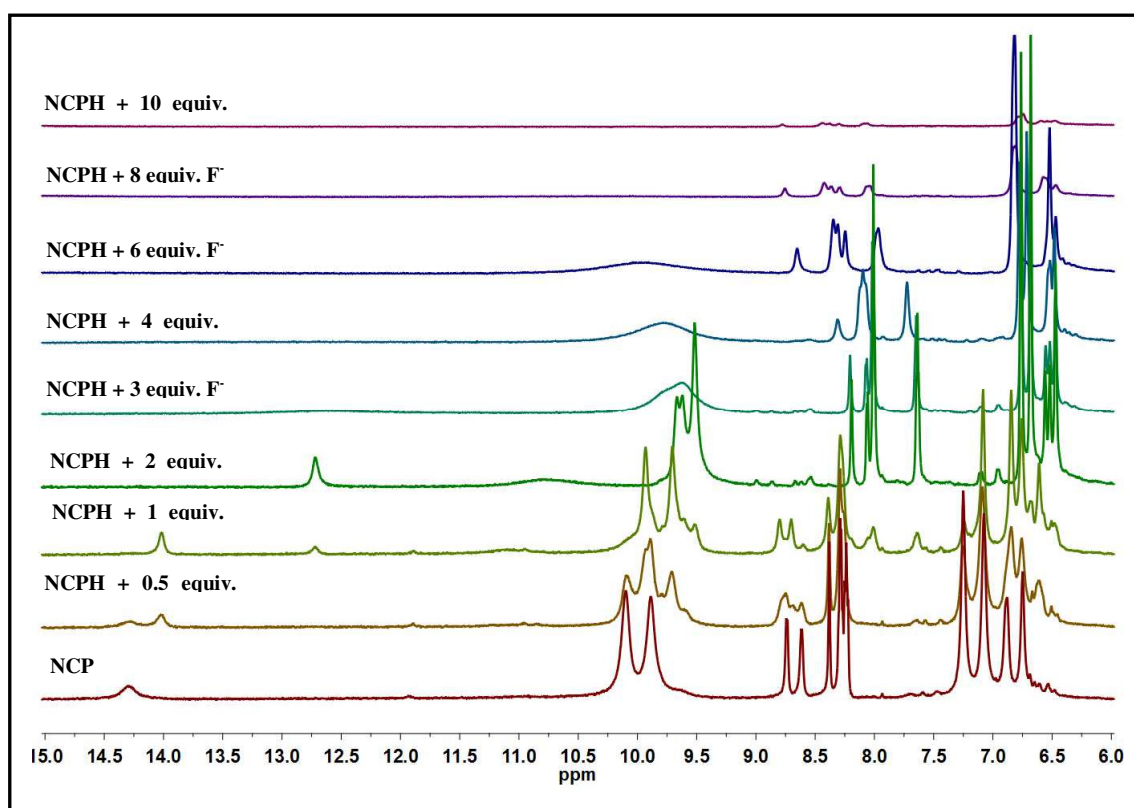


Figure 2.22. ^1H NMR spectral change of **NCPH** with increased F^- ion concentration.

^1H NMR titration analysis of **NCPH** has been performed with tetrabutyl ammonium salt of fluoride in varying concentration to get an insight into the structural change occurred in the presence of anion as well as to get information regarding the binding sites (Figure 2.22). Addition of 0.5 equiv. of F^- to a 15 mM solution of **NCPH** in $\text{DMSO-}d_6$ resulted in significant change in the ^1H NMR pattern. The outer NH proton ($\delta = 14.3$ ppm) of **NCPH** split into two with an unanticipated upfield shift, due to increased

electron density near NH proton. Further addition of F^- resulted in more shielding of NH, OH protons (two broad peaks centered at $\delta = 10$ ppm) and to the other phenylic and pyrrolic protons, attributed to the dramatic structural change experienced by the molecule during the process. But, the change in the splitting pattern of NH and OH protons give indication about the binding sites. At 3 equiv. of F^- both NH and OH peaks merge each other to give a broad peak, which disappears completely at 8 equiv. of F^- ion. As there were many binding sites the whole binding process were complex to determine the stoichiometry by using NMR analysis.

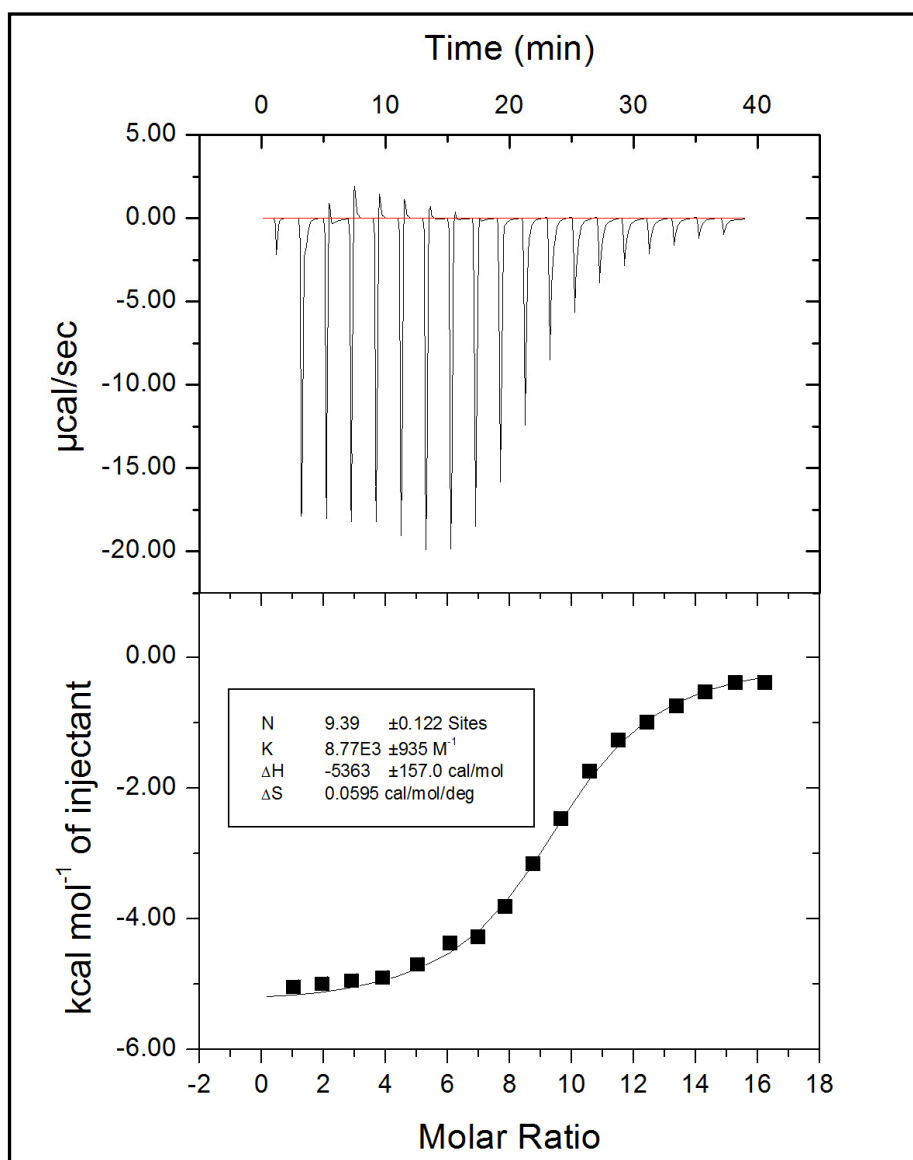


Figure 2.23. ITC analysis for the complexation of **NCPH** and F^- ions in DMSO.

The stoichiometry for the interaction of F^- with **NCPH** during aggregation was quantitatively investigated by isothermal titration calorimetry (ITC) in DMSO (Figure 2.23). The addition of F^- to a 0.4 mM solution of **NCPH** produced a heat response indicative of an exothermic process. The heat change measured during the binding process were -5363 ± 57 cal/mol, where the equilibrium association constants (K) was calculated to be $8.77 \times 10^3 M^{-1}$. The binding ratio obtained was 1:9 which was matching with number of possible binding sites available in **NCPH**, including outer NH and phenylic OH.

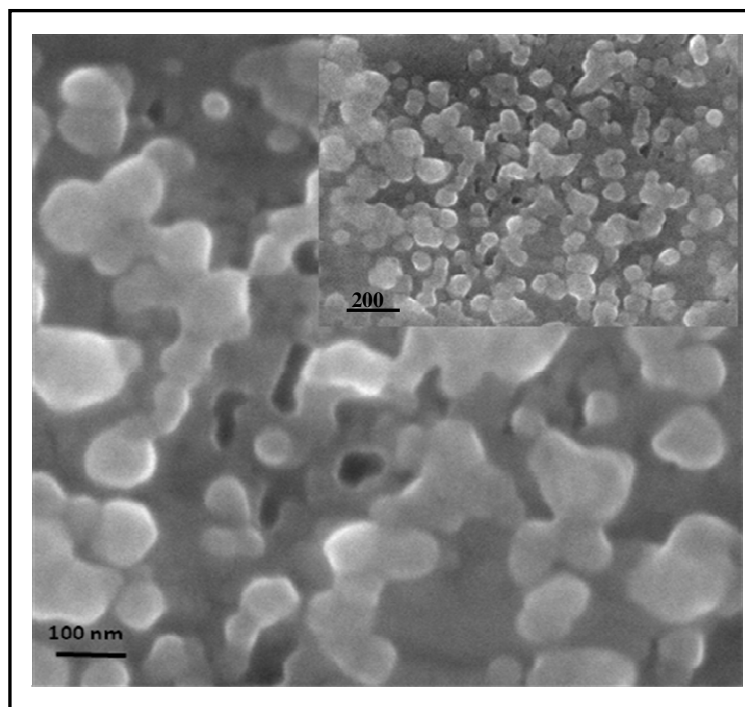


Figure 2.24. SEM images of **NCPH** in DMSO after the addition of F^- ions.

Morphological changes during anion assisted aggregation were investigated by SEM analysis (Figure 2.24). 30 μM solution of **NCPH** in DMSO with 10 equiv. of F^- was used for SEM analysis. Formation of nano sized (~ 100 nm) spheres was observed during the analysis. The formation of spheres was consistent with aggregated structures formed for the 2H tautomeric structure during the solvent assisted aggregation as described in the previous section. The presence of nine hydrogen bonding making sites and the possible

π - π stacking interaction for the 2H tautomer of **NCPH** promotes the formation of nanospheres. The size of nanospheres formed was further confirmed by DLS measurement (Figure 2.25), where data show an average size of 130 nm.

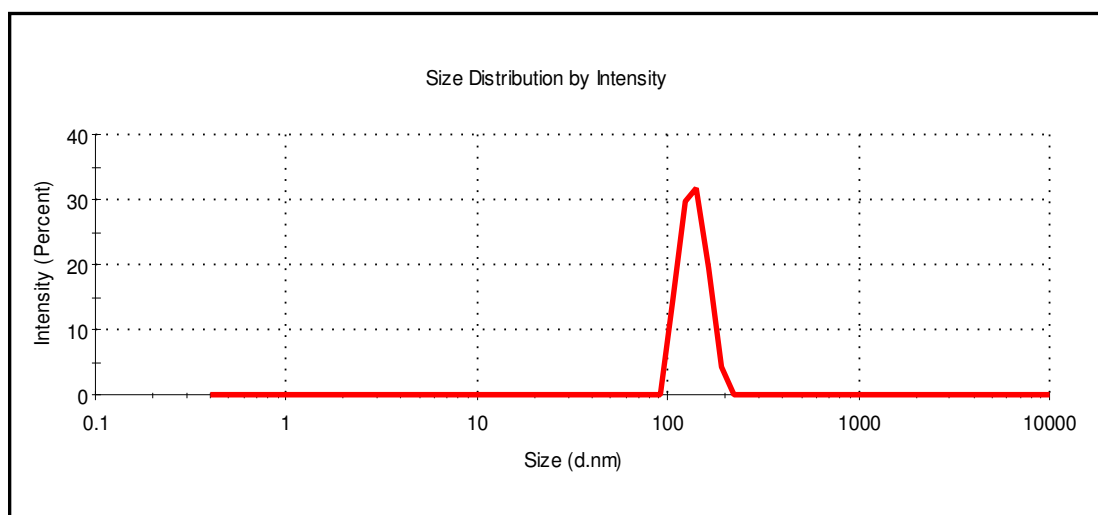


Figure 2.25. DLS analysis of **NCPH** in DMSO with F⁻ ion.

2.5 Conclusions

In conclusion, we have demonstrated the synthesis, spectral and structural characterization of a hitherto unknown octahydroxy derivative of N-confused porphyrin (**NCPH**). Also, apart from the previous reports, the switch over of the tautomeric forms from 3H to 2H and vice versa was controlled exclusively with respect to protic and aprotic solvents rather than polarity controlled transformation, which was probed through various spectroscopic techniques. Further, the role of tautomeric structures on generating self-assemblies of different size and shape, such as nanoshells and fibres, through solvent-assisted aggregation was described, which is unprecedented in N-confused porphyrin chemistry. Also, investigations revealed the anion-assisted aggregation of **NCPH** where F⁻ ion can complex with 2H tautomer of **NCPH** to generate nanospheres.

2.6 Experimental Section

2.6.1 Materials and methods

The reagents for the synthesis as well as photophysical studies were obtained from Sigma-Aldrich and Merck, India and used as such. All solvents were distilled and dried before use. Deionized water was from Millipore. ^1H and ^{13}C NMR spectra were recorded on a Bruker Biospin 400 MHz spectrometer. NMR experiments were done in $\text{DMSO-}d_6$. Spectra were referenced internally by using the residual solvent (^1H , $\delta = 2.5$ and ^{13}C , $\delta = 39.4$ for $\text{DMSO-}d_6$) resonances relative to $\text{Si}(\text{CH}_3)_4$ and the solvent peak were removed for clarity in the main text. Matrix assisted laser desorption ionization-time of flight (MALDI-TOF) mass spectra was recorded in Shimadzu Biotech Axima mass spectrometer. Infrared spectrum of the compound was recorded on a Perkin Elmer FT-IR spectrometer, spectrum RXI. Electronic absorption spectra and steady state fluorescence spectra were recorded on Perkin Elmer Lambda-750 UV-Vis absorption spectrometer and Perkin Elmer LS55 Fluorescence spectrometer respectively. Time-resolved fluorescence measurements were carried out by using a time-correlated single photon counting (TCSPC) spectrometer (Edinburgh, OB920). A diode laser ($\lambda_{\text{exc.}} = 445$ nm, FWHM = 98 ps) was used to excite the compound and MCP photomultiplier (Hamamatsu R3809U-50) was used as the detector (response time 40 ps). The lamp profile was recorded by using a scatterer (dilute ludox solution in water) in place of the sample. Decay curves were analyzed by a nonlinear least-squares iteration procedure using F900 decay analysis software. The quality of the fit was judged by the χ^2 values and weighted deviation was obtained by fitting. ITC data were obtained from microcal iTC 200. The raw data obtained were fitted and analysed using origin 7.0 software provided along with the instrument. SEM imaging was performed on a Zeiss EVO 18 Cryo Special Edn. with variable pressure detector working at 20-30 kV. Atomic Force

Microscopy images were recorded under ambient conditions using a NTEGRA (NT-MDT) operating with a use tapping mode regime. Micro-fabricated TiN cantilever tips (NSG10) with a resonance frequency of 299 kHz and a spring constant of 20-80 Nm^{-1} were used. AFM section analysis was done offline. Samples for the imaging were prepared by drop casting the solution on freshly cleaved mica surface at the required concentrations at ambient conditions. DLS analyses were carried out with a Zetasizer Nano S from Malvern Instruments at 25 °C. The average hydrodynamic radii were calculated from Stork-Einstein equation ($R_h = k_B T / (6\pi\eta D)$), where k_B = Boltzmann's constant, T = Absolute temperature, η = Viscosity, D = Diffusion constant.

2.6.2 Synthesis of NCPH

Synthesis of **NCPH** was achieved through a two step synthetic strategy. In the first step, *meso*-tetrakis(3,5-dimethoxyphenyl) N-Confused Porphyrin(**NCP-OCH₃**) was prepared by Lindsey's method [64] by using MSA (methane sulfonic acid) as catalyst. In the second step, dry DCM (15 mL) was taken in a 100 mL two neck RB flask at -78 °C under argon atmosphere and 0.5 mL boron tribromide (**BBr₃**) was added to this. Solution of **NCP-OCH₃** (100 mg) in 15 mL dichloromethane was added slowly to the **BBr₃** solution and allowed to stir for 2h at -78 °C and then gradually brought to RT. The mixture was refluxed at 65 °C for 8h and then room temperature for 12h. To the solution water was added and heated at 85 °C for 6h. The water layer was decanted and the compound recrystallised from dichloromethane and 2-propanol mixture. ¹H NMR (400MHz, DMSO-*d*₆): δ 14.30 (s, 1H, exch. D₂O, pyrrolic outer NH), 10.11 (s, 4H, exch. D₂O, phenolic OH), 9.9 (s, 4H, exch. D₂O, phenolic OH), 8.74-8.75 (d, $J=4$ Hz, 1H, pyrrolic β H), 8.62-8.63 (d, $J=4$ Hz, 1H, pyrrolic β H), 8.39 (s, 1H, pyrrolic α H), 8.29-8.39 (m, 2H, pyrrolic β H), 8.23-8.28 (m, 2H, pyrrolic β H), 7.27 (s, 4H, phenyl), 7.09 (s, 4H, phenyl), 6.90-6.91 (d, $J=4$ Hz, 2H, phenyl), 6.77 (s, 2H, Phenyl), 2.14 (s, 1H, exch.

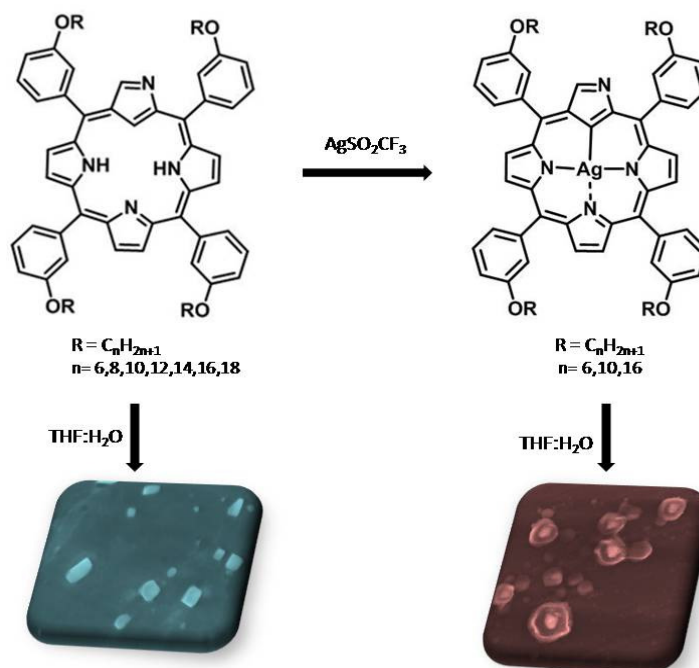
D₂O, pyrrolic inner NH), -1.82 (s, 1H, pyrrolic inner β H) ¹³C NMR (100 MHz, DMSO-*d*₆): δ 167.29, 158.45, 157.83, 138.84, 138.57, 137.62, 128.82, 124.86, 124.47, 124.00, 115.34. IR (KBr): 3422(br), 2929, 2856, 1606, 1479, 1368, 1308, 1167 cm⁻¹. FAB-MS: *m/z* 743.83 (C₄₄H₃₀N₄O₈ + H, M + 1). Anal. Calcd for C₄₄H₃₀N₄O₈: C, 71.15; H, 4.07; N, 7.54. Found: C, 71.01, H, 4.02, N, 7.31.

CHAPTER 3

***meso*-Tetrakis(3-alkoxyphenyl)N-Confused Porphyrins and Their Ag(III) Complexes; Synthesis, Characterization and Aggregation Behaviour**

3.1	Abstract	110
3.2	Introduction	111
	3.2.1 Alkyl chain substituted porphyrins	111
3.3	Objective of our work	117
3.4	Results and discussions	117
	3.4.1 Synthesis and structural characterization of NCP-n and NCP-n-Ag	117
	3.4.2 Aggregation behaviour of NCP-n	123
	3.4.3 Aggregation behaviour of NCP-n-Ag	126
3.5	Conclusions	128
3.6	Experimental section	130
	3.6.1 General information	130
	3.6.2 Synthesis	130

3.1 Abstract



This chapter describes the synthesis, spectral, structural characterization and aggregation behaviour of long chain substituted NCP derivatives, meso-tetrakis(3-alkoxyphenyl)N-confused porphyrins and its Ag(III) complexes. The number of carbon atoms in the alkyl side chain varies from 6 to 18 in the free base NCP. The Ag(III) complexes of NCP derivatives were synthesized for the 6, 8 and 10 derivatives. Both the NCP and Ag(III) complexes were confirmed by different spectral analyses. Further, the influence of metallation on the morphological features during aggregation were discussed, where aggregation in each case was achieved by increasing the volume of H₂O in a THF solution of compounds. Both in the case of free base and metallated forms, as the H₂O volume increases from 50% to 90%, due to extended hydrophobic interaction the morphology of aggregated structures deforms continuously to attain cubic (free base state) and flower like structures (metallated form) at 10:90 (v/v, THF/H₂O) ratio of solvents respectively. The different morphological features exhibited by the free base and metallated NCP are explained on the basis of structural difference between these two forms.

3.2 Introduction

Porphyrin molecules are known to form aggregates under certain conditions and this phenomenon has been studied by a number of research groups in the last two decades. In general, two types of aggregates are found to be very important: face-to-face (H-type) and side-by-side (J-type) aggregates [158]. Usually, a ‘bottom-up’ strategy was adopted widely to generate such self-assembled structures and have attracted considerable attention in the area of storage and conversion of solar energy, sensors and catalysis [159-161]. The precise control of aggregate morphologies in long-range order are of prime interest, because nanostructures display unusual optical and optoelectronic properties, which is quite different with respect to single molecules and the bulk material. Thus, the morphology of the functional material plays an essential role in determining the functionality of the final devices. These self-assembled nanoarchitectures of organic molecules are formed through non-covalent interactions such as van der Waals interaction, electrostatic interactions, π - π stacking, coordination bonds and hydrogen bonding between monomeric molecules.

3. 2. 1 Alkyl chain substituted porphyrins

Various structural modifications have been done on the basic porphyrin structure which includes suitable substitution at *meso*, β -positions or even at its core, in order to tune the photophysical properties of the porphyrin molecule. One such modification is alkyl chain substitution at β -positions and *meso*-positions. However, the synthesis of porphyrins with alkyl chains at β -positions is difficult due to high steric hindrance induced by the alkyl substituents, where it is comparatively easy to insert the alkyl chains on the *meso*-aryl rings. Usually, alkyl substitution at the porphyrin framework increases the solubility of the porphyrin in organic solvents. However, for the molecules with long alkyl side chains (possessing strong hydrophobic interaction), the aggregation often proceeds too fast due

to the enhanced intermolecular association and may lead to chunky aggregates rather than defined nanostructures. Hence, appropriate substitution of alkyl group is important for the directional nature and thereby to form structured nanoaggregates. Introduction of different functional groups onto the peripheral positions of conjugated molecules normally induces additional intermolecular interactions in combination with π - π interaction lead to self-assembly of functional molecular materials into novel nanostructures with different morphology.

Porphyrins substituted with alkyl chains are known to generate various nanostructures and found applications in areas such as liquid crystalline materials. Depending upon the chemical structure of the porphyrin, different types of aggregation mechanisms can be observed from laterally to axially stacked aggregates. A great amount of work has been done to identify the role of π - π interactions in the cofacial or lateral molecular arrangements, whereas lateral aggregation can be favoured if side chains are involved in hydrogen bonds and is characterized by a strong apparent exciton splitting and shift of the Soret band. Thus, substitution of the peripheral part of porphyrins with alkyl chains will provide an additional effect in ordering the aggregates as discussed above. In one of the earliest example, Terech and co-workers showed aggregate formation of Zn(II) complex of a long-chain triester of *meso*-tetrakis[*p*-carboxyphenyl] porphyrin (**ZnP3**) in saturated hydrocarbons [162]. The aggregation behaviours of **ZnP3** revealed the formation of nano rods during aggregation. The Zn element as well as the carboxylic group are determinant to establish the intermolecular connections (intra and/or inter) responsible for the formation of gelatinous specimens. In addition to the π - π extended interactions between the porphyrinic cores, the presence of both Zn and a carboxylic ligand leads to formation of nanorods with specific molecular arrangement

with tetrameric associations (Figure 3.1), where **ZnP3** molecules are involved in a J-aggregate with four molecules per section of rod.

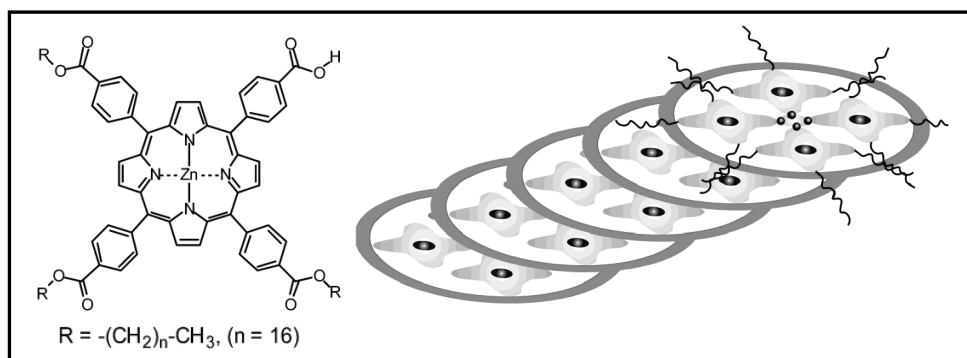


Figure 3.1. Schematic representation of the **ZnP3** rod [162].

Recently, Seddon and co-workers reported a homologous series of three β -octaalkyl porphyrin derivatives with alkyl chain lengths of C_8 , C_{10} and C_{12} , where the number of mesophases is related to the alkyl chain length and found that zinc complexes for each alkyl chain length exhibit liquid-crystalline behaviour [163]. At low temperatures, all three metal coordinated compounds formed a solid phase with a square packing of columns. As the temperature increases the square packed solid phases undergo phase transitions to liquid-crystalline columnar phases. X-ray data exhibited two discontinuous jumps with increasing temperature prior to melting to the isotropic phase for C_8 , implying the existence of three columnar phases. For the longer chain length compounds, the number of mesophases formed was reduced to two for C_{10} and one for C_{12} .

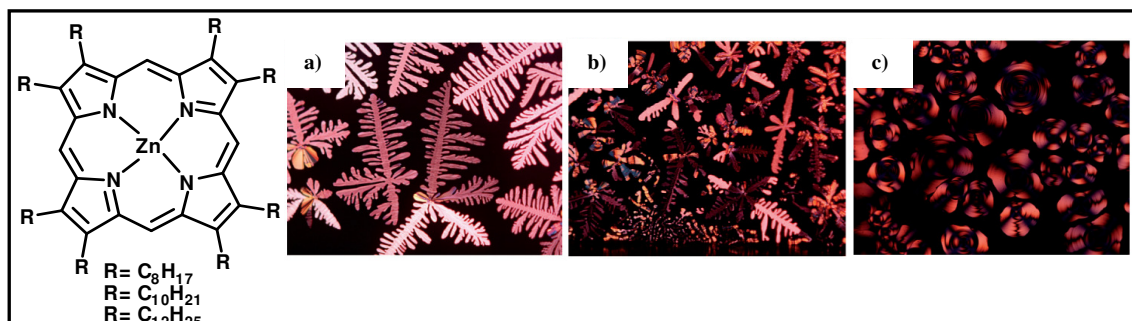


Figure 3.2. Optical textures for the Zn porphyrins with differing chain lengths after cooling slowly from the isotropic phase. (a) dendritic texture of the C_8 , (b) flower-like texture of the C_{10} , and (c) spherulitic texture of the C_{12} [163].

M. J. Crossley reported that the length of alkyl chains and deposition surface can influence the optical properties and self-assembly of porphyrins. 5-Nitro-10,15,20-trialkylporphyrins [(C₅H₁₁)₃-NO₂P, (C₇H₁₅)₃-NO₂P, (C₁₁H₂₃)₃-NO₂P and (C₁₉H₃₉)₃-NO₂P] when deposited on silica surface, form micro rods except (C₁₉H₃₉)₃-NO₂P, which forms only powder, where the corresponding tetraalkyl porphyrin generates micro sheets (Figure 3.3) [164].

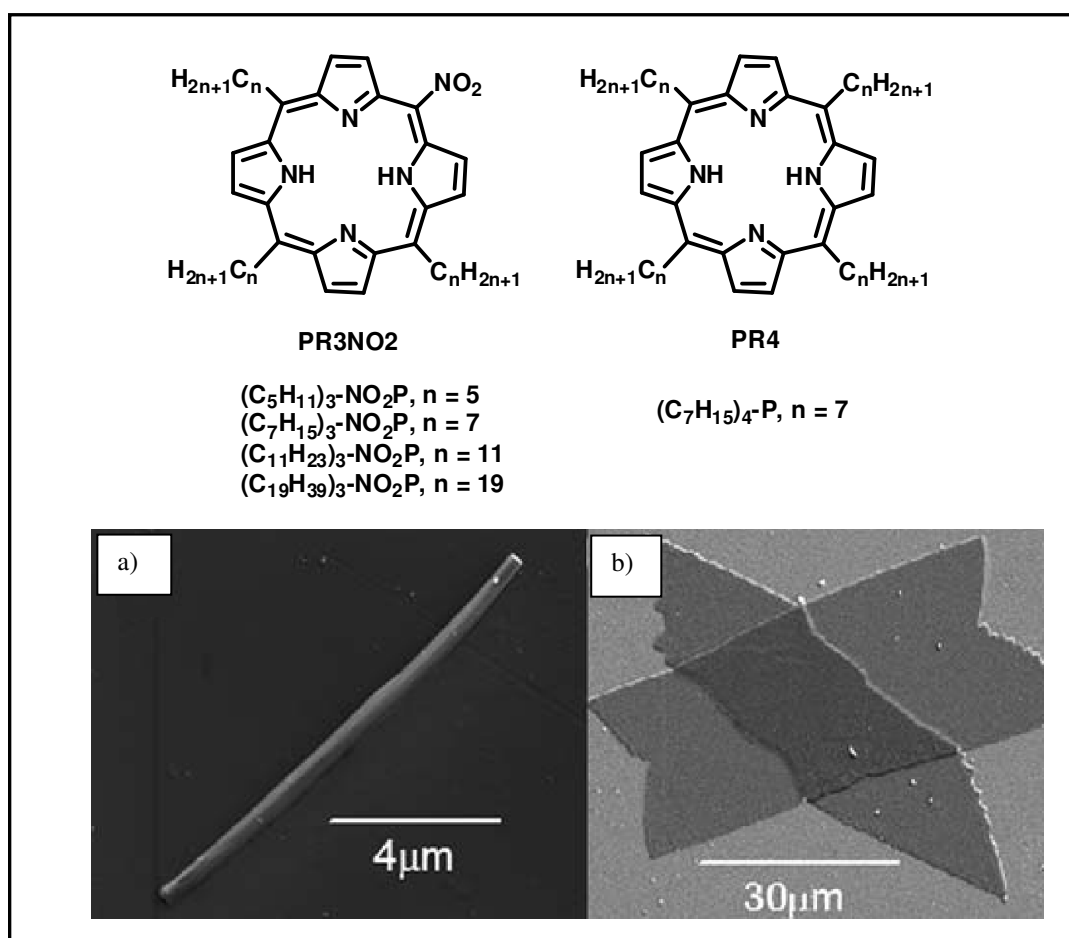


Figure 3.3. SEM images of (a) a single (C₇H₁₅)₃-NO₂P microrod and (b) sheet of (C₇H₁₅)₄-P [164].

When a droplet of DMF/DCM (1:1) solution of (C₇H₁₅)₃-NO₂P was deposited on a quartz, molecules self-assembled into microrods through the two dimensional alignment of the heptyl chains, and staggering of aromatic regions, which in turn influenced by

dipole-alignment by the NO₂ group. Visual iridescence of the (C₇H₁₅)₃-NO₂P solid after recrystallization was different from the bulk solid form.

In another example, Yang and co-workers synthesized a series of alkyl chains substituted platinum–acetylide bridged Zn-porphyrin derivatives (**Pt-AceZnPor**), and studied their aggregation behaviour in different solvent systems [165]. The hydrophobic interaction of alkyl chains enabled the orientation and well-ordered aggregation of the molecules via spontaneous self-assembly. The UV-Vis and emission spectral changes are consistent with the formation of J-type assemblies promoted by the intermolecular π – π interaction in cooperation with the hydrophobic interactions.

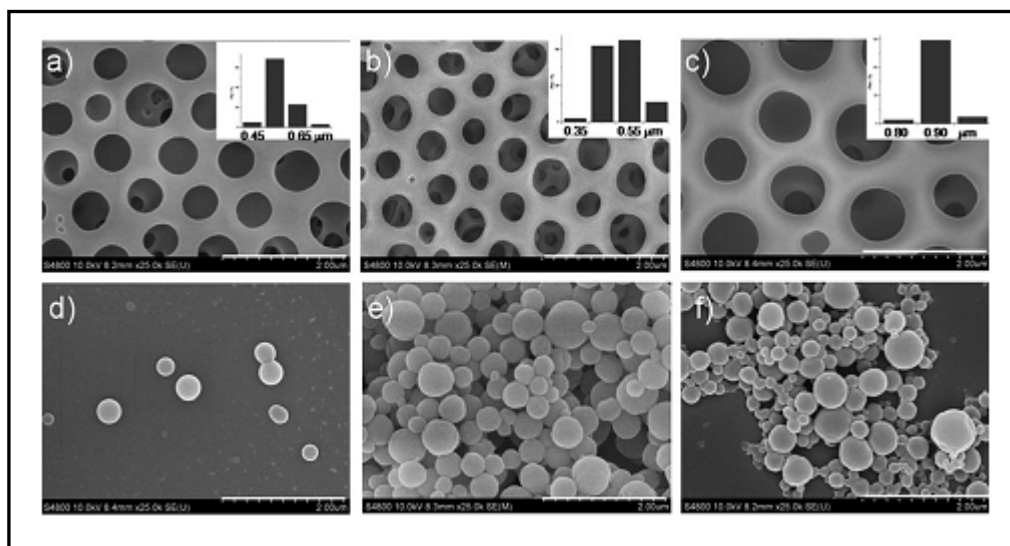


Figure 3.4. SEM images of **Pt-AceZnPor** prepared in DCM–hexane (a-c) and DCM–MeOH (d-f), respectively. Scale bars: 2.0 μm [165].

SEM images of **Pt-AceZnPor** with varying alkyl chain length exhibited highly ordered honeycomb patterns in the mixed solvent of DCM/hexane (v/v, 1:1), whereas the nanospheres were formed in the highly polar solvents such as DCM/MeOH(v/v, 1:1) (Figure 3.4). This is an example where nature of the interaction (changes with the solvent combinations) plays an important role in the formation of supramolecular aggregation. In hexane, due to the enhanced hydrophobic interaction, molecules have a strong

tendency to form an ordered array of honeycomb-patterned microporous films upon solvent evaporation. But, in MeOH, the hydrophilic interaction depolymerized the supermolecular polymer into an oligomer and further crimped the oligomer to form nanospheres on the substrate.

Jiang *et al.* reported the first example, where morphology of a long chain substituted porphyrin is changing with metallation at the centre in different solvents [166]. Comparative study on the morphological changes between the free base and metallated form revealed that intermolecular metal ligand coordination bonding in the metallated form and the π - π interaction between tetrapyrrole rings in the free base tetrapyrrole molecules leads to different molecular packing conformation and in turn different self-assembled nanostructure morphology. For example, in a hexane solution the free base aggregated to form nanoribbons, where the Zn metallated porphyrin was self-assembled in hollow spherical structures as shown in Figure 3. 5. However, in MeOH solution free base aggregated as nanospheres while the metallated derivative as nanorods [166].

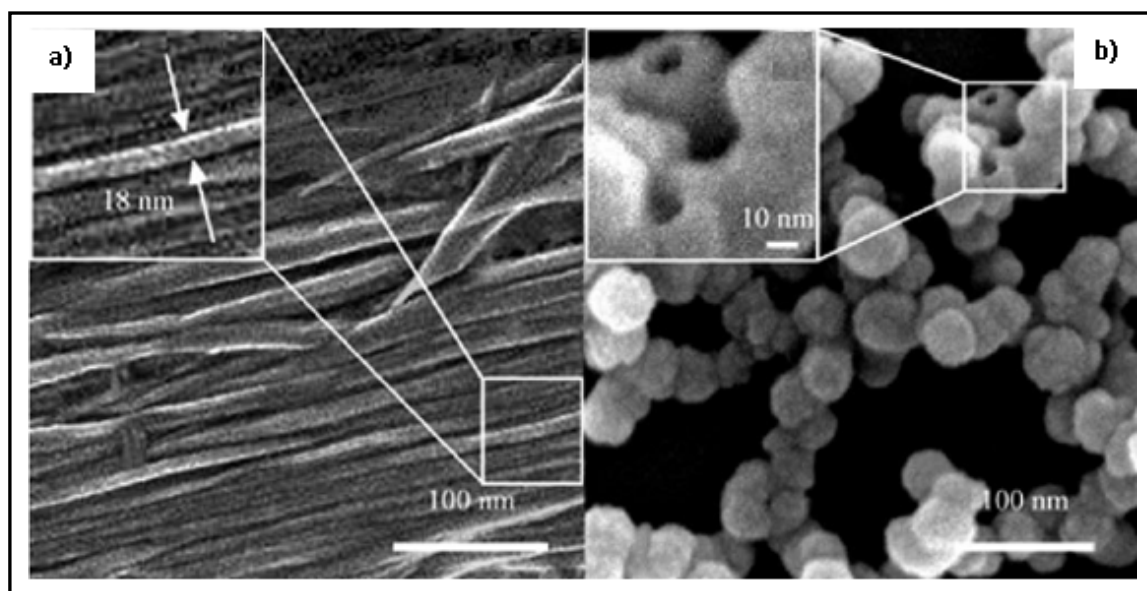


Figure 3.5. SEM images of (a) Free base porphyrin and (b) Zn metallated form in hexane.

3.3 Objective of the work

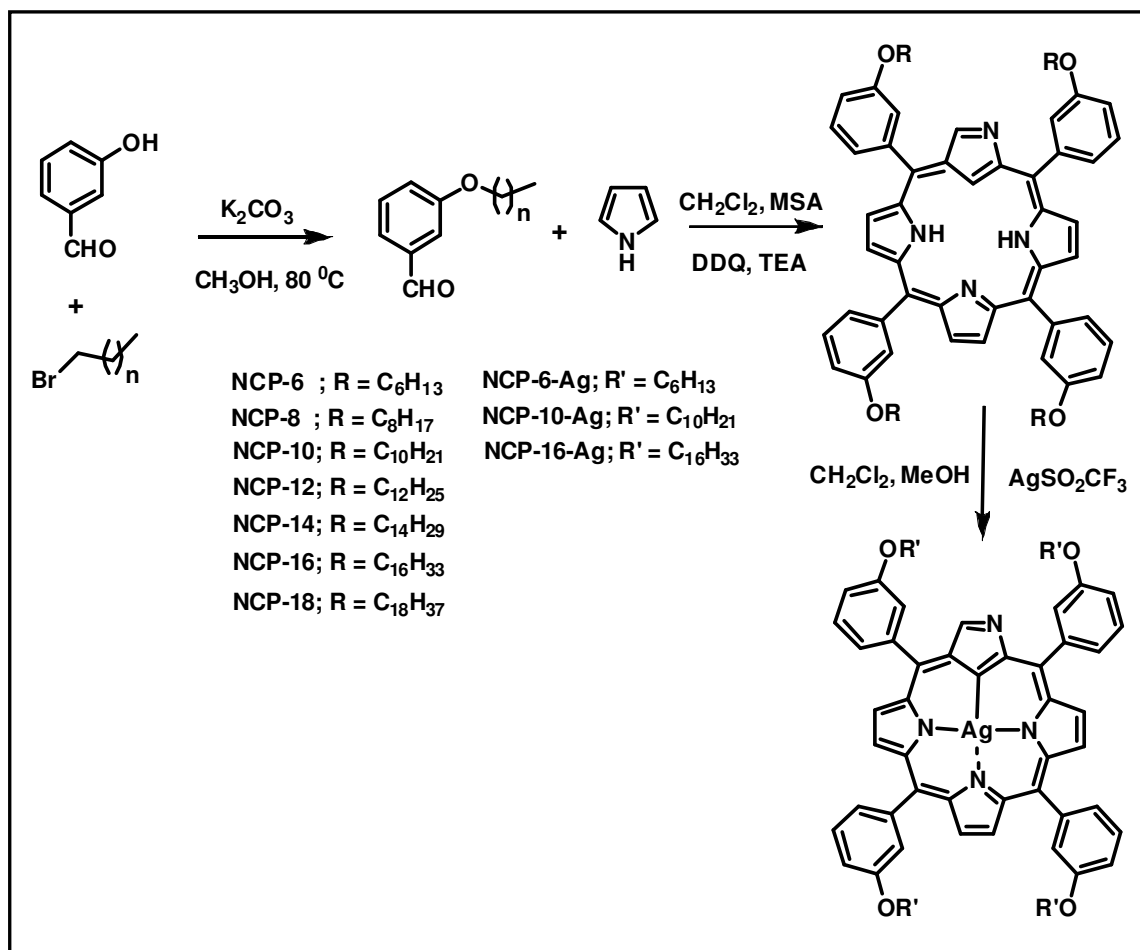
The literature survey revealed that the alkyl chain substituted planar porphyrin derivative can stack together by π - π interactions, where the presence of properly substituted long alkyl chains gives extra directionality to the assembled structures during aggregation. Also, morphology of these aggregated structures can be controlled, or are sensitive towards the aggregation conditions such as solvents, temperature etc. and metallation at the porphyrin centre. However, there was no report on morphological features during aggregation for the long alkyl substituted free base **NCP** derivatives and its metallated complex. Hence, this chapter discusses the synthesis of *meso*-tetrakis(3-alkoxyphenyl)*N*-confused porphyrins (**NCP-n**) and its Ag(III) metal complexes (**NCP-n-Ag**). Further, the effect of alkyl chain length and metallation on aggregation was also investigated.

3.4 Results and discussion

3.4.1 Synthesis and structural characterization of **NCP-n** and **NCP-n-Ag**

A series of *meso*-tetrakis(3-alkoxyphenyl)*N*-confused porphyrins (**NCP-n**), where the number of carbon atoms in the alkyl side chain vary from 6 to 18 were synthesized by a two step synthetic strategy. In the first step, the corresponding 3-alkoxyl benzaldehyde was prepared from 3-hydroxybenzaldehyde and required alkyl bromide using potassium carbonate (K_2CO_3). The yield of the O-alkylated product ranges from 70-90% for different alkyl chain length. In the second step, the acid-catalyzed condensation reaction between pyrrole and respective aryl aldehyde by using MSA followed by oxidation with DDQ affords **NCP-n** in 10-20% yield. Metallated derivatives are synthesized for **NCP-6**, **NCP-10** and **NCP-16** derivatives, where a silver(I)triflate salt is used for the reaction to form the corresponding Ag(III) complexes in 60-65% yield (Scheme 3.1). The free bases as well as metallated complexes were characterized by different spectroscopic techniques

such as ^1H NMR, ESI-Q-TOF-MS and UV-Vis spectroscopy. A representative ^1H NMR spectrum of **NCP-6** and **NCP-6-Ag** is shown in Figure 3.6.a and Figure 3.6.b respectively.



Scheme 3.1. Synthetic scheme for **NCP-n** and **NCP-n-Ag**.

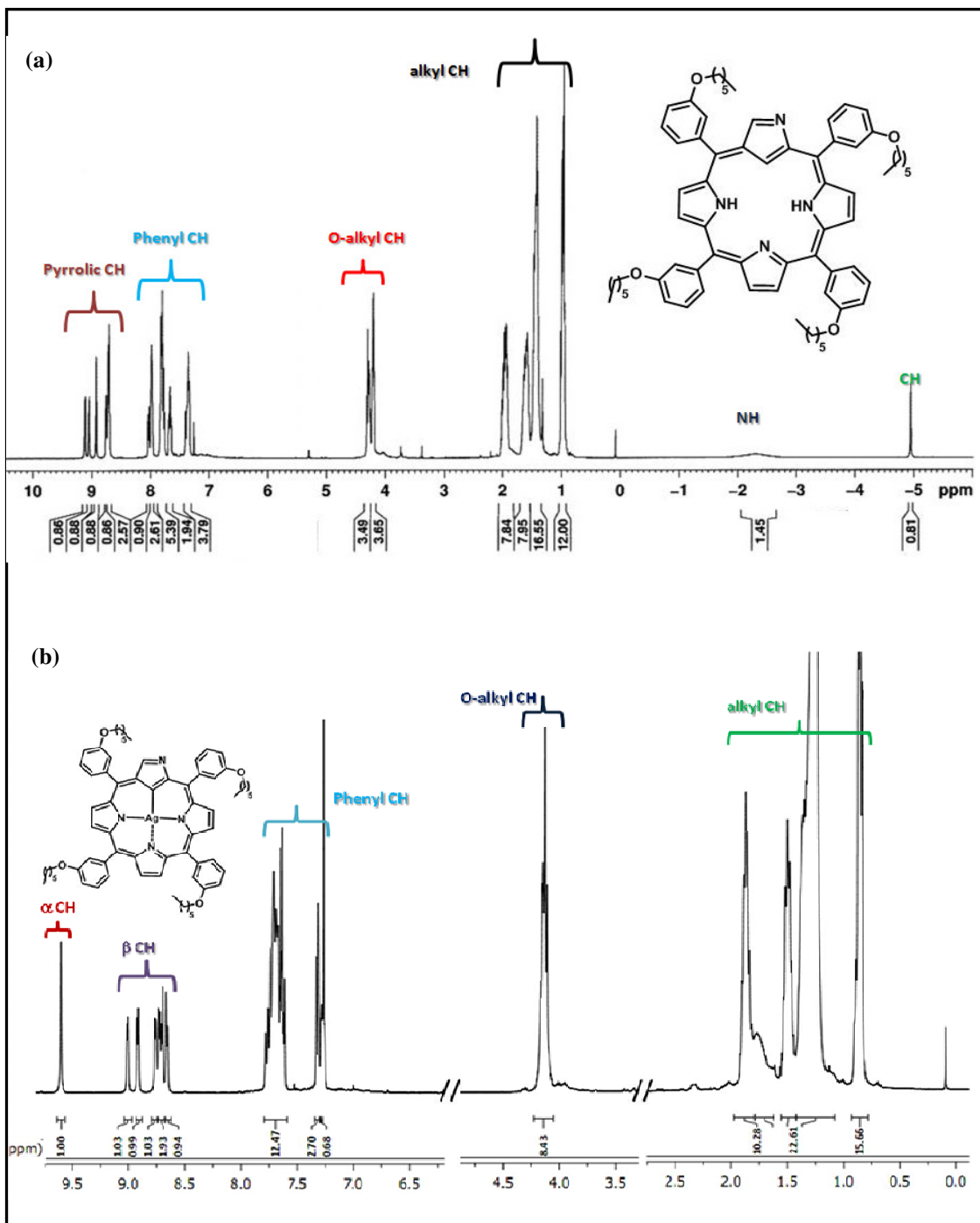


Figure 3.6. ¹H NMR spectrum of (a) **NCP-6** and (b) **NCP-6-Ag** in CDCl₃.

The ¹H NMR spectra of **NCP-6** (Figure 3.6.a) and **NCP-6-Ag** (Figure 3.6.b) were recorded in CDCl₃. For **NCP-6**, the signal resonated at $\delta = -4.95$ ppm corresponded to the inner CH protons, which is in the plane of ring current, whereas the two inside NH protons resonated at $\delta = -2.31$ ppm. The other pyrrolic and phenylic protons resonated in

the aromatic region (7.3-9.1 ppm) as shown in Figure 3.6.a. The eight protons resonating between 4.20-4.32 ppm was assigned for the immediate CH₂ protons to the oxygen atom in the alkyl chain. The end CH₃ proton gave triplet signal ranging from 0.95-1.02 ppm, where the other CH₂ protons were resonating between 1.42 to 2.03 ppm. The formation of Ag(III) complexes were verified by the disappearance of both inner CH and NH protons in the ¹H NMR spectrum (Figure 3.6.b) indicating their participation in the Ag(III) complex formation. Also, the sharp singlet resonated at 9.5 ppm in the spectrum was assigned for the outer α-CH protons, indicates that the outer nitrogen is not protonated and confirms the existence of Ag(III) complex instead of Ag(II). For Ag(II) complex, we expect the outer NH proton in the spectrum and split the α-CH signal into doublet, which is not happening here. The ¹H NMR pattern of **NCP-6-Ag** was similar to the **Ag(III) NCTPP** spectrum reported by Furuta *et al* [167].

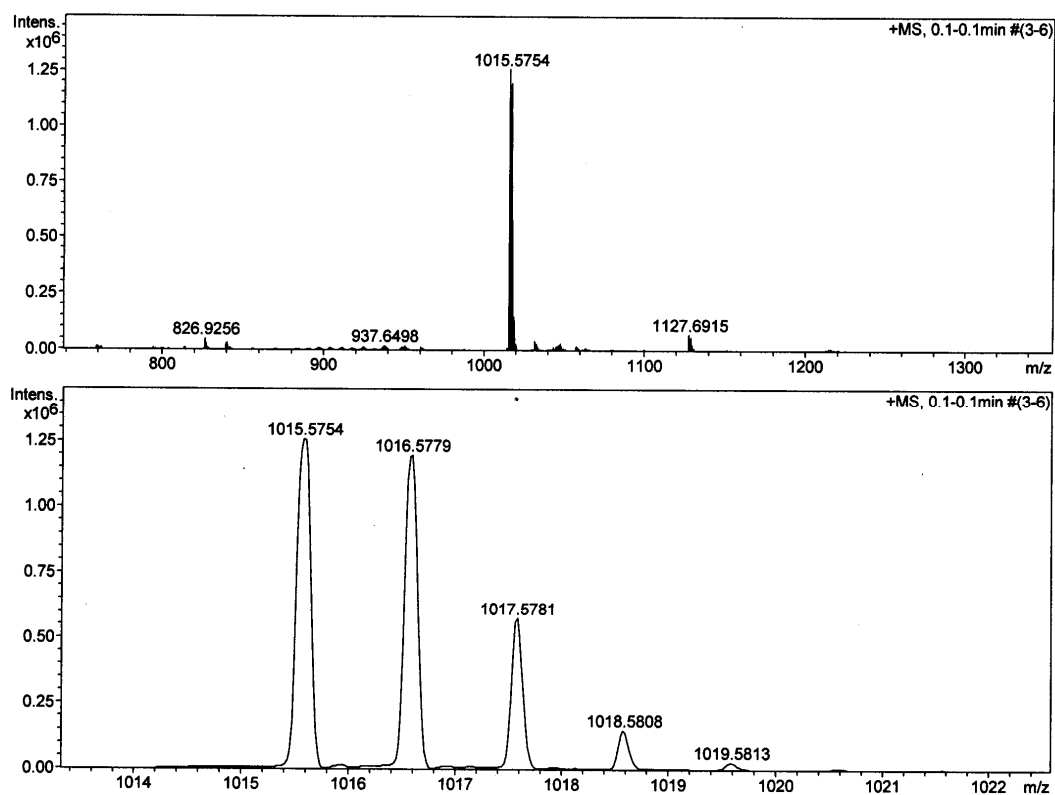


Figure 3.7. ESI-TOF-MS of **NCP-6**.

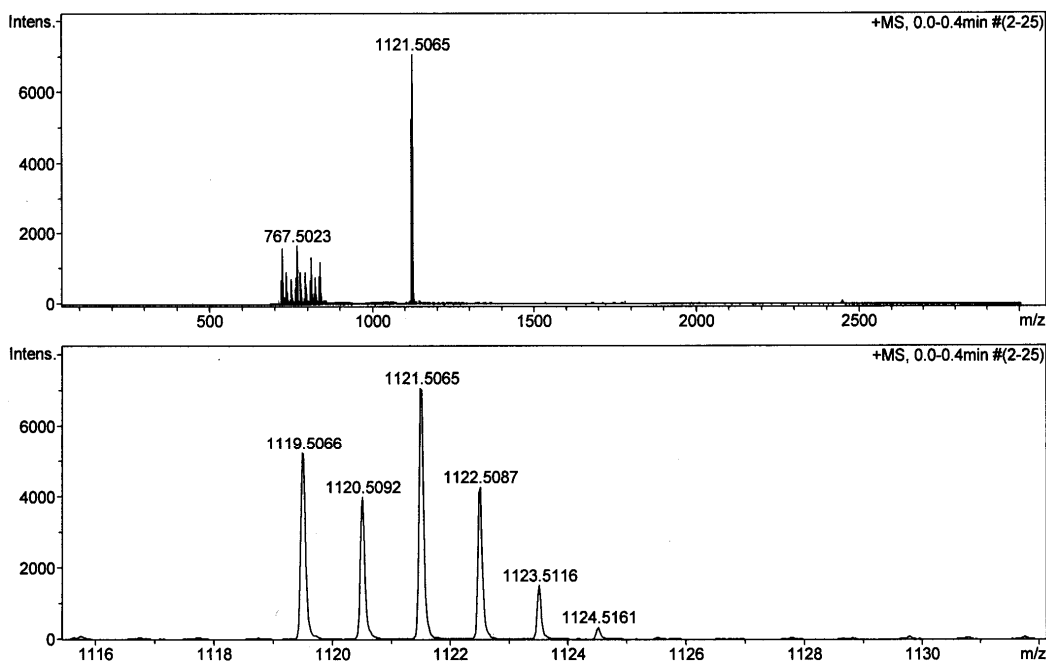


Figure 3.8. ESI-TOF-MS of **NCP-6-Ag**.

The ESI-TOF-MS analysis for both **NCP-6** (Figure 3.7) and **NCP-6-Ag** (Figure 3.8) further confirm the exact composition of the molecules, where the molecular ion peak at 1015.5754 and 1121.5065 correspond to **NCP-6** and **NCP-6-Ag** respectively.

The UV-Vis absorption spectrum of **NCP-6** and **NCP-6-Ag** showed distinguish difference in the λ_{max} and in the Q-band pattern as shown in Figure 3.9. The Soret band of **NCP-6** was exhibited at 440 nm in THF, where **NCP-6-Ag** showed at 449 nm, which is 9 nm red-shifted as compared to **NCP-6**. The Q-bands of **NCP-6** showed four peaks at 541, 583, 650 and 718 nm. Interestingly, **NCP-6-Ag** also showed four Q-peaks at 521, 557, 586 and 637 nm, where the pattern was similar to the Ag(III) complex reported [167]. Attempts to grow single crystal of **NCP-6-Ag** was not successful, however based on the previous report, the red-shifted Soret band and similar Q-band pattern as of **Ag-NCTPP**, it is expected that **NCP-6-Ag** is more planar compared to **NCP-6** and have nearly square planar geometry [167].

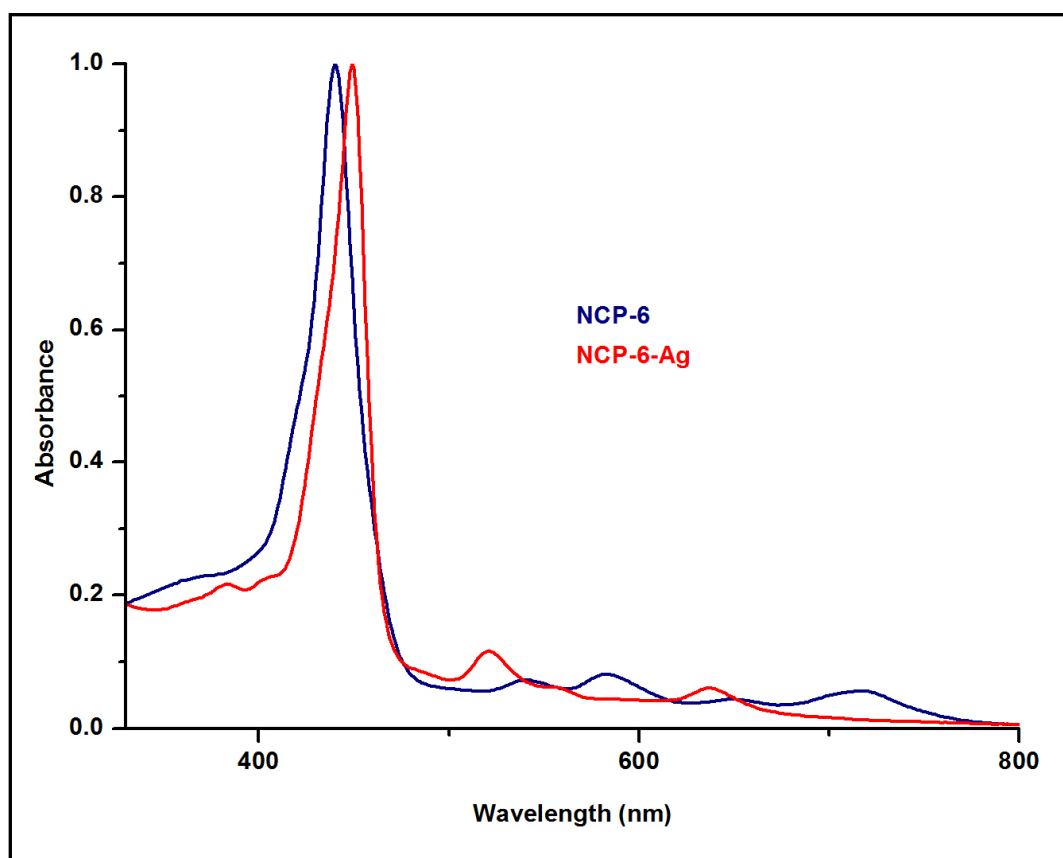


Figure 3.9. UV-Vis absorption spectra of **NCP-6** and **NCP-6-Ag** in THF.

3.4.2 Aggregation behaviour of NCP-n

In continuation of our investigations on aggregation behaviour of **NCP** derivatives, the aggregation properties of **NCP-n** derivatives were studied to know the effect of alkyl side chain length during aggregation. Three molecules were selected for the investigations, **NCP-6**, **NCP-10** and **NCP-16**, where aggregation was achieved by increasing the volume of H_2O in a THF solution of **NCP-n** derivatives and the progress of aggregation was monitored by UV-Vis absorption spectroscopy as shown in Figure 3.10, 3.11 and 3.12 for **NCP-6**, **NCP-10** and **NCP-16** respectively.

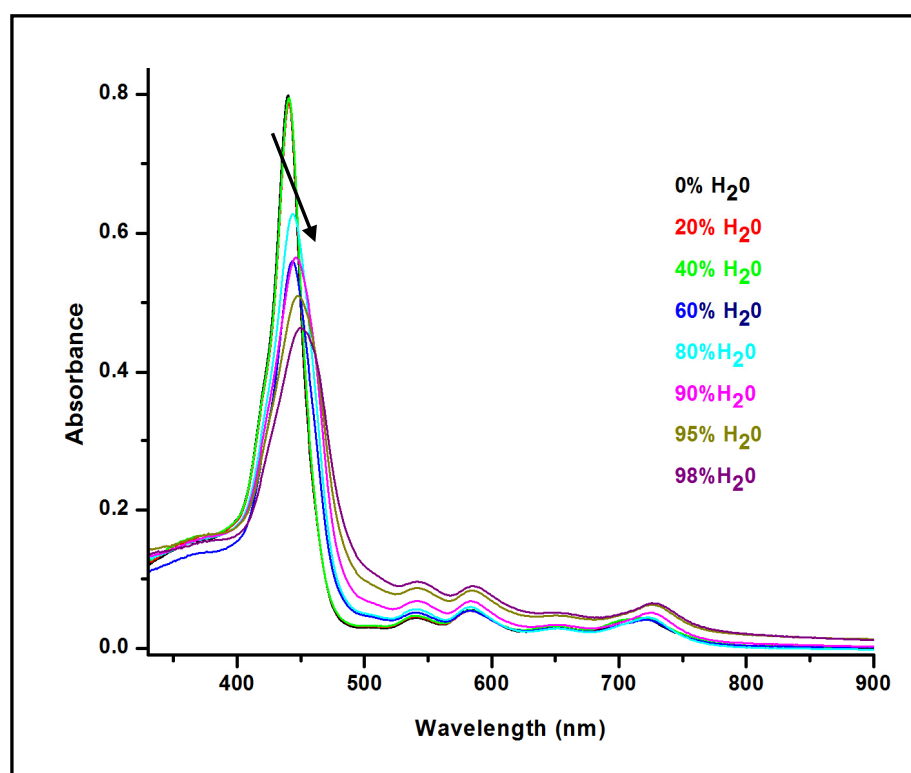


Figure 3.10. UV-Vis absorption changes of **NCP-6** during aggregation in THF/ H_2O .

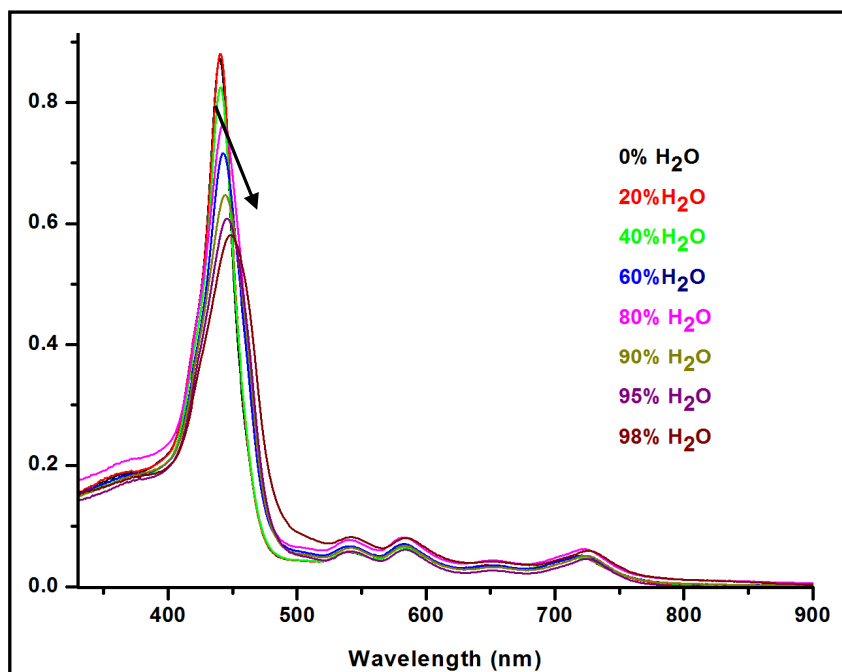


Figure 3.11. UV-Vis absorption changes of **NCP-10** during aggregation in THF/H₂O.

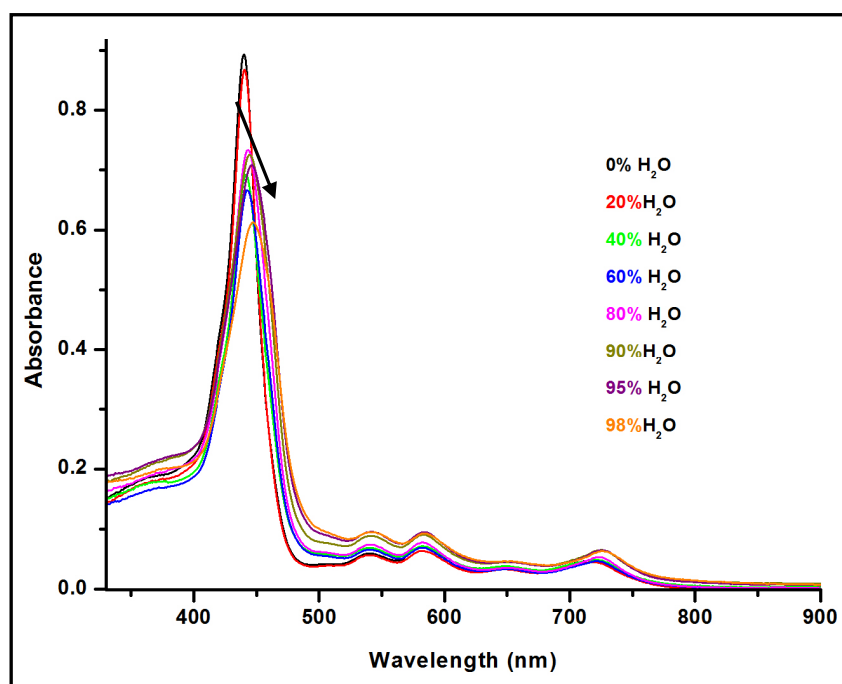


Figure 3.12. UV-Vis absorption changes of **NCP-16** during aggregation in THF/H₂O.

Absorption studies were conducted with 8 μM solution of the compounds and found that with the increase in H₂O volume from 0% to 98%, the Soret band was red-shifted from 440 nm (0% H₂O) to 449 nm (98% H₂O) with spectral broadening, indicates preferential J-type aggregate formation in the solution. However, there was no shift in the

Q-band pattern and position during the event. The change in absorption spectra was similar for the derivative irrespective of the chain length, implies that the alkyl chain length doesn't influence the electronic environment significantly during aggregation, rather than contributing towards increased hydrophobic interactions as the chain length increases from 6 to 16.

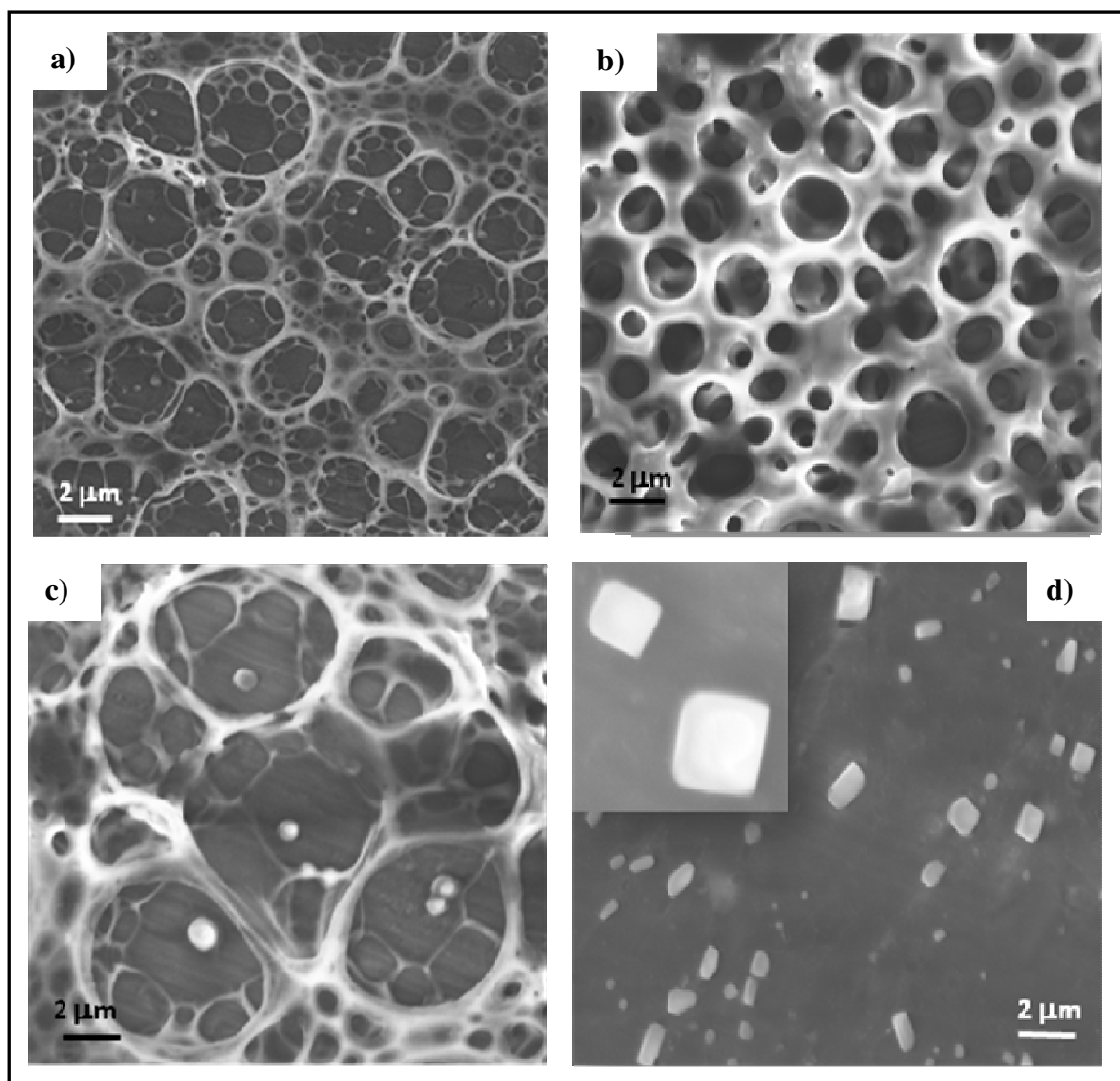


Figure 3.13. SEM images of **NCP-10** in different volume of H₂O in a THF/H₂O mixture (v/v) (a) 50:50, (b) 40:60, (c) 30:70 and (d) 10:90.

Morphological features during aggregation were followed by SEM analysis. Samples were prepared by casting a drop of sample solution on an aluminium film coated on glass plate in desired concentration. Initially, a 10:80 (v/v, THF/H₂O) solution of all the derivative (25 μM) were prepared for the imaging, but found that all the **NCP** derivatives are forming cubic structure in this solvent combination irrespective of the chain length. Further, to investigate the gradual structural changes during aggregation with different amount of water, as can be expected due to the increased hydrophobic interactions, **NCP-10** was used as a representative compound. The morphological changes observed at different H₂O concentration is shown in Figure 3.13.

In a 50:50 (v/v, THF/H₂O) mixture, the solution of **NCP-10** forms network structure after slow evaporation of the solvent. On the other hand, a 40:60 (v/v) mixture generates honeycomb like structure after evaporating, attributed to increase in the hydrophobic interactions. Further increase in the H₂O volume breaks the honeycomb like morphology to form network structure along with aggregated solid structures and finally at 20:80 (v/v) attain cubic structure. The investigations proved that at higher volume of H₂O due to extensive hydrophobic interactions, intermolecular interactions enhance the alignment of individual units in cubic structures through J-type aggregate formation.

3.4.3 Aggregation behaviour of NCP-n-Ag

The effect of metallation on aggregation behaviour of long alkyl chain substituted **NCPs** were investigated with three derivatives, **NCP-6-Ag**, **NCP-10-Ag** and **NCP-16-Ag**. Similar to the free base derivatives all the complexes showed similar changes in the absorption spectra during aggregation irrespective of the chain length. As a representative example, Figure 3.14 shows the change in the absorption spectrum of **NCP-10-Ag** with increased volume of H₂O.

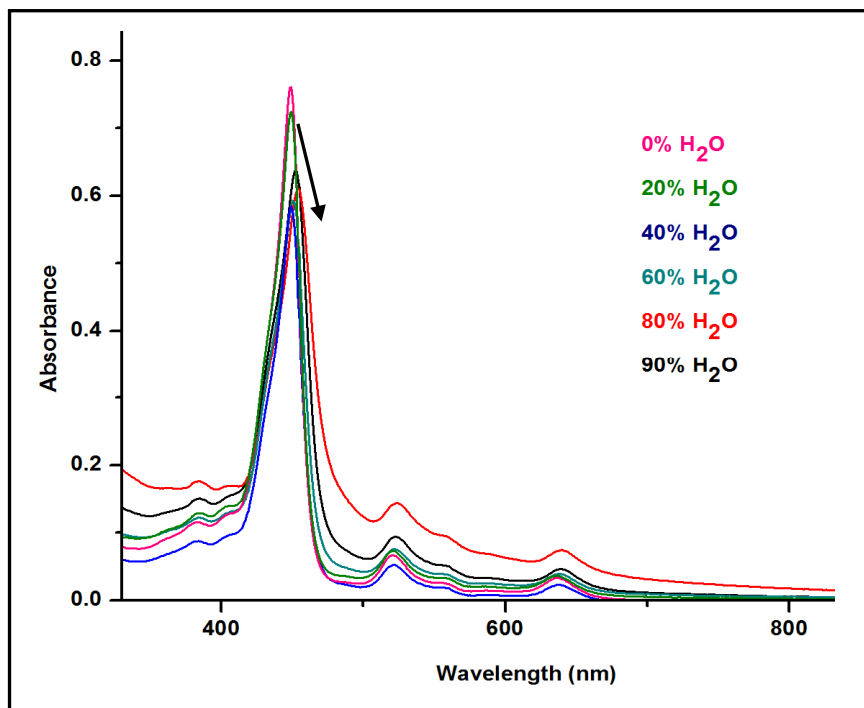


Figure 3.14. UV-Vis absorption changes of **NCP-10-Ag** during aggregation in THF/H₂O.

Absorption changes during aggregation was investigated using a 8 μM solution of **NCP-10-Ag** and found that the increase in H₂O volume from 0% to 90%, the Soret band was red-shifted from 449 nm (0% H₂O) to 456 nm (90% H₂O) with spectral broadening, indicates J-type aggregate formation in the solution as in the case of free base form. Also, there was no significant shift in the Q-band pattern and position during the titration.

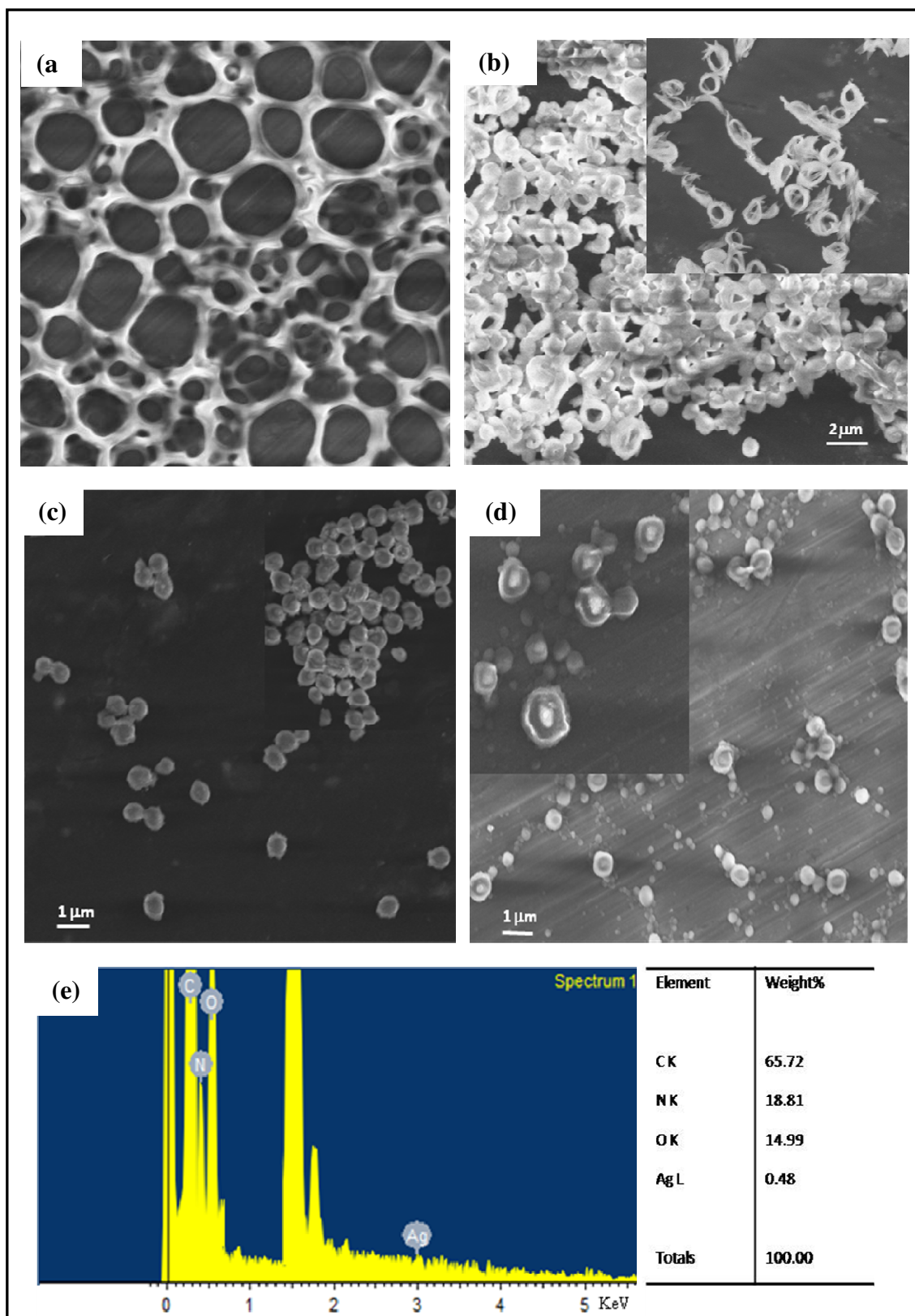


Figure 3.15. SEM images of NCP-10-Ag in different volume of H₂O in a THF/H₂O (v/v) mixture; (a) 40:60, (b) 30:70, (c) 20:80, (d) 10:90 and (e) EDX analysis of NCP-10-Ag.

SEM analyses of **NCP-10-Ag** revealed interesting morphological properties of the metallated derivative as shown in Figure 3.15. As in the case of **NCP-10**, at 50:50 (v/v, THF:H₂O) mixture, the solution of **NCP-10-Ag** was also assembled in a network structure, which gradually changes the structure as the volume of water increases in the mixture. Honeycomb morphology formed in 40:60 (v/v, THF/H₂O, Figure 3.15.a) transformed into feathery aggregated forms at 30:70 (v/v, THF/H₂O, Figure 3.15.b) mixture. This becomes more compact structure in 20:80 (v/v, THF/H₂O, Figure 3.15.c) mixture and finally attains flower type structure at 10:90 (v/v, THF/H₂O, Figure 3.15.d) mixture. Based on the results, a possible mechanism for the morphological difference between the aggregated structures of **NCP-10** and **NCP-10-Ag** can be proposed by the planarity difference. The more planar nature of the metallated derivatives promotes the oligomer formation in the initial stage with J-type aggregate which could be driven by the π - π stacking between porphyrin cores. Subsequently, the oligomer further extended to form a supramolecular structure shown above (Figure 3.16.d). EDX (Energy dispersive X-ray) analysis (Figure 3.15.e) for **NCP-10-Ag** further confirms the presence of Ag in the aggregated structure which shows corresponding peak for Ag metal.

3.5 Conclusions

To conclude, the chapter describes the synthesis, spectral, structural characterization and aggregation behaviour of long chain substituted **NCP** derivatives, *meso*-tetrakis(3-alkoxyphenyl)*N*-confused porphyrins and its Ag(III) complexes. The number of carbon atoms in the alkyl side chain varies from 6 to 18 in the free base **NCP**. Ag(III) complexes of **NCP** derivatives were synthesized for alkyl chain length of 6, 8 and 10. All the compounds were characterized by various spectral analyses. Aggregation behaviour of both free base and metallated forms were investigated elaborately to have insight into the influence of alkyl chain length and metallation on determining the morphology of the

aggregated structures. The chapter concludes that the alkyl chain length doesn't play much role in determining the morphology, but interestingly metallation at the core of **NCP** changes the morphology significantly during the aggregation process. The free base derivative generates a cubic structure, where the metallated derivative forms flower like supramolecular structures during aggregation. The different morphological features exhibited by the free base and metallated **NCP** is explained on the basis of structural changes occurred to the free base structure on metallation.

3.6 Experimental Section

3.6.1 General information

The reagents for the synthesis as well as photophysical studies were obtained from Sigma-Aldrich and Merck, India and used as such. All solvents were distilled and dried before use. Deionized water was from Millipore. ^1H and ^{13}C NMR spectra were recorded on a Bruker Biospin 400 MHz spectrometer. ESI-TOF-MS spectra were recorded on a Bruker micro TOF LC instrument using positive-ion mode. Electronic absorption spectra were recorded on Perkin Elmer Lambda-750 UV-Vis absorption spectrometer. FE-SEM imaging and EDX (Energy dispersive X-ray) spectroscopy were performed on a Zeiss EVO 18 Cryo Special Edn. with an accelerating voltage of 5 kV and 10 kV respectively.

3.6.2 Syntheses

3.6.2.1 Synthesis of 3-(hexyloxy)benzaldehyde (BA-6): To MeOH (30 ml) solution of 3-hydroxybenzaldehyde (2 g, 0.0163 mol) K_2CO_3 (3.39 g, 0.0246 mol) was added along with a pinch of tetrabutylammonium bromide in N_2 atmosphere. The mixture was allowed to stir for 5 min at RT. 1-Bromohexane (3.22 g, 0.0195 mol) was added slowly to the solution and refluxed overnight. The reaction was quenched with 1M HCl and the mixture was washed with water and the compound was extracted in hexane:EtOAc (3:1 v/v %). After drying over anhydrous Na_2SO_4 , solvent was evaporated under vacuum and

the compound was purified by column chromatography in silica gel (100-200 mesh) eluted with hexane:EtOAc (9:1 v/v %) to afford BA-6 in 75% yield. ^1H NMR (400 MHz, CDCl_3 , 298 K): δ 9.96 (s, 1H, CHO), 7.42-7.44 (m, 2H, phenyl), 7.37-7.38 (d, $J=4$ Hz, 1H, phenyl), 7.14-7.19 (m, 1H, phenyl), 3.99-4.02 (t, $J=12$ Hz, 2H, -O-CH₂), 1.75-1.83 (m, 2H, -CH₂), 1.45-1.51 (m, 2H, -CH₂), 1.26-1.37 (m, 4H, -CH₂), 0.92-0.93 (t, $J=4$ Hz, 3H, -CH₃); ^{13}C NMR (100 MHz, CDCl_3 , 298 K): δ 190.58, 165.82, 138.11, 129.12, 121.57, 120.04, 115.34, 69.02, 32.11, 29.61, 25.44, 22.32, 15.11, ESI-Q-TOF: m/z Calcd. for $\text{C}_{13}\text{H}_{18}\text{O}_2$ 206.28; Observed 206.15.

3.6.2.2 Synthesis of 3-(octyloxy)benzaldehyde (BA-8): Following the procedure for BA-6, 3-hydroxy benzaldehyde (2 g, 0.0163 mol) was reacted with 1-bromooctane (4.41 g, 0.0213 mol) and K_2CO_3 (3.39 g, 0.0246 mol) to afford BA-8 in 82% yield. ^1H NMR (400 MHz, CDCl_3 , 298 K): δ 9.96 (s, 1H, CHO), 7.42-7.44 (m, 2H, phenyl), 7.37-7.38 (d, $J=4$ Hz, 1H, phenyl), 7.14-7.19 (m, 1H, phenyl), 3.99-4.02 (t, $J=12$ Hz, 2H, -O-CH₂), 1.75-1.83 (m, 2H, -CH₂), 1.45-1.51 (m, 2H, -CH₂), 1.26-1.37 (m, 8H, -CH₂), 0.92-0.93 (t, $J=4$ Hz, 3H, -CH₃); ^{13}C NMR (100 MHz, CDCl_3 , 298 K): δ 190.58, 165.82, 138.11, 129.12, 121.57, 120.04, 115.34, 69.02, 32.11, 29.71, 25.44, 22.32, 15.11; ESI-Q-TOF: m/z Calcd. for $\text{C}_{15}\text{H}_{22}\text{O}_2$ 234.34; Observed 234.05.

3.6.2.3 Synthesis of 3-(decyloxy)benzaldehyde (BA-10): Following the procedure for BA-6, 3-hydroxy benzaldehyde (2 g, 0.0163 mol) was reacted with 1-bromodecane (4.71 g, 0.0213 mol) and K_2CO_3 (3.39 g, 0.0246 mol) to afford BA-10 in 88% yield. ^1H NMR (400 MHz, CDCl_3 , 298 K): δ 9.96 (s, 1H, CHO), 7.42-7.44 (m, 2H, phenyl), 7.37-7.38 (d, $J=4$ Hz, 1H, phenyl), 7.14-7.19 (m, 1H, phenyl), 3.97-4.01 (t, $J=16$ Hz, 2H, -O-CH₂), 1.74-1.87 (m, 2H, -CH₂), 1.45-1.51 (m, 2H, -CH₂), 1.26-1.37 (m, 12 H, -CH₂), 0.90-0.91 (t, $J=4$ Hz, 3H, -CH₃); ^{13}C NMR (100 MHz, CDCl_3 , 298 K): δ 190.88, 164.82, 138.11,

127.12, 121.57, 120.04, 115.34, 69.02, 32.91, 29.71, 27.34, 25.44, 22.32, 15.11; ESI-Q-TOF: m/z Calcd. for C₁₇H₂₆O₂ 262.39; Observed 262.11.

3.6.2.4 Synthesis of 3-(dodecyloxy)benzaldehyde (BA-12): Following the procedure for **BA-6**, 3-hydroxy benzaldehyde (2 g, 0.0163 mol) was reacted with 1-bromododecane (5.31 g, 0.0213 mol) and K₂CO₃ (3.39 g, 0.0246 mol) to afford **BA-12** in 80% yield. ¹H NMR (400 MHz, CDCl₃, 298 K): δ 9.97 (s, 1H, CHO), 7.42-7.45 (m, 2H, phenyl), 7.38-7.39 (d, *J*=4 Hz, 1H, phenyl), 7.14-7.19 (m, 1H, phenyl), 3.97-4.01 (t, *J*=16 Hz, 2H, -O-CH₂), 1.75-1.83 (m, 2H, -CH₂), 1.45-1.51 (m, 2H, -CH₂), 1.23-1.38 (m, 16H, -CH₂), 0.90-0.91 (t, *J*=4 Hz, 3H, -CH₃); ¹³C NMR (100 MHz, CDCl₃, 298 K): δ 190.61, 165.82, 138.11, 129.12, 121.57, 120.04, 115.34, 68.02, 32.01, 29.41, 25.94, 22.69, 14.11; ESI-Q-TOF: m/z Calcd. for C₁₉H₃₀O₂ 290.44; Observed 290.25.

3.6.2.5 Synthesis of 3-(tetradecyloxy)benzaldehyde (BA-14): Following the procedure for **BA-6**, 3-hydroxy benzaldehyde (2 g, 0.0163 mol) was reacted with 1-bromotetradecane (5.90 g, 0.0213 mol) and K₂CO₃ (3.39 g, 0.0246 mol) to afford **BA-14** in 86% yield. ¹H NMR (400 MHz, CDCl₃, 298 K): δ 9.97 (s, 1H, CHO), 7.41-7.44 (m, 2H, phenyl), 7.37-7.39 (d, *J*=4 Hz, 1H, phenyl), 7.14-7.19 (m, 1H, phenyl), 3.99-4.02 (t, *J*=12 Hz, 2H, -O-CH₂), 1.75-1.83 (m, 2H, -CH₂), 1.45-1.51 (m, 2H, -CH₂), 1.23-1.40 (m, 20 H, -CH₂), 0.90-0.91 (t, *J*=4 Hz, 3H, -CH₃); ¹³C NMR (100 MHz, CDCl₃, 298 K): δ 190.61, 165.82, 138.11, 129.12, 121.57, 120.04, 115.34, 68.42, 32.31, 29.61, 25.99, 22.79, 15.11; ESI-Q-TOF: m/z Calcd. for C₂₁H₃₄O₂ 318.49; Observed 318.28.

3.6.2.6 Synthesis of 3-(hexadecyloxy)benzaldehyde (BA-16): Following the procedure for **BA-6**, 3-hydroxy benzaldehyde (2 g, 0.0163 mol) reacted with 1-bromohexadecane (6.50 g, 0.0213 mol) and K₂CO₃ (3.39 g, 0.0246 mol) to afford **BA-16** in 90% yield. ¹H NMR (400 MHz, CDCl₃, 298 K): δ 9.97 (s, 1H, CHO), 7.43-7.44 (m, 2H, phenyl), 7.37-7.38 (d, *J*=4 Hz, 1H, phenyl), 7.14-7.19 (m, 1H, phenyl), 3.99-4.03 (t, *J*=16 Hz, 2H, -O-

CH₂), 1.75-1.83 (m, 2H, -CH₂), 1.45-1.51 (m, 2H, -CH₂), 1.23-1.38 (m, 24H, -CH₂), 0.90-0.91 (t, *J*=4 Hz, 3H, -CH₃); ¹³C NMR (100 MHz, CDCl₃, 298 K): δ 190.61, 165.82, 138.11, 129.12, 121.57, 120.04, 115.34, 68.02, 32.01, 29.41, 25.94, 22.69, 14.11; ESI-Q-TOF: *m/z* Calcd. for C₂₃H₃₈O₂ 346.55; Observed 346.28.

3.6.2.7 Synthesis of 3-(octadecyloxy)benzaldehyde (BA-18): Following the procedure for **BA-6**, 3-hydroxy benzaldehyde (2 g, 0.0163 mol) was reacted with 1-bromooctadecane (7.10 g, 0.0213 mol) and K₂CO₃ (3.39 g, 0.0246 mol) to afford **BA-18** in 87% yield. ¹H NMR (400 MHz, CDCl₃, 298 K): δ 9.96 (s, 1H, CHO), 7.41-7.44 (m, 2H, phenyl), 7.37-7.38 (d, *J*=4 Hz 1H, phenyl), 7.14-7.19 (m, 1H, phenyl), 3.99-4.03 (t, *J*=16 Hz, 2H, -O-CH₂), 1.74-1.83 (m, 2H, -CH₂), 1.45-1.51 (m, 2H, -CH₂), 1.21-1.38 (m, 28H, -CH₂), 0.89-0.91 (t, *J*=8 Hz, 3H, -CH₃); ¹³C NMR (100 MHz, CDCl₃, 298 K): δ 190.61, 165.82, 138.11, 129.12, 121.57, 120.04, 115.34, 68.02, 32.01, 29.41, 25.94, 22.69, 14.11; ESI-Q-TOF: *m/z* Calcd. for C₂₅H₄₂O₂ 374.60; Observed 374.41.

3.6.2.8 Synthesis of NCP-6: 500 ml dry DCM was taken in a 1 L RB, purged with N₂ and kept in dark. Pyrrole (0.7 g, 0.0104 mol) was added into the RB and allowed to stir for 5 min. **BA-6** (2.15 g, 0.0104 mol) was added to the solution and mixed well for 5 min. To the mixture, MSA (0.701 g, 0.0073 mol) was added and allowed to react for 30 min. Further, DDQ (2.37 g, 0.0104) was added and kept open for 5 min. Triethylamine (TEA, 3.5 ml) was added and waited for 10 min. before filtered through a basic alumina column. After removing the solvent in vacuum, the compound was further purified in silica gel (100-200) column and eluted with DCM:hexane (9:1) mixture in 15% yield. ¹H NMR (400 MHz, CDCl₃, 298 K): δ 9.01-9.02 (d, *J*=4 Hz, 1H, pyrrole β-CH), 8.94-8.95 (d, *J*=4 Hz, 1H, pyrrole β-CH), 8.81 (s, 1H, pyrrole α-CH), 8.64-8.65 (d, *J*=4 Hz, 2H, pyrrole β-CH), 8.60-8.61 (d, *J*=4 Hz, 2H, pyrrole β-CH), 8.02-8.04 (d, *J*=8 Hz, 1H, phenyl), 7.98 (s, 3H, phenyl), 7.76-7.82 (m, 6H, phenyl), 7.65-7.69 (t, *J*=16 Hz, 2H,

phenyl), 7.34-7.41 (m, 4H, phenyl), 4.27-4.32 (m, 4H, -O-CH₂), 4.20-4.26 (m, 4H, -O-CH₂), 1.91-2.03 (m, 8H, -CH₂), 1.58-1.66 (m, 8H, -CH₂), 1.42-1.47 (m, 16H, -CH₂), 0.95-1.02 (m, 12H, -CH₃), -2.31 (s, 2H, exch. D₂O, pyrrolic inner NH), -4.95 (s, 1H, pyrrolic inner β -CH) ; ¹³C NMR (100 MHz, CDCl₃, 298 K): δ 157.84, 149.59, 141.16, 140.01, 137.25, 135.14, 134.42, 128.43, 127.57, 125.31, 123.17, 121.24, 118.31, 114.43, 99.32, 68.42, 31.73, 29.53, 25.95, 22.71, 14.13; ESI-Q-TOF: m/z Calcd. for C₆₈H₇₈N₄O₄ 1015.37; Observed 1015.57.

3.6.2.9 Synthesis of NCP-8: Following the procedure for **NCP-6**, pyrrole (0.7 g, 0.0104 mol), **BA-8** (2.44 g, 0.0104 mol), MSA (0.701 g, 0.0073 mol), DDQ (2.37 g, 0.0104) and TEA (3.5 ml) were reacted to afford **NCP-8** in 18% yield. ¹H NMR (400 MHz, CDCl₃, 298 K): δ 9.00-9.01 (d, $J=4$ Hz, 1H, pyrrole β -CH), 8.94-8.95 (d, $J=4$ Hz, 1H, pyrrole β -CH), 8.81 (s, 1H, pyrrole α -CH), 8.64-8.65 (d, $J=4$ Hz, 2H, pyrrole β -CH), 8.60-8.61 (d, $J=4$ Hz, 2H, pyrrole β -CH), 7.92-7.94 (d, $J=8$ Hz, 1H, phenyl), 7.87 (s, 3H, phenyl), 7.70-7.74 (m, 6H, phenyl), 7.60-7.64 (t, $J=16$ Hz, 2H, phenyl), 7.29-7.35 (m, 4H, phenyl), 4.19-4.23 (m, 4H, -O-CH₂), 3.97-4.16 (m, 4H, -O-CH₂), 1.85-1.95 (m, 8H, -CH₂), 1.51-1.73 (m, 8H, -CH₂), 1.26-1.37 (m, 32H, -CH₂), 0.85-0.90 (m, 12H, -CH₃), -2.52 (s, 2H, exch. D₂O, pyrrolic inner NH), -5.05 (s, 1H, pyrrolic inner β -CH); ¹³C NMR (100 MHz, CDCl₃, 298 K): δ 156.84, 147.59, 140.16, 138.01, 137.25, 133.14, 134.42, 127.43, 125.81, 121.17, 119.31, 114.93, 99.32, 68.42, 31.73, 29.53, 23.95, 21.71, 13.93; ESI-Q-TOF: m/z Calcd. for C₇₆H₉₄N₄O₄ 1127.58; Observed 1127.68.

3.6.2.10 Synthesis of NCP-10: Following the procedure for **NCP-6**, pyrrole (0.7 g, 0.0104 mol) was reacted with **BA-10** (2.74 g, 0.0104 mol), MSA (0.701 g, 0.0073 mol), DDQ (2.37 g, 0.0104) and TEA (3.5 ml) to afford **NCP-10** in 20% yield. ¹H NMR (400 MHz, CDCl₃, 298 K): δ 9.02-9.03 (d, $J=4$ Hz, 1H, pyrrole β -CH), 8.95-8.96 (d, $J=4$ Hz, 1H, pyrrole β -CH), 8.83 (s, 1H, pyrrole α -CH), 8.64-8.66 (d, $J=8$ Hz, 2H, pyrrole β -

CH), 8.60-8.62 (d, $J=8$ Hz, 2H, pyrrole β -CH), 7.94-7.96 (d, $J=8$ Hz, 1H, phenyl), 7.87 (s, 3H, phenyl), 7.70-7.74 (m, 6H, phenyl), 7.60-7.64 (t, $J=16$ Hz, 2H, phenyl), 7.29-7.35 (m, 4H, phenyl), 4.22-4.26 (m, 4H, -O-CH₂), 4.14-4.21 (m, 4H, -O-CH₂), 1.89-1.98 (m, 8H, -CH₂), 1.54-1.78 (m, 8H, -CH₂), 1.22-1.39 (m, 48H, -CH₂), 0.84-0.89 (m, 12H, -CH₃), -2.54 (s, 2H, exch. D₂O, pyrrolic inner NH), -5.04 (s, 1H, pyrrolic inner β -CH); ¹³C NMR (100 MHz, CDCl₃, 298 K): δ 156.84, 147.59, 140.16, 138.01, 137.25, 133.14, 134.42, 127.43, 125.81, 121.17, 119.31, 114.93, 99.32, 68.42, 31.73, 29.53, 23.95, 21.71, 13.93; ESI-Q-TOF: m/z Calcd. for C₈₄H₁₁₀N₄O₄ 1239.80; Observed 1239.82.

3.6.2.11 Synthesis of NCP-12: Following the procedure for **NCP-6**, pyrrole (0.7 g, 0.0104 mol) was reacted with **BA-12** (3.02 g, 0.0104 mol), MSA (0.701 g, 0.0073 mol), DDQ (2.37 g, 0.0104) and TEA (3.5 ml) to afford **NCP-12** in 16% yield. ¹H NMR (400 MHz, CDCl₃, 298 K): δ 9.00-9.02 (d, $J=8$ Hz, 1H, pyrrole β -CH), 8.93-8.95 (d, $J=4$ Hz, 1H, pyrrole β -CH), 8.81 (s, 1H, pyrrole α -CH), 8.62-8.64 (d, $J=8$ Hz, 2H, pyrrole β -CH), 8.59-8.61 (d, $J=8$ Hz, 2H, pyrrole β -CH), 7.92-7.94 (d, $J=8$ Hz, 1H, phenyl), 7.87 (s, 3H, phenyl), 7.69-7.73 (m, 6H, phenyl), 7.59-7.63 (t, $J=16$ Hz, 2H, phenyl), 7.28-7.34 (m, 4H, phenyl), 4.18-4.23 (m, 4H, -O-CH₂), 4.13-4.16 (m, 4H, -O-CH₂), 1.84-1.95 (m, 8H, -CH₂), 1.50-1.58 (m, 8H, -CH₂), 1.22-1.39 (m, 64H, -CH₂), 0.85-0.89 (m, 12H, -CH₃), -2.54 (s, 2H, exch. D₂O, pyrrolic inner NH), -5.04 (s, 1H, pyrrolic inner β -CH); ¹³C NMR (100 MHz, CDCl₃, 298 K): δ 156.84, 147.59, 140.16, 138.01, 137.25, 133.14, 134.42, 127.43, 125.81, 121.17, 119.31, 114.93, 99.32, 68.42, 31.73, 29.53, 23.95, 21.71, 13.93; ESI-Q-TOF: m/z Calcd. for C₉₂H₁₂₆N₄O₄ 1352.01; Observed 1352.85.

3.6.2.12 Synthesis of NCP-14: Following the procedure for **NCP-6**, pyrrole (0.7 g, 0.0104 mol) was reacted with **BA-14** (3.30 g, 0.0104 mol), MSA (0.701 g, 0.0073 mol), DDQ (2.37 g, 0.0104) and TEA (3.5 ml) to afford **NCP-14** in 11% yield. ¹H NMR (400 MHz, CDCl₃, 298 K): δ 8.97-8.98 (d, $J=4$ Hz, 1H, pyrrole β -CH), 8.90-8.91 (d, $J=4$ Hz,

1H, pyrrole β -CH), 8.77 (s, 1H, pyrrole α -CH), 8.61-8.62 (d, $J=4$ Hz, 1H, pyrrole β -CH), 8.55-8.59 (m, 3H, pyrrole β -CH), 7.89-7.91 (d, $J=8$ Hz, 1H, phenyl), 7.83 (s, 3H, phenyl), 7.65-7.69 (m, 6H, phenyl), 7.55-7.59 (t, $J=16$ Hz, 2H, phenyl), 7.25-7.30 (m, 4H, phenyl), 4.14-4.19 (m, 4H, -O-CH₂), 4.09-4.12 (m, 4H, -O-CH₂), 1.81-1.92 (m, 8H, -CH₂), 1.46-1.55 (m, 8H, -CH₂), 1.22-1.34 (m, 80H, -CH₂), 0.79-0.83 (m, 12H, -CH₃), -2.53 (s, 2H, exch. D₂O, pyrrolic inner NH), -5.09 (s, 1H, pyrrolic inner β -CH); ¹³C NMR (100 MHz, CDCl₃, 298 K): δ 156.14, 146.99, 140.06, 137.11, 137.05, 132.44, 133.92, 127.13, 125.11, 121.07, 118.71, 114.33, 99.02, 67.92, 31.73, 29.41, 23.95, 21.11, 13.93; ESI-Q-TOF: m/z Calcd. for C₁₀₀H₁₄₂N₄O₄ 1464.22; Observed 1464.00.

3.6.2.13 Synthesis of NCP-16: Following the procedure for **NCP-6**, pyrrole (0.7 g, 0.0104 mol) was reacted with **BA-16** (3.60 g, 0.0104 mol), MSA (0.701 g, 0.0073 mol), DDQ (2.37 g, 0.0104) and TEA (3.5 ml) to afford **NCP-16** in 14% yield. ¹H NMR (400 MHz, CDCl₃, 298 K): δ 9.00-9.02 (d, $J=8$ Hz, 1H, pyrrole β -CH), 8.93-8.95 (d, $J=8$ Hz, 1H, pyrrole β -CH), 8.81 (s, 1H, pyrrole α -CH), 8.64-8.66 (d, $J=8$ Hz, 1H, pyrrole β -CH), 8.59-8.63 (m, 3H, pyrrole β -CH), 7.93-7.94 (d, $J=8$ Hz, 1H, phenyl), 7.88 (s, 3H, phenyl), 7.70-7.73 (m, 6H, phenyl), 7.59-7.63 (t, $J=16$ Hz, 2H, phenyl), 7.28-7.34 (m, 4H, phenyl), 4.20-4.25 (m, 4H, -O-CH₂), 4.12-4.19 (m, 4H, -O-CH₂), 1.84-1.94 (m, 8H, -CH₂), 1.50-1.56 (m, 8H, -CH₂), 1.22-1.25 (m, 96H, -CH₂), 0.84-0.87 (m, 12H, -CH₃), -2.47 (s, 2H, exch. D₂O, pyrrolic inner NH), -5.06 (s, 1H, pyrrolic inner β -CH) ; ¹³CNMR (100 MHz, CDCl₃, 298 K): δ 156.74, 147.09, 140.76, 137.91, 135.05, 132.44, 133.92, 127.13, 125.11, 121.07, 118.71, 114.33, 99.02, 67.92, 31.73, 29.41, 23.95, 21.11, 13.93. ESI-Q-TOF: m/z Calcd. for C₁₀₈H₁₅₈N₄O₄ 1576.43; Observed 1576.40.

3.6.2.14 Synthesis of NCP-18: Following the procedure for **NCP-6**, pyrrole (0.7 g, 0.0104 mol) was reacted with **BA-18** (3.89 g, 0.0104 mol), MSA (0.701 g, 0.0073 mol), DDQ (2.37 g, 0.0104) and TEA (3.5 ml) to afford **NCP-18** in 10% yield. ¹H NMR (400

MHz, CDCl₃, 298 K): δ 9.00-9.02 (d, $J=8$ Hz, 1H, pyrrole β -CH), 8.91-8.92 (d, $J=4$ Hz, 1H, pyrrole β -CH), 8.79 (s, 1H, pyrrole α -CH), 8.62-8.64 (d, $J=8$ Hz, 1H, pyrrole β -CH), 8.52-8.57 (m, 3H, pyrrole β -CH), 7.89-7.91 (d, $J=8$ Hz, 1H, phenyl), 7.82 (s, 3H, phenyl), 7.67-7.70 (m, 6H, phenyl), 7.56-7.60 (t, $J=16$ Hz, 2H, phenyl), 7.25-7.30 (m, 4H, phenyl), 4.16-4.20 (m, 4H, -O-CH₂), 4.04-4.13 (m, 4H, -O-CH₂), 1.81-1.89 (m, 8H, -CH₂), 1.50-1.53 (m, 8H, -CH₂), 1.18-1.24 (m, 112H, -CH₂), 0.82-0.87 (m, 12H, -CH₃), -2.49 (s, 2H, exch. D₂O, pyrrolic inner NH), -5.07 (s, 1H, pyrrolic inner β -CH); ¹³C NMR (100 MHz, CDCl₃, 298 K): δ 156.04, 146.39, 140.76, 137.91, 134.85, 132.44, 133.12, 127.00, 125.11, 121.07, 117.41, 114.33, 99.02, 67.92, 31.73, 28.11, 23.15, 21.11, 13.93; ESI-Q-TOF: m/z Calcd. for C₁₁₆H₁₇₄N₄O₄ 1688.65; Observed 1688.33.

3.6.2.15 Synthesis of NCP-6-Ag: To a solution of **NCP-6** (20 mg, 0.0197 mmol) in DCM (20 ml), silver(I)triflate (10 mg, 0.0394 mmol) dissolved in MeOH (2 ml) was added and allowed to stir for 2 h in dark at RT. The solvent was removed and purified by silica gel column (100-200 mesh). Compound was eluted with DCM in 65% yield. ¹H NMR (400 MHz, CDCl₃, 298 K): δ 9.60 (s, 1H, pyrrole α -CH), 9.00-9.01 (d, $J=4$ Hz, 1H, pyrrole β -CH), 8.90-8.92 (d, $J=8$ Hz, 1H, pyrrole β -CH), 8.75-8.76 (d, $J=4$ Hz, 1H, pyrrole β -CH), 8.71-8.73 (d, $J=8$ Hz, 1H, pyrrole β -CH), 8.69-8.70 (d, $J=4$ Hz, 1H, pyrrole β -CH), 8.65-8.66 (d, $J=4$ Hz, 1H, pyrrole β -CH), 7.61-7.77 (m, 12H, phenyl), 7.27-7.33 (m, 4H, phenyl), 4.10-4.15 (m, 8H, -O-CH₂), 1.85-1.88 (m, 8H, -CH₂), 1.47-1.51 (m, 8H, -CH₂), 1.24-1.25 (m, 16H, -CH₂), 0.83-0.86 (m, 12H, -CH₃); ¹³C NMR (100 MHz, CDCl₃, 298 K): δ 162.54, 143.01, 141.54, 140.76, 138.77, 137.91, 135.34, 134.85, 133.11, 132.44, 133.12, 127.00, 125.11, 121.37, 67.92, 31.73, 29.41, 23.95, 21.11, 13.93; ESI-Q-TOF: m/z Calcd. for C₆₈H₇₅AgN₄O₄ 1120.21; Observed 1120.51.

3.6.2.16 Synthesis of NCP-10-Ag: Following the procedure for **NCP-6-Ag**, **NCP-10** (20 mg, 0.0161 mmol) in DCM (20 ml) was reacted with silver(I)triflate (8.28 mg, 0.0322

mmol) dissolved in MeOH (2 ml) to afford **NCP-10-Ag** in 62% yield. ^1H NMR (400 MHz, CDCl_3 , 298 K): δ 9.62 (s, 1H, pyrrole α -CH), 9.01-9.02 (d, $J=4$ Hz, 1H, pyrrole β -CH), 8.90-8.92 (d, $J=8$ Hz, 1H, pyrrole β -CH), 8.73-8.75 (d, $J=8$ Hz, 1H, pyrrole β -CH), 8.71-8.73 (d, $J=8$ Hz, 1H, pyrrole β -CH), 8.69-8.70 (d, $J=4$ Hz, 1H, pyrrole β -CH), 8.65-8.66 (d, $J=4$ Hz, 1H, pyrrole β -CH), 7.61-7.77 (m, 12H, phenyl), 7.17-7.23 (m, 4H, phenyl), 4.10-4.15 (m, 8H, -O-CH₂), 1.85-1.88 (m, 8H, -CH₂), 1.47-1.51 (m, 8H, -CH₂), 1.24-1.25 (m, 16H, -CH₂), 0.83-0.86 (m, 12H, -CH₃); ^{13}C NMR (100 MHz, CDCl_3 , 298 K): δ 162.54, 143.01, 141.54, 140.76, 138.77, 137.91, 135.34, 134.85, 133.11, 132.44, 133.12, 127.00, 125.11, 121.37, 67.92, 31.73, 29.41, 23.95, 21.11, 13.93; ESI-Q-TOF: m/z Calcd. for $\text{C}_{84}\text{H}_{107}\text{AgN}_4\text{O}_4$ 1344.64; Observed 1344.71.

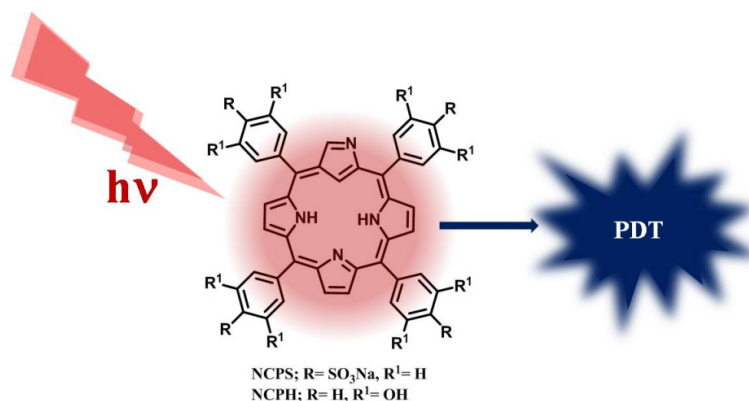
3.6.2.17 Synthesis of NCP-16-Ag: Following the procedure for **NCP-6-Ag**, **NCP-16** (20 mg, 0.0127 mmol) in DCM (20 ml) was reacted with silver(I)triflate (6.52 mg, 0.0254 mmol) dissolved in MeOH (2 ml) to afford **NCP-16-Ag** in 60% yield. ^1H NMR (400 MHz, CDCl_3 , 298 K): δ 9.65 (s, 1H, pyrrole α -CH), 9.02-9.04 (d, $J=8$ Hz, 1H, pyrrole β -CH), 8.92-8.94 (d, $J=8$ Hz, 1H, pyrrole β -CH), 8.74-8.76 (d, $J=8$ Hz, 1H, pyrrole β -CH), 8.74-8.76 (d, $J=8$ Hz, 1H, pyrrole β -CH), 8.71-8.73 (d, $J=8$ Hz, 1H, pyrrole β -CH), 8.66-8.67 (d, $J=4$ Hz, 1H, pyrrole β -CH), 7.63-7.79 (m, 12H, phenyl), 7.18-7.23 (m, 4H, phenyl), 4.10-4.14 (m, 8H, -O-CH₂), 1.85-1.88 (m, 8H, -CH₂), 1.47-1.51 (m, 8H, -CH₂), 1.21-1.25 (m, 16H, -CH₂), 0.85-0.88 (m, 12H, -CH₃); ^{13}C NMR (100 MHz, CDCl_3 , 298 K): δ 162.94, 143.81, 141.94, 140.76, 138.87, 138.01, 135.74, 135.15, 133.91, 132.44, 133.12, 127.00, 125.11, 121.37, 67.92, 31.73, 29.41, 23.95, 21.11, 13.93; ESI-Q-TOF: m/z Calcd. for $\text{C}_{108}\text{H}_{155}\text{AgN}_4\text{O}_4$ 1681.28; Observed 1681.08.

CHAPTER 4

N-Confused Porphyrin Derivatives as PDT Sensitizers

4.1	Abstract	140
4.2	Introduction	141
4.2.1	History of Photodynamic therapy	142
4.2.2	Sensitizers in PDT	143
4.2.2.1	Non-porphyrin photosensitizers	144
4.2.2.2	Porphyrin photosensitizers	145
4.2.3	Light sources in PDT	149
4.2.4	Role of oxygen in PDT	151
4.2.5	Apoptosis; mechanism of cell death	153
4.3	Objective of Our Work	154
4.4	Results and Discussions	154
4.4.1	NCPH as a PDT sensitizer	154
4.4.2	NCPS as a PDT sensitizer	160
4.4.2.1	Photophysical investigations of NCPS for PDT application	160
4.4.3	<i>In Vitro</i> Studies	166
4.4.3.1	Cytotoxicity Studies of NCPS in Different Cell Lines	166
4.4.3.2	NCPS Sensitized ROS Generation	168
4.4.3.3	Cytotoxicity Studies of NCPH	174
4.5	Conclusions	178
4.6	Experimental Section	179
4.6.1	Materials and methods	179
4.6.2	Synthesis of NCPS	181
4.6.3	Cell Lines and Culture Conditions	182
4.6.4	Photocytotoxicity Assay	182
4.6.5	Detection of cellular ROS using CM-H2DCFDA assay	183
4.6.6	Chromatin condensation analysis by Hoechst staining	183
4.6.7	Mitochondrial membrane potential assay using JC1 Dye	184
4.6.8	Flow cytometric Annexin V apoptotic studies and Immunoblot analysis	184

4.1 Abstract



In recent years, photodynamic therapy (PDT) has emerged as a promising and noninvasive treatment for various types of cancer. The technique involves controlled generation of short-lived cytotoxic agents within a cell on irradiation of a prodrug or photosensitizer, which in turn destroys the affected cells. This chapter describes the PDT application of two NCP derivatives, meso-hydroxy (NCPH) and p-sulfonato-phenyl substituted (NCPS) derivatives, which have better molar extinction coefficient in the red region of visible light compared with normal porphyrin derivatives. Photophysical studies of the molecules have been conducted in polar solvents such as deionized water and MeOH, which gives promising values for parameters required for PDT such as triplet quantum yield and singlet oxygen quantum yield. In vitro anticancer studies were conducted with both the derivative, where a series of cancer cell lines showed promising IC₅₀. Upon illumination, the NCPS exhibited more photocytotoxicity to adenocarcinomas than the other epithelial cell lines, and maximum activity has been attributed toward breast adenocarcinoma MDA-MB-231 cells, with an IC₅₀ value as low as 6 μM, where corresponding value for NCPH was 12 μM. Generation of reactive oxygen species and apoptosis induced pathway of cell death was established through various experiments such as flow cytometry, fluorescent imaging, mitochondrial membrane potential assay and PARP cleavage.

4.2 Introduction

Photodynamic therapy (PDT) is a non invasive technique for treatment of cancer, in which cell death and tissue eradication are achieved on irradiation of a photosensitizer and the subsequent production of cytotoxic species, in particular singlet molecular oxygen [168]. The technique works as combination of three components; photosensitizer (drug), light and oxygen. Controlled generation and deactivation of short-lived cytotoxic agents within a cell on irradiation of a prodrug or photosensitizer is the key step in PDT. Light excitation of a dye causes an intermolecular triplet-triplet energy transfer that generates the highly reactive cytotoxic agent, singlet oxygen molecule ($^1\text{O}_2$), within a target region, which in turn destroys the affected cells. The whole photochemical process during PDT is described in Figure 4.1.

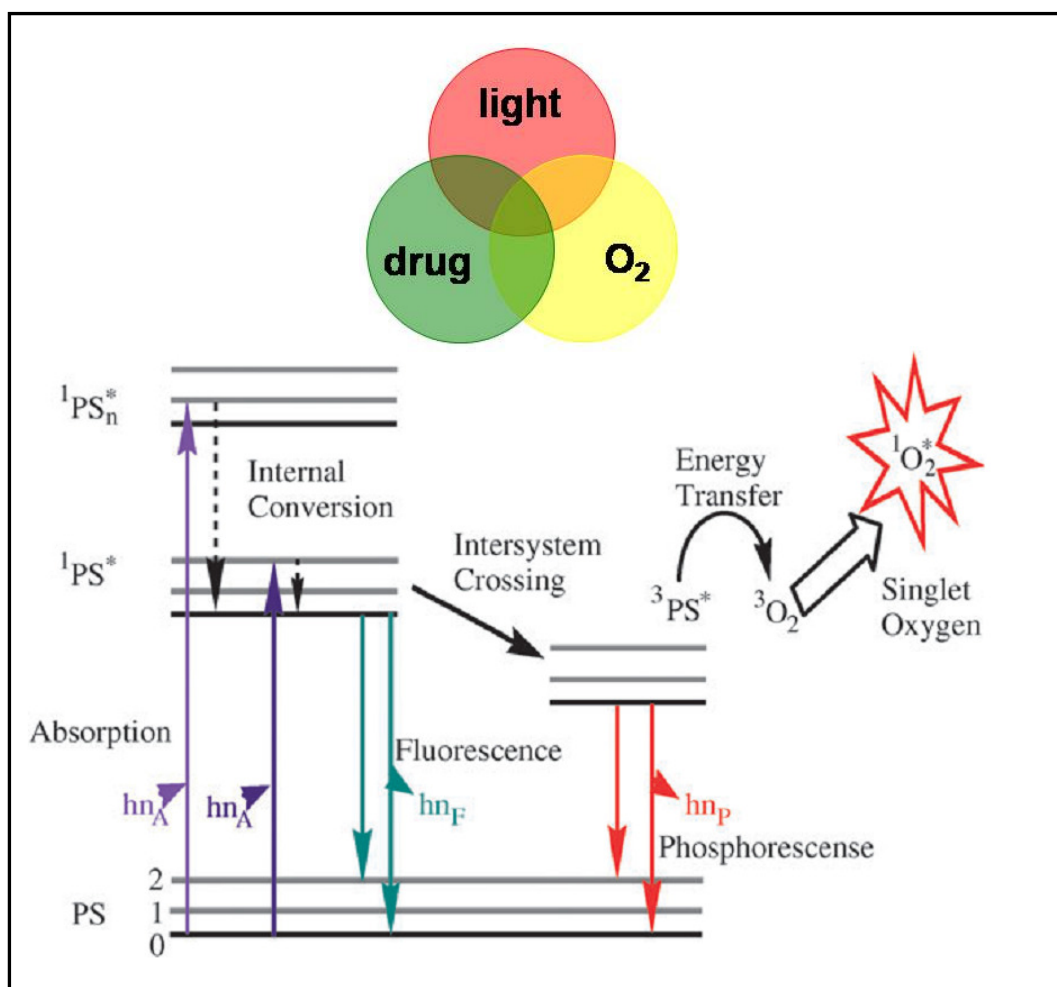


Figure 4.1. Modified Jablonski diagram for the formation of singlet oxygen [168].

4.2.1. History of Photodynamic therapy

The history of usage of light for the treatment of various diseases is starting from antiquity, where the light energy has been employed as such or coupled with a drug. Even thousand years before people in Egypt, China and India utilized light for different skin diseases such as psoriasis, vitiligo, rickets and even psychosis and known as phototherapy [169-171]. The ancient Greeks employed whole-body sun exposure or heliotherapy in the treatment of disease and the Greek physician Herodotus is known as the father of this treatment. Light was used for treatment of various diseases, including tuberculosis, rickets, scurvy, rheumatism, paralysis, edema and muscle weakness in France [172].

However, the technique of using light as a treatment tool attained phenomenal development and popularity in the medicinal field only in the last few decades. Phototherapy was further developed by the Danish physician, Niels Finsen, who described the successful treatment of smallpox using red light and was rewarded with Nobel Prize in 1903 for his contributions [173].

In 1907, two German scientists, Herman Von Tappeiner and his student Oscar Raab, introduced the concept of cell death by the interaction of light and chemicals. During their investigation on the effects of acridine on malaria causing protozoa, Raab found that the combination of acridine red and light had a lethal effect on infusoria, a species of paramecium [174]. However, the first medical application of the interaction between a compound or a drug and light was demonstrated by von Tappeiner along with Jesionek, in which they used a combination of topical eosin and white light to treat skin tumors and also explained the requirement of oxygen for the treatment. And it was Von Tappeiner, who called the technique for the first time as 'Photodynamic therapy' [175-177].

4.2.2 Sensitizers in PDT

A suitable sensitizer is the primary requirement in PDT, and it should have the following criteria [178-179].

a) Maximum absorption in the 600-800 nm region and minimum in the 400-600 nm: The incident intensity of light irradiance is reduced by absorption by chromophores in tissue (400-600 nm) or by scattering. This efficiency loss can be minimized by using higher wavelength light sources. On the other side, absorption by water molecules increases at wavelengths above 800 nm. Consequently, the window for optimum penetration lies between 600 and 800 nm, i.e. in the region of red light, and in PDT it is known as the therapeutic window.

b) High singlet oxygen quantum yields ($^1\text{O}_2$): Singlet oxygen is the reactive oxygen species that destroys the cancerous tissues in PDT. Hence high efficiency of a sensitizer to generate singlet oxygen is related to the possibility to use that sensitizer as a PDT drug. The efficiency of singlet oxygen generation by the sensitizer *in vivo* depends on various factors such as interaction of the sensitizer with surrounding biopolymers, aggregation of the sensitizer, oxygen depletion and other side reactions. However, the photophysical calculation of quantum yield should not be over estimated.

c) Specific retention in the malignant tissue: The specific retention of a sensitizer in the malignant tissue and effective removal from the malignant and healthy tissue are other important criteria.

d) Photostability, non-toxicity and phototoxicity: A suitable sensitizer should be stable against photodegradation or photobleaching and oxidation by $^1\text{O}_2$ or other reactive oxygen species generated in situ during the therapy. Photobleaching of sensitizers in biological systems is a complex process, decreases the skin sensitization and the specificity of phototreatment. Also, low “dark” toxicity (non-toxic in the absence of

light) is desirable so as to avoid unnecessary strain on the organism prior to irradiation, but the destructive photodynamic effect only in the presence of light, phototoxicity. In addition, high solubility in water, purity and fluorescence properties are other criteria desirable for the therapy. Sensitizers used in PDT can be classified as porphyrinoid sensitizers and non-porphyrin sensitizers. The technique became popular and is used widely in medicinal applications recently, only because of some important porphyrin based photosensitizers. However, there are many non-porphyrin based photosensitizers tested and used for the therapy even from ancient times.

4.2.2.1 Non-porphyrin photosensitizers

The non-porphyrin based photosensitizers such as psoralens, anthracyclines, hypericin and hypocrellin, methylene blue, acridine and Nile blue analogue were used for treatment of various skin diseases and tumors [180]. For example, the oral administration of the psoralen drug leads to its uptake by malignant T-cells in the blood stream. The blood aliquot taken was illuminated with white light and found that the light illumination leads to DNA damage via photoadduct formation and thus to direct cytotoxicity. A member in the anthracyclines family, Doxorubicin has also shown phototoxicity *in vitro* with high selectivity. Sensitizers in Hypericin and Hypocrellin family were found to be inhibitors of protein kinase C (PKC), a key enzyme in the proliferation of tumour cells. Methylene blue (MB) on the other hand was not used much in direct application in PDT but found applications in the clinical diagnosis of a variety of diseases and as a tumour marker in surgery. Also, Nile blue is taken up extremely well by tumour cells, thus making it an excellent tumour marker. However, these compounds suffer from a major drawback due to their inherent dark cytotoxicity [180-181].

Recently, many borondipyrromethane (BODIPY) based sensitizers were reported with promising PDT activity. Nagano and co-workers demonstrated the synthesis of a

diiodo substituted BODIPY molecule with enhanced singlet oxygen quantum yield and PDT application, which is explained by heavy atom effect and subsequently enhanced the intersystem crossing efficiency from singlet to triplet state that controls the singlet oxygen production [182]. A series of azadipyrromethenes were synthesised by O'Shea and co-workers with high molar extinction coefficient in the far-red region and demonstrated their efficacy in light-induced toxicity in a panel of tumor cell line [183, 184].

4.2.2.2 Porphyrin photosensitizers

Majority of sensitizers investigated and approved for medical use were with porphyrinoid structure. Eventhough porphyrins were identified in the mid-19th century, until the early 20th century there was no report for their medicinal application, when hematoporphyrin, a mixture of porphyrin derivative was first isolated by Scherer in 1841 during investigating the nature of blood [185]. Dried blood was heated with con.H₂SO₄ the precipitate was washed free of iron and then treated with alcohol to isolate the porphyrin derivative. But, it was only in 1911, Hausmann performed the first studies of the biological effects of hematoporphyrin, where he investigated the effect of hematoporphyrin and light on paramecium and red blood cells and described skin reactions in mice exposed to light after hematoporphyrin administration [186]. However, the first report of human photosensitization by porphyrins was in 1913 by the German, Friedrich Meyer-Betz. He injected himself with 200 mg of hematoporphyrin and subsequently noticed prolonged pain and swelling in light-exposed areas [187].

In 1955, Schwartz *et al.* revealed the multi component nature of hematoporphyrin, where after partial purification, the pure hematoporphyrin produced localized only very poorly in tumors, whereas the residue left behind had great affinity for tumor tissues. Schwartz continued to purify the non-hematoporphyrin fraction, finally end up with a

single fraction, hematoporphyrin derivative (**HpD**). Interestingly, this substance was found to be approximately twice as phototoxic as crude hematoporphyrin [188]. Later, Lipson along with Baldes demonstrated effective in tumor localization property of **HpD** [189, 190].

The milestone in the history of PDT development was achieved in 1975, when Dougherty and co-workers reported the first successful complete tumor cure with **HpD** activated with red light in the treatment of experimental animal tumors [191]. In the same year, J. F. Kelly demonstrated that human bladder tumor cells transplanted into mice could be destroyed using PDT [192]. After a year Kelly tested the PDT activity of **HpD** in human with bladder cancer [193], followed by other report on human for various carcinoma such as skin and esophageal using **HpD** as the photosensitizer [194-196].

In 1983 Dougherty proposed that the active component of **HpD** was composed of two porphyrin units linked by an ether bond and the compound was given the abbreviated name as dihematoporphyrin ether (**DHE**). Further analysis suggested that the active component of **HpD** comprised of a mixture of porphyrin rings, linked by a number of ether and ester bonds, which is now commercially known as 'Photofrin[®]' (Figure 4.2) and is the first photosensitizer approved for clinical use by different health organizations [197-199]. Followed by Photofrin[®], there were few more drugs approved for clinical use, such as Foscan[®], Protoporphyrin IX, Visudyne[®], Motexafin lutetium, Podoporphin and Padeliporfin etc (Figure 4.2). Among these, Temoporfin (Foscan[®]) was the first sensitizer used in a formal clinical study of PDT for prostate cancer [200, 201]. Endogenous Protoporphyrin IX photosensitization induced by exogenous administration of ALA led to the FDA approval in 2000, which marked another historic event for PDT. Another clinically used porphyrin sensitizer, a benzoporphyrin derivative, Verteporfin, commercially known as Visudyne[®], has been used primarily for ocular PDT and

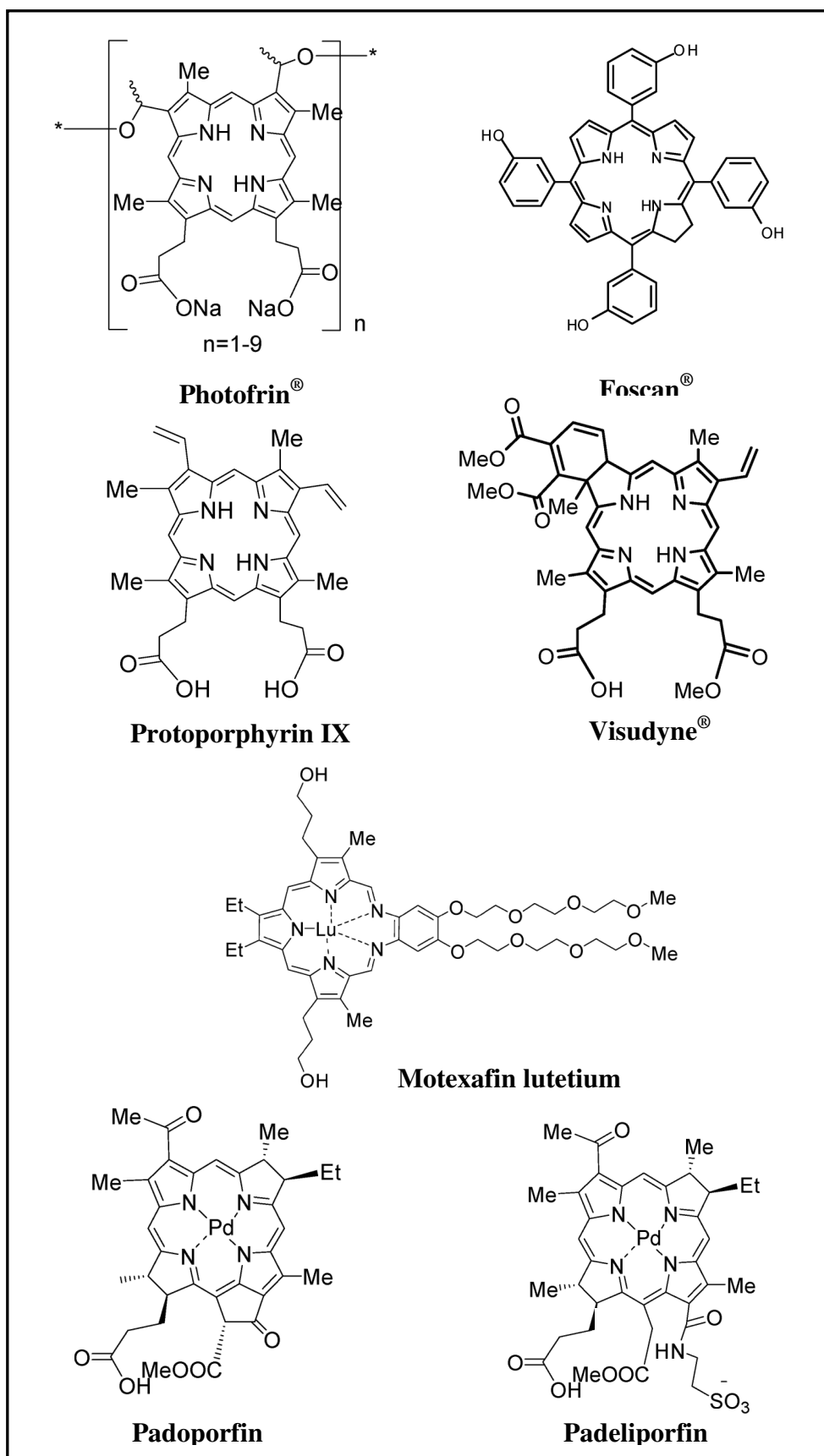


Figure 4.2. Clinically used porphyrin photosensitizers.

approved for age-related macular degeneration (AMD) worldwide [203]. Motexafin lutetium, a texaphyrin derivative, has been used in the post radiotherapy, breast cancer and ophthalmic disease [204-206]. Padoporfin and Padeliporfin are two palladium based photosensitizers, where Padoporfin was lipophilic and Padeliporfin was water soluble. Both the sensitizers were investigated for prostate clinical studies [207, 208]. The historical developments of PDT sensitizers were summarized in Figure 4.3.

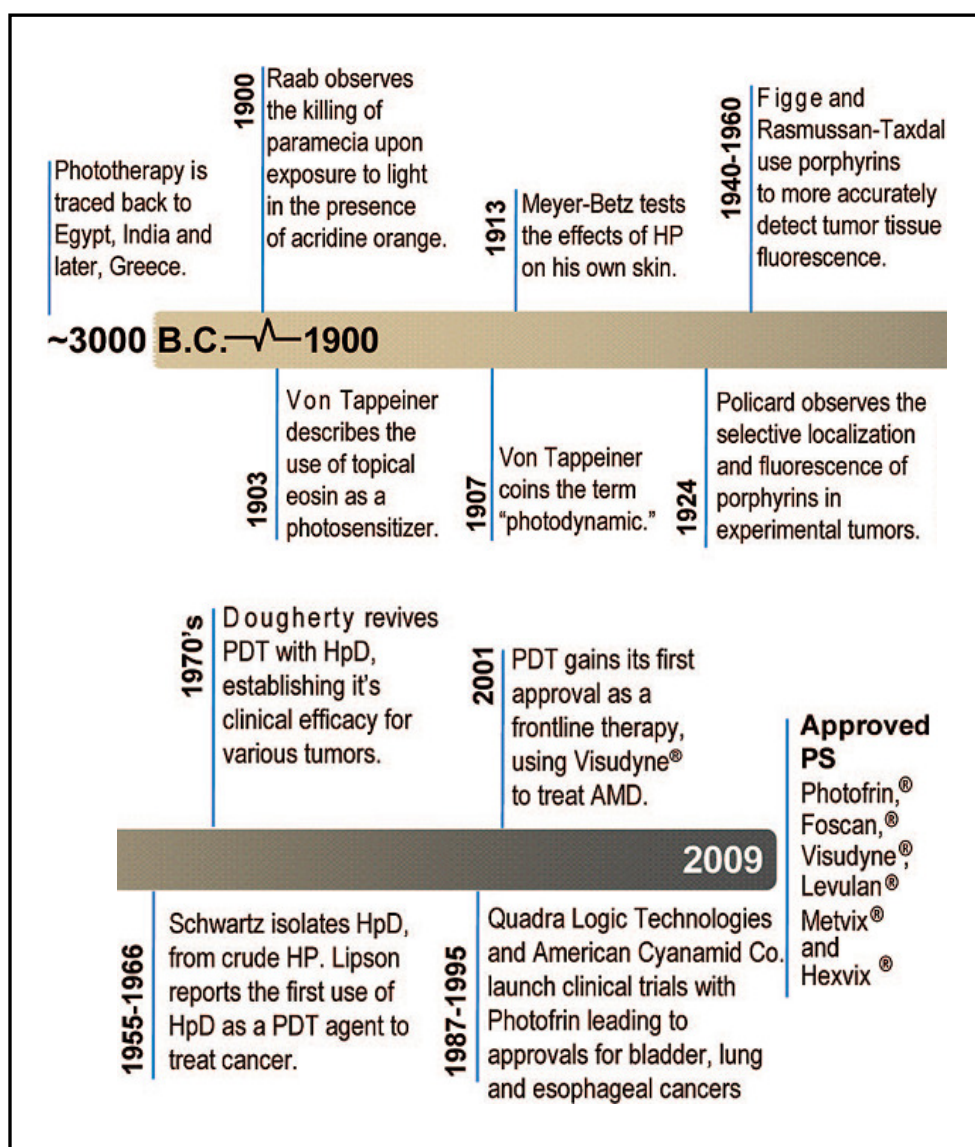


Figure 4.3. Timeline of selected milestones in the historical development of PDT [209].

Curiosity and enthusiasm of researchers all over the world facilitates the introduction of many more photosensitizers including normal, expanded, core-modified, metalloporphyrins, phthalocyanines, chlorin derivatives and porphycene, which shows enhanced singlet oxygen quantum yield and photocytotoxicity [210-214]. The photosensitizers reported were classified as first, second and third generation photosensitizers. The first generation sensitizers were the early stage sensitizers where mixture of porphyrin derivative used as such for therapy, which includes the clinically approved Photofrin[®]. The major drawbacks of these sensitizers were their complex nature, long retention in tissues and low molar extinction coefficient at the therapeutic window, which in fact, encourage the introduction of second generation photosensitizers [215]. The second generation photosensitizers, on the other hand were chemically pure and exhibit high absorbance in the red region of visible light with high singlet oxygen quantum yield, which include majority of porphyrins and phthalocyanines based sensitizers reported recently [210-214]. Still, selectivity towards the malignant tissues remained unsolved, which is tried to rectify in the third generation sensitizers. The third generation sensitizers were combination of a carrier and sensitizer, where the drug was released only at the respective sites [216, 217].

4.2.3 Light sources in PDT

As discussed earlier, light is an important component in PDT and have a critical role in determining the efficiency of the therapy, which in turn related to penetration depth. The penetration depth is the distance that light can travel through body and dependant on power and wavelength of the light used, and optical properties of the tissue including reflection, scattering, transmission and absorption. Light with wavelength shorter than 580 nm is not suitable because of strong absorption by haemoglobin and pigment-rich tissues, such as those of melanoma and typically, the depth of penetration is from 3 to 8

mm for light in the range from 630 to 800 nm. Light dosimetry, which includes two parameters, fluence and fluence rate is an important vector to determine the efficiency of PDT treatment. Fluence is the total energy of exposed light across a sectional area of irradiated spot (energy per unit area of exposed light, J/m^2), whereas fluence rate is the radiant energy incident per second across a sectional area of irradiated spot (power per unit area of light, W/m^2). It has been reported by Wilson *et al.* that an increased fluence rate can reduce the photodynamic effect due to depletion of oxygen [218].

Accurate light dosimetry in internal organs can be achieved only by appropriate light sources. For some time, lasers have been considered as the perfect light sources for PDT, as they could provide monochromatic light corresponding to different absorption maxima of photosensitizers. But, these 'old generation' laser sources were rather complicated to use, to install and were very expensive compared to the new available sources. For the last fifteen years diode lasers coupled with optical fibres emerged as new light source for PDT, which are simple to use, easy to transport, due to their relatively small sizes. Recently, an innovative diode laser with dedicated software has been developed for interstitial PDT, which enables real time, patient specific and optimized interstitial PDT [219]. The weakness of diode lasers' systems is that they can offer only one wavelength and are not tunable.

In recent years, improvements in semiconductor technology have substantially increased the light output of light emitting diode (LED) chips. An aluminium gallium arsenide (AlGaAs) based semiconductor was developed to emit light with peak wavelengths of 680 to 730 nm which are optimal wavelengths for the absorption spectrum of second generation photosensitizers used for cancer PDT. When large surfaces are to be treated, LED light sources are a safer and lower cost source of light. In modern technology, optical delivery system carries the light to the respective organs for

the therapeutic action. Here, optical fibres fitted with specific devices at distal end so as to distribute a defined, controlled and homogeneous subthermal light dose to organs to be treated. The core size of such fibres varies from 200 to 600 microns with overall sizes around 1 to 1.5 mm and is used through the working channel of endoscopes [219]. Also, better distribution of light was assured by using diffusers of same geometry of the organ to be treated (skin, lung, uterus; Figure 4.4).

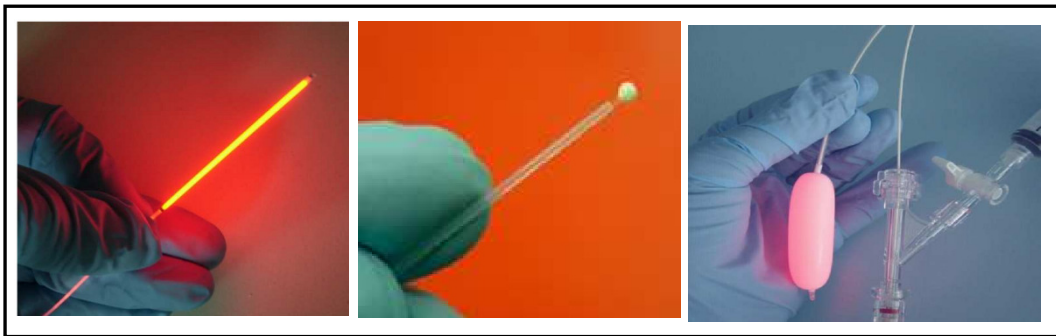


Figure 4.4. Different shape diffusers for PDT.

4.2.4 Role of oxygen in PDT

The crucial step in PDT is generation of molecular singlet oxygen from ground state oxygen, which is in triplet state. The singlet molecular oxygen was discovered in 1924, but attained the interest of many researchers only after 1963 mainly by the research of Khan and Kasha [220]. The growing interest in the formation and deactivation of singlet oxygen revealed the mechanism and amount of energy involved in the whole process of generation and deactivation as shown in Figure 4.5.

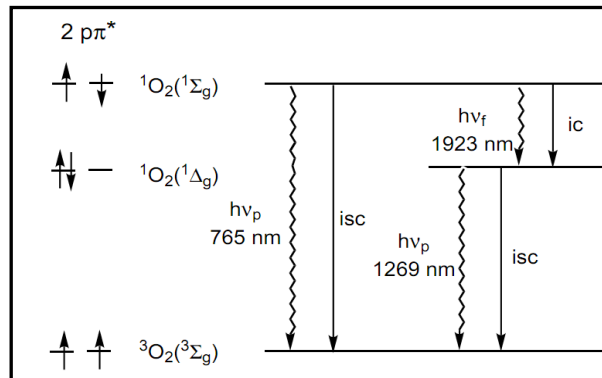


Figure 4.5. Electronic transitions involved in the generation of singlet oxygen in a solution [179].

Molecular oxygen has two low-lying singlet excited states, $^1\Delta_g$ (95 kJ mol⁻¹ or 22.5 kcal mol⁻¹) and $^1\Sigma_g^+$ (158 kJ mol⁻¹ or 31.5 kcal mol⁻¹) above the triplet state (Figure 4.5). For ground-state oxygen, the two highest energy electrons reside separately in the outermost antibonding orbitals with same spin: $(\sigma_{2p})^2(\pi_{2px})^2(\pi_{2py})^2(\pi_{2px}^*)^1(\pi_{2py}^*)^1$, while in the singlet oxygen, the two highest energy electrons reside together in the same antibonding orbital with opposite spin: $(\sigma_{2p})^2(\pi_{2px})^2(\pi_{2py})^2(\pi_{2px}^*)^2$. The first excited state, $O_2(^1\Delta_g)$ is more stable compared to the second excited state $O_2(^1\Sigma_g^+)$ due to spin allowed transition to the first excited state, where the transition from the first singlet to ground excited state is spin forbidden [221].

In fact, generation and quenching of the highly reactive singlet oxygen is the key step in PDT. In photosensitized generation of 1O_2 , the sensitizer excitation is generally achieved *via* a one photon excitation, followed by transition from ground state (S_0) to singlet excited state (S_n). Energy transfer through intersystem crossing makes available a long lived triplet state (T_1) of the sensitizer, which can avail various paths to deactivate including radiative and non-radiative. In non radiative relaxation it can follow two mechanisms, Type I and type II mechanisms. Type I mechanism involves the energy transfer to a substrate molecule by hydrogen-atom abstraction or electron-transfer between the excited sensitizer and a substrate, yielding free radicals. These radicals can react with oxygen to form an active oxygen species such as the superoxide radical anion. Where in Type II mechanism, a triplet-triplet energy transfer from the excited triplet state of the sensitizer to the ground state triplet oxygen to generate singlet [221].

Once, after the generation of 1O_2 it can follow mainly two channels for deactivation, physical and chemical. In physical quenching there will be no conception of oxygen or product formation, but in chemical quenching the 1O_2 react with the quencher to form a new product. The stability of singlet excited state is expressed in terms of lifetime values,

which are 45 min and 7-12 sec in the gas phase and 10^{-6} - 10^{-3} and 10^{-11} - 10^{-9} sec in the solution for the first and second excited states respectively [221-223]. Hence, normally the term singlet oxygen refers to the first excited state of molecular oxygen ($^1\Delta_g$) and can be represented as 1O_2 . However, the lifetime of 1O_2 is considerably shorter in cellular systems, ranging from 100 ns in the lipid regions of membranes to 250 ns in the cytoplasm and hence, the diffusion range of 1O_2 is predicted to be limited to approximately 45 nm in cellular media [224]. On the other hand the diameter of human cells ranges from approximately 10 to 100 μ m, which limit the action of this reactive oxygen species within the cell limit [224].

4.2.5 Apoptosis; mechanism of cell death

Apoptosis is defined as programmed cell death, and is a normal physiological process essential for the control of tissue development and homeostasis. This tightly regulated cell suicide process is controlled by both intracellular and extracellular signals. Apoptosis contributes towards a characteristic sequence of morphological and biochemical changes for the systematic dismantling of the cell and preparation of the residual cell component. Most importantly, no tissue inflammation occurs due to the process as the intracellular leakage limits to the immediate environment [225-227].

In fact, during PDT the cell death is an outcome of induced apoptosis, and mitochondrion, one of the major targets inside the cell for PDT induced cell death. Mitochondrial damage occurs during PDT through inhibition of electron transport components, including succinate dehydrogenase and cytochrome c oxidase, and also disrupted the mitochondrial electrochemical gradient [228]. Apoptotic cells exhibit distinct morphological change, such as shrunken cells with condensed nuclear chromatin, mitochondrial potential difference, cleavage of poly(ADP-ribose) polymerase (PARP), which is a DNA repair protein etc. During physiological cell turnover, apoptosis is

initiated by depletion of a growth factor or by the interaction of cytokines or other ligands with cell surface receptors [227].

4.3 Objective of the work

The increased popularity of PDT in recent years, intensify the urge for developing new photosensitizers. In light of the above discussion, there are a few necessary requirements for such sensitizers for practical application, which include solubility in polar solvents and high molar extinction coefficient in the red region. On the other hand, the porphyrin isomer, **NCP** is known for their highly red-shifted absorption compared to the normal porphyrin derivative. Here, this chapter introduces two novel **NCP** derivatives as PDT sensitizer, hydroxyl and sulfonated derivatives of **NCP**. The compounds were highly soluble in polar solvents, especially sulfonated derivative, which is even water soluble. Various photophysical analyses such as UV-Vis absorption spectroscopy, triplet absorption spectra, energy transfer calculations, lifetime calculation and singlet oxygen generation quantum yield calculation reveals the potential candidacy of these derivatives as PDT drug. *In vitro* analyses of the sulfonated derivative was promising with competitive IC₅₀ values.

4.4 Result and discussion

4.4.1 NCPH as a PDT sensitizer

Synthesis and characterization of *meso*-tetrakis(3,5-dihydroxyphenyl)N-Confused Porphyrin (**NCPH**) is described in the previous chapter. Red-shifted absorption spectrum of **NCPH**, compared to the normal porphyrin derivative was encouraging enough to investigate the PDT application of the molecule. Molar extinction coefficient of **NCPH** at 443 nm and 730 nm was $9.07 \times 10^4 \text{ M}^{-1} \text{ cm}^{-1}$ and $5636 \text{ M}^{-1} \text{ cm}^{-1}$ respectively. As we discussed, a stable triplet state of the sensitizer is one of the preliminary criterion that a

sensitizer should have for being PDT active. Triplet state lifetime and triplet energy transfer efficiency are two parameters that really contribute towards the energy transfer to the ground state oxygen to generate singlet oxygen. Transient state properties of **NCPH** were calculated by using a nanosecond laser flash photolysis with 355 nm laser pulse. The efficiency of energy transfer was calculated with respect to the energy transfer efficiency of tris(bipyridyl)ruthenium(II) complex $[\text{Ru}(\text{bpy})_3^{2+}]$ to β -carotene, whose efficiency is considered as hundred percent [229, 230]. For transient absorption studies a 6 μM solution of **NCPH** in MeOH has taken and degassed with argon. A 355 nm laser pulse was used for excitation, where the excited state was probed by a xenon lamp. The triplet decay profile and absorption spectrum is given in Figure 4.6. Lifetime of **NCPH** was calculated as 1.44 μs with rate of decay is $0.69 \mu\text{s}^{-1}$. Triplet absorption of **NCPH** gives maxima at 500 nm with bleach at 450 nm, where ground state absorption of the molecule predominates. Existence of triplet state was confirmed by the quenching of triplet absorption in the presence of dissolved oxygen.

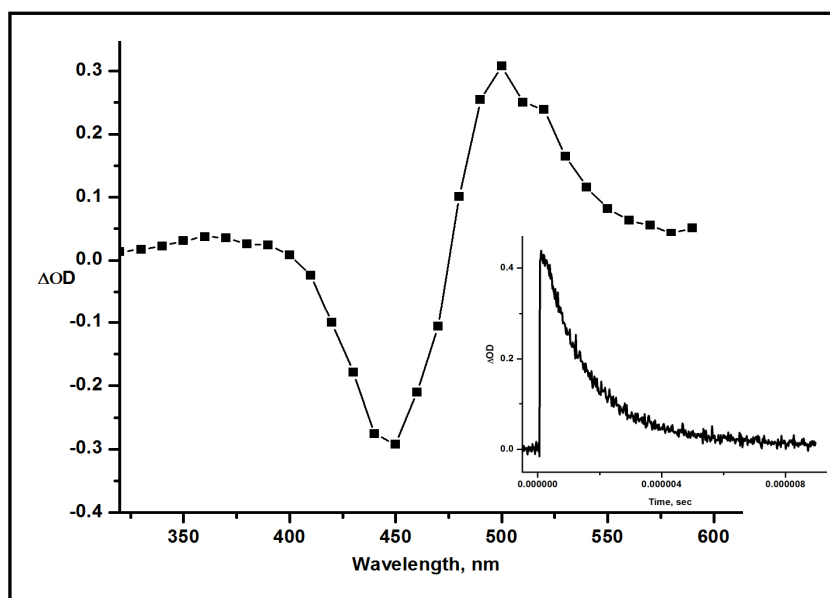


Figure 4.6. Triplet absorption of **NCPH** in methanol. Inset shows the transient decay at 500 nm.

Optically matched solutions of **NCPH** and $\text{Ru}(\text{bpy})_3^{2+}$ were taken at the irradiation wavelength (355 nm) with equal volume of known concentration of β -carotene, where the end concentration of β -carotene was 7.48×10^{-5} M. Here, the assumption was that the transient absorbance (ΔA) of the β -carotene triplet was monitored at 520 nm for both reference and the compound, which was formed by the energy transfer from $\text{Ru}(\text{bpy})_3^{2+}$ and **NCPH** triplet respectively. The quenching of the sensitizer's triplet absorption indicates the complete energy transfer to the β -carotene system. Comparison of plateau absorbance following the completion of sensitized triplet formation, properly corrected for the decay of the donor triplets in competition with energy transfer to β -carotene, enabled to estimate the triplet quantum yield (Φ_T) of **NCPH** based on the following equation.

$$\Phi_T^{\text{comp}} = \Phi_T^{\text{Ref}} \frac{\Delta A^{\text{comp}}}{\Delta A^{\text{Ref}}} \frac{K_{\text{Obs}}^{\text{comp}}}{K_{\text{Obs}}^{\text{comp}} - K_0^{\text{comp}}} \frac{K_{\text{Obs}}^{\text{Ref}} - K_0^{\text{Ref}}}{K_{\text{Obs}}^{\text{Ref}}} \longrightarrow \text{(i)}$$

Here, superscripts 'comp' and 'Ref' can be substituted by the corresponding value of **NCPH** and $\text{Ru}(\text{bpy})_3^{2+}$ respectively. K_{obs} is the pseudo-first-order rate constant for the growth of the β -carotene triplet at 520 nm and K_0 is the rate constant for the decay of the donor triplets at their respective triplet maximum for both the compound and reference, in the absence of β -carotene. ΔA represents the plateau absorbance and the quantum yield of the reference was taken as unity in methanol. The triplet quantum yield obtained for **NCPH** in methanol was 0.69 ± 0.05 .

Presence of stable triplet state and triplet energy transfer efficiency encouraged to calculate the singlet oxygen generation ability of the molecule, which is quantified in terms of singlet oxygen quantum yield, $\Phi(^1\text{O}_2)$. An indirect method was adopted to calculate the $\Phi(^1\text{O}_2)$, where a singlet oxygen scavenger, 1,3-diphenylisobenzofuran (**DPBF**) was used along with the compound, whose initial absorption was noted [231].

The generation of singlet oxygen will cause a decrease in the absorption spectrum of quencher which was followed by an absorption spectrometer. $\Phi(^1\text{O}_2)$ of **NCPH** in MeOH was determined by monitoring the photooxidation of **DPBF** during the formation of singlet oxygen using the absorption spectrometer. Concentration of the photosensitizer was adjusted with an optical density of 0.02-0.03 at the irradiation wavelength (600 nm) to minimise the possibility of singlet oxygen quenching at higher concentration. The solution containing the sensitizer and the scavenger was saturated with oxygen before irradiation. The photooxidation of **DPBF** was monitored at 411 nm, where the quencher exhibit maximum absorption, with an interval of 10 sec up to one and half minutes. No thermal recovery of **DPBF** (from a possible decomposition of endoperoxide product) was observed under the conditions of these experiments. In order to calculate the quantum yield, a reference compound with known quantum yield was also investigated with the same procedure. Here, in this investigation *meso*-tetrakis(*p*-sulfonatophenyl)porphyrin tetrasodium salt (**TPPS**) was used as the reference. The following equation was used to calculate the singlet oxygen quantum yield of the sensitizer with respect to the reference.

$$\Phi(^1\text{O}_2)^{\text{comp}} = \Phi(^1\text{O}_2)^{\text{Ref}} \frac{m^{\text{comp}}}{m^{\text{Ref}}} \frac{F^{\text{Ref}}}{F^{\text{comp}}} \longrightarrow \text{(ii)}$$

Where, $\Phi(^1\text{O}_2)$ is the quantum yield of singlet oxygen, superscripts ‘comp’ and ‘Ref’ represents **NCPH** and **TPPS** respectively, m is the slope of a plot of difference in change in absorbance of **DPBF** (at 411 nm) with the irradiation time and F is the absorption correction factor, which is given by $F = 1 - 10^{-\text{OD}}$ (OD at the irradiation wavelength). Change observed for the absorption spectra of **DPBF** in a MeOH solution of **NCPH** when irradiated with xenon lamp source with a long pass filter ($\lambda_{\text{irr}} > 600$ nm) in different time interval was shown in Figure 4.7. A reference solution of **TPPS** in MeOH with similar optical density at the irradiating wavelength (600 nm) also irradiated in similar

conditions. The singlet oxygen quantum yield obtained for **NCPH** in MeOH solution was 0.63 ± 0.05 and the yield obtained was comparable with other sensitizers reported in the literature.

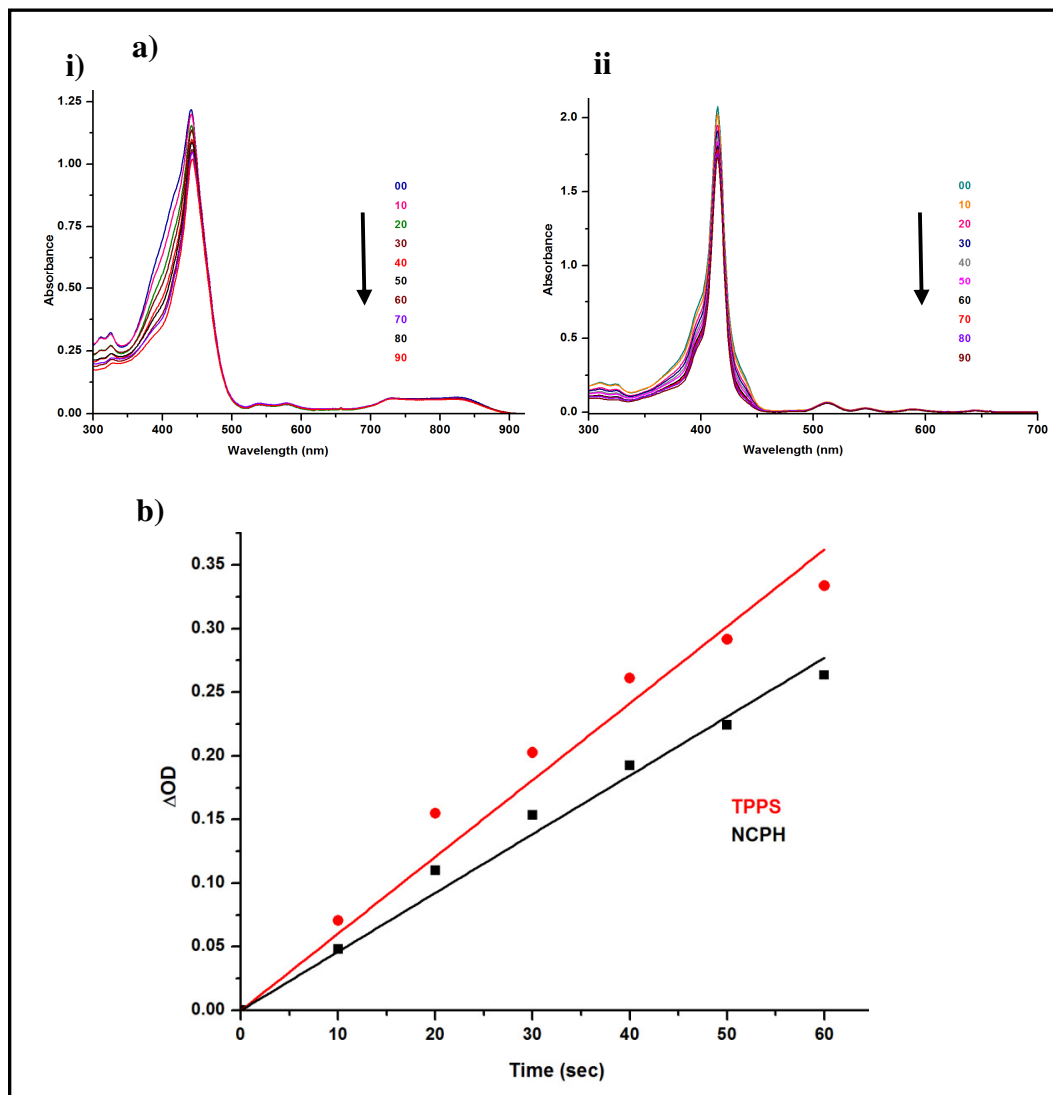


Figure 4.7.(a) Change in the absorption spectra of **DPBF** upon irradiation with (i) **NCPH** (ii) **TPPS** in MeOH and (b) Plot of change in absorbance of **DPBF** at 411 nm vs irradiation time ($\lambda_{irr} > 600$ nm) in the presence of **NCPH** against **TPPS** as the standard in MeOH.

Aggregations of photosensitizer normally decrease the efficacy of singlet oxygen generation [232, 233]. Singlet oxygen generation quantum yield of **NCPH** was

investigated in ACN/MeOH (9:1) mixture to analyze the aggregation effects (Figure 4.8). Interestingly, there was no decrease in the singlet oxygen quantum yield, more over observed slight enhancement in the quantum yield (0.67 ± 0.03) possibly due to the tautomeric change.

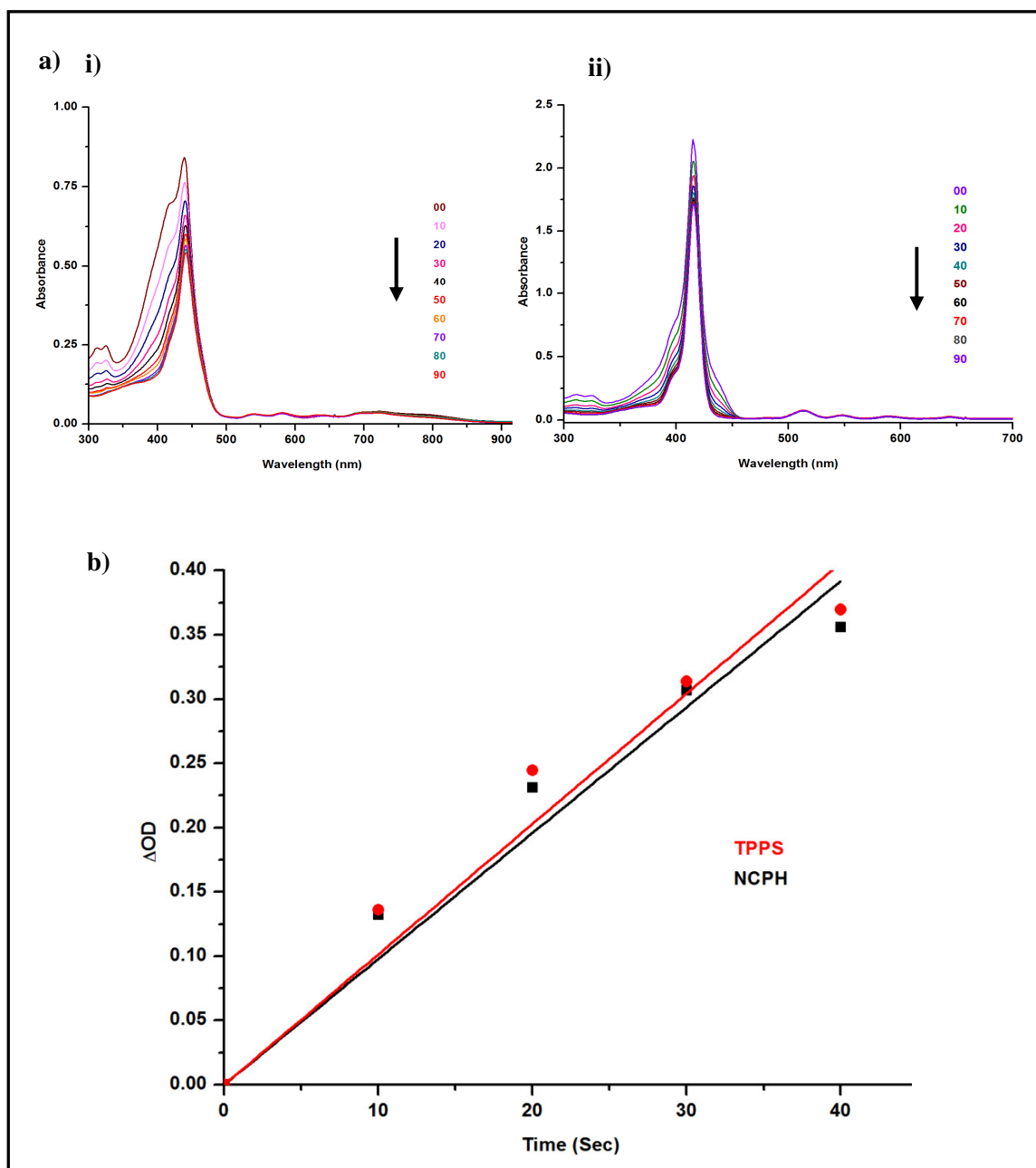
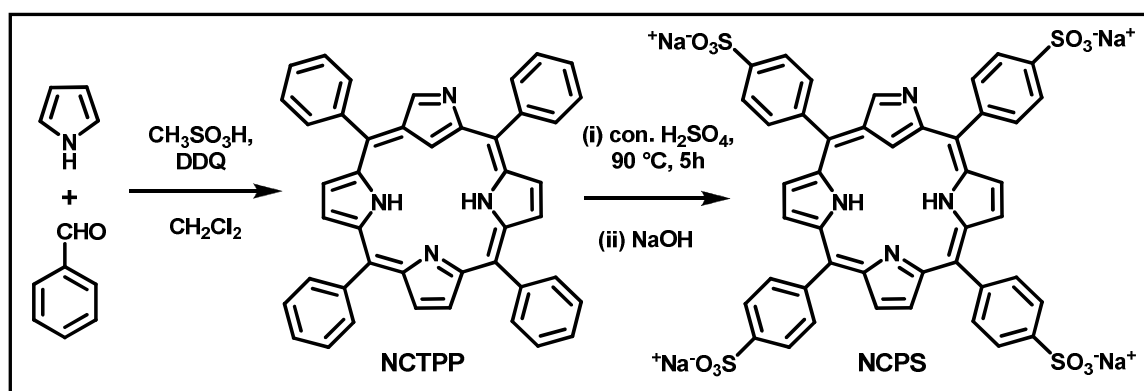


Figure 4.8. (a) Change in the absorption spectra of **DPBF** upon irradiation with (i) **NCPH** (ii) **TPPS** in MeOH/ACN and (b) Plot of change in absorbance of **DPBF** at 411 nm vs irradiation time ($\lambda_{irr} > 600$ nm) in the presence of **NCPH** against **TPPS** as the standard in MeOH/ACN.

4.4.2 NCPS as a PDT sensitizer

4.4.2.1 Photophysical investigations of NCPS for PDT application

Eventhough **NCPH** was showing promising singlet oxygen quantum yield, the compound was lacking water solubility. Search for new sensitizer with high water solubility and better absorption in the red region ended up in designing a tetrasulfonated N-confused porphyrin derivative, *meso*-tetrakis(*p*-sulfonatophenyl)N-confused porphyrin tetrasodium salt (**NCPS**). The synthesis of **NCPS** was achieved by following synthetic route as given in Scheme 4.1.



Scheme 4.1. Synthetic route for NCPS.

The synthesis of *meso*-tetrakis(*p*-sulfonatophenyl)N-confused porphyrin tetrasodium salt (**NCPS**) involves a two step process, starting from tetraphenyl N-confused porphyrin (**NCTPP**), which was prepared by using Lindsey's method [64]. To synthesize **NCPS**, we adopted the known method of sulfonation for normal porphyrin [234], where the tetraphenyl derivative was dissolved in $\text{con. H}_2\text{SO}_4$ and heated for 5 h at $90\text{ }^\circ\text{C}$, then stirred overnight at room temperature. After neutralizing the excess acid with sodium hydroxide solution, the reaction mixture was washed many times with MeOH to extract the compound and filtered to remove the sodium sulphate salt formed during neutralization. The MeOH solution was evaporated and the solid obtained was extracted

through a soxhlet apparatus using MeOH to derive **NCPS** in 56% yield from the corresponding tetraphenyl derivative [235].

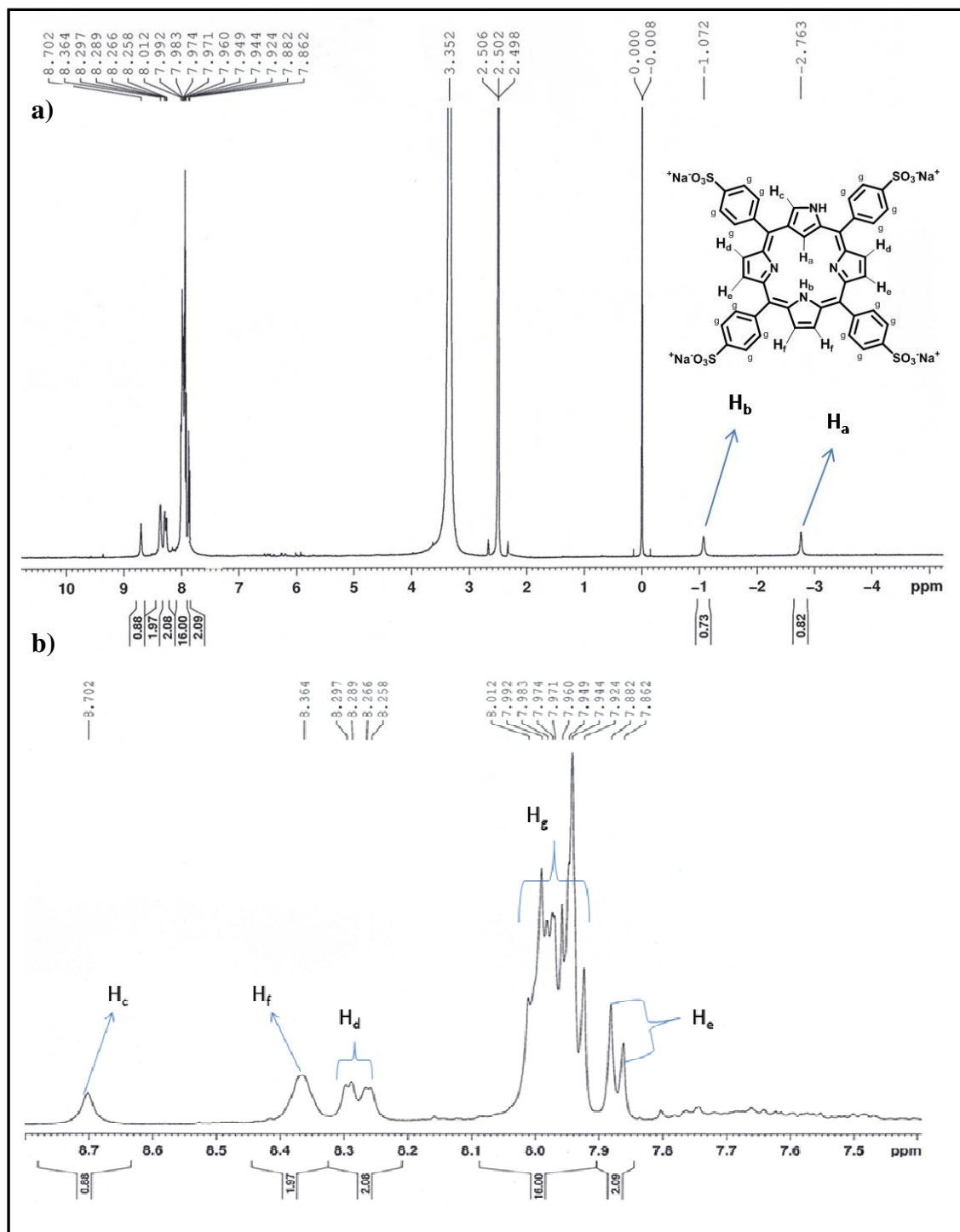


Figure 4.9. (a) ^1H NMR spectrum of **NCPS** in $\text{DMSO-}d_6$, (b) Expanded ^1H NMR spectrum of **NCPS** in the aromatic region.

The compound was highly soluble in water and characterized by using ^1H NMR, ^{13}C NMR, MALDI-TOF and IR analysis. Presence of two sharp peaks at the negative region of ^1H NMR (Figure 4.9) assigned to the inner CH and NH protons of **NCPS**, which has been confirmed with deuterium exchange studies with D_2O . Peak resonating at $\delta = -1.07$ was assigned to the inner NH proton and $\delta = -2.76$ was from the inner CH proton, where the outer NH resonates at the extreme downfield shifted region of ^1H NMR spectra.

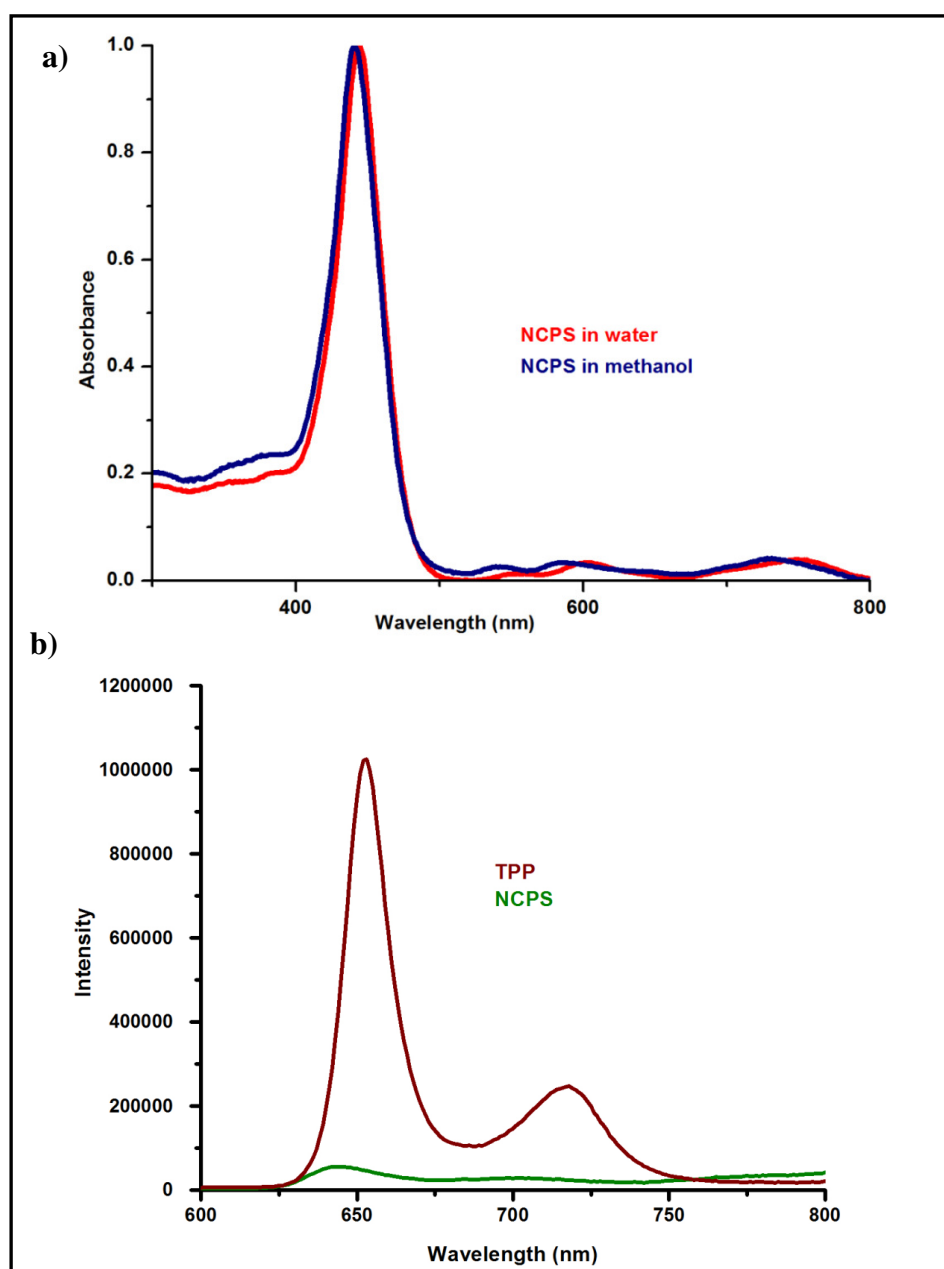


Figure 4.10. (a) Absorption spectra of **NCPS** in water and MeOH, (b) Emission spectra of **NCPS** with respect to **TPP**.

Absorption spectra of **NCPS** (Figure 4.10.a) was recorded both in deionized water and MeOH, and showed the Soret band at 444 nm and 440 nm respectively, with Q-bands ranging from 550-800 nm. The better absorption of **NCPS** compared to the counter part of normal porphyrin after 700 nm ($1400 \text{ M}^{-1}\text{cm}^{-1}$ at 747 nm in water for **NCPS**, where the absorbance of normal sulfonated derivative ends at 630 nm) enhances the utility of the sensitizer as a photodynamic therapeutic drug. On the other hand, the fluorescence quantum yield calculated (Figure 4.10.b) for **NCPS** with respect to tetraphenylporphyrin was too low and the yield obtained in MeOH is 0.0032, which is comparable with the similar N-confused systems [235, 236]].

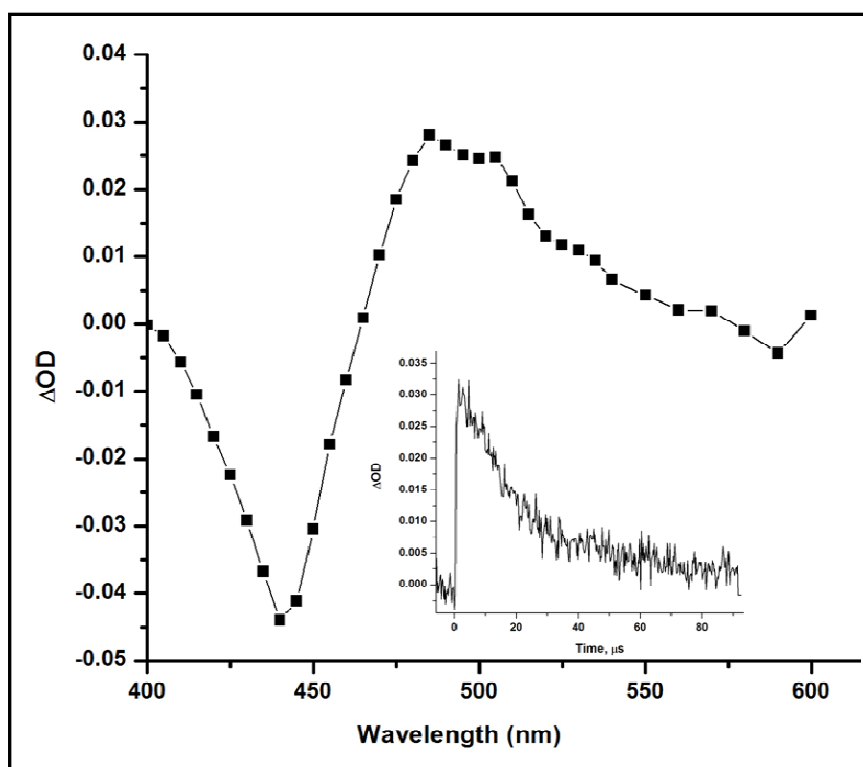


Figure 4.11. Triplet absorption of **NCPS** in deionized water recorded at 7.2 μs. Inset shows the transient decay at 490 nm.

As discussed in the case of **NCPH**, triplet-triplet energy transfer is the key step to generate singlet oxygen, which is the cytotoxic agent in photodynamic therapy. Figure 4.11 shows the triplet absorption of **NCPS** in deionized water with the decay profile at

490 nm inset, also the formation of triplet state was confirmed by the absorption quenching in the presence of dissolved oxygen. Transient absorption of the compound shows maxima at 490 nm in deionized water with bleach at 440 nm range where the compound has significant ground state absorption. Triplet absorption profile of the compound in MeOH was similar to that of in water. Triplet lifetime of the compound was measured both in deionized water and MeOH and found to be 16 and 1.2 μsec respectively. Since, low water solubility and triplet lifetime remain as the main barriers for many sensitizers on their real application, comparatively better triplet lifetime of the sensitizer in water was promising [235].

The efficiency of triplet-triplet energy transfer was quantified by calculating triplet quantum yield, using energy transfer method to β -carotene with tris(bipyridyl)ruthenium (II) complex, $\text{Ru}(\text{bpy})_3^{+2}$. However, the insolubility of β -carotene in water prevents to determine the triplet quantum yield of the sensitizer in water, but the respective value in methanol was obtained as 0.70 ± 0.05 [235].

The singlet oxygen quantum yield of **NCPS** both in MeOH and water was quantified by indirect method using **DPBF**. Irradiation of the sensitizer was done with a xenon lamp with a 600 nm long pass filter at different time intervals from 10-90 s. The decrease in the absorption of **DPBF** was monitored at 411 nm as shown in Figure 4.12, which is due to the dye sensitized generation of singlet oxygen followed by photooxidation of **DPBF**. Absorbance at the irradiating wavelength was adjusted to 0.02 for both the sensitizer and the reference. From the slope of the graph obtained by plotting change in optical density against the time interval (Figure 4.12) the singlet oxygen quantum yield was calculated as 0.70 ± 0.03 in MeOH and 0.55 ± 0.05 in water [235].

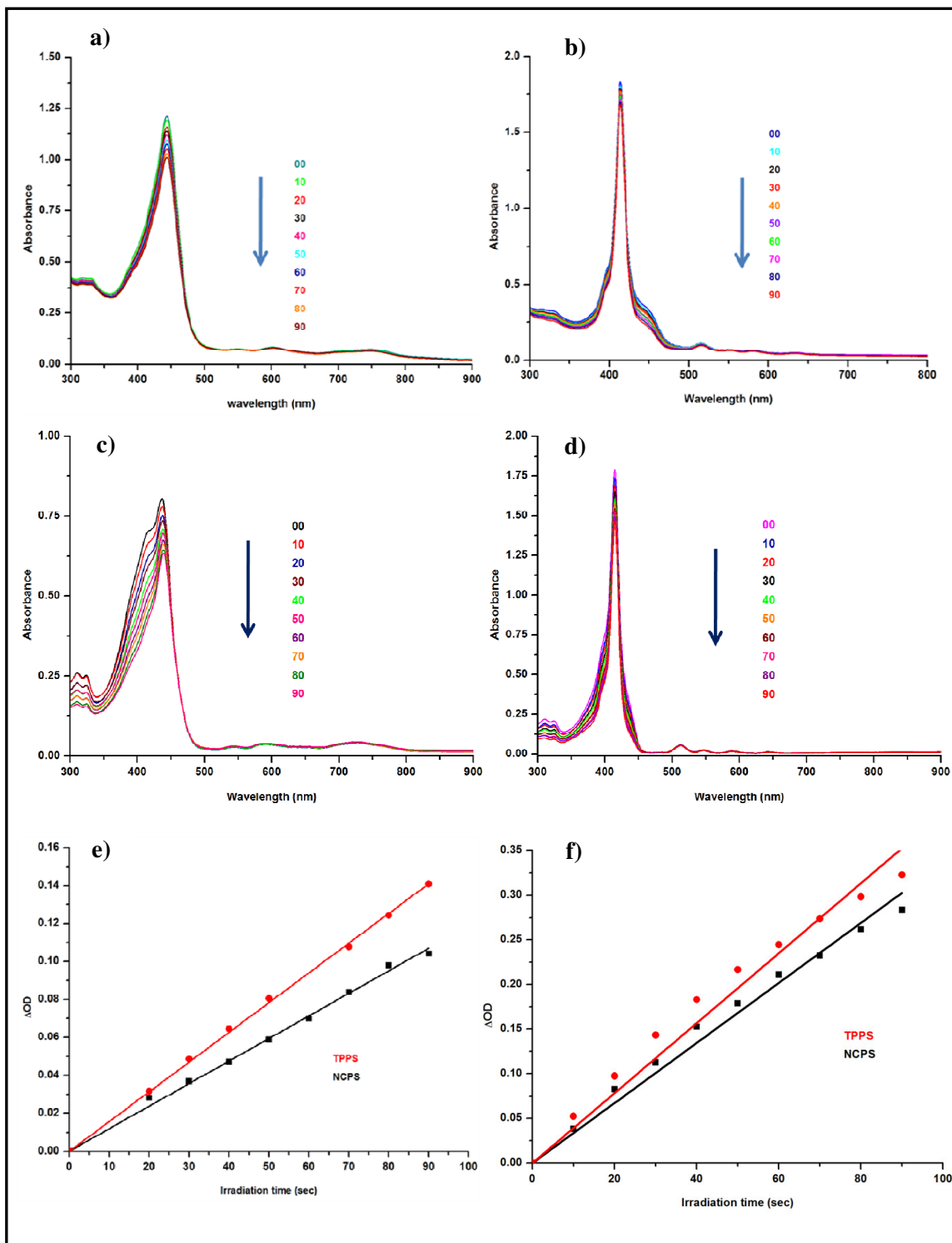


Figure 4.12. Change in the absorption spectra of **DPBF** upon irradiation with (a) **NCPS**, (b) **TPPS** in water (c) with **NCPS** (d) **TPPS** in MeOH. Plot of change in absorbance of **DPBF** at 411 nm vs irradiation time ($\lambda_{irr} > 600$ nm) in the presence of **NCPS** against **TPPS** as the standard in (e) water and (f) MeOH.

4.4.3 *In Vitro* Studies

4.4.3.1 Cytotoxicity Studies of NCPS in Different Cell Lines.

Photocytotoxicity of sulfonated derivatives of different porphyrin and phthalocyanines derivatives have been studied extensively during the past years. These sulfonated derivatives were known for their excellent membrane permeability and lysosomal accumulation in cells with high selectivity towards carcinomas [237]. The *in vitro* photodynamic activity of **NCPS** was evaluated against eight different cell lines, namely, human colon cancer cells (HCT-116), human breast cancer cells (MCF7-ER, PR positive and MDA-MB-231-ER, PR negative), human pancreatic cancer cells (MIA-PaCa-2), human cervical cancer cells (HeLa & SiHa) and human oral cancer cells (SCC-172 and SCC-131). The cytotoxicity of **NCPS** in these cell lines were investigated both in the presence and absence of light using MTT assay as shown in Figure 4.13. For the analysis a stock solution of **NCPS** was prepared in DMSO and diluted to appropriate concentrations with the culture medium. The cells, after being rinsed with phosphate buffered saline (PBS), were incubated with different concentration of **NCPS** in Dulbecco's Modified Eagle Medium (DMEM) solutions for 1 h at 37 °C before being illuminated at an ambient temperature. Growth inhibition was determined by means of the colourimetric assay called MTT [3-(4,5-Dimethylthiazol-2-yl)-2,5-diphenyltetrazolium bromide] assay. Approximately 5×10^3 cells were seeded in two 96 well cluster plate and allowed to reach the exponential phase of growth and then **NCPS** was added and analysed for cytotoxicity. Cytotoxic studies revealed that **NCPS** is essentially noncytotoxic in the absence of light but interestingly on the other hand exhibits high photocytotoxicity. The comparative study of IC_{50} values for **NCPS** on the above cell lines showed that the IC_{50} value of MDA-MB-231 cells (6 μ M,) are about five

fold lower than those for the HeLa cells (25 μM). Oral and cervical cancer showed an increase in IC_{50} values than the breast,

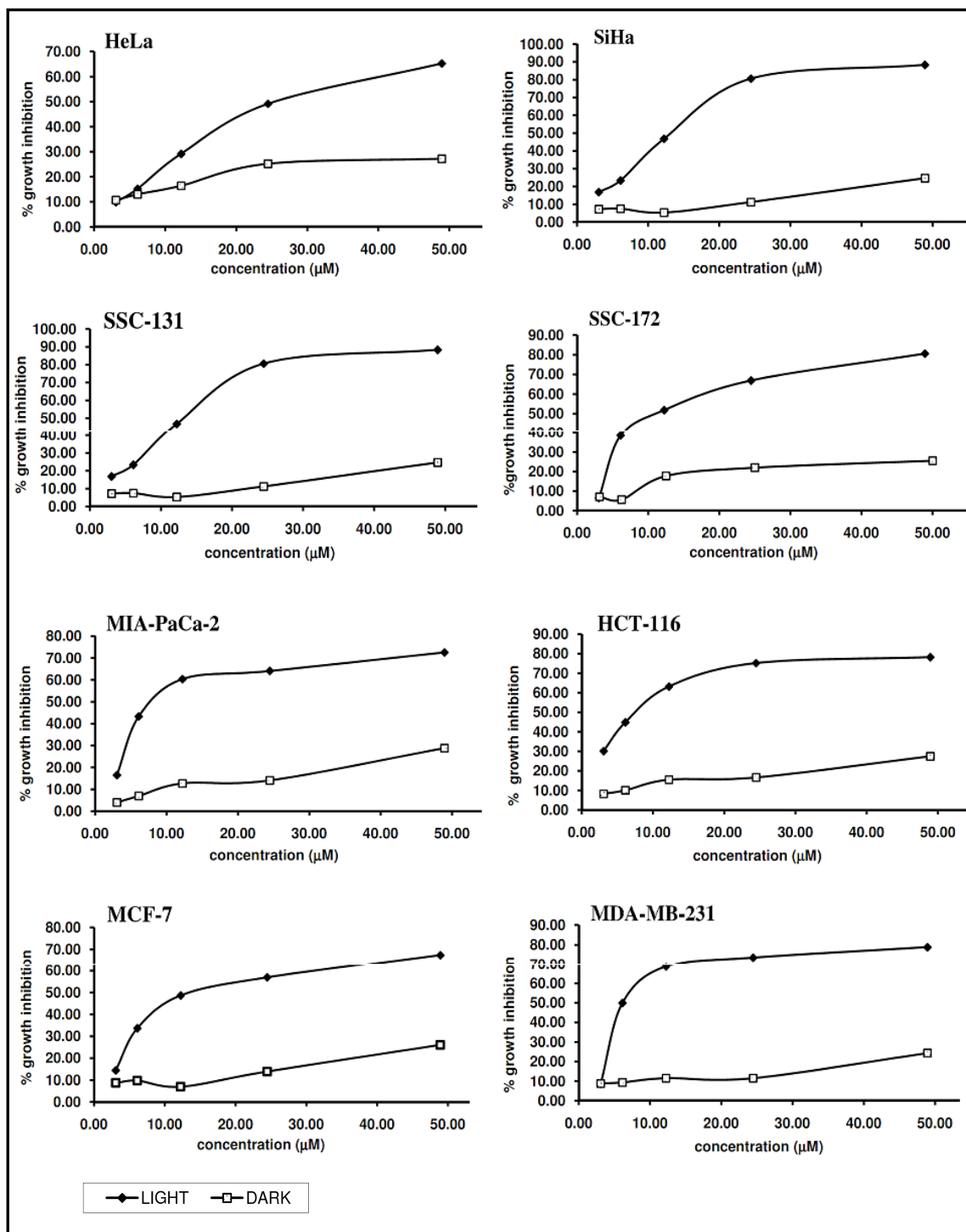


Figure 4.13. MTT assay was done on a panel of cancer cells and shows cytotoxicity of NCPS in the presence and absence of light. NCPS shows significant cytotoxicity in the presence of light in all cells but shows negligible cytotoxicity in the absence of light.

pancreatic and colon cancer cells (Table 4.1). Our observations suggest that **NCPS** exhibits more photocytotoxicity towards adenocarcinomas over the other epithelial cancer cell lines studied [235].

Table 4.1. Comparison of IC₅₀ Values of **NCPS** in a panel of cancer cells.

Cell Line	IC ₅₀ in μM
HeLa	25
SiHa	20
SCC-131	13
SCC-172	11
MIA-PaCa-2	8
HCT-116	8
MCF-7	12
MDA-MB-231	6

4.4.3.2 NCPS Sensitized ROS Generation.

Generation of singlet oxygen (Reactive oxygen species-ROS), during light irradiation has a central role in photodynamic cytotoxicity. The formation of cellular ROS after PDT with **NCPS** was determined using CM-H₂DCFDA, which is a fluorescein derivative and ROS detector. The probe emits a green fluorescence after the oxidation reaction with reactive oxygen species and the diacetate groups are removed by cellular esterase [238]. **NCPS** induced accumulation of ROS in the cells, resulting in a substantial increase in the number of fluorescent cells as detected by flow cytometry and fluorescent imaging. MDA-MB-231 cells showed the least IC₅₀ value (6 μM), hence selected as model system for further investigations. Flow cytometry analysis (Figure 4.14) shows the efficacy of **NCPS** on generating ROS during PDT and the concentration dependent increase in cellular ROS content after PDT with **NCPS**. High fluorescence intensity could observe in higher concentration of **NCPS** (12 μM) by flow cytometry and fluorescence microscopy

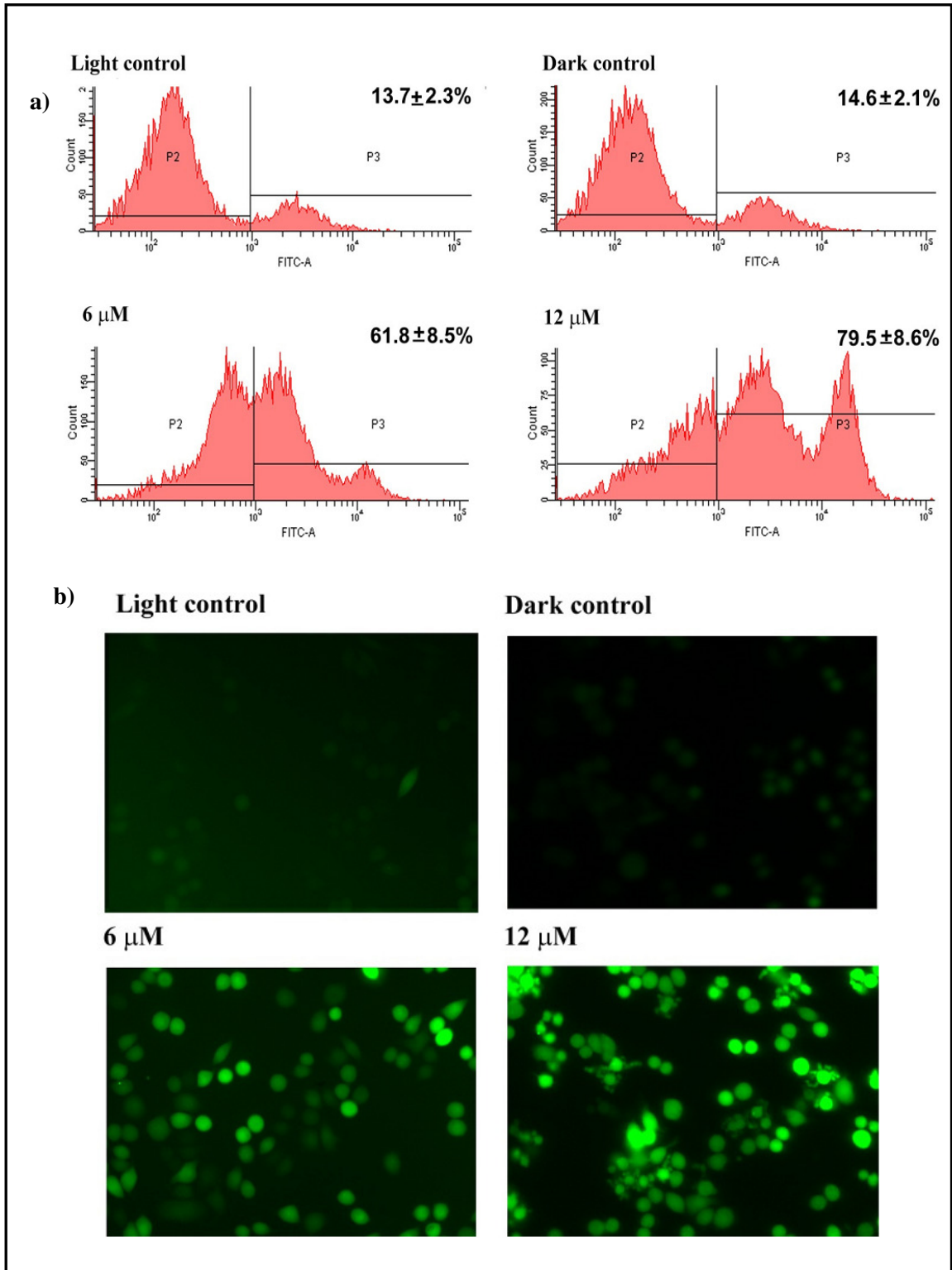


Figure 4.14. (a) Flow Cytometry analysis, (b) Fluorescence images of MDA-MB-231 cells shows enhanced fluorescence after PDT with 6 μM and 12 μM of NCPS.

analysis as an indicative of ROS generation. In flow cytometry, the population (P2) shows back ground fluorescence which represents cells with low ROS and the population at right hand side (P3) shows cells with enhanced fluorescence indicating cells with high ROS [235].

Cellular damage during photodynamic therapy is mediated through apoptosis. Apoptosis is a normal physiological process essential for the control of tissue development, involution and for tissue homeostasis. The earliest hallmark of apoptosis is the loss of plasma membrane asymmetry. In apoptotic cells, the membrane phospholipid phosphatidylserine is translocated from the inner to outer leaflet of the plasma membrane, thus exposing phosphatidylserine to the external cellular environment. AnnexinV (a cellular protein) tagged with FITC (Fluorescein isothiocyanate) has high affinity for phosphatidylserine and therefore serves as a sensitive probe for identifying apoptotic cells by fluorescence microscopy and flow cytometry [239].

Generally, Annexin V-FITC is used together with propidium iodide (PI), which is another fluorescent probe to distinguish viable cells from dead cells, as the former can penetrate through the intact and viable cells but the latter only with dead cells. The cell death mechanism induced by PDT was studied by using **NCPS** by examining the dual fluorescence of Annexin V-FITC/PI using flow cytometry as shown in Figure 4.15. The cell populations at different phases of cell death, namely, viable (AnnexinV-FITC-/PI-), early apoptotic (Annexin V-FITC+/PI-), and necrotic or late-stage apoptotic (Annexin V-FITC+ / PI+) were examined at different drug doses.

It was observed that most of the cells were negative for Annexin V-FITC and PI after treatment with **NCPS** (12 μ M) in the absence of light. This indicates that **NCPS** is non-cytotoxic toward MDA-MB-231 cells in darkness. However, upon illumination, the percentage of cells at the early apoptotic stage (i.e., externalization of phospholipid

phosphatidylserine but not membrane leakage, Annexin V-FITC + /PI-) increased from $3.5 \pm 0.41\%$ to $83.9 \pm 7.8\%$ when the concentration of **NCPS** increased from 0 to $12 \mu\text{M}$. From these results, it can be concluded that **NCPS** on PDT induces apoptosis extensively [235].

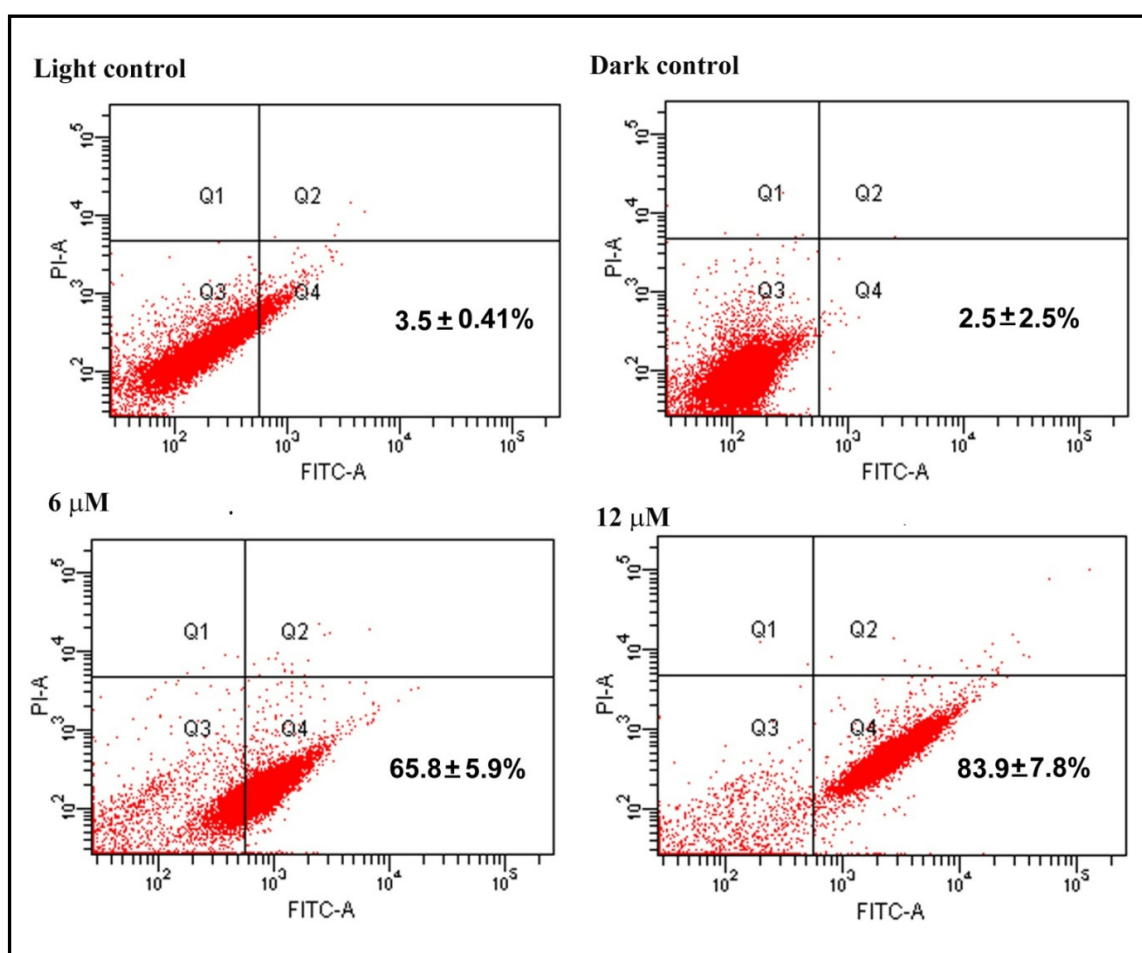


Figure 4.15. Flow cytometric analysis of the cell death mechanism induced by **NCPS** upon PDT treatment.

Chromatin condensation is another sensitive marker of apoptosis along with a decrease in membrane potential across the mitochondrial inner membrane. In the present study, Hoechst stain was employed to observe chromatin condensation and cells were viewed under a fluorescent microscope, and found that PDT with **NCPS** in MDA-MB-231 cells at $6 \mu\text{M}$ resulted in $72 \pm 4.46\%$ chromatin condensation, whereas at $12 \mu\text{M}$ showed $91 \pm 2.6\%$. Whereas in light and dark controls only $10.4 \pm 1.5\%$ and $7.6 \pm 1.2\%$

chromatin condensation was observed (Figure 4.16). This demonstrates that **NCPS** induces apoptosis in a concentration dependent manner [235].

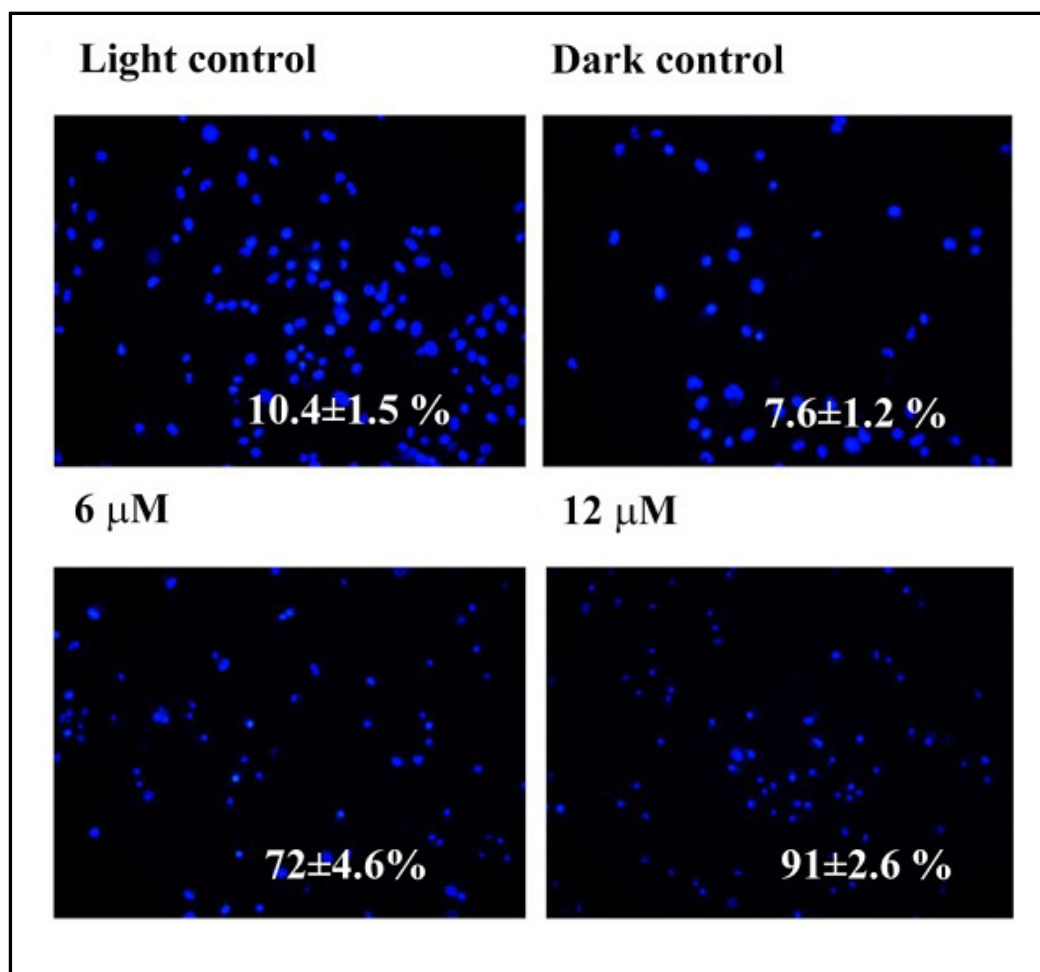


Figure 4.16. Characterization of cytotoxic actions of **NCPS** in PDT using Hoechst stain after PDT with **NCPS** (6 μ M and 12 μ M). In Hoechst staining, chromatin condensation was visualized using fluorescence microscope.

Also, the changes in mitochondrial membrane potential were monitored using the JC-1 cationic fluorescent dye, as shown in Figure 4.17. The accumulation of JC-1 in mitochondria yields both a green and red fluorescence. However, a decrease in the mitochondrial inner membrane potential due to apoptosis causes a decrease in red fluorescence that can be easily monitored by fluorescent microscopy. PDT with **NCPS** in MDA-MB-231 cells at 6 μ M resulted in about 69.9 \pm 5.4% decrease in membrane

potential where as at 12 μ M, $88.5 \pm 4.9\%$ decrease in mitochondrial membrane potential was observed. Whereas in light and dark controls only $12.1 \pm 4.9\%$ and $10.3 \pm 1.3\%$ chromatin condensation was observed, which illustrate mitochondrial mediated cell death pathway through apoptosis during PDT with NCPS [235].

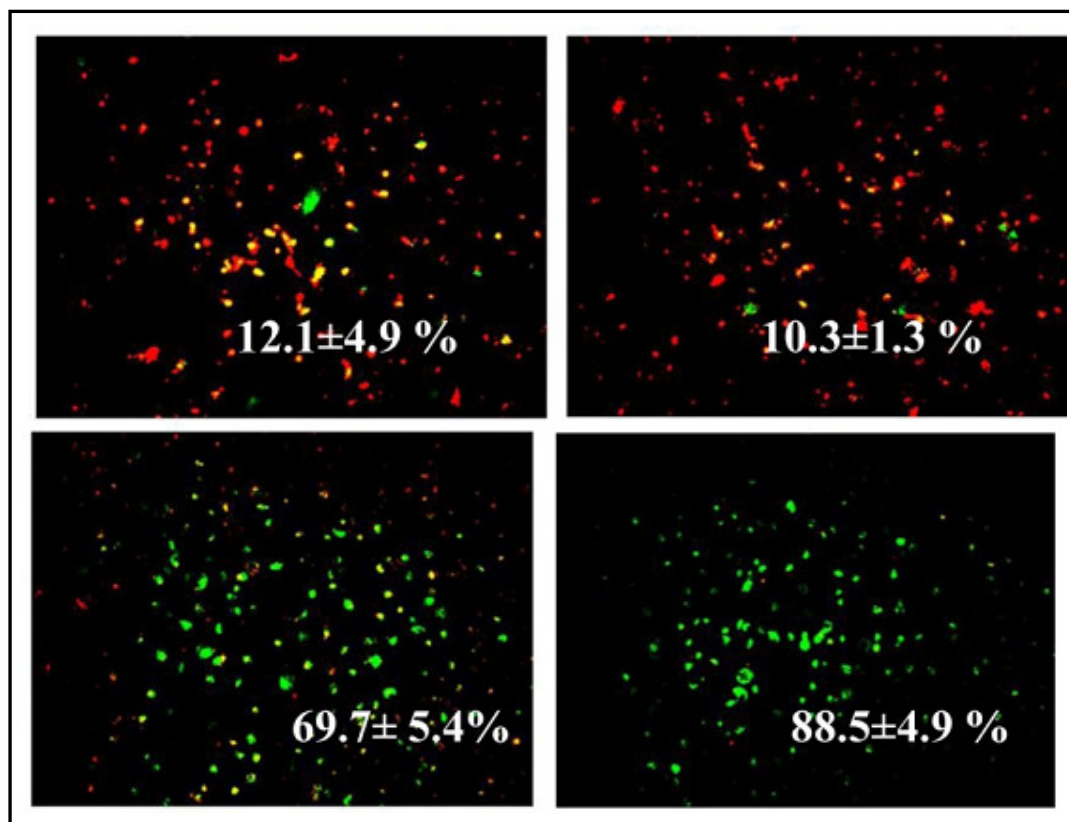


Figure 4.17. Characterization of cytotoxicity of NCPS during PDT using JC1 Fluorescence cytochemistry. In JC1 staining, cells with red colour indicate healthy cells with high mitochondrial membrane potential and green coloured apoptotic cells with low mitochondrial membrane potential.

Another confirmation for the NCPS induced apoptosis was from the cleavage of PARP, a 116 KDa nuclear poly (ADP-ribose) polymerase which is involved in DNA repair reaction to cellular stress. This protein can be cleaved by many ICE-like caspases *in vitro* and is one of the main cleavage targets of caspase-3 *in vivo*. In human PARP, the cleavage occurs between Asp214 and Gly215, which separates the PARP

amino-terminal DNA binding domain (24 kDa) from the carboxy-terminal catalytic domain (89 kDa) [240, 241]. PARP helps cells to maintain their viability; cleavage of PARP facilitates cellular disassembly and serves as a marker of cells undergoing apoptosis. During our experiment, no PARP cleavage was observed after treatment with **NCPS** (12 μM) in the absence of light, which again confirms the non-cytotoxic nature of **NCPS** in the absence of light (Figure 4.18). However, upon illumination, **NCPS** induces PARP cleavage at both the concentrations of 6 and 12 μM , thus confirms that **NCPS** induces cell death via apoptosis [235].

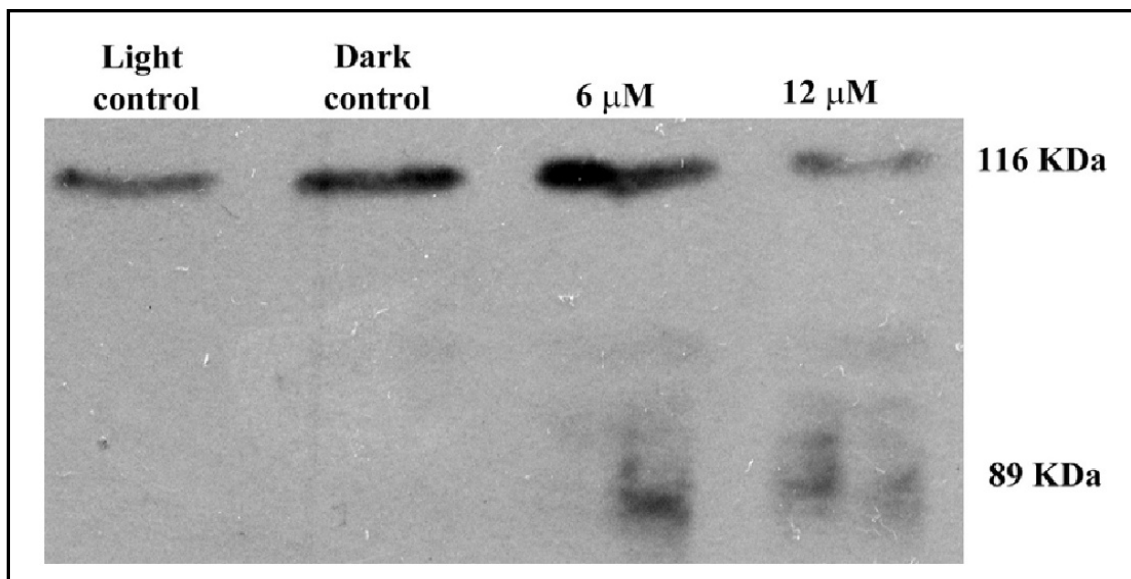


Figure 4.18. PARP cleavage observed after PDT with **NCPS**. Here there is no PARP cleavage observed in both light and dark controls but there is significant cleavage at a concentration of 6 and 12 μM of **NCPS**.

4.4.3.3 Cytotoxicity Studies of **NCPH**

In order to compare the cytotoxicity of **NCPS** and **NCPH**, cytotoxicity of **NCPH** was evaluated with human breast cancer cell (MDA-MB-231-ER, PR negative). The cytotoxicity of **NCPH** in MDA-MB-231 was investigated both in the presence and absence of light using MTT assay as shown in Figure 4.19. For the analysis a stock solution of **NCPH** was prepared in DMSO and diluted to appropriate concentrations with

the culture medium. The cells, after being rinsed with phosphate buffered saline (PBS), were incubated with different concentration of **NCPH** in Dulbecco's Modified Eagle Medium (DMEM) solutions for 1 h at 37 °C before being illuminated at an ambient temperature. Growth inhibition was determined by means of the colourimetric assay MTT. Approximately 5×10^3 cells were seeded in two 96 well cluster plate and allowed to reach the exponential phase of growth and then **NCPH** was added at analysed for cytotoxicity. Cytotoxic studies revealed that the cytotoxicity of **NCPH** in the absence of light was negligible, but interestingly on the other hand exhibits high photocytotoxicity. The IC_{50} value obtained for **NCPH** in MDA-MB-231 was 12 μ M, where that of **NCPS** was only 6 μ M, which indicate better photocytotoxicity of **NCPS** against **NCPH**.

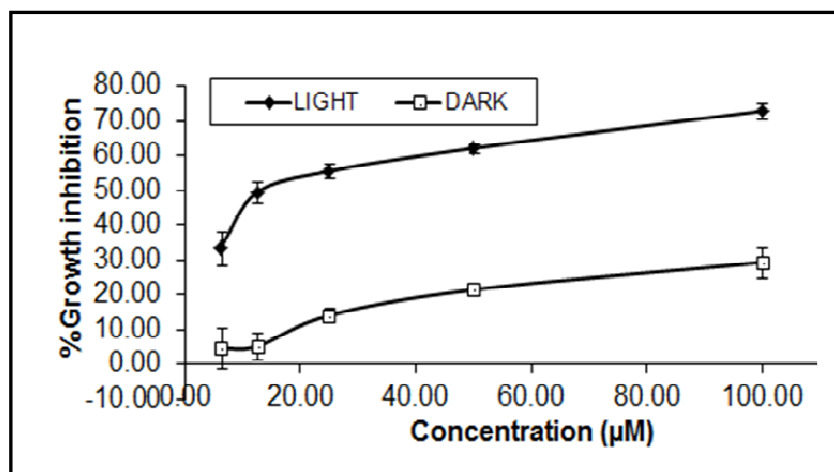


Figure 4.19. MTT assay of **NCPH** in the presence and absence of light. **NCPH** shows significant cytotoxicity in the presence of light but shows negligible cytotoxicity in the absence of light.

As discussed earlier, the membrane phospholipid phosphatidylserine translocation from the inner to outer leaflet of the plasma membrane is a significant indication of the apoptotic path way of cell death. AnnexinV (a cellular protein) tagged with FITC (Fluorescein isothiocyanate) used as a sensitive probe for identifying apoptotic cells by fluorescence microscopy and flow cytometry.

Annexin V-FITC was used together with propidium iodide (PI), which is another fluorescent probe to distinguish viable cells from dead cells, as the former can penetrate through the intact and viable cells but the latter only with dead cells. The cell death mechanism induced by PDT was studied by using **NCPH** by examining the dual fluorescence of Annexin V-FITC/PI using flow cytometry as shown in Figure 4.20. The cell populations at different phases of cell death, namely, viable (AnnexinV-FITC-/PI-), early apoptotic (Annexin V-FITC+/PI-), and necrotic or late-stage apoptotic (Annexin V-FITC+ / PI+) were examined at different drug doses.

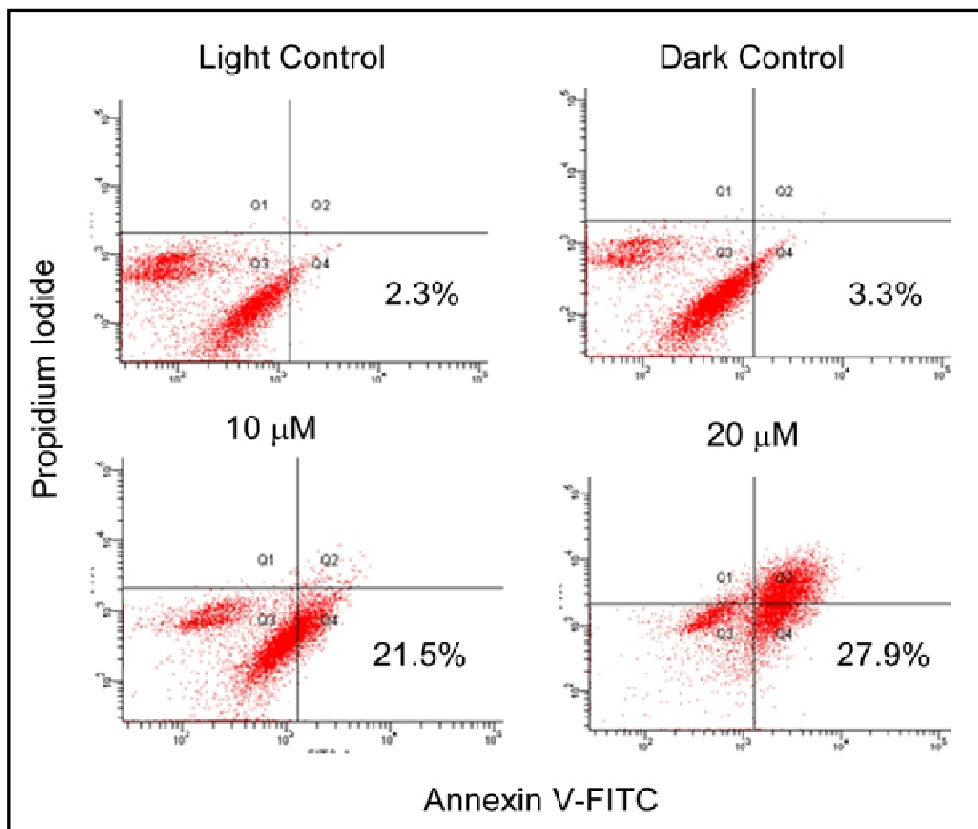


Figure 4.20. Flow cytometric analysis of the cell death mechanism induced by **NCPH** upon PDT treatment.

It was observed that most of the cells were negative for Annexin V-FITC and PI after treatment with **NCPH** (20 μM) in the absence of light (dark control). This indicates that **NCPH** is non-cytotoxic toward MDA-MB-231 cells in darkness. However, upon illumination, the percentage of cells at the early apoptotic stage (i.e., externalization of phospholipid phosphatidylserine but not membrane leakage, Annexin V-FITC + /PI-) increased from 3.3% to 21.5% when the concentration of **NCPH** increased from 0 to 10 μM , however further increase in the concentration of **NCPH** (20 μM) increases the value to 27.9%, which is only a slight increase from the lower concentration. A comparative analysis shows less rate of apoptosis with **NCPH** with respect to **NCPS**, which shows 83.9% increase in the apoptotic cell population with 12 μM concentration of **NCPS**.

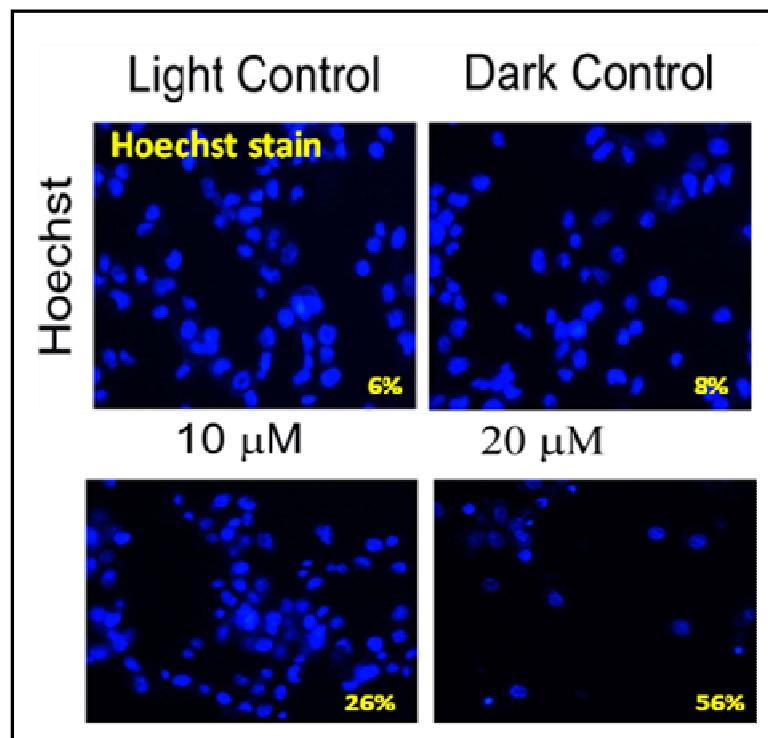


Figure 4.21. Characterization of cytotoxic actions of **NCPH** in PDT using Hoechst stain after PDT with **NCPH** (10 μM and 20 μM). In Hoechst staining, chromatin condensation was visualized using fluorescence microscope.

In order to confirm the apoptotic pathway of cell death during PDT with **NCPH**, chromatin condensation analysis has been conducted where Hoechst stain was employed to track the apoptotic cells (Figure. 21.). Hoechst stain was employed to observe chromatin condensation and cells were viewed under a fluorescent microscope, and found that PDT with **NCPH** in MDA-MB-231 cells at 10 μM resulted in 26% chromatin condensation, whereas at 20 μM showed 56% condensation. However, light and dark controls showed only 6% and 8% chromatin condensation (Figure 4.20) respectively. This demonstrates that **NCPH** also induces apoptosis in a concentration dependent manner as in the case of **NCPS**. However, the overall PDT activity of **NCPH** was found to be less when compared with **NCPS**.

4.5. Conclusions

In conclusion, a tetra sulfonated derivative of N-confused porphyrin derivative, **NCPS** with better molar extinction coefficient in the red region of visible light compared to normal porphyrin derivatives have been synthesized and characterized. The PDT applications of **NCPS** and **NCPH** were investigated. **NCPH** was highly soluble in methanol but not in water, where **NCPS** derivative was highly soluble in MeOH as well as water. Photophysical studies of the molecules have been conducted which shows promising singlet oxygen quantum yields. *In vitro* analysis of **NCPS** in a series of cancer cell lines showed promising IC_{50} values. Upon illumination **NCPS** exhibited more photocytotoxicity to adenocarcinomas over the other epithelial cell lines and maximum activity has been attributed toward breast adenocarcinomas MDA-MB-231 cells, with an IC_{50} value as low as 6 μM . As shown by flow cytometry and fluorescent imaging using ROS probe CM-H₂DCFDA, **NCPS** induces accumulation of ROS in the cells in a concentration dependant manner. Apoptosis induced cell death during PDT with **NCPS** was found to be mediated in a mitochondrial dependent manner as evidenced by JC1

mitochondrial membrane potential assay. Apoptotic potential of **NCPS** was also confirmed by DNA condensation, Annexin V apoptotic assay and PARP cleavage. *In vitro* analysis of **NCPH** showed that the photocytotoxicity and overall PDT activity of the sensitizer is low in comparison with **NCPS**.

4.6 Experimental Section

4.6.1 Materials and methods

Tetrasulfonated derivative of N-confused porphyrin (**NCPS**) was prepared from corresponding tetraphenyl N-confused porphyrin which in turn was prepared by using Lindsey's method [64]. The reagents for the synthesis as well as photophysical studies were obtained from Sigma-Aldrich and Merck, India and used as such. All solvents were distilled and dried before use. Deionized water was from Millipore.

^1H and ^{13}C NMR spectra were recorded on a Bruker Biospin 400 MHz spectrometer. NMR experiments were done in $\text{DMSO-}d_6$. ^1H NMR spectra was obtained in 512 scans, where ^{13}C in 17000 scans. Spectra were referenced internally by using the residual solvent (^1H , $\delta = 2.5$ and ^{13}C , $\delta = 39.4$ for $\text{DMSO-}d_6$) resonances relative to SiMe_4 . Matrix assisted laser desorption ionization-time of flight (MALDI-TOF) mass spectra was recorded in Shimadzu Biotech Axima mass spectrometer. Elemental analysis have conducted using Perkin Elmer 2400 seriesII instrument and the purity of the compound was determined as $> 95\%$. Infrared spectrum of the compound was recorded on a Perkin Elmer FT-IR spectrometer, spectrum RXI.

Electronic absorption spectra and steady state fluorescence spectra were recorded on Agilent diode array UV-Visible spectrophotometer (model 8453) and Perkin Elmer LS55 Fluorescence spectrometer respectively. The transient absorption studies were carried out using a nanosecond laser flash photolysis experiments by employing an Applied Photophysics model LKS-20 laser kinetic spectrometer using OCR-12 Series Quanta Ray

Nd:YAG laser. The analyzing and laser beams were fixed at right angles to each other. The laser energy was 62-66 mJ at 355 nm during the experiments. Energy transfer method to β -carotene was employed to calculate the triplet yields (Φ_T) of **NCPS** using $\text{Ru}(\text{bpy})_3^{2+}$ as the reference, assuming the 100% energy transfer from the reference to β -carotene. Optically matched solutions of **NCPS** and $\text{Ru}(\text{bpy})_3^{2+}$ were taken at the irradiation wavelength with equal volume of known concentration of β -carotene, where the end concentration of β -carotene was 7.48×10^{-5} M. Here, the assumption was that the transient absorbance (ΔA) of the β -carotene triplet was monitored at 520 nm for both reference and the compound, which was formed by the energy transfer from $\text{Ru}(\text{bpy})_3^{2+}$ and **NCPS** triplet respectively. The quenching of the sensitizer's triplet absorption indicates the complete energy transfer to the β -carotene system. Comparison of plateau absorbance following the completion of sensitized triplet formation, properly corrected for the decay of the donor triplets in competition with energy transfer to β -carotene, enabled us to estimate the quantum yield.

In order to find the singlet oxygen quantum yield, a steady state method was adopted using 1,3-diphenylisobenzofuran (**DPBF**) as scavenger of singlet oxygen and *meso*-tetrakis(*p*-sulfonatophenyl)porphyrin tetrasodium salt (**TPPS**) as the reference. The experiments were carried out with a light source 200 W xenon lamp (model 3767) on an Oriel optical bench (model 11200) with a grating monochromator (model 77250). The intensity of light was maintained constant throughout the irradiations by measuring the output using an Oriel photodiode detection system (model 7072). Quantum yield for singlet oxygen generation of **NCPS** in deionized water and methanol were determined by monitoring the photooxidation of **DPBF** during the formation of singlet oxygen using the absorption spectrometer. Concentration of the photosensitizer was adjusted with an optical density of 0.02-0.03 at the irradiation wavelength (600 nm) to minimise the

possibility of singlet oxygen quenching at higher concentration. The solution containing the sensitizer and the scavenger was purged with oxygen before irradiation. The photooxidation of **DPBF** was monitored with an interval of 10 sec up to one and half minutes. No thermal recovery of **DPBF** (from a possible decomposition of endoperoxide product) was observed under the conditions of these experiments

4.6.2 Synthesis of NCPS

To synthesize **NCPS**, tetraphenyl N-confused porphyrin (800 mg, 1.3 mmol) was made into paste with 5 ml con. sulfuric acid, then transferred to a 100 ml round bottom flask using another 15 ml acid. The mixture was then heated at 90 °C for 5 h and then at room temperature for 12 h. Dil. sodium hydroxide solution was added slowly to the reaction mixture at 0 °C to neutralize the excess acid present. The formed sodium sulfate salt was filtered, and washed many times with methanol to extract the compound. The solution was evaporated to dryness and soxhlet extracted using methanol to obtain pure **NCPS** in 56% yield as greenish black solid, m.p > 300 °C: ¹H NMR (400 MHz, DMSO-*d*₆) δ 8.7 (s, 1H, Pyrrolic α-CH), 8.36 (s, 2H, Pyrrolic β-CH), 8.28-8.29 (d, *J*=4 Hz, 1H, Pyrrolic β-CH), 8.25-8.26 (d, *J*=4 Hz, 1H, Pyrrolic β-CH), 7.86-7.88 (d, *J*=8 Hz, 2H, Pyrrolic β-CH), 7.92-8.01(m, 16H, Phenyl), -1.07(s, 1H, Exch. D₂O, Pyrrolic NH), -2.76(s, 1H, Pyrrolic β-CH). ¹³C{¹H}NMR(100 MHz, DMSO-*d*₆): δ 167.29, 158.43, 146.18, 134.84, 134.57, 133.62, 128.82, 124.86, 124.47, 124. IR (KBr): 3448 (br), 2925, 2372, 2345, 1648, 1459, 1178, 1123, 1040 cm⁻¹. MALDI-TOF MS: *m/z* 1016.58 (C₄₄H₂₅N₄Na₃O₁₂S₄ + H₂O), 1000.98 (C₄₄H₂₇N₄Na₃O₁₂S₄), 936.84 (C₄₄H₃₀N₄O₁₂S₄ + 2H), 930.04 (C₄₄H₂₆N₄O₁₂S₄)⁻⁴, 792.75 (C₄₄H₂₅N₄NaO₆S₂)⁻². Anal.Calcd. for C₄₄H₂₆N₄Na₄O₁₂S₄: C, 51.66; H, 2.56; N, 5.48; Found: C, 51.01, H, 2.12, N, 5.11.

4.6.3 Cell Lines and Culture Conditions

Human cervical cancer (HeLa&SiHa), breast cancer cells (MDA-MB-231 & MCF7), colorectal cancer cells (HCT-116), pancreatic cancer cells (MIA-PaCa-2), were purchased from ATCC (USA) and Human oral cancer cells (SCC-131 and SCC-171) were obtained as a gift from Dr. Susanne M Gollin, University of Pittsburgh-USA and were maintained in DMEM (Sigma, USA) containing 10% foetal bovine serum (Sigma, USA) and 1% antibiotic antimycotic cocktail (Invitrogen, USA). All experimental steps, after seeding the cells, including photosensitizer incubation, illumination and post-illumination incubation were performed in the same medium. For measurement of dark and light cytotoxicity, cells were seeded (5×10^3 per well in 100 μ L medium) in 96-well microplates (BD-Falcon, USA).

4.6.4 Photocytotoxicity Assay

NCPS was first dissolved in DMSO to give 106.9 mM solution and diluted to appropriate concentrations with the culture medium. The cells, after being rinsed with phosphate buffered saline (PBS), were incubated with different concentration of **NCPS** in DMEM solutions for 1 h at 37 °C before being illuminated at an ambient temperature. A 70 W sodium vapour lamp was used as the light source with fluence rate ($\lambda > 590$ nm) of 55 mWcm⁻². Illumination for 30 min led to a total fluence of 100 Jcm⁻².

Growth inhibition was determined by means of the colourimetric MTT assay. Approximately 5×10^3 cells were seeded in two 96 well cluster plate and allowed to reach the exponential phase of growth. Then **NCPS** was added in serial dilution 3.34 μ M to 53.45 μ M. Out of two plates, one plate was kept in the dark for studying dark cytotoxicity. The second plate was photoirradiated using sodium vapour lamp and kept in an incubator. After illumination, the cells were incubated at 37 °C under 5% CO₂ for 24 h. MTT (Sigma Aldrich) solution in PBS (10 mg mL⁻¹, 10 μ L) was added to each well

followed by incubation for 4 h under the same environment. Later the media was replaced by 100 μ L of isopropanol. The plate was agitated on a Bio-Rad microplate reader at ambient temperature for 10 s before the absorbance at 570 nm for each well was taken. The cell viability was then determined by the following equation, percentage growth inhibition = (OD value of control-OD value of test/OD value of control) x 100.

4.6.5 Detection of cellular ROS using CM-H2DCFDA assay

For ROS Stress studies approximately 10^6 MDA-MB-231 cells were plated in 60 mm and 96 well (BD falcon) plates with serum containing media. After 24 h the cells were treated with 6 and 12 μ M **NCPS** for one hand photoirradiation was done using sodium vapour lamp for 30 min. To one plate 12 μ M **NCPS** added and kept in dark as taken as dark control. After 24 h of PDT with **NCPS** cellular ROS content was determined using the CM-H2DCFDA probe according to the manufacturer's instructions (Invitrogen) and a flow cytometric analysis was then carried out using FACS Aria II (BD, USA). Images were taken using pathway imager (BD, USA).

4.6.6 Chromatin condensation analysis by Hoechst staining.

To study chromatin condensation, approximately 10^5 MDA-MB-231 cells were seeded in 35 mm culture dishes and incubated for 18 h. Cells were incubated with 6 μ M and 12 μ M **NCPS** for 1 h followed by photoirradiation using sodium vapour lamp. Light and Dark control were taken as previously described. After 24 h of treatment MDA-MB-231 cells were rinsed twice with PBS, cells were stained with 5 μ g/ml Hoechst dye 33342 (Invitrogen) for 15 min at room temperature. Cells were then washed twice with PBS and visualized under an inverted fluorescence microscope.

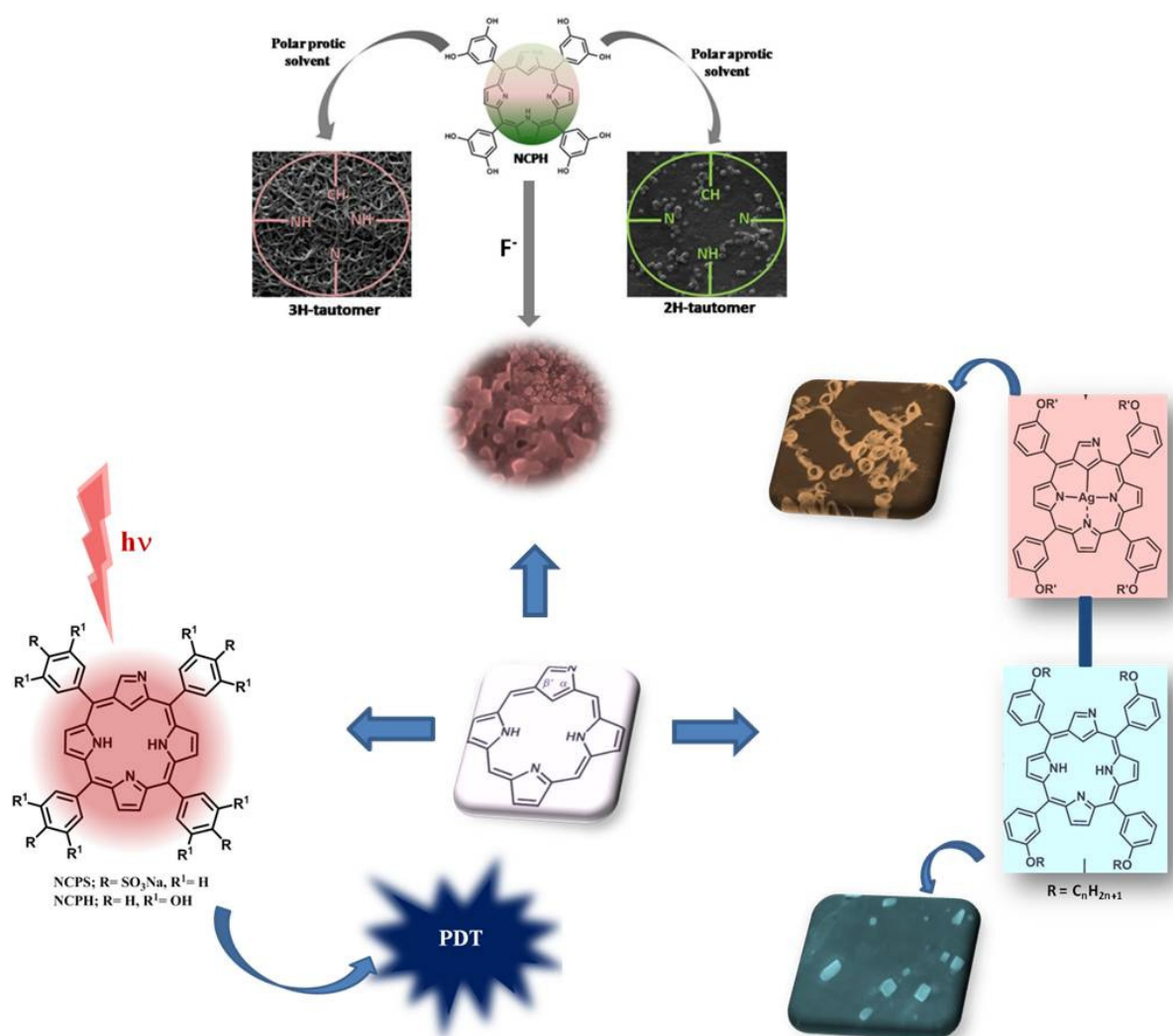
4.6.7 Mitochondrial membrane potential assay using JC1 Dye.

For Mitochondrial membrane potential assay, approximately 10^5 MDA-MB-231 cells were seeded in 35 mm culture dishes and incubated for 18 h. Cells were incubated with 6 μ M and 12 μ M NCPS for 1 h followed by photoirradiation using sodium vapour lamp. Light and Dark control were taken as previously described. After 24 h of treatment MDA-MB-231 cells were rinsed twice with PBS and cells were stained with JC1 dye mitochondrial membrane potential Detection Kit (Sigma Aldrich) according to the manufacturer's instruction, and the cell were examined under an inverted fluorescence microscope.

4.6.8 Flow cytometric Annexin V apoptotic studies and Immunoblot analysis

Approximately 10^6 MDA-MB-231 cells were seeded on 60 mm dishes and incubated for 24 h at 37°C under 5% CO₂. Cells were incubated with 6 μ M and 12 μ M NCPS for 1 h followed by photoirradiation using sodium vapour lamp. In this experiment light and dark control were taken as previously described. Cells were stained with FITC-labelled Annexin using Annexin V-FITC Apoptosis Detection Kit (Sigma Aldrich) according to the manufacturer's instruction, and a flow cytometric analysis was then carried out using FACS Aria (BD, USA). For immunoblot analysis, after light irradiation, cells were lysed and the total protein content was measured using Bradford's reagent. 50 mg of total protein was loaded for SDS-PAGE and immunoblotting was carried out using PARP antibody (cell signalling) Horseradish peroxidase-conjugated secondary antibodies (Santa Cruz) were used followed by detection using enhanced chemiluminescence (ECL) method.

SUMMARY



References

1. Kadish, K. M.; Smith, K. M.; Guillard, R. *The Porphyrin Handbook*, Academic Press: San Diego, CA, **2000**.
2. Jasat, A.; Dolphin, D. *Chem. Rev.* **1997**, *97*, 2267-2340.
3. Sessler, J. L.; Weghorn, S. J. *Tetrahedron Organic Chemistry series*, Expanded, Contracted and Isomeric Porphyrins, Pergamon, New York, **1997**.
4. Berzelius, J. J. *Lehrbuch der Chemie.* **1840**, 67-69.
5. Scherer, J. *Ann. Chem. Phar.* **1841**, *40*, 1-64.
6. Miilder, G. H. *J. Prakt. Chem.* **1844**, *32*, 186-197.
7. Rothmund, P. *J. Am. Chem. Soc.* **1935**, *57*, 2010-2011.
8. Adler, A. D.; Longo, F. R.; Finarelli, J. D.; Goldmacher, J.; Assour, J.; Korsakoff, L. *J. Org. Chem.* **1967**, *32*, 476-476.
9. Lindsey, J. S.; Schreiman, I. C.; Hsu, H. C.; Kearney, P. C.; Marguerettaz, A. M. *J. Org. Chem.* **1987**, *52*, 827-836.
10. Littler, B. J.; Ciringh, Y.; Lindsey, J. S. *J. Org. Chem.* **1999**, *64*, 2864-2872.
11. Wiehe, A.; Shaker, Y. M.; Brandt, J. C.; Mebs, S.; Senge, M. O. *Tetrahedron* **2005**, *61*, 5535-5564.
12. Sessler, J. L. *J. Porphyrins Phthalocyanines* **2000**, *4*, 331-336.
13. Baeyer, A. *Ber. Dtsch. Chem. Ges.* **1886**, *19*, 2184-2185.
14. Gale, P. A.; Sessler, J. L.; Král, V.; Lynch, V. *J. Am. Chem. Soc.* **1996**, *118*, 5140-5141.
15. Gale, P. A.; Sessler, J. L.; Král, V. *Chem. Commun.* **1998**, 1-8.
16. Gale, P. A.; Anzenbacher, P. Jr.; Sessler, J. L. *Coord. Chem. Rev.* **2001**, *222*, 57-102.
17. Floriani, C. *Chem. Commun.* **1996**, 1257-1263.

18. Sessler, J. L.; An, D.; Cho, W.-S.; Lynch, V.; Yoon, D.-W.; Hong, S.-J.; Lee, C.-H. *J. Org. Chem.* **2005**, *70*, 1511-1517.
19. Sessler, J. L.; Cho, W.-S.; Gross, D. E.; Shriver, J. A.; Lynch, V. M.; Marquez, M. J. *J. Org. Chem.* **2005**, *70*, 5982-5986.
20. Warriner, C. N.; Gale, P. A.; Light, M. E.; Hursthouse, M. B. *Chem. Commun.* **2003**, 1810-1811.
21. Allen, W. E.; Gale, P. A.; Brown, C. T.; Lynch, V. M.; Sessler, J. L. *J. Am. Chem. Soc.* **1996**, *118*, 12471-12472.
22. Sessler, J. L.; Zimmerman, R. S.; Bucher, C.; Král, V.; Andrioletti, B. *Pure Appl. Chem.* **2001**, *73*, 1041-1057.
23. Benech, J. M.; Bonomo, L.; Solari, E.; Scopelliti, R.; Floriani, C. *Angew. Chem. Int. Ed.* **1999**, *38*, 1957-1959.
24. Bucher, C.; Seidel, D.; Lynch, V.; Král, V.; Sessler, J. L. *Org. Lett.* **2000**, *2*, 3103-3106.
25. Král, V.; Sessler, J. L.; Zimmerman, R. S.; Seidel, D.; Lynch, V.; Andrioletti, B. *Angew. Chem. Int. Ed.* **2000**, *39*, 1055-1058.
26. Bucher, C.; Devillers, C. H.; Moutet, J. C.; Pecaut, J.; Royal, G.; Saint-Aman, E.; Thomas, F. *Dalton Trans.* **2005**, 3620-3631.
27. Hung, C. H.; Chang, G. F.; Kumar, A.; Lin, G. F.; Luo, L. Y.; Ching, W. M.; Wei-Guang Diao, E. *Chem. Commun.* **2008**, 978-980.
28. Senge, M. O.; Runge, S.; Speck, M.; Ruhlandt-Senge, K. *Tetrahedron* **2000**, *56*, 8927-8932.
29. Hong, S.-J.; Ka, J.-W.; Won, D.-H.; Lee, C. -H. *Bull. Korean Chem. Soc.* **2003**, *24*, 661-663.
30. Johnson, A.W.; Price, R. *J. Chem. Soc.* **1960**, 1649-1653.

31. Gross, Z.; Galili, N.; Saltsman, I. *Angew. Chem. Int. Ed.* **1999**, *38*, 1427-1429.
32. Simkhovich, L.; Mahammed, A.; Goldberg, I.; Gross, Z.; *Chem. Eur. J.* **2001**, *7*, 1041-1055.
33. Vogel, E. *J. Heterocyclic Chem.* **1996**, *33*, 1461-1487.
34. Bröring, M.; Köhler, S.; Kleeberg, C. *Angew. Chem. Int. Ed.* **2008**, *47*, 5658-5661.
35. Kobayashi, N.; Kondo, R.; Nakajima, S.-I.; Osa, T. *J. Am. Chem. Soc.* **1990**, *112*, 9640-9641.
36. Inokuma, Y.; Kwon, J. H.; Ahn, T. K.; Yoon, M.-C.; Kim, D.; Osuka, A. *Angew. Chem. Int. Ed.* **2006**, *45*, 961-964.
37. First reported by R. B. Woodward in: Aromaticity: An International Symposium, Sheffield, U.K., Special publication no. 21; The Chemical Society London: **1966**.
38. Bauer, V. J.; Clive, D. L. J.; Dolphin, D.; Paine, J. B. III ; Harris, F. L.; King, M. M.; Loder, J., Wang, S.W. C.; Woodward, R. B. *J. Am. Chem. Soc.* **1983**, *105*, 6429-6436.
39. Broadhurst, M. J.; Grigg, R.; Johnson, A.W. *J. Chem. Soc. Perkin Trans.* **1972**, *1*, 1124-1135.
40. Sessler, J. L.; Cyr, M.; Lynch, V.; McGhee, E.; Ibers, J. A. *J. Am. Chem. Soc.* **1990**, *112*, 2810-2813.
41. Callot, H. J.; Tschamber, T. *J. Am. Chem. Soc.* **1975**, *97*, 6175-6180.
42. Narayanan, S. J.; Sridevi, B.; Chandrashekar, T. K.; English, U.; Ruhlandt-Senge, K. *Org. Lett.* **1999**, *1*, 587-590.
43. Sessler, J. L.; Weghorn, S. J.; Hiseada, Y.; Linch, V. *Chem. Eur. J.* **1995**, *1*, 56-61.
44. Miller, D. C.; Johnson, M. R.; Becker, J. J.; Ibers, J. A. *J. Heterocycl. Chem.* **1993**, *30*, 1485-1490.
45. Rexhausen, H.; Gassauer, A. *J. Chem. Soc., Chem. Commun.* **1983**, 275.
46. Gassauer, A. *Bull. Soc. Chim. Belg.* **1983**, *92*, 793-795.

47. Sessler, J. L.; Morishima, T.; Linch, V. *Angew. Chem. Int. Ed. Engl.* **1991**, *30*, 977-980.
48. Johnson, M. R.; Miller, D. C.; Bush, K.; Becker, J. J.; Ibers, J. A. *J. Org. Chem.* **1992**, *57*, 4414-4417.
49. Miller, D. C.; Johnson, M. R.; Ibers, J. A. *J. Org. Chem.* **1994**, *59*, 2877-2879.
50. Sessler, J. L.; Weghorn, S. J.; Morishima, T.; Rosingana, M.; Linch, V.; Lee, V. *J. Am. Chem. Soc.* **1992**, *114*, 8306-8307.
51. Sessler, J. L.; Seidel, J.; Lynch, V. *J. Am. Chem. Soc.* **1999**, *121*, 11257-11258.
52. Bucher, C.; Seidel, D.; Lynch, V.; Sessler, J. L. *Chem. Commun.* **2002**, 328-329.
53. Vogel, E.; Broring, M.; Fink, J.; Rosen, D.; Schmickler, H.; Lex, J.; Chan, K. W. K.; Wu, Y. D.; Plattner, D. A.; Nendel, M.; Houk, K. N. *Angew. Chem. Int. Ed. Engl.* **1995**, *34*, 2511-2514.
54. Seidel, D.; Lynch, V.; Sessler, J. L. *Angew. Chem. Int. Ed.* **2002**, *41*, 1422-1425.
55. Shin, J.-Y.; Furuta, H.; Yoza, K.; Igarashi, S.; Osuka, A. *J. Am. Chem. Soc.* **2001**, *123*, 7190-7191.
56. Sessler, J. L.; Weghorn, S. J.; Lynch, V.; Johnson, M. R. *Angew. Chem. Int. Ed. Engl.* **1994**, *33*, 1509-1512.
57. Vogel, E.; Kocher, M.; Schmickler, H.; Lex, J. *Angew. Chem. Int. Ed.* **1986**, *25*, 257-259.
58. Sessler, J. L.; Brucker, E. A.; Weghorn, S. J.; Kisters, M.; Schafer, M.; Lex, J.; Vogel, E. *Angew. Chem. Int. Ed.* **1994**, *33*, 2308-2312.
59. Callot, H. J.; Rohrer, A.; Tschamber, T. *New. J. Chem.* **1995**, *19*, 155-159.
60. Aukauloo, M. A.; Guillard, R. *New J. Chem.* **1994**, *18*, 1205-1207.
61. Srinivasan, A.; Furuta, H. *Acc. Chem. Res.* **2005**, *38*, 10-20.
62. Furuta, H.; Asano, T.; Ogawa, T. *J. Am. Chem. Soc.* **1994**, *116*, 767-768.

63. Chmielewski, P. J.; Latos-Grażyński, L.; Rachlewicz, K.; Głowiak, T. *Angew. Chem. Int. Ed. Engl.* **1994**, *33*, 779-781.
64. Geier, G. R. III; Haynes, D. M.; Lindsey, J. S. *Org. Lett.* **1999**, *1*, 1455-1458.
65. Geier, G. R. III; Lindsey, J. S. *J. Org. Chem.* **1999**, *64*, 1596-1603.
66. Maeda, H.; Osuka, A.; Ishikawa, Y.; Aritome, I.; Hisaeda, Y.; Furuta, H. *Org. Lett.* **2003**, *5*, 1293-1296.
67. Liu, B. Y.; Brückner, C.; Dolphin, D. *Chem. Commun.* **1996**, 2141-2143.
68. Lash, T. D.; Richter, D. T.; Shiner, C. M. *J. Org. Chem.* **1999**, *64*, 7973-7982.
69. Furuta, H.; Maeda, H.; Osuka, A. *J. Am. Chem. Soc.* **2000**, *122*, 803-807.
70. Maeda, H.; Osuka, A.; Furuta, H. *J. Am. Chem. Soc.* **2003**, *125*, 15690-15691.
71. Heo, P.-Y.; Shin, K.; Lee, C.-H. *Tetrahedron Lett.* **1996**, *37*, 197-200.
72. Lee, C.-H.; Kim, H.-J. *Tetrahedron Lett.* **1997**, *38*, 3935-3938.
73. Pacholska, E.; Latos-Grażyński, L.; Szterenber, L.; Ciunik, Z. *J. Org. Chem.* **2000**, *65*, 8188-8196.
74. Sprutta, N.; Latos-Grażyński, L. *Org. Lett.* **2001**, *3*, 1933-1936.
75. Pushpan, S. K.; Srinivasan, A.; Anand, V. G.; Chandrashekar, T. K.; Subramanian, A.; Roy, R.; Sugiura, K.-i.; Sakata, Y. *J. Org. Chem.* **2001**, *66*, 153-161.
76. Pushpan, S. K.; Srinivasan, A.; Anand, V. G.; Venkatraman, S.; Chandrashekar, T. K.; Joshi, B. S.; Roy, R.; Furuta, H. *J. Am. Chem. Soc.* **2001**, *123*, 5138-5139.
77. Srinivasan, A.; Ishizuka, T.; Osuka, A.; Furuta, H. *J. Am. Chem. Soc.* **2003**, *125*, 878-879.
78. Xie, Y.-S.; Yamaguchi, K.; Toganoh, M.; Uno, H.; Suzuki, M.; Mori, S.; Saito, S.; Osuka, A.; Furuta, H. *Angew. Chem. Int. Ed.* **2009**, *48*, 5496-5499.
79. Gokulnath, S.; Yamaguchi, K.; Toganoh, M.; Mori, S.; Uno, H.; Furuta, H. *Angew. Chem. Int. Ed.* **2011**, *50*, 2302-2306.

80. Lim, J. M.; Lee, J. S.; Chung, H. W.; Bahng, H. W.; Yamaguchi, K.; Toganoh, M.; Furuta, H.; Kim, D. *Chem. Commun.* **2010**, *46*, 4357-4359.
81. Chmielewski, P. J. *Angew. Chem. Int. Ed.* **2004**, *43*, 5655-5658.
82. Chmielewski, P. J.; Latos-Grażyński, L.; Głowiak, T. *J. Am. Chem. Soc.* **1996**, *118*, 5690-5701.
83. Chmielewski, P. J.; Latos-Grażyński, L. *Inorg. Chem.* **1997**, *36*, 840-845.
84. Furuta, H.; Ogawa, T.; Uwatoko, Y.; Araki, K. *Inorg. Chem.* **1999**, *38*, 2676-2682.
85. Chmielewski, P. J.; Latos-Grażyński, L.; Schmidt, I. *Inorg. Chem.* **2000**, *39*, 5475-5482.
86. Ogawa, T.; Furuta, H.; Takahashi, M.; Morino, A.; Uno, H. *J. Organomet. Chem.* **2000**, *611*, 551-557.
87. Harvey, J. D.; Ziegler, C. J. *Coord. Chem. Rev.* **2003**, *247*, 1-19.
88. Furuta, H.; Kubo, N.; Maeda, H.; Ishizuka, T.; Osuka, A.; Nanami, H.; Ogawa, T. *Inorg. Chem.* **2000**, *39*, 5424-5425.
89. Chen, W.-C.; Hung, C.-H. *Inorg. Chem.* **2001**, *40*, 5070-5071.
90. Srinivasan, A.; Furuta, H.; Osuka, A. *Chem. Commun.* **2001**, 1666-1667.
91. Srinivasan, A.; Toganoh, M.; Niino, T.; Osuka, A.; Furuta, H. *Inorg. Chem.* **2008**, *47*, 11305-11313.
92. Bohle, D. S.; Chen, W.-C.; Hung, C.-H. *Inorg. Chem.* **2002**, *41*, 3334-3336.
93. Harvey, J. D.; Ziegler, C. J. *Chem. Commun.* **2002**, 1942-1943.
94. Furuta, H.; Ishizuka, T.; Osuka, A. *J. Am. Chem. Soc.* **2002**, *124*, 5622-5623.
95. Hung, C.-H.; Chen, W.-C.; Leeb, G.-H.; Pengc, S.-M. *Chem. Commun.* **2002**, 1516-1517.
96. Furuta, H.; Youfu, K.; Maeda, H.; Osuka, A. *Angew. Chem. Int. Ed.* **2003**, *42*, 2186-2188.

97. Maeda, H.; Ishikawa, Y.; Matsuda, T.; Osuka, A.; Furuta, H. *J. Am. Chem. Soc.* **2003**, *125*, 11822-11823.
98. Furuta, H.; Morimoto, T.; Osuka, A. *Inorg. Chem.* **2004**, *43*, 1618-1624.
99. Harvey, J. D.; Ziegler, C. J. *Chem. Commun.* **2004**, 1666-1667.
100. Toganoh, M.; Furuta, H. *Chem. Lett.* **2005**, *34*, 1034-1035.
101. Toganoh, M.; Ikeda, S.; Furuta, H. *Inorg. Chem.* **2007**, *46*, 10003-10015.
102. Zhu, X.; Wong, W.-K.; Lo, W.-K.; Wong, W.-Y. *Chem. Commun.* **2005**, 1022-1024.
103. Harvey, J. D.; Shaw, J. L.; Herrick, R. S.; Ziegler, C. J. *Chem. Commun.* **2005**, 4663-4665.
104. Toganoh, M.; Konagawa, J.; Furuta, H. *Inorg. Chem.* **2006**, *45*, 3852-3854.
105. Xie, Y.; Morimoto, T.; Furuta, H. *Angew. Chem. Int. Ed.* **2006**, *45*, 6907-6910.
106. Młodzianowska, A.; Latos-Grażyński, L.; Szterenberga, L.; Stepień, M. *Inorg. Chem.* **2007**, *46*, 6950-6957.
107. Toganoh, M.; Niino, T.; Furuta, H. *Chem. Commun.* **2008**, 4070-4072.
108. Sripathongnak, S.; Ziegler, C. J. *Inorg. Chem.* **2010**, *49*, 5789-5791.
109. Cao, W.; Wang, H.; Wang, X.; Lee, H. K.; Ng, D. K. P.; Jiang, J. *Inorg. Chem.* **2012**, *51*, 9265-9272.
110. Gokulnath, S.; Yamaguchi, K.; Toganoh, M.; Mori, S.; Uno, H.; Furuta, H. *Angew. Chem. Int. Ed.* **2011**, *50*, 2302-2306.
111. Niino, T.; Toganoh, M.; Andrioletti, B.; Furuta, H. *Chem. Commun.* **2006**, 4335-4337.
112. Maeda, H.; Morimoto, T.; Osuka, A.; Furuta, H. *Chem. Asian J.* **2006**, *1*, 832-844.
113. Ching, W.-M.; Chuang, C.-H.; Wu, C.-W.; Peng, C.-H.; Hung, C.-H. *J. Am. Chem. Soc.* **2009**, *131*, 7952-7953.
114. Fields, K. B.; Engle, J. T.; Sripathongnak, S.; Kim, C.; Zhang, X. P.; Ziegler, C. J. *Chem. Commun.* **2011**, *47*, 749-751.

115. Senge, M. O. *Angew. Chem. Int. Ed.* **2011**, *50*, 4272-4277.
116. Aronoff, S.; Calvin, M. *J. Org. Chem.* **1943**, *8*, 205-223.
117. Von Lippman, E. O. *Chem.-Ztg.* **1910**, 39-49.
118. Laar, P. C. *Ber.* **1885**, *18*, 648-657.
119. Gold, V. *Pure Appl. Chem.* **1979**, *51*, 1725-1801.
120. Frankland, E.; Duppa, B. J. *Ann.* **1865**, *135*, 217-226.
121. Wislicenus, W. *Ann.* **1877**, *186*, 163.
122. Claisen, L. *Liebigs Ann. Chem.* **1896**, *291*, 17-25.
123. Wislicenus, W. *Liebigs Ann. Chem.* **1896**, *291*, 147-216.
124. Knorr, L. *Liebigs Ann. Chem.* **1896**, *293*, 70-120.
125. Ghosh, A. *Angew. Chem. Int. Ed. Engl.* **1995**, *34*, 1028-1030.
126. Chmielewski, P. J.; Latos-Grażyński, L.; Głowiak, T. *J. Am. Chem. Soc.* **1996**, *118*, 5690-5701.
127. Chmielewski, P. J.; Latos-Grażyński, L. *Inorg. Chem.* **1997**, *36*, 840-845.
128. Szterenberg, L.; Latos-Grażyński, L. *Inorg. Chem.* **1997**, *36*, 6287-6291.
129. Ghosh, A.; Wondimagegn, T.; Nilsen, H. J. *J. Phys. Chem. B* **1998**, *102*, 10459-10467.
130. Belair, J. P.; Ziegler, C. J.; Rajesh, C. S.; Modarelli, D. A. *J. Phys. Chem. A* **2002**, *106*, 6445-6451.
131. Furuta, H.; Ishizuka, T.; Osuka, A.; Dejima, H.; Nakagawa, H.; Ishikawa, Y. *J. Am. Chem. Soc.* **2001**, *123*, 6207-6208.
132. Alemán, E. A.; Rajesh, C. S.; Ziegler, C. J.; Modarelli, D. A. *J. Phys. Chem. A* **2006**, *110*, 8605-8612.
133. Jones, B. A.; Ahrens, M. J.; Yoon, M.-H.; Facchetti, A.; Marks, T. J.; Wasielewski, M. R. *Angew. Chem. Int. Ed.* **2004**, *43*, 6363-6366.

134. Cui, S.; Liu, H.; Gan, L.; Li, Y.; Zhu, D. *Adv. Mater.* **2008**, *20*, 2918-2925.
135. Wang, C.; Wang, Z.; Zhang, X. *Acc. Chem. Res.* **2012**, *45*, 608-618.
136. Wang, Z.; Lybarger, L. E.; Wang, W.; Medforth, C. J.; Miller, J. E.; Shelnut, J. A. *Nanotechnology* **2008**, *19*, 395604.
137. Drain, C. M.; Varotto, A.; Radivojevic, I. *Chem. Rev.* **2009**, *109*, 1630-1658.
138. Saga, Y.; Tamiaki, H. *J. Biosci. Bioeng.* **2006**, *102*, 118-123.
139. Ganapathy, S.; Oostergetel, G. T.; Wawrzyniak, P. K.; Reus, M.; Chew, A. G. M.; Buda, F.; Boekema, E. J.; Bryant, D. A.; Holzwarth, A. R.; de Groot, H. J. M. *Proc. Natl. Acad. Sci. U.S.A.* **2009**, *106*, 8525-8530.
140. Wang, Z.; Medforth, C. J.; Shelnut, J. A. *J. Am. Chem. Soc.* **2004**, *126*, 15954-15955.
141. Wang, Z.; Ho, K. J.; Medforth, C. J.; Shelnut, J. A. *Adv. Mater.* **2006**, *18*, 2557-2560.
142. Wang, Z.; Li, Z.; Medforth, C. J.; Shelnut, J. A. *J. Am. Chem. Soc.* **2007**, *129*, 2440-2441.
143. Guo, X. M.; Jiang, C.; Shi, T. S. *Inorg. Chem.* **2007**, *46*, 4766-4768
144. Engelkamp, H.; Middelbeek, S.; Nolte, R. J. M. *Science* **1999**, *284*, 785-788.
145. Howie, R. A.; de Lima, G. M.; Menezes, D. C.; Wardell, J. L.; Wardell, S. M. S. V.; Young, D. J.; Tiekink, E. R. T. *Cryst. Eng. Comm.* **2008**, *10*, 1626-1637.
146. Beer, P. D.; Gale, P. A. *Angew. Chem. Int. Ed.* **2001**, *40*, 486-516.
147. Pramanik, A.; Das, G. *Tetrahedron* **2009**, *65*, 2196-2200.
148. Katayev, E. A.; Pantos, G. D.; Reshetova, M. D.; Khrustalev, V. N.; Lynch, V. M.; Ustynyuk, Y. A.; Sessler, J. L. *Angew. Chem. Int. Ed.* **2005**, *44*, 7386-7390.
149. Kavallieratos, K.; de Gala, S. R.; Austin, D. J.; Crabtree, R. H. *J. Am. Chem. Soc.* **1997**, *119*, 2325-2326.
150. Xie, H.; Yi, S.; Yang, X.; Wu, S. *New J. Chem.* **1999**, *23*, 1105-1110.
151. Lee, K. H.; Lee, H. -Y.; Lee, D. H.; Hong, J. *Tetrahedron Lett.* **2001**, *42*, 5447-

5449.

152. Král, V.; Schmidtchen, F. P.; Lang, K.; Berger, M. *Org. Lett.* **2002**, *4*, 51-54.
153. Arai, Y.; Segawa, H. *J. Phys. Chem. B* **2011**, *115*, 7773-7780.
154. Maeda, H.; Osuka, A.; Furuta, H. *J. Incl. Phenom. Macrocycl. Chem.* **2004**, *49*, 33-36.
155. Furuta, H.; Nanami, H.; Morimoto, T.; Ogawa, T.; Král, V.; Sessler, J. L.; Lynch, V. *Chem. Asian J.* **2008**, *3*, 592-599.
156. Ikawa, Y.; Ogawa, H.; Harada, H.; Furuta, H. *Bioorg. Med. Chem. Lett.* **2008**, *18*, 6394-6397.
157. Thomas, A. P.; Sreedevi, K. C. G.; Adinarayana, B.; Ramakrishnan, S.; Srinivasan. A. *RSC Adv.* **2013**, *3*, 16967-16972.
158. Bohn, P.W. *Annu. Rev. Phys. Chem.* **1993**, *44*, 37-60.
159. Piepenbrock, M.-O. M.; Lloyd, G. O.; Clarke, N.; Steed, J. W. *Chem. Rev.* **2010**, *110*, 1960-2004.
160. Ke, D.; Zhan, C.; Li, A. D. Q.; Yao, J. *Angew. Chem. Int. Ed.* **2011**, *50*, 3715-3719.
161. Maggini, L.; Bonifazi, D. *Chem. Soc. Rev.* **2012**, *41*, 211-241.
162. Terech, P.; Scherer, C.; Demé, B.; Ramasseul, R. *Langmuir* **2003**, *19*, 10641-10647.
163. Shearman, C.; Yahioğlu, G.; Kirstein, J.; Milgrom, L. R.; Seddon, J. M. *J. Mater. Chem.* **2009**, *19*, 598-604.
164. Martelli, C.; Canning, J.; Khoury, T.; Skivesen, N.; Kristensen, M.; Huyang, G.; Jensen, P.; Neto, C.; Sum, T. J.; Hovgaard, M. B.; Gibsons, B. C.; Crossley, M. J. *J. Mater. Chem.* **2010**, *20*, 2310-2316.
165. Xu, X.-D.; Zhang, J.; Chen, L.-J.; Guo, R.; Wang, D.-X.; Yang, H.-B. *Chem. Commun.* **2012**, *48*, 11223-11225.
166. Gao, Y.; Zhang, X.; Ma, C.; Li, X.; Jiang, J. *J. Am. Chem. Soc.* **2008**, *130*, 17044-17052.

167. Furuta, H.; Ogawa, T.; Uwatoko, Y.; Araki, K. *Inorg. Chem.* **1999**, *38*, 2676-2682.
168. Kuimova, M. K.; Botchway, S. W.; Parker, A. W.; Balaz, M.; Collins, H. A.; Anderson, H. L.; Suhling, K.; Ogilby, P. R. *Nat. Chem.* **2009**, *1*, 69-73.
169. Spikes, J. D. In *Primary Photoprocesses in Biology and Medicine* (Edited by R.V. Bergasson, G. Jori, E. J. Land and T. G. Truscott), Plenum Press, New York. **1985**, 209-227.
170. Epstein, J. M. *N. Engl. J. Med.* **1990**, *32*, 1149-1151.
171. Ackroyd, R.; Kelty, C.; Brown, N.; Reed, M. *Photochemistry and Photobiology* **2001**, *74*, 656-669.
172. Cauvin, J. F. *Des bienfaits de l'insolation. Ph.D. Thesis*, University of Paris, France. **1815**.
173. Finsen, N. R. *Phototherapy.* **1901**, 1-36.
174. Raab, O. *Z. Biol.* **1900**, *39*, 524-546.
175. Von Tappeiner, H.; Jodlbauer, A. *Dtsch. Arch. Klin. Med.* **1904**, *80*, 427-487.
176. Von Tappeiner, H. *Münch. Med. Wochenschr.* **1900**, *47*, 5-7.
177. VonTappeiner, H.; Jesionek, A. *Münch. Med. Wochenschr.* **1903**, *47*, 2042-2044.
178. Bonnet, R. *Chem. Soc. Rev.* **1995**, *24*, 19-33.
179. Lang, K.; Mosinger, J.; Wagnerová, D. M. *Coord. Chem. Rev.* **2004**, *248*, 321-350.
180. Wainwright, M. *Chem. Soc. Rev.* **1996**, *25*, 351-359.
181. Schmitt, M.; Chimenti, S.; Gasparro, F. P. *J. Photochem. Photobiol. B* **1995**, *27*, 101-105.
182. Yogo, T.; Urano, Y.; Ishitsuka, Y.; Maniwa, F.; Nagano, T. *J. Am. Chem. Soc.* **2005**, *127*, 12162-12163.
183. Gorman, A.; Killoran, J.; O'Shea, C.; Kenna, T.; Gallagher, W. M.; O'Shea, D. F. *J. Am. Chem. Soc.* **2004**, *126*, 10619-10631.

184. Byrne, A. T.; O'Connor, A. E.; Hall, M.; Murtagh, J.; O'Neill, K.; Curran, K. M.; Mongrain, K.; Rousseau, J. A.; Lecomte, R.; McGee, S.; Callanan, J. J.; O'Shea, D. F.; Gallagher, W. M. *Br. J. Cancer* **2009**, *101*, 1565-1573.
185. Scherer, H. *Ann. Chem. Pharm.* **1841**, *40*, 1-64.
186. Hausmann, W. *Biochem. Z.* **1911**, *30*, 276-316.
187. Meyer-Betz, F. *Dtsch. Arch. Klin. Med.* **1913**, *112*, 476-503.
188. Schwartz, S. K., Absolon, K.; Vermund, H. *Univ. Minn. Med. Bull.* **1955**, *27*, 7-8.
189. Lipson, R. L.; Baldes, E. J. *Arch. Dermatol.* **1960**, *82*, 508-516.
190. Lipson, R. L., Baldes, E. J.; Olsen, A. M. *J. Natl. Cancer Inst.* **1961**, *26*, 1-11.
191. Dougherty, T. J., Grinday, G. B.; Fiel, R.; Weishaupt, K. R.; Boyle, D. G. *J. Natl. Cancer Inst.* **1975**, *55*, 115-121.
192. Kelly, J. F., Snell, M. E.; Berenbaum, M. C. *Br. J. Cancer* **1975**, *31*, 237-244.
193. Kelly, J. F.; Snell, M. E. *J. Urol.* **1976**, *115*, 150-151.
194. Dougherty, T. J. *Cancer Res.* **1978**, *36*, 2628-2635.
195. Tsuchiya, A.; Obara, N.; Miwa, M.; Ohi, T.; Kato, H.; Hayata, Y. *J. Urol.* **1983**, *130*, 79-82.
196. McCaughan, J. S., Hicks, W.; Laufman, L.; May, E.; Roach, R. *Cancer* **1984**, *54*, 2905-2910.
197. Dougherty, T. J. *Photochem. Photobiol.* **1983**, *38*, 377-379.
198. Dougherty, T. J.; Levy, J. G. *Biomedical Photonics Handbook*, ed. T. Vo-Dinh, CRC Press, New York, **2003**, Chapter 38, 1-16.
199. Sutedja, T.; Baas, P.; Stewart, F.; van Zandwijk, N. *Eur. J. Cancer* **1992**, *28*, 1370-1373.

200. Nathan, T. R.; Whitelaw, D. E.; Chang, S. C.; Lees, W. R.; Ripley, P. M.; Payne, H.; Jones, L.; Parkinson, M. C.; Emberton, M.; Gillams, A. R.; Mundy, A. R.; Bown, S. G. *J. Urol.* **2002**, *168*, 1427-1432.
201. Moore, C. M.; Nathan, T. R.; Lees, W. R.; Mosse, C. A.; Freeman, A.; Emberton, M.; Bown, S. G. *Lasers Surg. Med.* **2006**, *38*, 356-363.
202. Kennedy, J. C.; Pottier, R. H. *J. Photochem. Photobiol. B* **1992**, *14*, 275-292.
203. Keam, S. J.; Scott, L. J.; Curran, M. P. *Drugs* **2003**, *63*, 2521-2554.
204. Zhu, T. C.; Dimofte, A.; Finlay, J. C.; Stripp, D.; Busch, T.; Miles, J.; Whittington, R.; Malkowicz, S. B.; Tochner, Z.; Glatstein, E.; Hahn, S. M. *Photochem. Photobiol.* **2005**, *81*, 96-105.
205. Dimofte, A.; Zhou, T. C.; Hahn, S. M.; Lustig, R. A. *Lasers Surg. Med.* **2002**, *31*, 305-312.
206. Lim, J. I. *Ophthalmol. Clin. N. Am.* **2002**, *15*, 473-478.
207. Berdugo, M.; Bejjani, R. A.; Valamanesh, F.; Savoldelli, M.; Jeanny, J.-C.; Blanc, D.; Ficheux, H.; Scherz, A.; Salomon, Y.; BenEzra, D.; Behar-Cohen, F. *Invest. Ophthalmol. Visual Sci.* **2008**, *49*, 1633-1644.
208. Ethirajan, M.; Chen, Y.; Joshi, P.; Pandey, R. K. *Chem. Soc. Rev.* **2011**, *40*, 340-362.
209. Celli, J. P.; Spring, B. Q.; Rizvi, I.; Evans, C. L.; Samkoe, K. S.; Verma, S.; Pogue, B. W.; Hasan, T. *Chem. Rev.* **2010**, *110*, 2795-2838.
210. Snyder, J. W.; Skovsen, E.; Lambert, J. D. C.; Ogilby, P. R. *J. Am. Chem. Soc.* **2005**, *127*, 14558-14559.
211. Hilmey, D. G.; Abe, M.; Nelen, M. I.; Stilts, C. E.; Baker, G. A.; Baker, S. N.; Bright, F. V.; Davies, S. R.; Gollnick, S. O.; Oseroff, A. R.; Gibson, S. L.; Hilf, R.; Detty, M. R. *J. Med. Chem.* **2002**, *45*, 449-461.

212. Schmitt, F.; Govindaswamy, P.; Süß-Fink, G.; Ang, W. H.; Paul J. Dyson, Juillerat-Jeanneret, L.; Therrien, B. *J. Med. Chem.* **2008**, *51*, 1811-1816.
213. Taquet, J.-P.; Frochot, C.; Manneville, V.; Barberi-Heyob, M. *Curr. Med. Chem.* **2007**, *14*, 1673-1687.
214. Arnbjerg, J.; Jiménez-Banzo, A.; Paterson, M. J.; Nonell, S.; Borrell, J. I.; Christiansen, O.; Ogilby, P. R. *J. Am. Chem. Soc.* **2007**, *129*, 5188-5199.
215. Gomer, C. J. *Photochem. Photobiol.* **1991**, *54*, 1093-1107.
216. Wang, S.; Gao, R.; Zhao, F.; Selke, M. *J. Mater. Chem.* **2004**, *14*, 487-493.
217. Tada, D. B.; Vono, L. L. R.; Duarte, E. L.; Itri, R.; Kiyohara, P. K.; Baptista, M. S.; Rossi, L. M. *Langmuir* **2007**, *23*, 8194-8199.
218. Wilson, B. C.; Patterson, M. S.; Lilge, L. *Lasers Med. Sci.* **1997**, *12*, 182-199.
219. Boucher, D. *AIP Conf. Proc.* **2011**, 1364, 73-86.
220. Khan, A.U.; Kasha, M. *J. Chem. Phys.* **1963**, *39*, 2105-2106.
221. De Rosa, M. C.; Crutchley, R. J. *Coord. Chem. Rev.* **2002**, *233/234*, 351-371.
222. Arnold, S. J.; Kubo, M.; Ogryzlo, E. A. *Adv. Chem. Ser.* **1968**, *77*, 232-241.
223. Merkel, P. B.; Kearns, D. R. *J. Am. Chem. Soc.* **1972**, *94*, 1029-1030.
224. Franck, B.; Nonn, A. *Angew. Chem. Int. Ed. Engl.* **1995**, *34*, 1795-1811.
225. Kerr, J. F.; Wyllie, A. H.; Currie, A. R. *Br. J. Cancer* **1972**, *26*, 239-257.
226. Ashkenazi, A.; Dixit, V. M. *Science* **1998**, *281*, 1305-1308.
227. Oleinick, N. L.; Morris, R. L.; Belichenko, I. *Photochem. Photobiol. Sci.* **2002**, *1*, 1-21.
228. Perlin, D. S.; Murant, R. S.; Gibson, S. L.; Hilf, R. *Cancer Res.* **1985**, *45*, 653-658.
229. Kumar, C. V.; Qin, L.; Das, P. K. *J. Chem. Soc., Faraday Trans. 2* **1984**, *80*, 783-793.
230. Ramaiah, D.; Joy, A.; Chandrasekhar, N.; Eldho, N. V.; Das, S.; George, M. V. *Photochem. Photobiol.* **1997**, *65*, 783-790.

231. Jiang, X. J.; Yeung, S. L.; Lo, P. C.; Fong, W. P.; Ng, D. K. P. *J. Med. chem.* **2011**, *54*, 320-330.
232. Králová, J.; Bríza, T.; Moserová, I.; Dolenský, B.; Vasek, P.; Poucková, P.; Kejík, Z.; Kaplánek, R.; Martásek, P.; Dvorák, M.; Král, V. *J. Med. Chem.* **2008**, *51*, 5964-5973.
233. Ragàs, X.; Sánchez-García, D.; Ruiz-González, R.; Dai, T.; Agut, M.; Hamblin, M. R.; Nonell, S. *J. Med. Chem.* **2010**, *53*, 7796-7803.
234. Krishnamurthy, M. *Inorg. Chim. Acta* **1977**, *25*, 215-218.
235. Thomas, A. P.; Saneesh Babu, P. S.; Asha Nair, S.; Ramakrishnan, S.; Ramaiah, D.; Chandrashekar, T. K.; Srinivasan, A.; Radhakrishna Pillai, M. *J. Med. Chem.* **2012**, *55*, 5110-5120.
236. Belair, J. P.; Ziegler, C. J.; Rajesh, C. S.; Modarelli, D. A. *J. Phys. Chem. A* **2002**, *106*, 6445-6451.
237. Van Lier, J. E.; Tian, H.; Ali, H.; Cauchon, N.; Hassèsian, H. M. *J. Med. Chem.* **2009**, *52*, 4107-4110.
238. Mroz, P.; Bhaumik, J.; Dogutan, D. K.; Aly, Z.; Kamal, Z.; Khalid, L.; Kee, H. L.; Bocian, D. F.; Holten, D.; Lindsey, J. S. *Cancer Lett.* **2009**, *282*, 63-76.
239. Vermes, I.; Haanen, C.; Steffens-Nakken, H.; Reutellingsperger, C. *J. Immunol. Methods* **1995**, *184*, 39-51.
240. Lazebnik, Y. A.; Kaufmann, S. H.; Desnoyers, S.; Poirier, G. G.; Earnshaw, W. C. *Nature* **1994**, *371*, 346-347.
241. Nicholson, D. W.; Ali, A.; Thornberry, N. A.; Vaillancourt, J. P.; Ding, C. K.; Gallant, M.; Gareau, Y.; Griffin, P. R.; Labelle, M.; Lazebnik, Y. A. *Nature* **1995**, *376*, 37-43.